FIBRE-BASED WEARABLE SENSORS FOR MONITORING HUMAN HEALTH AND ACTIVITIES

A thesis submitted to the University of Manchester for the degree of

Doctor of Philosophy

in the Faculty of Science and Engineering

2022

Zekun Liu

School of Natural Sciences

List of Contents

List of Figures

List of Abbreviations

PAMD	Polymer-assisted metal deposition
BSNs	Body sensing networks
CNT	Carbon nanotube
PDMS	Polydimethylsiloxane
SEM	Scanning electron microscopy
TEM	Transmission electron microscopy
EDS	Energy dispersive spectroscopy
XPS	X-Ray photoelectron spectroscopy
TPU	Thermoplastic polyurethane
GF	Gauge factor
SBS	Styrene-butadiene-styrene
PVDF	Polyvinylidene fluoride
GO	Graphene oxide
rGO	Reduced graphene oxide
NWs	Nanowires
PTFE	Polytetrafluoroethylene
NPs	Nanoparticles
CVD	Chemical vapour deposition
PVA	Poly (vinyl alcohol)
SDS	Sodium dodecyl sulfate
PA	Polyamide
PET	Polyester
RFID	Radiofrequency identification
NFC	Near field communication
VR	Virtual reality
AR	Augmented reality
GKHF	Graphited knitted hemp fabric
r-GKHF	Rib-graphited knitted fabric
p-GKHF	Plain-graphited knitted fabric
pd-GKHF	Plain derivative-graphited knitted fabric
CF	Carbonized fabric

CDCF	Copper-deposited carbonized fabric
CNN	Convolutional neural network
FFT	Fast Fourier transform
OCF	Oxidized carbonized fabric
RH	Relative humidity
OCG	Oxygen-related carbon group
WWC	Water weight change
RC	Resistance change
EMRI	Electricity-moisture response index
LSTM	Long short-term memory
PBIS	Pressure and bending insensitive strain

List of Publications and Awards

Journal Papers

[1] **Z. Liu#(Co-first author)**, T. Zhu#, J. Wang, Z Zheng, Y. Li, J Li, Y. Lai. Functionalized fibre-based strain sensors: pathway to next-generation wearable electronics. Nano-Micro Letters. 14 (2022) 1-39.

[2] **Z. Liu,** Y. Zheng, L. Jin, K. Chen, H. Zhai, Q. Huang, Z. Chen, Y. Yi, M. Umar, L. Xu, Y. Li, Z. Zheng, Highly breathable and stretchable strain sensors with insensitive response to pressure and bending, Advanced Functional Materials, 31 (2021) 2007622.

[3] **Z. Liu,** Z. Li, H. Zhai, L. Jin, K. Chen, Y. Yi, Y. Gao, L. Xu, Y. Zheng and S. Yao, Y. Li, Z. Zheng A highly sensitive stretchable strain sensor based on multi-functionalized fabric for respiration monitoring and identification, Chemical Engineering Journal, 426 (2021) 130869.

[4] **Z. Liu,** K. Chen, A. Fernando, Y. Gao, G. Li, L. Jin, H. Zhai, Y. Yi, L. Xu, Y. Zheng, Y. Li, Z. Zheng, Permeable graphited hemp fabrics-based, wearing-comfortable pressure sensors for monitoring human activities, Chemical Engineering Journal, 403 (2021) 126191.

[5] Y. Yi, C. Yu, H. Zhai, L. Jin, D. Cheng, Y. Lu, Z. Chen, L. Xu, J. Li, Q. Song, P. Yue, **Z. Liu*,** Y. Li*, Molecular engineering humidity sensing for environmental and wearable detection. Submitted to Nature Communications. 2022.

Conference Presentation

[1] An anti-jamming strain sensor for the construction of body sensing networks. Textile Bioengineering and Informatics Society Conference. France. 2021. (Oral presentation, Online)

[2] Fibre-based pressure sensor for the applications of monitoring human activities and health. 2nd-Manchester China-UK forum of international young scholars. Manchester, UK. 2020. (Oral presentation, Online)

[3] Structural colours in the applications of textiles. Textile Bioengineering and Informatics Society Conference. Suzhou, China. 2019. (Oral presentation)

Awards

[1] Outstanding Oral Presentation of Textile Bioengineering Informatics Society. France. 2021. (Online).

[2] Outstanding Volunteer in Textile Bioengineering and Informatics Society Conference. France. 2021. (Online)

[3] Honorable Mention Award in UK Doctoral Research Awards Competition. 2020.

Abstract

Wearable sensors are arousing increasing research interests in recent years due to their great potential in motion detection, personal and public healthcare, future entertainment, man-machine interaction, artificial intelligence, and so forth. Much research has focused on fibre-based wearable sensing devices because of the appealing performance of fibres, including processing flexibility, wearing comfortability, outstanding lifetime and serviceability, low-cost and large-scale capacity. However, some vital performance of the sensing devices in practical applications is still far from optimal, such as wearable comfort, sensitivity, sensing reliability in the fickle microclimate of wearable interfaces and multi-direction dynamic tactile stimulations. This thesis proposes novel design and fabrication of fibre-based wearable pressure, strain, and humidity sensors by the material functionalization approaches of carbonization, in-situ oxidation, and polymer-assisted metal deposition (PAMD). The devices overcome the abovementioned challenges, aiming to construct body sensing networks (BSNs) with high wearing comfort and sensing reliability for monitoring human health and activities.

The project mainly focuses on fibre functionalization and sensing device fabrication through many novel approaches for monitoring human health and activities. 1) Breathable wearable pressure sensors are fabricated by directly carbonizing knitted hemp fabrics at high temperatures. Unlike mostly reported pressure sensors made with active materials with the encapsulation of elastomers, the encapsulation-free sensor shows high permeability by taking advantage of the porous structure of the textile. 2) By combining carbonization and the PAMD, a strain sensor made with carbonized linen fabric with copper deposition presents a very high sensitivity (GF~3557.6 in the strain range from 0 to 48%). The concept of improving sensor sensitivity by using two-layer sensing elements can be extended to many sensing devices. 3) This work firstly finds that carbonized fabrics can directly detect humidity, the sensitivity is controllable by changing the oxidation time after the carbonization. The strategy is extendable to many carbonized substates. 4) A strain sensor based on the PAMD and an innovative embroidery technique is developed. The sensor processes both breathability and insensitivity to bending and pressuring inputs. The BSNs based on the developed pressure, strain and humidity sensors show high performance in addressing the issue of complicated wearable mechanical inputs and microclimate changes.

This project develops many high-performance, fibre-based wearable sensors via novel fibre functionalization and device fabrication and demonstrates their great application potential in the high-accuracy and anti-jamming BSNs. It proposes many concepts and strategies for wearable sensing devices, which will arouse much attention in the research area of wearable and flexible electronics.

Declaration

No portion of the work referred to in this thesis has been submitted in support of an application for another degree or qualification of this or any other university or other institutes of learning.

Copyright Statement

Acknowledgments

I am greatly indebted to my supervisor, Professor Yi Li, for providing me the great opportunity to study in the group, the valuable instructions and suggestions on my experiments, the support, inspiration and encouragement in both my research and life. He has been an optimistic, kind-hearted and accommodating person that can be considerate of others. Under his supervision, I get improved in the methodology of researching and thinking as well as the living. He also gave me many supports in life and trained me in many sports activities such as tennis, table tennis, and badminton that I am extremely interested in. He is the example worth learning in my life.

Great acknowledgment is also made to Prof. Zijian Zheng, and Dr. Jiashen Li for their support of my research work. I appreciate their guidance and help during my PhD even though they are not my official supervisors. They broaden my boundary knowledge in polymer-assisted metal deposition and conductive polymer networks respectively, which is of significance to my PhD research at the technology level. I also would like to thank my MSc supervisor, Prof. Gang Li, for his recommendation in my PhD application at the very beginning.

I also owe a special dept of gratitude to all our group members and some friends including Mr. Heng Zhai, Dr. Lu Jin, Miss Yan Zheng, Dr. Lulu Xu, Mr. Yangpeiqi, Yi, Mr. Yangyang Fan, Miss Sirui Yao, Dr. Zhongda Chen, Mr. Zhangchi Liu, Dr. Muhammad Umar, Dr. Juanyu Piao, Dr. Zhenhong Li, Dr. Chuang Yu, and Miss Ludanni Li for their assistance in sample characterizations and experiment set-up in research. They are helpful and outgoing people. I also enjoy the time we spent together

in the laboratory and daily activities. The PhD study would suffer an eclipse without them.

I would like to express my special gratitude to Miss Kaili Chen who gave me encouragement and support in my life during PhD study. She is a good listener that I like to share my pleasure and unpleasure with. Many thanks for her encouragement when I was down. There is much memorable time I spent with her together. Wish her would have a happy and successful PhD journey throughout.

Last, my huge thanks would go to my beloved family for their deep and constant love throughout my life. I much appreciate their loving support and consideration with asking for nothing in return. They will always be my motivation to be a kind-hearted, helpful and altruistic person in my whole life.

The PhD study is funded through China Scholarship Council (CSC), department of materials, The University of Manchester. I would like to express my deep appreciation to these funding supports and more importantly, the recommendation from Prof. Yi Li.

Chapter 1
Introduction

1.1 Background and Motivation

Real-time perception by skin-mountable wearable sensors plays a vital role in the applications of personal and public healthcare management, artificial intelligence, and future fictitious entertainment.[1-5] Such devices can immediately and directly convert physical stimulation into electrical signals with the advantages of flexibility, wearability, lightweight, high efficiency, and accuracy. They overcome the limited sensing range and non-portability of conventional rigid sensors, driving a technological revolution in next-generation electronics. There are mainly resistive, capacitive, piezoelectric, triboelectric, and optical wearable sensing devices from a sensing mechanism perspective.[6-9] The resistance-based ones possess uncomplicated fabrication and configuration, and signal-collect systems, as well as decent flexibility and sensing reliability. By contrast, the piezoelectric, capacitive and triboelectric sensing electronics still face many challenges including poor sensing reliability in static or dynamic conditions. Though previous research has shown optical fibre-based sensors with promising results in terms of durability, the sensing measurement often needs sophisticated read-out equipment, which restricts their application scenarios.[10] Therefore, we will mainly focus on resistive sensing devices in this work.

Several materials have illustrated their potential for wearable sensors, and materials in fibre form are a competitive candidate. Fibres have been widely used for human clothes and other commodities in daily life for thousands of years. Mankind benefits from them by utilizing their outstanding features including excellent resilience and durability of

hemp, remarkable touch and structure controllability of silk, as well as outstanding thermal protection, moisture absorption, and excellent perspiration conductivity of cotton.[11-16] In recent years, it has been found that they are also competitive as substrate materials of wearable electronics on account of both outstanding flexibility and permeability, as well as validated harmlessness to the human body.[17-19] These flexible substrates can be developed as wearable electronics via various processing: carbonization, graphitization, printing, chemical/electrolytic deposition, graft copolymerization, and so forth.[20-24] Besides, some synthetic fibres made with graphene, carbon nanotube, metals, and conductive polymers endow them with good conductivity and flexibility in nature.[25-28] The attributes pave a new way for the low-cost and scalable fabrication of fibre-based wearable sensing devices.

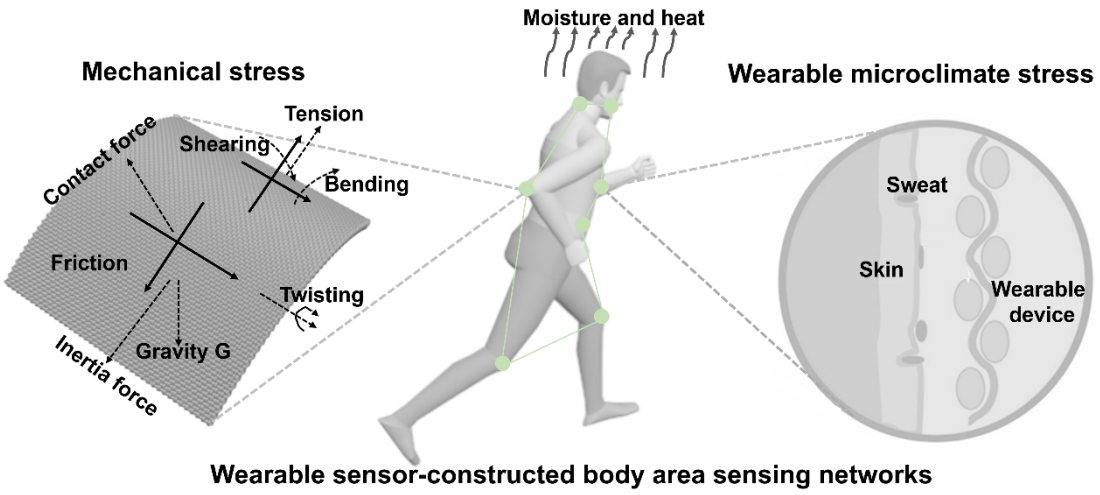

Figure 1-1. Illustration of key challenges of body area wearable sensors towards mechanical and wearable microclimate stress.

Even with several-year development in wearable sensors, whether they are based on fibres or polymers, body area sensing networks constructed with the devices have been suffering complex mechanical inputs and changeable wearable microclimate. The mechanical inputs include gravity, friction, contact pressuring, twisting, bending,

shearing, tension and so on, and the wearable microclimate mainly refers to heat and moisture from both the human body and the external environment as illustrated in Figure 1-1. Most reported sensors fail to address the challenges, leading to a suboptimal sensing accuracy in monitoring human activities and health.

1.2 Research Gaps of Fibre-based Sensors

Based on the summary and analysis in Section 2, fibre-based sensors for tactile and noncontact sensing, include mechanical (e.g., pressure and strain) and humidity sensors by converting the corresponding inputs into electrical signals. Previous research has always focused on sensing performance improvement, while some vital properties such as wearing comfort, washing ability, sensing reliability in complicated and volatile wearable microclimate, and insensitive response to untargeted stimulation, are highly ignored. Such gaps will be pointed out below, and this work aims to overcome the challenges.

1.2.1 Research Gaps of Pressure and Strain Sensors

1) Conventional pressure and strain sensors lack breathability, which may bring about unpleasant wearing feelings. Most reported pressure and strain sensors are made with active materials with the encapsulation of elastic polymers (e.g., Ecoflex, PDMS). This configuration, however, has to sacrifice the permeability to air, water vapour and moisture that is of vital importance to wearing comfort, due to the poor pore structure of polymers. Pure fibre-based wearable sensing devices with high porous structures show potential in addressing this challenge, which is rarely reported to date.

2) Most reported fibre-based strain sensors fabricated through one active element show limited sensing performance. The limited performance is far from optimal in practical application scenarios. It lacks an effective approach to significantly improve sensing properties (e.g., sensitivity and sensing range).

3) Previously reported flexible strain sensors reveal a non-negligible response to pressuring and bending, while most surface movements at the time of tensile strain also contain a combination of bending and compression. Body area detection becomes inaccurate through the implementation because of multi-direction mechanical inputs. Developing a strain sensor only sensitive to applied strain while insensitive to other stimulation is a challenge today.

1.2.2 Research Gaps of Humidity Sensor

1) Fibre-based wearable humidity sensors are not machine washable due to the hydrophilicity and redispersion of the humidity-response materials to water. Unlike tactile sensors, the active materials must be exposed to the environment to detect humidity without protection. They will dissolve into washing liquid to some extent during machine washing. The humidity sensor cannot endure long-time wearing because of performance degradation. It has been a critical challenge not addressed.

2) Controlling initial resistance and sensitivity to meet various detection needs is another key challenge of wearable fibre-based humidity sensors. The initial resistance and sensitivity are important to data collection throughout humidity detection. It lacks a straightforward and effective approach to controlling the initial resistance and sensitivity of humidity sensors.

3) Humidity sensors, applied to detect humidity, also respond to many mechanical inputs such as bending and compression because of the non-integrated structure of

humidity-response materials. In this case, humidity detection has to endure signal interference on many occasions, leading to a suboptimal accuracy.

1.3 Research Objectives

To address the abovementioned challenges of fibre-based pressure, strain and humidity sensors, the research objectives include:

1) To develop a pure fibre-based, encapsulation-free pressure sensor with both high performance and good permeability to air, water vapour and moisture to ensure wearing comfort. This work will also investigate the wearability of rubber-encapsulated pressure sensors to compare the feeling when wearing the two-type sensors.

2) To find an effective approach to significantly improve the sensitivity and stretchability of a fibre-based strain sensor by applying two layers of sensing elements (i.e., carbonized fibre and copper particles).

3) To explore a straightforward and effective strategy for the fabrication of fibre-based wearable humidity sensor with machine wash ability, insensitivity to bending and compression, and controllability of initial resistance and sensitivity. At the same time, the effectiveness of this approach will also be evaluated by changing various fibre substrates.

4) To fabricate a strain sensor through a novel design to achieve high permeability to air, water vapour and moisture, high sensitivity, and stretchability, as well as negligible response to bending and compression.

1.4 Research Methodology

The research methodology for each objective is listed as follows.

1) To develop an encapsulation-free pressure sensor by directly carbonizing kitting hemp fabrics at high temperatures with the protection of inert gas. Conductive silver paste is coated at both ends of the carbonized fabrics serving as electrodes. It will investigate the carbonization temperature in determining fabric structure, fabric conductivity and sensor sensitivity, which are characterized through a light microscope, SEM, TEM, Raman spectrum, digital multimeters, and universal mechanical test instrument, etc. The sensing mechanism will be explained through simple electrical models. This work will also explore the wearing comfort of the sensor by testing its breathability to air, water vapour and moisture. The wearing comfort in wearing the breathable and conventional unbreathable sensors is evaluated by long-term wearing. Finally, it will assess the application potential of the device in monitoring human motion and activities via attaching it to different locations of the human body.

2) To explore an effective approach to improve both sensitivity and stretchability of wearable strain sensors using two layers of sensing elements. Pristine woven fabric will be carbonized at high temperature with the protection of inert gas, and a layer of copper particles is deposited onto the carbonized fabric through polymer-assisted metal deposition (PAMD). The morphology and structure changes after the carbonization and the PAMD are characterized by light microscope, SEM, EDS, TEM, Raman spectrum, etc. This work will investigate the carbonization temperature and PAMD time in determining sensing performance, which is measured by a digital multimeter and universal mechanical test instrument. Both geometry diagrams and electrical models will be demonstrated to show the sensing mechanism. Demonstration in applications

includes motion and health detection, and a respiration monitoring and warning system, showing its potential in future healthcare.

3) To fabricate a free-standing humidity sensor based on carbonatization and in-situ oxidation of pristine cotton fabric, endowing it with washability, insensitivity to bending and compression, and tuneable sensing performance. It will investigate the carbonization temperature and oxidation time in determining the sensor performance. The material structure and property induced by carbonization and oxidation will be surveyed through SEM, EDS, TEM, XPS, Raman spectrum, contact angle, etc. The controllable humidity is applied in a humidity cabinet with a digital multimeter detecting resistance to measure the sensor sensitivity and sensing reliability. Commercialized washing machines and universal mechanical test instruments will be used to evaluate the washability and response to mechanical inputs. This work will also apply the approach to linen and silk fabrics to prove the effectiveness of the strategy in the fabrication of the high-performance and free-standing humidity sensor. Finally, the humidity sensor will be utilized for environmental monitoring and noncontact detection such as the sensing of respiration and fingertip motion.

4) To develop a strain sensor with high breathability and sensing property, as well as insensitivity to bending and compression, which is artistically constructed by embroidering elastic and conductive yarns (developed through PAMD) on a water-dissolvable substrate. The continuously conductive yarns will make up a strain sensing network after removing the water-dissolvable substrate. It is going to evaluate the wearing comfort by testing its permeability to air, water vapour and moisture. By comparing its electrical response between applied tensile strain and bending to show its negligible sensitivity to the bending and pressuring inputs. After the wearing and

sensing performance evaluation, the sensor will be used to detect motion and health signals by serving as a full-range body sensing network.

1.5 Thesis Structure

The thesis will mainly focus on fibre functionalization through carbonization, PAMD, in situ oxidation, and wearable sensing device fabrication by knitting, woven, and embroidery, for the applications of pressure, strain and humidity detection in body area sensing networks. Figure 1-2 shows the outline of the thesis.

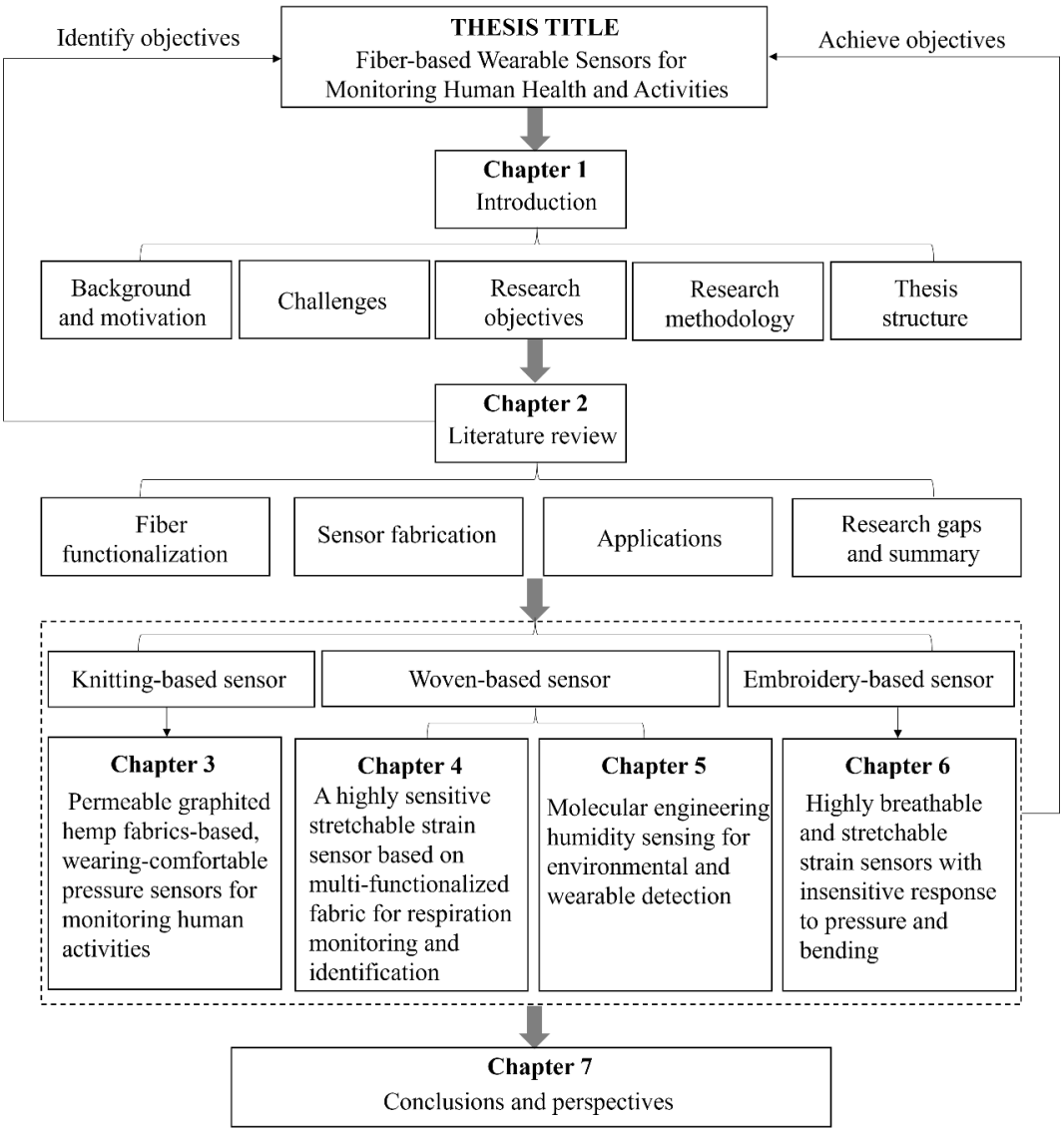

Figure 1-2. The outline of the thesis.

Chapter 2
Literature Review

2.1 Introduction

In this chapter, recent development and advance on fibre material functionalization, fibre-based wearable pressure, strain and humidity sensors are reviewed with typical examples. It aims to identify research gaps of state-of-art devices reported in published research.

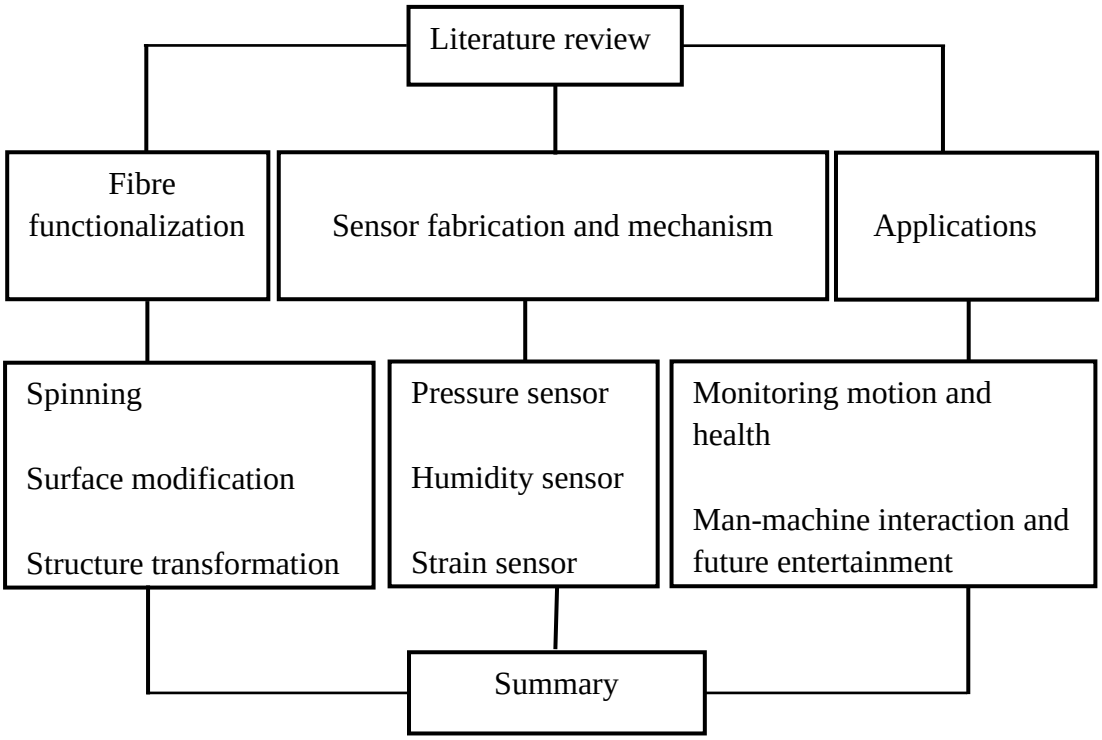

Figure 2-1. The outline of the literature review.

Figure 2-1 illustrates the outline of the literature review. In section 2.2, it summarizes the superiority of fibres as flexible sensing devices, and their functionalization approaches including direct spinning, surface modification, as well as structure transformation. In section 2.3, the sensor fabrications of pressure, strain and humidity are introduced, which is mainly focused on resistance-based ones as such devices with

a high sensing performance and straightforward construction. It also analyses corresponding sensing mechanisms with typical devices as examples. The review then summaries the application of the abovementioned wearable sensors in motion and health monitoring, as well as man-machine interaction and future entertainment (In section 2.4). In section 2.5, it finally forecasts the research gaps and future expectations according to the review.

2.2 Fibre Materials and Functionalization Strategies

Fabrication of wearable sensors via conductive fibres is a facile and low-cost approach to implement both flexibility and high performance of the devices.[29, 30] Conductive fibres can be developed via spinning, surface modification, and inducing structural transformation, which mainly includes blending active materials into fibres, and modifying existing nonconductive fibres. The spinning technique can massively develop conductive fibres with adjustable conductivity, and controllable diameter and cross-sectional shape by changing spinning parameters such as active material concentration, spinning pinhole and speed. While high conductivity and mechanical performance are not easy to achieve together without further processing, surface modification is one of the most effective and feasible approaches for the fabrication of conductive fibres, which can be achieved through coating or depositing active elements on fibre surfaces. The conductive elements endow the fibre with good conductivity together with poor washability and friction stability. Inducing transformation from a nonconductive into a conductive structure is another practical method. A typical example is carbonization, where pristine structures will become carbon-based structures as a result of high-temperature treatment. The conductivity can be simply

controlled by changing processing temperature, but the carbonized fibres always lack good mechanical strength.

2.2.1 Spinning

Spinning is an efficient way to prepare conductive fibres by directly adding conductive materials to fibrous structures.[29-32] A versatile method that has been widely utilized for large-scale fabrication of fibres is wet-spinning. In early works, the coaxial wet-spinning approach with chemical reprocessing (Figure 2-2a) was employed to prepare belt-like fibres from single-walled CNT for strain sensing.[33] The belt-like fibres have width and thickness of 1050 and 200 μm respectively, with good conductivity of 142.6 Ω per 2 cm. After being covered with a thermoplastic elastomer sheath, the high-density staple fibres could detect strain due to the crack formation during the stretching process. Similarly, through wet-spinning, another conductivity-adjustable fibre was developed by mixing thermoplastic polyurethane (TPU) and multi-walled CNT with a weight percentage of 8:1.[34] The fibre is proved to have high tensile strength of ~28 MPa and a maximum failure strain of 310% (Figure 2-2b). By taking advantage of the remarkable mechanical property of TPU and good electro-conductibility of the CNT, the composited fibres were able to detect tensile strain up to 100% with the high sensitivity of GF value of 2800. As shown in Figure 2-2c, the wet-spinning technique can also be utilized to achieve another performance-controllable, core-sheath fibre made with multi-walled CNT and platinum-catalyzed Ecoflex-30.[35] The dimensions can be well controlled via the regulation of nozzle sizes and flow rates of CNT and Ecoflex-30 inks. By increasing the loaded CNT content, the core-sheath strain sensor shows a broader sensing range (>300% strain) and an outstanding GF of 1378.

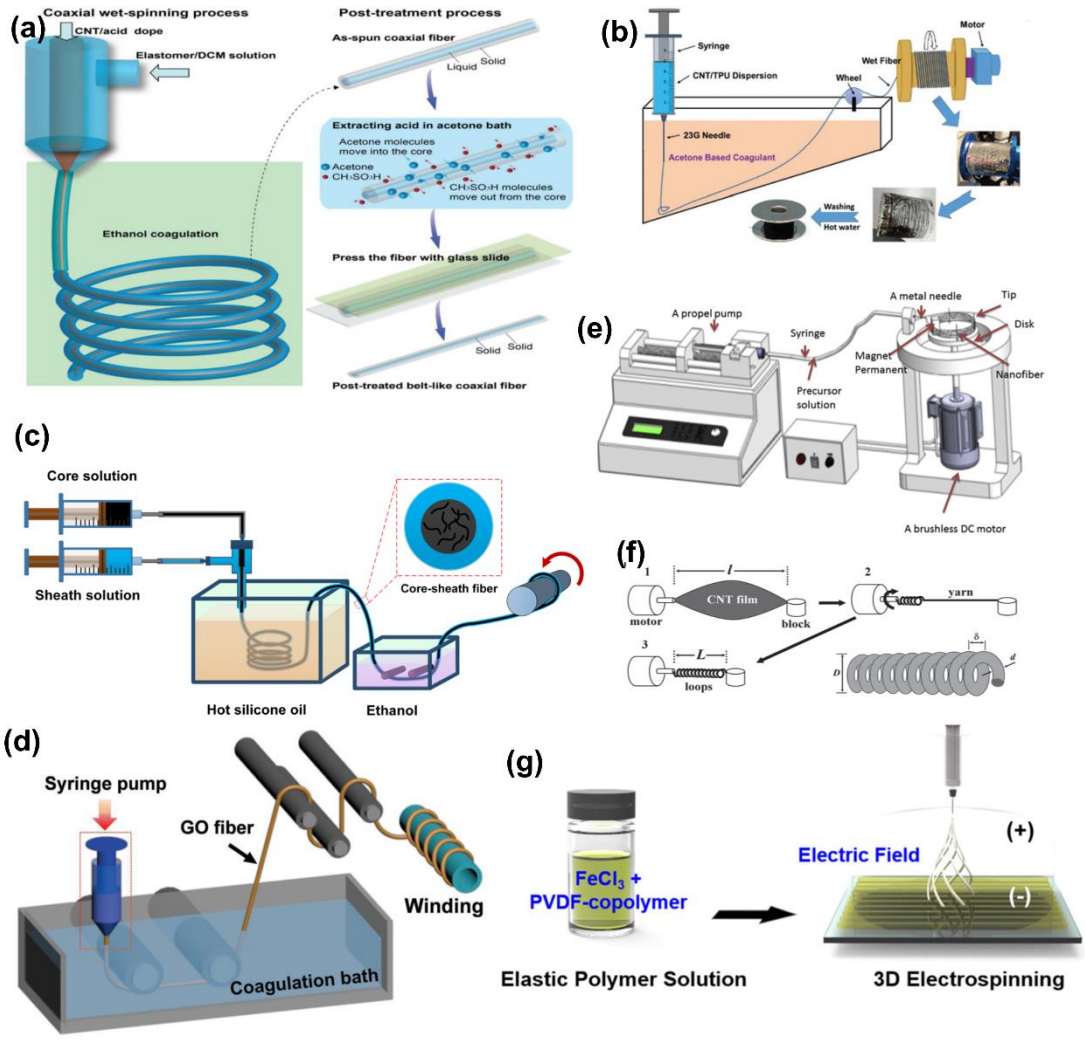

Figure 2-2. Conductive fibres made with spinning. (a) Wet-spinning and post-treatment process for the fabrication of thermoplastic elastomer and CNT composted fibres.[33] (b) The production of thermoplastic polyurethane/CNT fibres for strain sensing via wet-spinning.[34] (c) Wet-spinning process for the fabrication of Ecoflex-30 and CNT composited fibres.[35] (d) Fabrication of graphene fibre through wet spinning for humidity detection.[36] (e) Schematic diagram of magnetic-mechanical spinning.[37] (f) Schematic diagram of fabrication of spring-like CNT rope from CNT film by spinning technique.[38] (g) Construction of 3D-structure nanofibre through electrospinning.[39]

Besides, other composited fibres such as graphene/polydimethylsiloxane (PDMS),[40] poly(styrene-butadiene-styrene) (SBS)/CNT,[41] or TPU/CNT[42] can also be produced via wet-spinning for assembling sensors. In another example, graphene was coated onto a plastic substrate through wet spinning (Figure 2-2d), and the composite shows humidity

sensing ability by taking advantage of the feature that graphene is sensitive to humidity.[36] These fibres made by wet spinning mainly include conductive and elastic materials, serving as sensing elements and mechanical protection, respectively. In addition to wet spinning of conductive fibres, mechanical spinning also provides a new route to produce strain-detectable fibres. For example, a solution containing polyaniline/polyvinylidene fluoride/γ-Fe_2O_3 (PANI/PVDF/γ-Fe_2O_3) was combined with conductive fibres through magnetic-mechanical spinning (Figure 2-2e), illustrating the advantages of large scale capacity and property controllability.[37] Such fibres with an average diameter of 850 nm made up a twisted rope with high elongation up to the strain of 440% and good conductivity of 6.4×10^4 S/cm. Alternatively, spring-like CNT ropes produced by mechanical spinning with neat and uniform loops over long-distance arrangements were also reported (Figure 2-2f),[38] exhibiting an outstanding stretchability and tolerable tensile strain up to 285%. These fibre-based, twisted ropes display great potential in strain detection because of their eminent stretchability and conductivity.

Electrospinning is another commonly utilized spinning technique to produce conductive fibre materials. Generally, the fibres are electro-spun by incorporating conductive fillers such as graphene, CNT, conductive polymer, and carbon into the polymer. However, this method shows negative influence on the electrical properties of the fibres in that the polymer always lacks conductivity. An alternative approach is to produce electrospinning elastic fibres before modifying the fibres with conductive materials. For instance, a previous work prepared an electrospinning TPU fibre modified with CNT and PDMS.[43] The conductivity of the fibre-based membranes shows a significant increase trend when enhancing ultrasonication time during the

modification process. It can reach 10 S/m after ultrasonication for 10 min. The concept was also reported in an early work by modifying TPU nanofibres with reduced graphene oxide (rGO) for strain sensing.[44] A previous work reported a 3D-structure composite made with conductive polymer-modified electrospinning nanofibres (Figure 2-2g).[39] It can detect applied pressure due to its novel structure. Several other approaches using modified electrospinning techniques have been demonstrated to yield similar strain-responsive fibres.[45, 46] Dry spinning [47] and melt spinning [48] were utilized to fabricate conductive fibres in previous studies as well. Early work established a simple dry spinning to prepare graphene mesh fabrics.[47] The mesh consists of several orthogonal GO fibres that can detect strain due to the high conductivity (703 S/cm) and outstanding tensile strength (582±17 MPa) of the GO fibre.

2.2.2 Surface Modification

Surface modification to non-conductive fibres, yarns, or fabrics is an effective and practical approach to producing fibre-based wearable sensors. This approach can be achieved through dip coating, roller coating, spray and rod coatings, printing, as well as surface depositions. For example, a bundle of silk fibres was firstly modified by graphite flakes through the rod coating process, then encapsulated with Ecoflex for strain detection.[49] There are considerable breakages among the graphited silk fibres during elongation, resulting in a resistance increase. Meanwhile, the remarkable elasticity and fatigue durability of Ecoflex enables a stable electrical signal output of up to 3000 cycles with 10% strain. Similar encapsulation approaches were also reported for many inelastic fibre-based strain sensors, such as PDMS encapsulated cotton fibres,[50] Ecoflex encapsulated CNT, and silk fibres.[51, 52]

Additionally, surface coating on elastic fibres by conductive elements is an effective approach to implementing strain detection.[53] Previous research developed an Ag nanowires (Ag NWs) dip-coated strain sensor with a core-shell structure. The commercial elastic thread acting as the core substrate is coated by Poly(vinylidenefluoride-co-trifluoroethylene) (P(VDF-TrFE)) nanofibres through electrostatic spinning, and the outermost layer is conductive Ag NWs (Figure 2-3a).[54] The outstanding stretchability and fatigue durability of elastic thread and P(VDF-TrFE), as well as the high conductivity of Ag, render the composted sensor a wide sensing range over the strain of 100%, and excellent durability (strain of 5%, frequency of 6 Hz) up to 10000 cycles. Similarly, another work reported ZnO NWs coated polyurethane (PU) fibres for fabricating strain sensors.[55] The high elastic PU fibre sensors feature a wide working range, up to 150% strain without any degeneration. It is also worthwhile to mention that one previous research exhibited a performance-controllable sensor manufactured from gold film/CNT coated PMDS fibre with beats.[56] The delicate beats structure of PDMS fibre can redistribute the surface deformation to perceive applied strain, which can be coated by many conductive elements to fabricate strain sensors. Significantly, fibre coating through polymer-assisted metal deposition (PAMD) is a creative approach to developing strain sensors. By coating a variety of metals (e.g., Cu, Ag, Ni, Co, Au, etc.), fibre and many soft substrates could maintain flexibility, stability as well as controllable conductivity, which are significant for the application of wearable detection.[57] In previous studies, Cu and reduced graphene-modified rose petals, and the Ni-modified fibres through PAMD played a function in stretching strain detection.[58, 59] However, such PAMD-functionalized fibre sensors showed limited working ranges, needing further enhancement in the future.

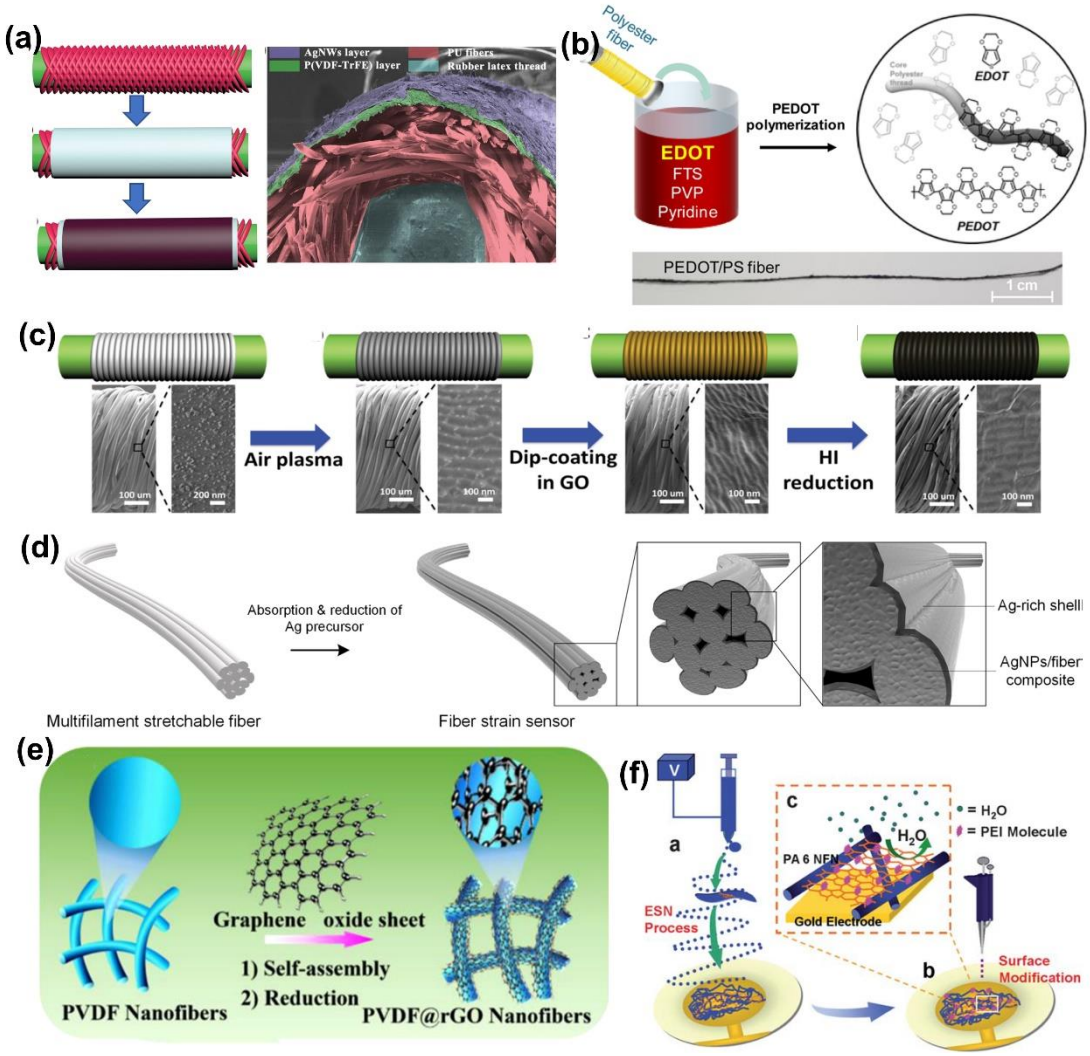

Figure 2-3. Preparation of conductive fibres by surface coating. (a) Illustration of P(VDF-TrFE) and Ag NWscoated elastic thread.[54] (b) In-situ polymerization of polyester yarns by PEDOT.[60] (c) Fabrication process of a spring-like strain sensor, with the structure of graphene-coated cover layer and PU core. (d) The illustration of Ag modified PU yarn with Ag-rich shell.[61] (e) Schematic diagram of graphene-modified PVDF nanofibres.[62] (f) Illustration of the preparation of sensing coatings on a quartz crystal microbalance.[63]

Conductive polymers coating is one commonly used approach. In one research, by using in situ polymerization, Poly(3,4-ethylenedioxythiophene) (PEDOT)-coated polyester yarns (with the conductivity of 600 Ω/cm after modification) were demonstrated to make up strain sensing elements after being sewed into fabrics (Figure

2-3b).[60] With the advantage of the yarns' outstanding wearability and assembling flexibility, a sensor-integrated glove was fabricated to rebuild various body motions such as finger bending and other movements. Another similar work reported charged chitosan-modified PU yarn from layer-by-layer dip coating for strain sensing.[64] Nevertheless, without further rubber encapsulation, the sensor shows a very limited working range due to unstable attachment of the coating layer under large-range elongation. The concept can also be extended to graphene or CNT-modified yarns. More interestingly, the elastic yarns covered by conductive yarns form a helix structure, enabling strain sensing ability due to the contact and separation of the out-layer conductive yarns. Figure 2-3c shows graphene-coated composites, including the spring-like architecture of functionalized cover layer and PU core.[65] The elastic PU drives the separation of spring-like covering yarns during the deformation process, endowing it with strain sensing ability. Similarly, both CNT-coated cotton yarns and polytetrafluoroethylene (PTFE) thread-covered silicone fibre were demonstrated for strain detection.[66] These spring-like sensors present remarkable fatigue resistance by taking advantage of their novel structure, as their coated layer suffers minor damage in repetitious stretching. Figure 2-3d displays an Ag-coated PU yarn achieved by a chemical reaction process on the fibre surface.[61] The rich-Ag particles formed a dense shell wrapped around the PU fibre, acting as electric response elements. However, even though the device exhibits remarkable sensitivity to tensile strain (GF=9.3×10^5 in the first stretching), the sensitivity cannot be well maintained in the following stretching process. The stability needs to be further enhanced by rubbers or other elastomers encapsulation. Another work reported a Cu-based yarn modified by graphene and poly(vinyl alcohol) (PVA).[67] The sensor with a core−sheath structure presents good electrical conductivity (9.6×10^3 S/m) and mechanical stretchability (590 MPa tensile

strength with 16% elongation), paving a facile and straightforward way to develop wearable sensors. The modification can also be achieved by the coating of graphene and Ag NPs. The conductive layer is further encapsulated by silicone to ensure its stability.[68] Figure 2-3e shows the modification of PVDF nanofibres by graphene GO and further reduction.[62] The rGO-modified nanofibres were then encapsulated by PDMS with copper at both ends as electrodes. It can detect pressure due to pressure-induced fibre deformation in geometry, and resistance decrease in electrical response. Similar modification of nanofibres by humidity-response materials can also be made to implement humidity detection, of which illustration can be seen in Figure 2-3f.[63] It displays a flexible humidity sensor based on electro-spinning a polyamide 6 nanofibre modified by polyethyleneimine.

Much research in recent years has also focused on functional fabric coatings to develop wearable sensors. A woven copper mesh was modified with graphene through chemical vapour deposition (CVD) growth, and then the copper was removed to get a fabric-like graphene substrate (Figure 2-4a), followed by PDMS encapsulation for the fabrication of a sensor.[69] This approach was also extended to a graphene-modified woven Ni fabric to produce strain-response sensors.[70] In Figure 2-4b, CNT and reduced graphene are coated as active layers for a polyester fabric to produce a conductive network that will be modified by ZnO NW arrays.[71] The sensor with PDMS protection enables detecting a maximum bending strain of 6.2% with a superior GF of 7.6. In addition to these elastomer-protected fabric sensors, wearable sensors can be directly produced by modifying stretchable fabrics with conductive material. Among them, graphene-coated ones have been reported most extensively. Figure 2-4c exhibits the pad-dyeing process of reduced graphene functionalized woven fabric. This functionalized fabric (Figure 2-

4d) presents strain sensing ability due to the separation of coating flakes under tensile strain.[72] However, such woven fabric sensors process minimal sensing range because of the poor stretchability of the woven fabric.[73-75] Alternatively, a graphene pad-dyed knitted wool fabric acting as a sensor revealed a wider working range of up to 40% tensile strain.[76] By taking advantage of the hydrophobicity of both wool and reduced graphene, the sensor can stably work under complex humidity environments, which is of great significance to human wearable devices. However, the sensor shows poor durability (500 cycles) and obvious hysteresis as well as low recovery response speed. This type of knitting sensors could also be developed through graphene-coated polyester, cotton fabrics, [77, 78] as well as CNT-coated cotton fabric.[79] Many fabric strain sensors based on alternative conductive polymers or metal coatings have also been reported, such as Ag/Ni coated woven fabric,[80] cellulose nanocrystal/graphene-coated nonwoven fabric,[81] and polypyrrole (PPy)-coated woven fabric.[82] Even though these devices can detect mechanical stimulation, the long-term stability and durability are always not ideal because of the lack of protection, especially under large deformation, which needs to be further optimized. Figure 2-4e shows a pressure sensor made with rGO-modified tissue paper, of which surface morphology can be seen in Figure 2-4f.[83] This work investigates the number of modified tissue layers in determining sensing performance and finds that increased layers can enhance sensitivity. In addition to the single component functionalization, Figure 2-4g shows a multifunctional fabric-based humidity sensor by the modification of GO-NH_2, and mSiO_2.[84] The GO-NH_2 is expected to provide better hygroscopic, and the mSiO_2 is to improve hygroscopic and dehumidifying performance by taking advantage of its mesoporous structure.

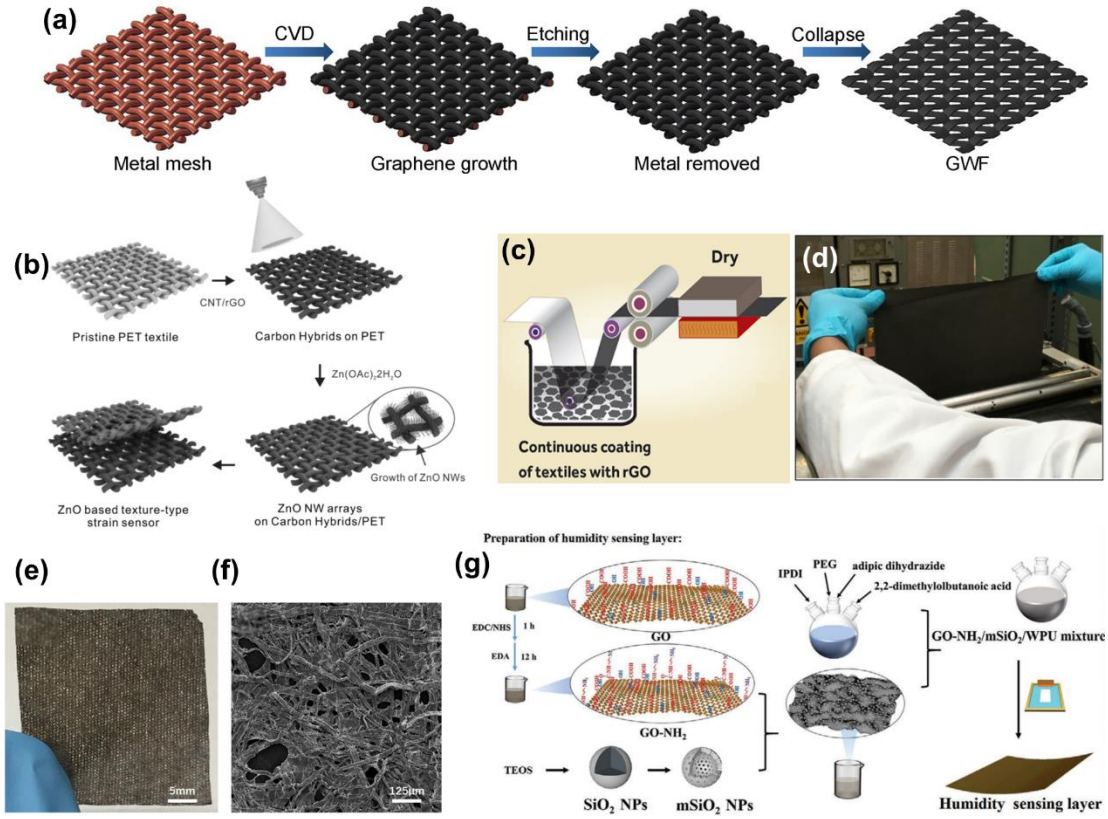

Figure 2-4. Preparation of conductive fabrics by surface coating. (a) A fabric-like graphene substrate is fabricated through CVD growth on a woven copper mesh, and then removing the copper.[69] (b) A CNT, graphene, and ZnO NWs coated PET fabric for the detection of bending strain.[71] (c) The process of a graphene-coated fabric by pad dying, and (d) the image of dyed woven fabric.[72] (e) Tissue paper with rGO modification, and (f) SEM image of the tissue paper surface.[83] (g) Illustration of the preparation of humidity sensing layer through GO-NH_2/$mSiO_2$ modification on a fabric.[84]

2.2.3 Structural Transformation

Some natural and artificial fibres can directly be conductive through structural transformation to produce wearable sensors. The electrical conductivity and mechanical properties are well affected by heat temperature. A fundamental study reported that silk fibres suffering sufficient heat with inert atmosphere protection would be conductive because the silk structure was restructured and transformed into an sp^2-hybridized

carbon hexagonal structure with pseudo-graphitic crystalline layers during heat treatment.[85]

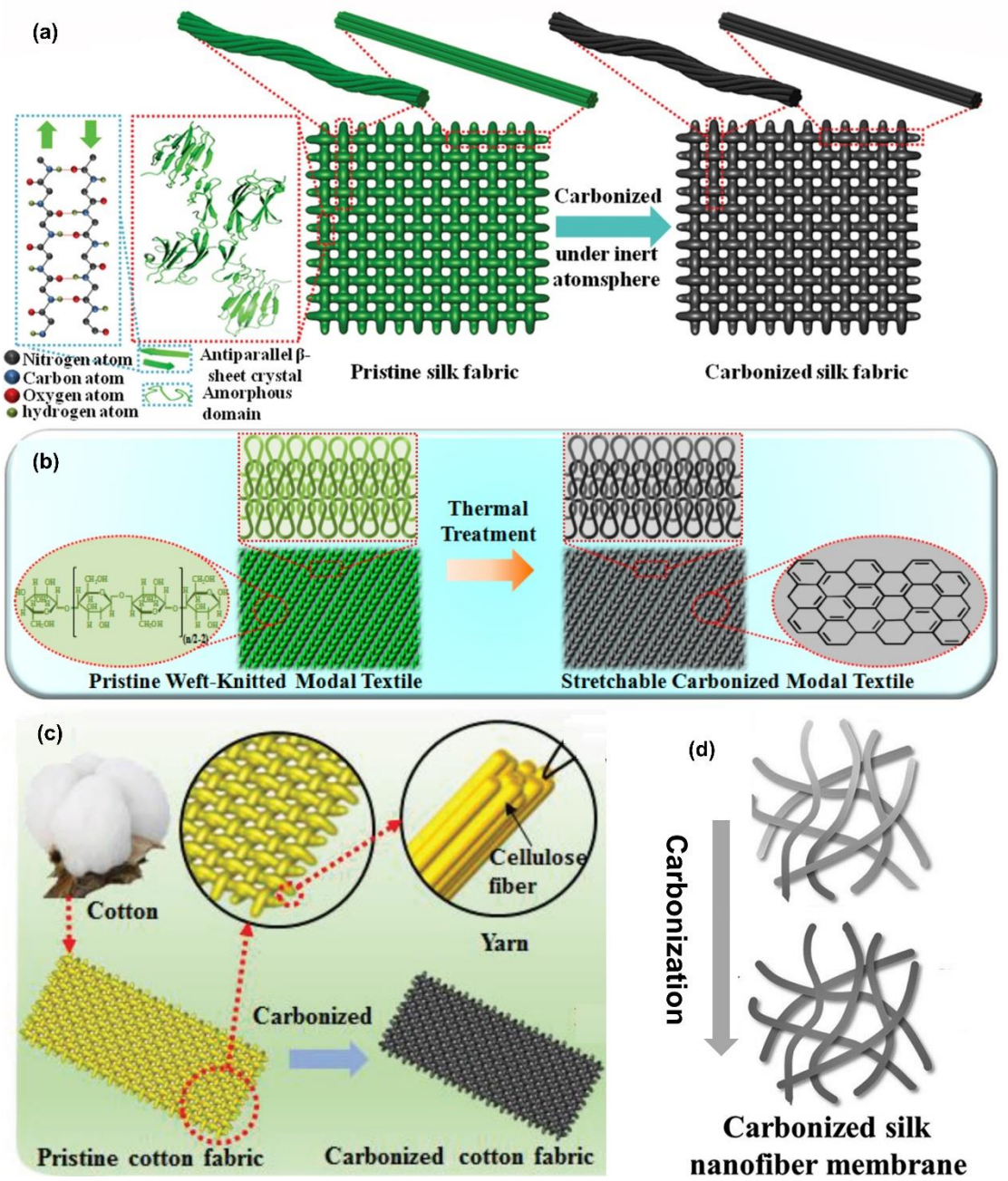

Figure 2-5. Conductive fibres and fabrics made with carbonisation. (a) Illustration of carbonizing silk fabric with plain structure.[52] (b) Illustration of carbonizing a modal fabric.[86] (c) The carbonisation of cotton fabric.[87] (d) Carbonisation of silk nanofibre membrane.[88]

By taking advantage of this facile carbonisation approach, another group first produced

ultra-stretchable and highly sensitive strain sensors with carbonized silk fabrics (Figure 2-5a).[52] Their work investigated the sensor made with different-structure woven silk fabrics, showing the better stability and sensitivity of plain sensors. More importantly, this work has inspired the manufacture of strain sensors through carbonized fibres and fabrics, such as carbonized modal fabrics (Figure 2-5b), cotton fabrics (Figure 2-5c), and silk georgette for tensile strain sensors, and carbonized crepe paper for bending strain sensor.[86, 87, 89, 90] The carbonisation can also be applicable to fabricating pressure sensors by carbonizing electrospinning silk fibres with PDMS encapsulation (Figure 2-5d).[88] The carbonisation technique has paved a new route for the fabrication of low-cost and high-performance strain sensors, mainly covering the materials of cocoon silk and spider silk, natural and artificial cellulose fibres to date. The conductivity can be simply controlled by changing carbonisation temperature. However, this type of material lacks mechanical strength, which needs encapsulation by elastomers in sensor fabrication. More efforts should be focused on the balance between electrical conductivity and mechanical performance in the future.

2.3 Sensor Fabrication and Sensing Mechanism

2.3.1 Pressure Sensor

Resistance-based wearable pressure sensors with the advantages of simple configuration and high sensitivity have attracted much more attention than the sensors with alternative sensing mechanisms (i.e., capacitance, piezoelectricity, triboelectricity, transistor). This type of pressure sensor detects pressure-induced mechanical deformation by converting pressure into electrical resistance changes. According to whether the existence of elastic encapsulation layers, the sensors can be divided into

elastomer-encapsulated and encapsulation-free construction. Elastomer-encapsulated one has the merits of high mechanical and sensing stability because the active materials are protected by the elastomers. While such devices always have to sacrifice the permeability to air, water vapour and moisture, thus increasing the risk of skin irritation in wearable applications. By contrast, body metabolites can freely go across encapsulation-free sensors due to the abundant porous structure in the devices. Figure 2-6a shows the fabrication of a flexible pressure sensor made with CNT-coated 3D fabric that is constructed by two outer layers and a spacer yarns layer.[91] The fabric modification is achieved by three steps: (1) O_2 plasma treatment to create more functional groups on fibre surfaces, (2) polyurethane dispersion (PUD) coating, and (3) drop coating by CNT. After the procedure, there is a layer of CNT conformably attached to the fibre surfaces, endowing them a good conductivity. Figure 2-6b illustrates the applied pressure-induced deformation of the fabric to show its sensing mechanism. The pressure would lead to a deformation in the top layer or enhance the bending deformation of the fibres in the middle layer. The top layer deformation would be a key component to decrease resistance at a low-pressure force, while it becomes the middle fibres at a high-pressure force. The deformation can result in a decrease in resistance of the fabric sensor to detect applied pressure. The 3D fabric sensor with a porous structure shows high breathability to air, water vapour and moisture, which is of importance to guarantee wearing comfort in body area sensing applications. However, the coating stability against machine washing and the skin friction is not satisfactory due to the lack of protection.

The encapsulation of conductive fibre networks is another approach for the fabrication of wearable pressure sensors. Figure 2-6c displays the fabrication of a pressure sensor

through three steps: (1) carbonisation of a cotton fabric via pyrolysis process, (2) encapsulation of the carbonized cotton fabric by PDMS, and (3) conductive wire as the electrode at both ends of the composite.[92] Taking advantage of the conductive fibre-interlaced matrixes, and stable sensor construction, it exhibits a wide working range up to 700 kPa, maximum sensitivity and wide response frequency, as well as high durability. The sensor can be integrated with sports shoes and waist belts in practical applications to implement pressure detection. In another example, a wearable pressure sensor is developed by encapsulating rGO-modified PVDF nanofibres.[62] GO sheets are firstly deposited onto the PVDF nanofibres, then the GO is reduced to improve the conductivity of the networks. The rGO-modified nanofibre is encapsulated by PDMS, and there are copper electrodes at both ends of the conductive matrixes (Figure 2-6d). The encapsulated sensor shows a lower resistance as a function of applied pressure because it forms more connect points in the conductive networks under pressure-induced deformation. After removing the pressure, the device can recover to its initial state in geometry, thus guaranteeing stable electrical response. This configuration pressure sensor is very popular to develop high-performance wearable pressure sensors. Figure 2-6e displays a flexible sensor that is fabricated by encapsulating carbonized electrostatic spinning silk fibres with PDMS.[88] The sensor is transparent as the very limited fibres at the nano-micro scale would not prevent the passage of light. This work investigates the density of carbonized nanofibres in determining the sensor sensitivity, and it finds that the sensor with low-density nanofibres processes a high sensitivity. Wearable pressure sensors with the construction (i.e., elastomer-encapsulated conductive networks) can be extended to many other conductive materials. However, this type of sensor always lacks breathability, which has not been paid enough attention to.

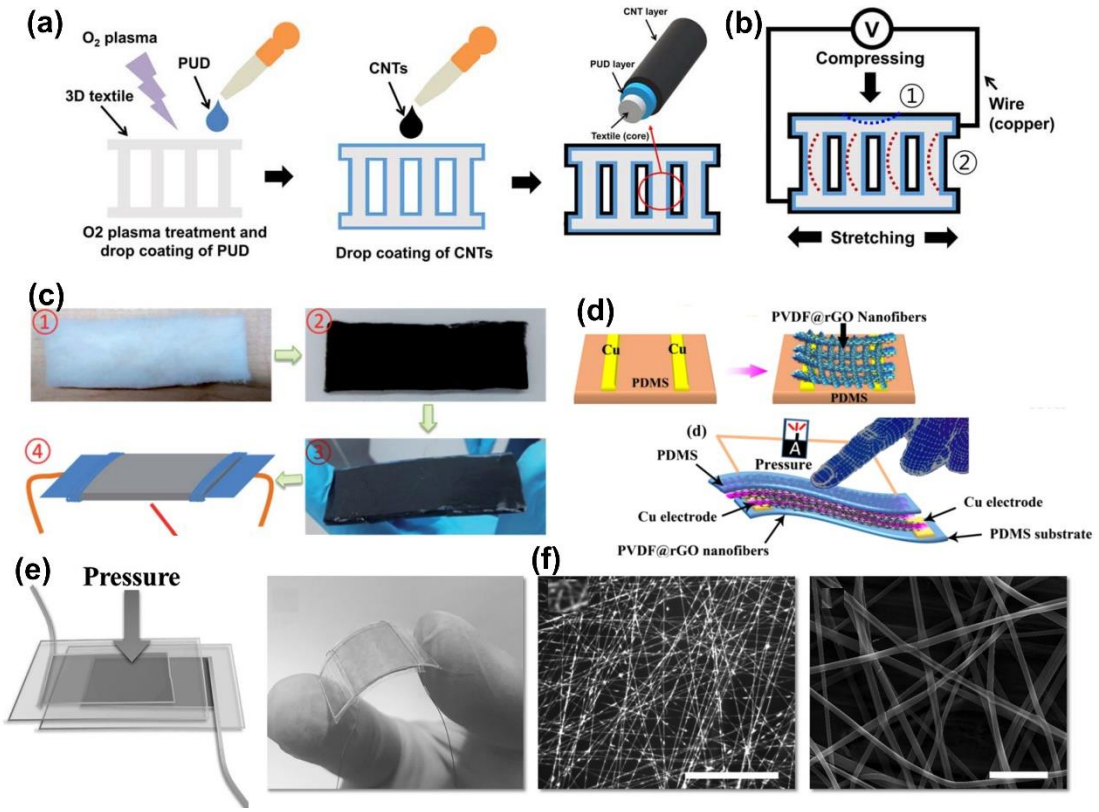

Figure 2-6. Illustration of pressure sensor fabrication and their sensing mechanism. (a) Step-by-step modification of a 3D fabric as a flexible pressure sensor, and (b) corresponding sensing mechanism.[91] (c) Fabrication of a pressure sensor made with PDMS-encapsulated carbonized fabric.[92] (d) Assembly of a pressure sensor by encapsulating rGO-modified nanofibres with PDMS.[62] (e) A transparent pressure sensor made with PDMS-encapsulated carbonized silk fibres, and (f) SEM image of the carbonized silk fibres.[88]

2.3.2. Humidity Sensor

Unlike tactile sensors with encapsulated and encapsulation-free constructions, humidity-response materials must be exposed to the environment to detect humidity. Resistance-based flexible humidity sensors can be classified into two types according to their positive/negative resistance response. They show a different sensing mechanism in responding to moisture. One is conductive materials integrated with water-absorbing substrates, where the resistance increases as a function of enhanced humidity. The

increased resistance can be attributed that swelling-induced deformation in substrates enlarges the resistance of conductive materials. On the contrary, another one is the functional groups in active materials bonded with moisture molecular, where the resistance decreases as a function of enhanced humidity. The decreased resistance is due to absorbed water molecules that can form more conductive pathways in the matrix. The two types of humidity sensors can detect humidity by converting moisture content into electrical signals.

Figure 2-7a shows the dispersion of single-walled CNTs (SWCNTs) in Poly(vinyl alcohol) PVA solution using sodium dodecyl sulfate (SDS) as a surfactant.[93] The composite is then fabricated into fibres by wet spinning (Figure 2-7b), where the acetone is to remove the surfactant during the spinning process. Figure 2-7c displays the SEM images of the fabricated fibre, showing that the SWCNTs are oriented parallel to the filament axis. The humidity sensing by converting humidity inputs into electrical signals can be explained that increased humidity leads to a swell in the PVA structure, thus the separated SWCNTs in the conductive networks would decrease the conductivity. In another example, a humidity sensor is developed by modifying PU fibre with acidified CNTs (Figure 2-7d), where the acidified CNTs are obtained by the treatment of HNO_3 and H_2SO_4 in an ultrasonic bath.[94] The as-obtained composite yarn can detect humidity by absorbing surrounding moisture molecules. The sensing mechanism can be understood that enhanced water content in the yarn increases the holes in the modified CNTs (Figure 2-7e), thus leading to the increase in resistance. Humidity sensors with the similar sensing mechanism are also reported in the combination of carbon nanocoils and liquid crystal polymer,[95] Mxene and cellulose fibres.[96] The basic principle is that moisture absorption promotes the separation of

swelling components, and the swelling increases the resistance of conductive components. Such a mechanism can be extended to many materials with the feature.

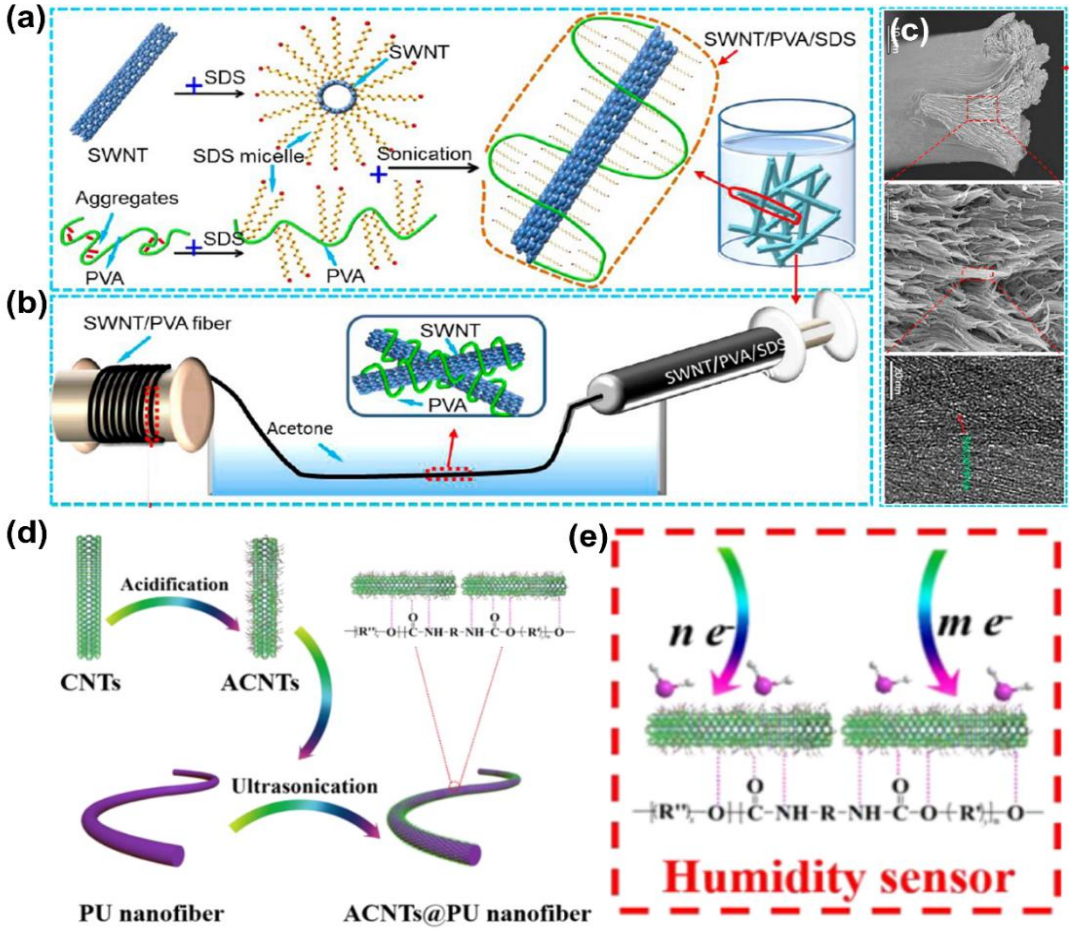

Figure 2-7. Flexible humidity sensors with positive resistance response. (a) Illustration of dispersing the MWCNTs into PVA solution, where the SDS serves as a surfactant, and (b) fabrication of fibre-type humidity sensor by wet spinning, and (c) SEM images of the prepared fibre.[93] (d) Fabrication illustration of a humidity sensor made with acidified CNT modified PU fibres, and (e) corresponding sensing mechanism.[94]

Alternatively, absorbing moisture molecules by conductive materials with humidity-response functional groups is another sensing mechanism of resistance-based humidity sensors. This type of material can detect humidity independently or combine flexible substrates to implement humidity detection. The electrical resistance decreases as a function of incremental humidity level. Figure 2-8a shows the fabrication of a humidity sensor by anchoring multilayer graphene into electrospinning polyamide (PA) 66

fibres.[97] The humidity-response graphene embedded in the fibre matrix (Figure 2-8b, c) can respond to humidity stimulation with high accuracy. The fibres serve as a flexible substrate to guarantee the sensor's flexibility and sensing reliability in various deformations. In another example, a humidity sensor made with GO-modified Coolmax yarns shows ultrafast response speed by taking advantage of its novel configuration.[98] Figure 2-8d displays the sensor fabricated by a hand-weaving machine, where the conductive wires and GO modified yarns serve as electrodes and humidity sensitive materials respectively. Because of the high specific surface area and hydrophobicity of the Coolmax fibres, moisture molecular enables to quickly evaporate, thus endowing the sensor high response speed.

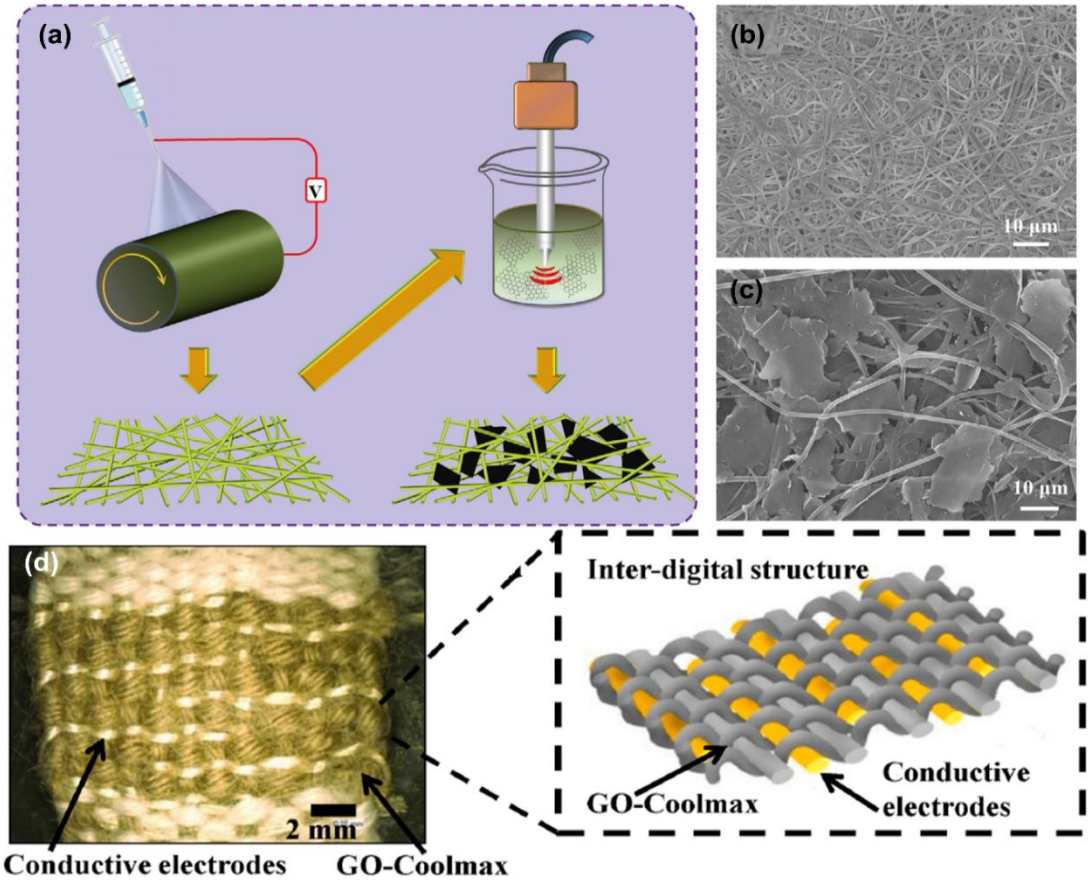

Figure 2-8. Flexible humidity sensors with negative resistance response. (a) Fabrication illustration of a humidity sensor by anchoring multilayer graphene into electrospinning polyamide (PA) 66 fibres, and (b, c) corresponding SEM images on the matrix surface.[97] (d) Illustration of a woven humidity sensor constructed with GO modified Coolmax

fibres and conductive electrodes.[98]

2.3.3 Strain Sensor

Fibre-based conductive materials supported by elastomers are very popular to fabricate strain sensors, where the fibre and elastomer act as sensing elements and electromechanical insurance components, respectively. The encapsulation thickness is of great importance in determining the flexibility and electromechanical performance of wearable strain sensors. The lower thickness of encapsulation brings about better skin assembling ability while poor stretchability due to possible defects on the encapsulation surface. Increased encapsulation thickness can guarantee good robustness but result in inconsistent compliance between encapsulation and sensing elements, which may deteriorate sensing reliability. Much research in recent years has focused on the relation between strain-caused cracks and the detection capability of strain sensors due to their outstanding sensitivity.[99-102] The unmatched mechanical properties between the fibre-based conductive elements and elastomers lead to functional cracks during strain deformation, further inducing the resistance increase. In one example, a fabric-based strain sensor was fabricated through a carbonisation process and Ecoflex encapsulation.[87] Based on the woven structure and hierarchical conductive network, the sensor enables the detection strain of ~140% after rupture training. During training, the sensor forms cracks due to the unmatched mechanical properties between carbonized cotton and Ecoflex, exhibiting an increasing resistance with step-up strains. This concept was also extensively reported for strain sensing devices in carbonized silk fabric,[52] carbonized silk georgette,[89] carbonized crepe paper,[90] graphene-modified copper mesh,[103, 104] graphene-modified cotton fabric with the treatment of ethanol flame,[105] CNT mesh,[106] and CNT film.[2]

In addition to these integrally conductive networks, cracks of functional coatings that form on the surface of substrate fibres also play a vital role in the fabrication of strain sensors. In an early work, a graphene-coated glass fabric with the protection of silicone resin was demonstrated for strain detection, where the silicone resin and graphene were employed to provide flexibility and sensing elements respectively.[75] When stretched, the graphene layer of the sensors experiences the crack formations due to stress concentration, leading to an increase in resistance. After releasing applied stress, the silicone resin drives the contact recovery for reversible strain detection. Interestingly, by taking advantage of the high strength of glass fabric, the sensor maintains structural integrity even sustaining external force over 800 N, which is beneficial to circumvent the damage of excessive tensile deformations. Figure 2-9a illustrates a yarn-like strain sensor containing thermoplastic elastomer supported CNT produced by a wet-spinning process, of which sensing theory is the crack formation of the CNT with strain stimulation to obtain resistance change.[33] Similarly, Figure 2-9b exhibits the fabrication of a hierarchical yarn-like strain sensor, which consists of spandex fibre substrate, coating of beaded carbon nanomaterials, and Ecoflex encapsulated layer.[99] In the above-mentioned research, the sensor's sensitivity is adjustable by changing the density of microbeads in the carbon coatings. The crack formation in functional coating layers was also studied in graphene-coated stretchable yarns,[107] polypyrrole coated porous PU,[108] Ag NWs coated elastomer with microstructure,[109] and carbon black coated paper,[110] which could be utilized in the fabrication of strains sensors.

Encapsulated sensing components with inherent electricity changes are another strain sensors' working mechanism. As shown in Figure 2-9c, a strain sensor with an Ag NWs

coating is constructed on patterned PDMS, where the microstructure pattern is achieved by pouring liquid PDMS on a fabric-like steel net.[111] The resistance variation of the sensor during deformation is caused by the microstructure change of the conductive Ag NWs network. To further understand the sensing mechanism, Figure 2-9d-f show surface images and resistance models of the sensor with gradually increased strain. The device resistance increases in the parallel concave lines due to the emergence and increase of tunneling resistance. By utilizing the tensile deformation-induced resistance increase of CNT fibres, they are tightly packed into yarn to detect strain, where the resistance increase is ascribed to the enhancement of bend gap energy of CNT fibres.[112, 113] Besides, ZnO NW modified carbon fibres, CNT, graphene, and ZnO NW modified PET fabrics were also demonstrated for strain sensing. The change of piezoelectric potential and band structure of the ZnO layer caused by strain is responsible for the electrical change of the sensors.[71, 114]

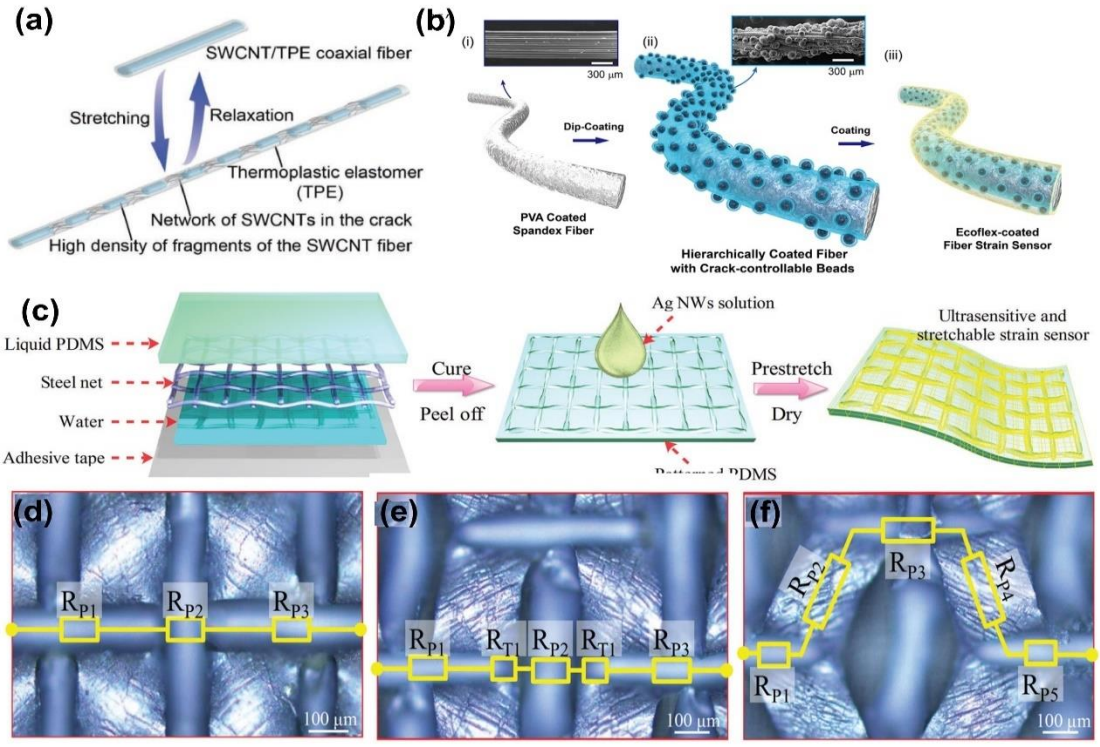

Figure 2-9. Strain sensors made with active material modified yarns. (a) Illustration of sensing mechanism of yarn-like strain sensors made with thermoplastic elastomer

supported CNT.[33] (b) Fabrication illustration of hierarchical strain sensor with spandex fibre substrate, coating of beaded carbon nanomaterials, and Ecoflex encapsulated layer.[99] (c) Fabrication illustration of the strain sensor with Ag NWs coating on patterned PDMS, (d-f) schematics of the strain sensor with increasing strain, and corresponding analog circuits.[111]

Inducing disconnection of conductive fibres is also very popular in producing elastomer-encapsulated fibre-based strain sensors. The disconnection will happen on conductive fibres, or the conductive coating layer of a nonconducting fibre. A composite made with CNTs and ethylene-α-octene block copolymer was demonstrated for strain sensing.[115] By utilizing the directional shearing force of melting mixing, the CNTs showed an obvious alignment along the impact direction. The polymer-encapsulated allied CNTs experience two-phase separation with different applied strains: sliding in minor strain and disconnecting in large-grade strain, leading to a diverse sensitivity in the whole sensing range. In Figure 2-10a, silk fibres are firstly coated with graphite flakes, and then the silk-graphite composite is encapsulated by Ecoflex to implement the production of low-cost strain sensors.[49] This work also compared the performance difference among several sensors made with graphite coated silk fibre, hair fibre, polypropylene fibre, as well as Spandex fibre. As shown in Figure 2-10b, when the graphite-modified silk fibre experiences elongation, the sensor exhibits a resistance climb due to the disconnecting of graphite flakes. Because of the high resilience of Ecoflex, the graphite flakes can recover to the initial contact state after releasing the deformation. The strain sensors with similar disconnection mechanism were also reported in graphene-based, layered percolative film,[116] graphene/PDMS mixture.[117] and graphene-nanocellulose paper.[118] Figure 2-10c displays the illustration of producing an Ag NW-PDMS nanocomposite for strain sensing. Similar to the strain sensor made with polystyrene-supported ZnO NWs,[119] the sensing mechanism of the

sensors can be summarized in two situations: during the elongation, the imposed strain drives the disconnection of conductive NWs to induce higher resistance, while the mutual contact condition will recover to the initial state after releasing the strain (Figure 2-10d).[120] In this work, the performance comparison between two different-structure sensors was also investigated, including simple (Ag NWs embedded on the surface of PDMS) and sandwich-structure (Ag NWs encapsulated with PDMS) nanocomposites. Results show that the sandwich-structured sensor processes a better electrical recovery than that of the simple-structure sample. The reason is that the first-time strain induces the buckling of Ag NWs in sensor with simple structure, and the buckling cannot completely regain after releasing the strain. On the contrary, the phenomenon does not appear to the sandwich-structure sensor in that homogeneous PDMS on the top and bottom of Ag NWs would not result in buckling.

Geometry alteration of stretchable materials based on Poisson's changes plays a critical role in regulating the strain detecting abilities of fibre-based, resistive and capacitive strain sensors.[116, 121-123] Elongation-induced electrical changes can be attributed to the increasing length and decreasing sectional area, while the electrical resistivity remains stable for strain sensors with the mechanism of geometry alteration. For example, elastic hollow fibres composed of a triblock copolymer, poly[styrene *b*-(ethylene- *co*-butylene)-*b*-styrene] resin, were fabricated into strain sensing devices. A liquid metal alloy (i.e., eutectic gallium indium) was subsequently injected into the cavity for better conductivity.[124] Similarly, another work reported the fabrication of strain sensors by injecting low toxicity liquid metal into hollow PDMS fibres.[125] These sensors enable to detect strain variation by the strain-induced sectional area changes and fibre length changes, of which mechanism can be classified into geometry alteration. For capacitive

sensors, the capacitance increases during stretching because of the additional length and decreasing thickness of the dielectric components. Figure 2-10e shows the fabrication process of stretchable Ag NWs conductor by combining with PDMS. The conductor experiences a surface buckling after cyclic stretching and releasing (Figure 2-10f), while the buckling will gradually disappear in high-grade elongation (Figure 2-10g).[126]

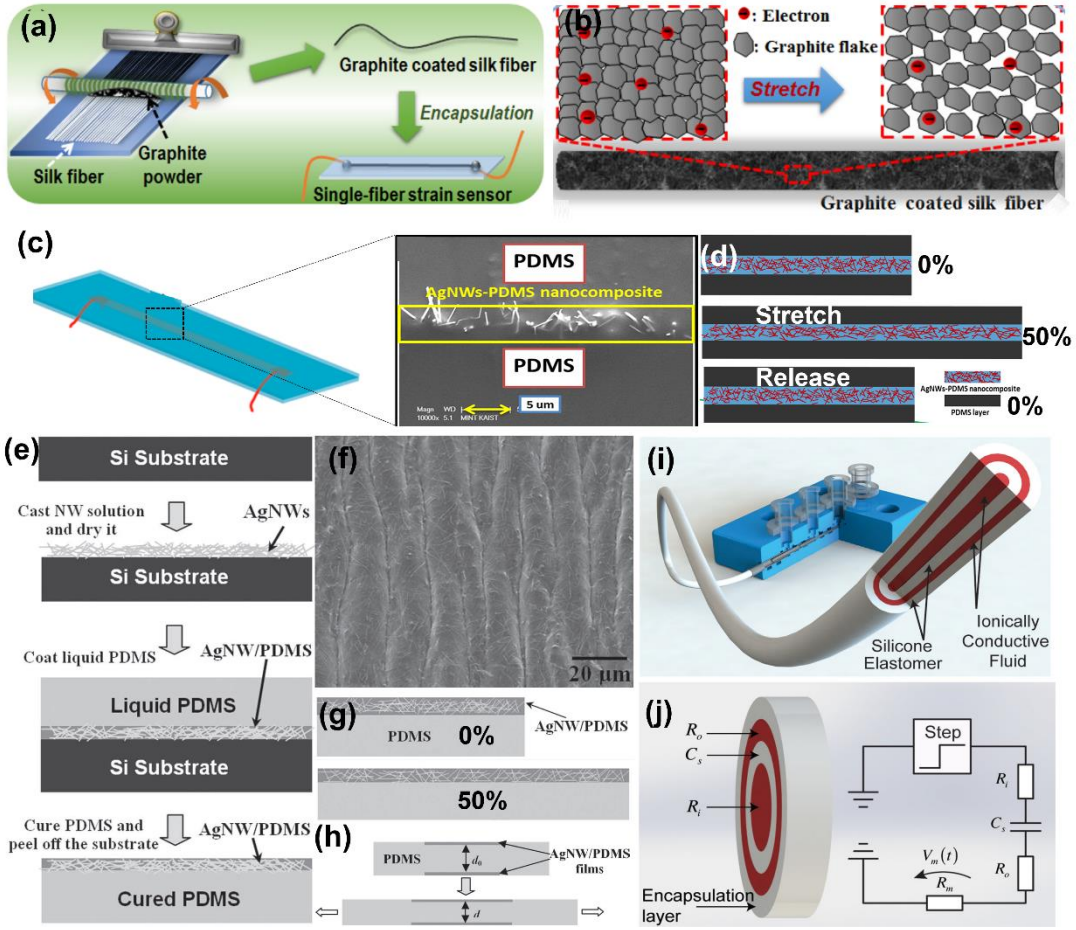

Figure 2-10. Strain sensors made with encapsulated conductive fibres (a) Illustration of strain sensor made with graphite coated silk fibre, and (b) the mechanism diagram of the sensor.[49] (c) A sandwich-structure strain sensor with Ag nanowire and PDMS, and (d) corresponding strain-sensing mechanism of the sensor.[120] (e) Fabrication illustration of the Ag nanowire/PDMS stretchable conductors, (f) the surface buckling of the conductor after stretching and releasing cycles, (g) the diagrams of the conductor in initial state and 50% strain respectively, (h) fabrication of a capacitance strain sensors with Ag nanowire/PDMS and corresponding sensing mechanism.[126] (i) Illustration of a

single-fibre strain sensor by multicore-shell printing process, and (j) corresponding circuit of the capacitance sensor.[127]

By utilizing this patterning technology, a capacitance strain sensor containing two Ag NW conductors in the top and bottom surfaces of PDMS was produced (Figure 2-10h). In another work, a piece of cotton fabric was firstly modified by PAMD, and then this metal-deposited fabric was coated by PDMS to protect the metal layers.[128] A capacitance sensor made with these two face-to-face fabrics was studied to explore the relationship between the two fabrics' capacitance and spatial location differences. Besides, a fancifully constructed single fibre in Figure 2-10i by multicore–shell printing approach was produced for strain sensing. The sensor consists of alternating layers of ionically conductive fluid and a silicone elastomer, serving as the conductor and dielectric/encapsulant, respectively.[127] Figure 2-10j exhibits the schematic cross section of the sensor and corresponding circuit, whose sensing mechanism is also attributed to the geometry alteration of the four concentric components during the stretching process.

Fibre-based strain sensors without the protection of elastic encapsulation layer are significant for truly wearable applications, as they allow metabolite excretion from the skin surface to the environment due to their porous structure.[76, 129-131] These sensors can be achieved by making conductive fibre into yarns and fabrics or modifying existing yarns or fabrics with active components. In the cases of the fabrication of strain sensing fabric, conventional textile forming technologies such as knitting, weaving, braiding, sewing, and nonwoven approaches are very popular due to their pattern flexibility, low consumption, and large-scale production.

Woven is a very proven technique to integrate orthogonal warp and weft yarns into

fabrics, which is also attractive to produce breathable strain sensors. The woven-structure sensors can be developed through modifying existing fabrics with conductive elements or weaving conductive yarns into fabrics. Figure 2-11a shows a spiderweb-inspired strain sensor with a woven plain structure, whose both warp and weft yarns are made with PDMS core and graphene shell.[132] Three main processes produce this spiderweb-like fabric sensor: graphene is firstly deposited on the surface of a nickel mesh, and then a layer of polymer is coated, following the etching of the nickel component; finally, the nickel interspace is filled with PDMS solution. The parallel yarns in the fabric strain sensor experience separation from each other during elongation (Figure 2-11b), and strain-induced cracks of the graphene layer in Figure 2-11c explain its sensing mechanism. Figure 2-11d shows the fabrication of another woven strain sensor, made with intertwined and functionalized yarns.[133] To produce the functionalized yarn, the pristine core yarn with inner PU fibres and helically-wounded nylon fibre is firstly modified by Ag NWs in a stretched state, after which the strain will be released for coating piezoresistive rubber on the surface. The functionalized yarns are weaved into a fabric (Figure 2-11e) for strain sensing, where the conductive yarn separation serves as the sensor mechanism. Very similarly, a woven strain sensor with the same structure was reported in another work. The PET yarn was immersed in dopamine solution, and then the processed PETs were braided on an elastic core yarn surface, followed by the reaction with conductive polymers (Figure 2-11f).[134] By integrating the as-fabricated yarn, the woven fabric achieved strain sensing ability. Figure 2-11g illustrates the sensing mechanism by showing that the increasing elongation causes the fibres to wind at a greater angle and distance, resulting in a lower ability to conduct electricity. The several conductive PET fibres acting as separate resistances with parallel connections (Figure 2-11h) can further explain the resistance

change, as the increase in value of each paralleled resistance will contribute to the augment of the overall resistance. Coating conductive elements on pre-existing fabrics can also produce the woven-structure strain sensor. Both elastic and inelastic yarns could be chosen as fabric raw materials.[135, 136] Figure 2-11i displays the processes of coating GO on pristine woven silk fabric and reducing the GO with a hot press to fabricate strain sensors.[137] Although the silk yarn has little stretchability, the woven structure endows the sensor with strain sensing ability in a limit range of up to 10% strain. Apart from that, this work also investigated the sensitivity of the sensors with different stretching angles. The results show that the 0°-direction (along with the twisted yarns) sensor owns better sensitivity due to the more microcracks on the graphene layer than other sensors (Figure 2-11j).

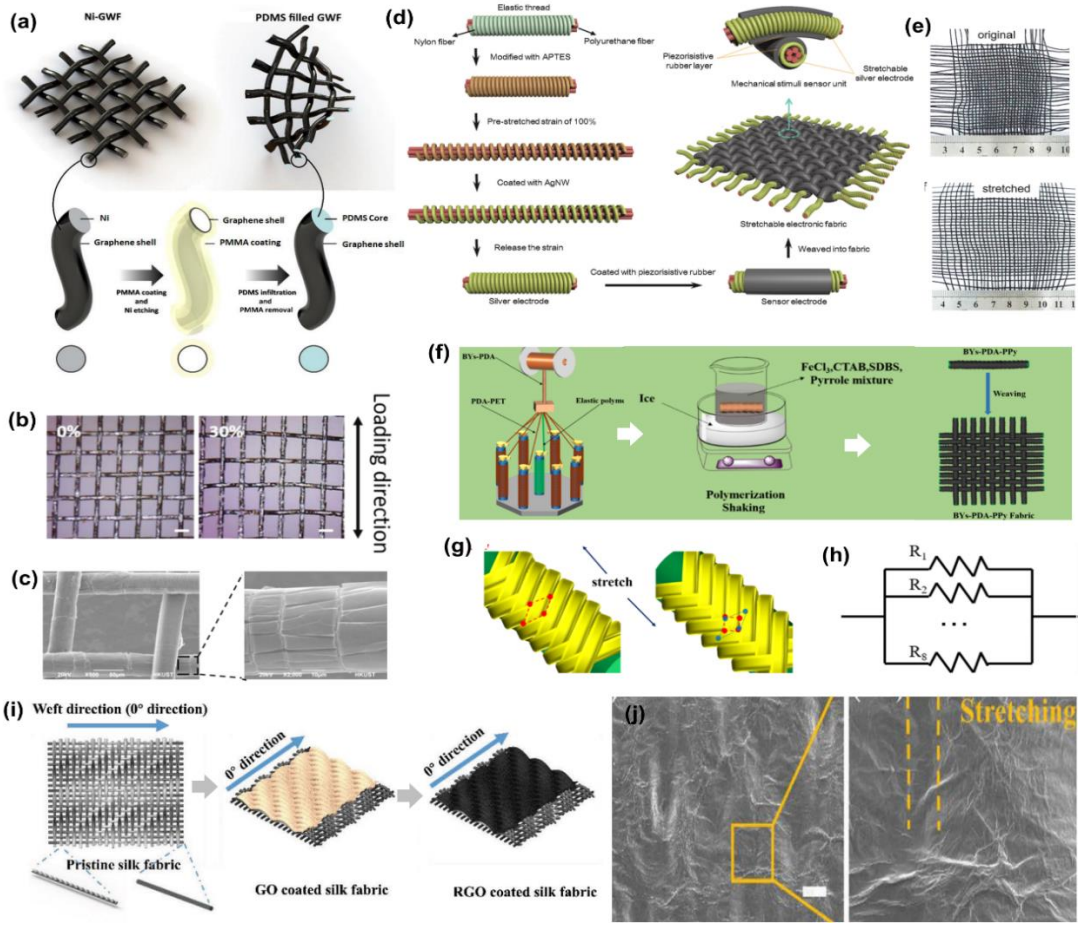

Figure 2-11. Breathable strain sensors. (a) A woven-structure strain sensor by depositing graphene on a nickel mesh and replacing the nickel by PDMS, (b) the surface

morphologies of the sensor under 0% and 30% strain respectively, and (c) the crack formation with applied strain to illustrate the sensing mechanism.[132] (d) Illustration of a woven strain sensor through weaving Ag NWsand piezoresistive rubber-coated yarns into a fabric, and (e) the images of the fabric sensors in the original and stretching state.[133] (f) Fabrication of a strain sensor by weaving conductive polymer-modified yarn into a plain fabric, (g) the illustration of the yarn without and with stretching, and (h) the resistance model of the sensor showing the sensing mechanism.[134] (i) The process of coating graphene on the surface on a woven silk fabric as a strain sensor, and (j) crack formation on the graphene layer to show the mechanism of the sensor.[137]

By making use of pattern flexibility of sewing, embroidering, and knitting, strain sensors can be achieved with desired performance. Figure 2-12a exhibits the fabrication of a strain sensor by sewing conductive yarns over a stretchable textile substrate.[138] This work investigated the performance variation of the sensors with different stretching degrees of substrates. Results show that the sensor with a lower stretched substrate owns a more significant and earlier strain response. The strain response can be ascribed to the disconnection and connection of the conductive lockstitches with strain applying and releasing respectively (Figure 2-12b). More importantly, by adjusting the pre-strain of the substrate, the work firstly developed a strain sensor that could program the starting point of strain detection. Developing strain sensors with knitted structures is also one of the most popular approaches, as knitted fabrics are naturally stretchable due to their unique interconnecting loops. Figure 2-12c shows the knitting process of Spandex/CNT fabric through a circular knitting machine. In this process, both fabric structure and density can be well controlled by changing the forms of CNT and Spandex (Figure 2-12d, e). [139] The formation of microcracks on the sensor surface can be observed in Figure 2-12f, g which correspond to the unstretched fabric and stretched fabric respectively.

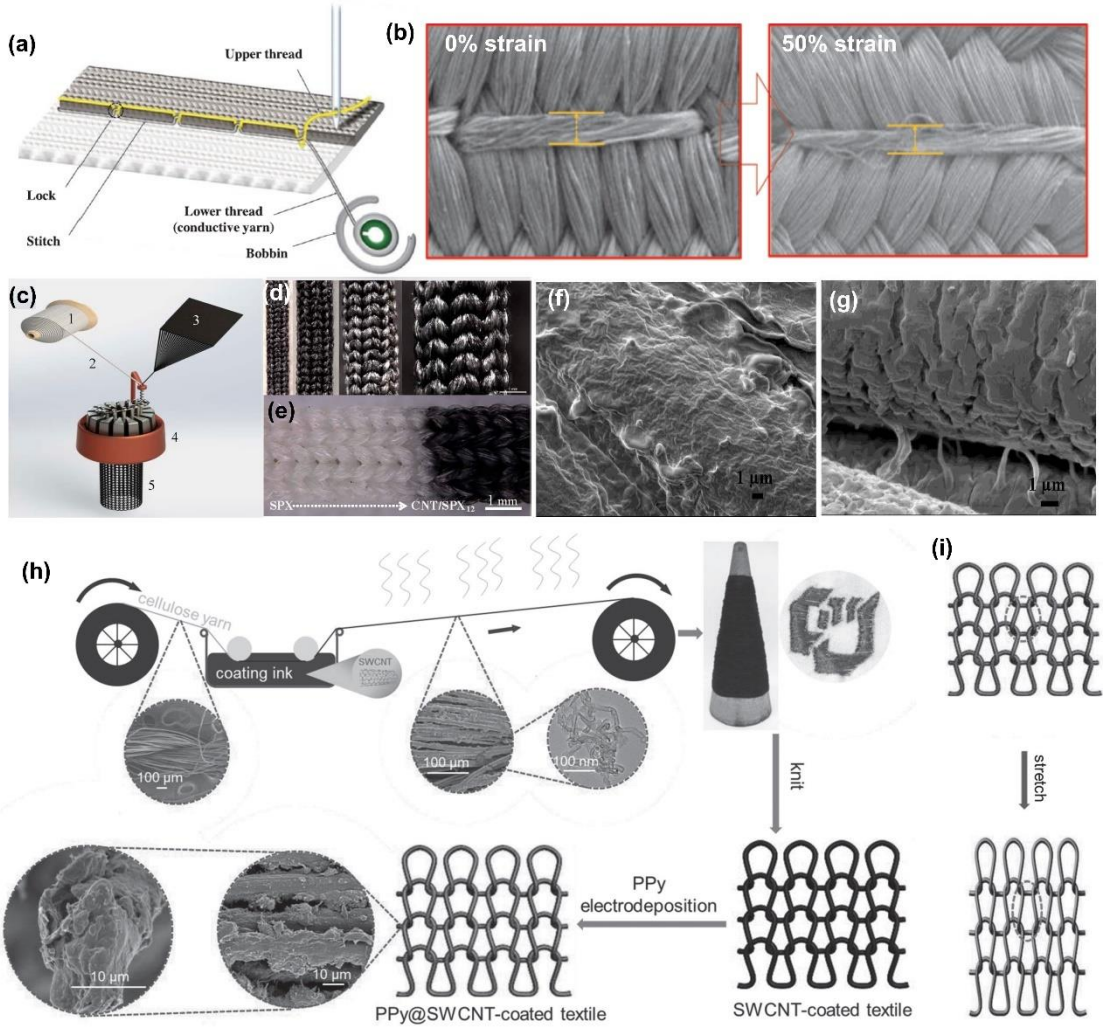

Figure 2-12. Encapsulation-free strain sensors fabricated by textile forming technology. (a) Illustration of locking conductive yarns over a textile substrate to fabricate strain sensors, and (b) the surface morphologies of the strain sensor under 0% and 50% strain respectively.[138] (c) Illustration of fabricating a knitted Spandex/CNT strain sensor through a circular knitting machine, (d, e) different-structure Spandex/CNT sensors showing the pattern flexibility of the technique, (f) the surface CNT on the pristine Spandex fibres, and (g) the CNT cracks on the stretched Spandex fibres to showing the sensing mechanism.[139] (h) The process of producing a knitting strain sensor through coating CNT and PPy on cellulosic yarns, and (i) the schematic diagrams of the sensor without and with elongation, showing the mechanism of the sensor can be attributed to geometry effects.[140]

Apart from that, experiencing a strain-induced separation of the interconnected conductive yarns will also increase the sensor's resistance. Consequently, the strain sensing mechanism of the sensor can be attributed to both crack formation and geometric effect. Figure 2-12h exhibits another knitting strain sensor made with CNT and PPy coating on cellulose yarns.[140] As shown in Figure 2-12i, the gaps between the conductive yarns become narrower during elongation, leading to more conductivity paths and driving lower overall resistance. Such knitting strain sensors follow a geometry change with stretch stimulation.[32, 76, 77] However, some knitting strain sensors indicated increasing resistance with applied strain.[141-143] How knitting parameters such as structures, density, and yarn diameter determine the sensor performance should be further investigated in the future.

2.4 Fibre Sensor Applications

Fibre-based wearable sensors have great application potential in a variety of wearable occasions. By converting tactile and noncontact stimulations into electrical signals, the devices can monitor body motions and vital signs with the advantages of accuracy, portability, and shortcut. Moreover, flexible sensors integrated sensing array enables to detect resolved strain. The sensing array could be utilized for the applications of human-machine interaction and future entertainment.

2.4.1 Body Monitoring

2.4.1.1 Motion Sensing

By attaching skin-mountable, fibre-based wearable sensors to different body parts, body movements ranging from small to large deformation can be monitored in real-

time. A previous achievement introduced a sensor made with Ecoflex-encapsulated carbonized silk fabric, which could detect blinking (Figure 2-13a).[52] The sensor was attached to the corner of one eye to sense tiny muscle movements of blinking. The outcomes exhibit that resistance change is highly consistent with corresponding motions. Figure 2-13b displays the real-time detection of another subtle facial movement by attaching a rubber-supported carbonized cotton sensor.[87] The resistance firstly increases with the cheek bulging and then gradually drops to the initial level, which is promptly in agreement with the facial motions. The wearable sensors can also record the epidermal vibration of the throat generated by speaking, water drinking as well as swallowing. Figure 2-13c shows a strain sensor attached to the throat, which can record the electrical signals resulting from speaking different words.[144] By clarifying different electrical outputs, the sensor can be utilized to differentiate monosyllable alphabet (e.g., a) or complex polysyllabic words such as “sensor” and “MXene”, of which signals present tiny peaks consistent with corresponding syllables. This real-time and precise detection reveals application potential in phonation reconstruction and singing training. Such monitoring can also be made by using pressure and humidity sensors (Figure 2-13d, e).[62, 97] Besides, placing a sensor on the throat could monitor the acts of lowering or raising heads, drinking, and swallowing.[76, 145] However, affected by the differences of human throats and sensing locations on the throat, signals collected by strain sensors present a reverse trend, which should be investigated in the future.[52, 76, 77, 87]

A multidirectional sensor, which contained multiple degrees of freedom, was attached to a human neck to monitor the motion of the neck (Figure 2-13f).[146] With repetitive ventral neck actions, there was a reduplicative increasing and decreasing resistance

change in the y-direction, while the value maintained stable in the x-direction. When the motion became rotational movements, different signals were observed. The strain sensors could identify the degree of bending fingers, wrists, and arms by altering the electrical signal.[147-149] Figure 2-13g exhibits an ultraminiaturized strain sensor acting as an e-skin to detect the wrist bend and release.[150] With the wrist bending up and back down, the relative resistance firstly increases and then recovers to the initial state, of which signals are in accordance with corresponding motion input throughout the cycles. Taking advantage of the ultraminiaturized structure, dense arrays made with multiple sensors are expected to be applied as the mapping of strain distribution. For instance, the angle of elbow bending was detected by wearing a capacitive-based strain sensor on the elbow.[151] During the process of step-by-step flexion and extension, corresponding relative capacitance change was simultaneously recorded. This real-time elbow angle measurement system can be utilized in body posture capture, motion state monitoring, and athletic training. In addition to these abovementioned examples, various body motions such as body swaying, bicycling and squatting were also successfully monitored by wearable sensors in real-time.[111, 152, 153] By applying sensors with suitable working ranges, almost all body movements can be monitored. It is worth mentioning that the data can be collected by wireless devices, even if the sensor is implanted in the body.[3, 71] Fibre-based sensors with good biocompatibility is promising in biomedical and implantable applications to monitor connective tissue movements.[154] It can perform the measurements of the knee ligament and Achilles tendon deformation of a pig, showing potential in the in vivo detection of body motion in the future.

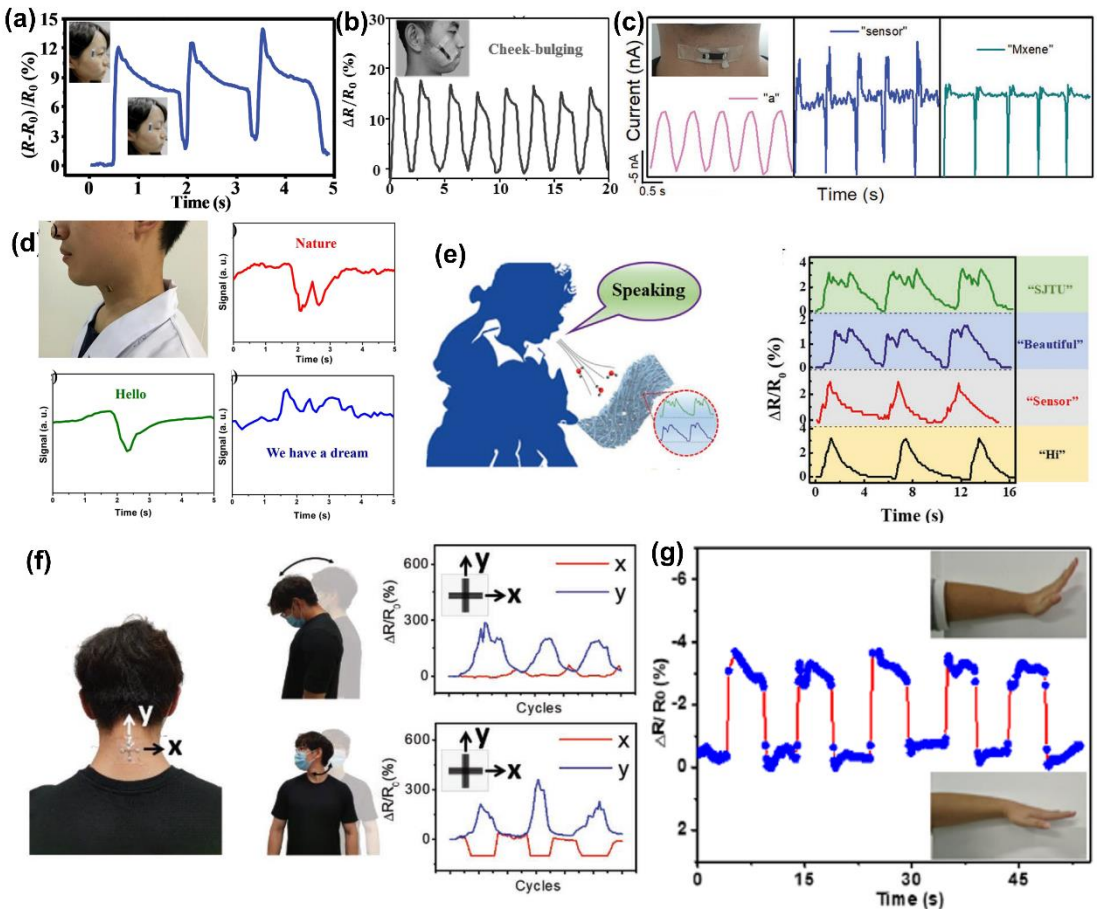

Figure 2-13. Wearable sensor applications for motion monitoring (a) The monitoring of the blinking by attaching a strain sensor to the corner of one eye.[52] (b) Detection of the signals generated by cheek bulking.[87] (c) Real-time recording and recognition of speaking different words.[144] (d) Monitoring speaking using a pressure sensor.[62] (e) Monitoring speaking using a humidity sensor.[97] (f) Detection of neck movements through a multidirectional strain sensor.[146] (g) Monitoring the motion of wrist bending by attaching the miniaturized strain sensor to the wrist. [150]

2.4.1.2 Health Indicators

Personal and public healthcare management plays an essential and indispensable role in social governance, epidemiology, and disease control. Wearable sensors may contribute to the large-scale classifier of individuals and the public accurately and unobtrusively. High-detection-limit and fibre-based sensors are capable of sensing vital sign signals such as heartbeat, pulse, and breathing with tiny deformation, which makes

them become suitable candidates as health indicators to monitor human health timely. In Figure 2-14a, a design for detecting the wrist pulses is shown by mounting a sensor made with Ecoflex-encapsulated carbonized silk fabric on the wrist surface.[52] Two-state wrist pulses under relaxed and exercised conditions can be effectively characterized by capturing changes in the relative resistance of the sensor. The repeatable and regular pulse shapes reflect the frequency of the wrist pulse in relaxation, reaching 70 beats min^{-1}. In comparison, the value ascends to 110 beats/min after exercise, because of the exercise-induced enhancement of metabolism. The close-up of one pulse waveform under relaxation conditions presents the percussion wave (P-wave), tidal wave (T-wave), and diastolic wave (D-wave), which exhibits the remarkable sensitivity of the sensor. The highly sensitive strain sensor is also capable of perceiving human respiration by assembling it on the chest. Relative resistance change in Figure 2-14b reveals that lative resistance change can reflect respiration under relaxation and exercise. The waveform for the respiration under relaxation exhibits a lower peak and frequency, while during exercise, it has a higher peak and frequency, consistent with the two-state respiration. Heartbeat, as an important vital physiological signal, closely relates to human health conditions. With the assistance of fibre-based wearable strain sensors, some diseases such as sudden infant death syndrome can be diagnosed effectively by detecting heartbeat. An application of conductive polymer-supported strain sensors is shown in Figure 2-14c.[155] By integrating the sensor on a tight and wearing it on the chest, the signals generated by the heartbeat show outstanding accuracy and remarkable repeatability throughout. It also manifests that the heartbeat reaches a frequency of ~1.5 beats/s.

In addition to the abovementioned health condition detection in a single body position,

wearable sensors can be integrated into body sensing networks (BSNs) to monitor full-range vital signs. A reliable BSN system utilizing Radiofrequency Identification (RFID) technique was reported (Figure 2-14d).[156] The five on-skin stretchable passive tags with thickness-gradient CNT network made contact with clothing via on-textile circuits. Significantly, the RFID technique helped researchers to achieve an all-flexible system. The absence of rigid substrates relieves integration density, providing better durability and enhancing the wearing comfort of this network. By collecting and integrating three different vital signals (breathing, pulse and joints activity) and sending them to the smartphone wirelessly, this strain sensing network illustrates its promising future in personal health care and exercise monitoring.

Apart from RFID, Near Field Communication (NFC) is also a reliable communication technology for building wearable wireless sensing networks. By integrating conductive thread and relays on clothing with a programmable pattern, Lin et al. fabricated a fabric-based sensing network, where clothes act as multiple relays system to connect with strain sensor nodes.[157] Researchers succeeded in monitoring various motions by changing the location of layers and sensors. For instance, the sensors and NFC labels in the cervical, thoracic, and lumbar sections provided instantaneous posture monitoring for different bending movements. Sensors were also integrated into running pants for monitoring knee movement. A clear stride time decrease from 0.98 to 0.65 s was collected when the tester increased his running speed from 2.8 to 9 km/h, closely corresponding to the interval change from data of gyroscopes. Temperature sensors were also added to the network; these systematic data may provide an overall result for athletic activity or medical testing in a convenient method. Different from the RFID route, the usage of NFC can remove the independent circuit and power supply in the

BSN system, improving its durability. In addition to wireless sensing platforms, wearable sensors with identification ability for emergency warning systems are also of great significance in real practical applications.

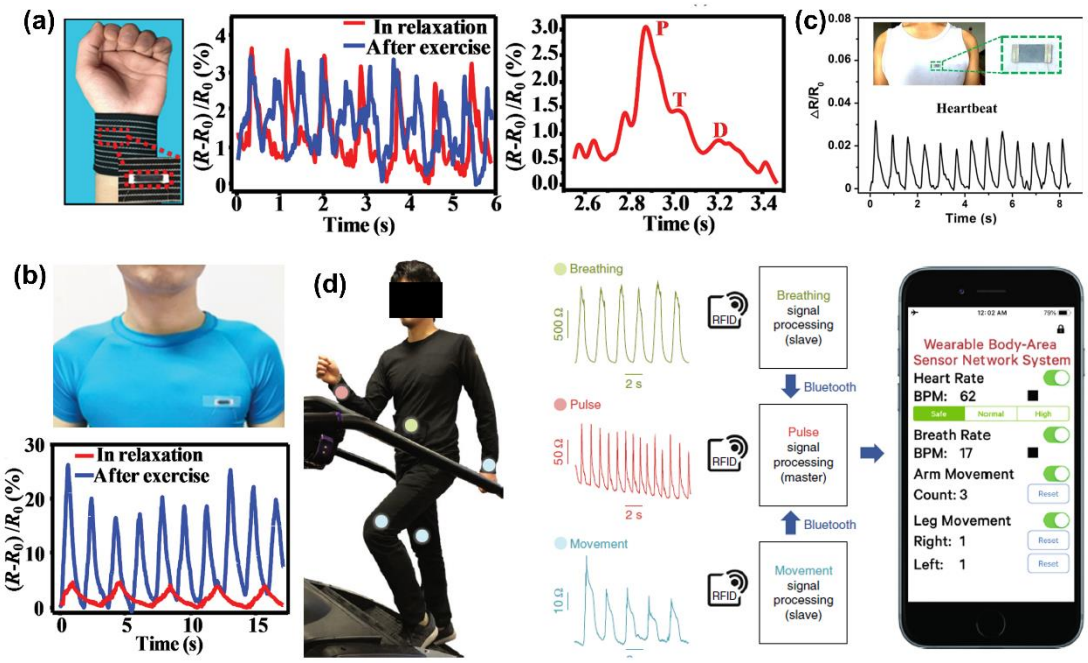

Figure 2-14. Wearable sensor applications for health monitoring (a) The detection of the wrist pulse by assembling a carbonized silk fabric-based sensor on the wrist surface, and (b) real-time respiration monitoring by attaching the sensor to the location of the chest surface.[52] (c) The signals of heartbeat collected by a PDMS-supported conductive polymer.[155] (d) The photograph of body sensing networks in monitoring breathing, pulse, and arm movement.[156]

2.4.2 Human-Machine Interaction and Entertainment

The rapid development of flexible electronics has stimulated the application of artificial intelligence services, or high immersion technologies such as virtual reality (VR) and augmented reality (AR). These applications usually relate to human motions, while traditional electronic products like keyboards or mouses cannot be competent. In this situation, wearable sensors have become increasingly popular because of their flexibility and high performance. As early as 2012, hand movement monitoring through

wearable strain sensors has already been mentioned, and an interlocking structure strain sensor with PU nanofibres on PDMS substrate was developed. By its sensitivity to shear (GF = 0.75), pressure (GF = 11.45), and torsion (GF = 8.53), the sensor arrays on the back of the hands can detect the movement of hands and the pressure on the sensor surface, illustrating the future of flexible strain sensors in interaction fields.[4] The demands of strain detection for large-deformation motion are considerable for many applications. A highly stretchable nanopaper/PDMS composite sensor was synthesized by Lee et al, where nanopapers were made by mixing nanocellulose and graphene.[118] By integrating five sensors responsible for different fingers, sensing gloves were prepared for hand motion detection. Benefitting from the high GF of 7.1 and the high stretchability of sensors, the resistances change can perfectly correspond to the bending of 5 fingers. Figure 2-15a shows a smart glove containing Ag NW sensors on fingers with a sandwich structure.[120] The research group successfully measured the position of different fingers more precisely by sensor resistance change with negligible latency. Moreover, the computer could display real-time images of finger motions by collection and communication system, emerging its possibility in complicated interactions like VR gaming or AR training.

The study of detection gestures with high accuracy has been continued for further optimization. Chen et al. combined fibre-based sensors with common gloves as a wearable interaction device.[54] The strain sensors, which have coated Ag NWs layer on PVDF fibres, illustrated outstanding sensitivity to monitor bending and strain. Researchers attached ten fibre sensors at interphalangeal joints and metacarpophalangeal joints to simulate gestures by analyzing the signal change from these ten joints. The sensor-computer system detected several gestures, such as numbers,

"OK" and "good" with high feasibility (Figure 2-15b). The ten sensitive sensors provide a high degree of freedom, and these data are meaningful for detecting complex hands motions comprehensively in interaction. In 2017, a skin-like strain sensor system was also reported to monitor human joint motions.[158] By coating rGO sheets on porous PDMS substrate, the sensor in this research demonstrates a reliable performance (GF = 7 at 10% strain and 173 at 40% strain). Sensors on the system were attached to knees and fingertips, enabling people to monitor different motions and frequencies on their phones. Outstanding biocompatibility for this device was also proved, which is quite essential for long-term wearing. Very recently, motion detection for both arm movements and hand gestures has also been achieved by using a wearable sensor system. Zhang et al. reported data gloves with ten high stretchable fibre-based strain sensors and sensor-assembled data bands, providing the capability of detecting motions of hands, wrist, elbows, and shoulders.[159] By these devices, researchers gathered human arm/hand gesture data and trained a neural network to recognize gestures. The system can recognize 20 alphabetic signs (in a total of 26 signs) with high accuracy of 93.33%. Arm gestures, especially dynamic police traffic gestures were monitored and recognized, illustrating its future in complicated motion interactions.

The applications for human-machine interaction and VR simulation were also studied. Figure 2-15c shows a fibre-based sensor system for gaming.[160] The fibre-based conductive strain sensors consist of two twisted PU-Ag NP fibres with hairy composite coating. The hairy microstructure successfully detected different stimuli such as pressure, stretching, and bending by different resistance change waveforms, which are significant for detecting complicated hand motions. The intelligent glove system, where two sensors were integrated into the thumb and index fingers, was proved to

immediately recognize different motions like pressing, bending, and stretching with high accuracy. Except for determining the hand motions by mapping resistance differences, different movements could also be detected by feature resistances of some parts of the hand. Zhu et al. designed smart gloves with wearable sensors and palm sliding sensors for comprehensive hand motion detection.[161] A triple-sections design for finger bending sensors was used, which projected the movement of fingers on a 30° scale by the virtual hand in Unity software successfully; researchers also achieved basic mouse control by the actions of different fingers. Additionally, the palm sensors can detect the normal force and shear force by detecting the amplitude of the negative triboelectric output and the opposite signal from different sections. This capability can assist researchers in recognizing gestures and actions more precisely. In identification tests, different grabbing actions and grabbed materials were recognized from distinct feature signals with an accuracy of 96% (Figure 2-15d). In VR surgery simulation applications, different characteristic signals caused by different holding habits were successfully analysed by gloves. The usage of gauze, scissors, and scalpels could also be simulated precisely, which provided a vivid interaction in VR gaming and virtual social network for users. Figure 2-15e exhibits a small-scale motion detector for fingers with graphene-modified fabric/PDMS composites piezoresistive strain sensors.[70] The interconnection structure and good adhesion between composites interface contribute to an orthotropic sensitivity, with more than 200% resistance change in 3% strain and a fast response time (0.072 s). When playing the piano, tiny muscle movements can be converted to unique signals by attached sensors to the fingers and wrist. Researchers corresponded different notes and chords to the feature signals and successfully played music by the strain sensors system and smartphones with the wireless connection between two devices. Very recently, a motion detection sleeve integrated with four

wearable strain sensors was reported (Figure 2-15f).[162] Sensors in this system exhibit an outstanding linear response ($R^2 > 0.98$), high sensitivity (GF > 9000), and low resistive change to off-axis deformation. Thanks to the sensors' high performance, the sleeve can detect the small muscle motions of the arm caused by hand movements. By neural network training, these movements of hand and wrist were successfully analysed and traced, such as different gestures and the rotation of the wrist, even the metacarpophalangeal angle in distinct motions. The precise detection of this glove-free system opened a novel approach to complicated human-machine interactive interfaces and applications which need high hands mobility.

Apart from sensing the motions of hands and arms, some other interaction methods like typing and facial movements are also vital for users. Keyboards are still high-efficiency input tools in human-machine interaction, and textile-based sensors may become a competitive candidate because of their relatively low cost and high durability. Figure 2-15g exhibits a stretchable capacitive electrodes keyboard with horseshoe structure knitted fabric and PEDOT:PSS conductive polymer.[163] Up to 8 times capacitance change (less than 1 pF to 8 pF) can be measured when pressing by fingers. This high stretchable textile-based sensor array is suitable for outdoor wearing applications, such as interaction with devices when exercising. Facial motions are also significant in some special conditions. A textile-based sensor system that could detect users' speaking and blinking in real-time was reported.[128] The capacitive topographical-structure sensor in this system provides high sensitivity at small deformation. Thus, blinking and speaking were monitored as capacitance changes by the motion-caused bending of sensors in this research. Language and head action interaction may be realized, which is significant for disabled or some patients. Besides, joint bending monitoring was studied in robot

hands, exhibiting the sensor's wide application potential. Most wearable strain sensor systems for human-machine interaction focused on hand motion since using hand is the most essential and efficient way for people to interact. Current sensor systems have already become accurate, illustrating their future in real applications. Apart from accuracy, durability, wearability, aesthetics, and other functions are still waiting for optimization in further study.

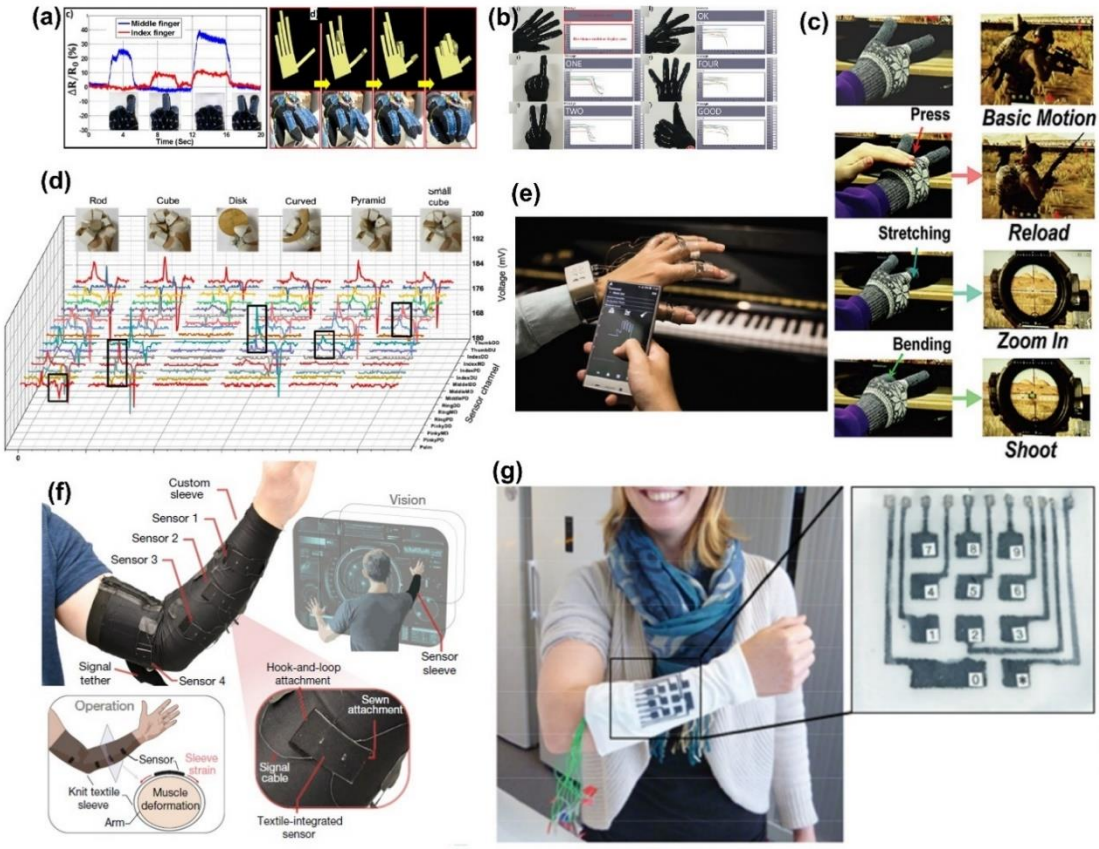

Figure 2-15. Wearable sensor application for man-machine interaction and future entertainment. (a) The motion detection of two different fingers (left), and the mapping of fingers motions by strain sensor gloves (right).[120] (b) The gesture recognition by gloves with strain sensors.[54] (c) Controlling video games with smart gloves.[160] (d) Recognizing different grabbing gestures by feature outputs.[161] (e) The optical image of the wireless instrument simulation system.[70] (f) Photograph of a strain sensor-integrated sleeve for the future human-computer interfaces.[162] (g) The image of the fibre-based wearable keyboard.[163]

2.5 Summary and Outlook

Though considerable headway has been made in terms of the preparation approaches, performance optimization, and application widening of fibre-based sensors, some fields are still worth exploring. A grand challenge is performance improvement. More efforts should be contributed to developing a sensor with both high sensitivity and a wide sensing range. The wide sensing range is more necessary than the sensitivity improvement, as the sensor signals can be easily amplified through specific electric apparatus in most cases. On the other hand, other vital sensing properties such as hysteresis, stability, and durability indicate the detection accuracy and lifetime, which have been largely overlooked. In addition, most properties of reported sensors were evaluated in the laboratories under certain conditions, while the electrical responses may be changed in real complex practical applications. The evolutions should be standardized in simulated wearable occasions in the future.

Wearability is another crucial evaluation index of wearable sensors, mainly including two aspects: how stable and flexible the sensor is when attaching to the moving surface; how comfortable and biocompatible the wearer is when wearing the sensor. The surface-mount ability and flexibility of sensors are the precondition in determining its reliability, which dramatically impacts the signals converted from the device. Although some sensors can be attached to the skin surfaces through microstructure generation, the adhesion is still not desirable under different-range and multi-dimensional deformations. The interfaces between fibre/yarn/fabric and the skin determine the wearing comfort. The involuntary physical breathing of the human body constantly produces sweat from the skin surface to the environment by water vapour, and the breathing would be more active in doing sports. Sensors should possess good

permeability to air, water moisture, and water vapour to expel body metabolites and guarantee a pleasant microenvironment between the sensor and the skin. The lack of breathability will lead to discomfort and even skin irritation. This index is of vital importance for wide-area detection such as the construction of full-range body sensing networks. Wearable sensors with the encapsulation of elastomers to render good stability often have to deteriorate their breathability and wearability, which have not been paid enough attention. In addition to the wearing comfort, good biocompatibility of on-skin and implantable sensors is also crucial in practical applications. It avoids the harm caused by immune rejection, which is of great significance in long-term detection.

Wearable sensors with sensing reliability under multi-direction mechanical inputs and complicated wearable microclimate are also very desirable for wearable applications. Tactile sensing devices detect surface motions by converting movements into electrical signals, while most of the surface motions at the time of deformations are not unidirectional. A wearable sensor is only sensitive to targeted inputs, while insensitive to others' mechanical stimulation is of vital importance to accurately perceive motions in real-time. On the other hand, the microclimate in wearable interfaces always involves fickle temperature, humidity, and potential of hydrogen, which may significantly deteriorate sensor reliability considering some active materials are sensitive to the stimulation of wearable microclimate. Wearable sensors should also maintain sensing reliability in the wearable microenvironment, without the concern of possible effects on sensing accuracy. We believe these challenges and opportunities for developing flexible sensors need more interdisciplinary collaborations to push this thriving field forward.

In summary, the research gaps of wearable strain, pressure and humidity sensors identified from literature review are as follows: 1) a pressure sensor possesses both sensing ability and breathability to achieve pressure sensing function and wearing comfort; 2) an effective approach to improving the sensitivity and sensing range of wearable strain sensors; 3) a humidity sensing strategy can be popular to many textile substrates, and the sensor shows remarkable breathability, water liquid wettability, and machine washability, while a limited response to many mechanical inputs; 4) a strain sensor with breathability and insensitive response to bending and pressuring inputs. This project aims to develop fibre functionalization and sensing device fabrication approaches to overcome the abovementioned challenges of wearable pressure, strain, and humidity sensors.

Chapter 3
Permeable Graphited Hemp Fabric-based Wearing-comfortable Pressure Sensors for Monitoring Human Activities

This chapter focuses on the first research objective. The work has been completed and published in Chemical Engineering Journal in 2021. The details are reported below.

Authors: Zekun Liu, Kaili Chen, Anura Fernando, Yuan Gao, Gang Li, Lu Jin, Heng Zhai, Yangpeiqi Yi, Lulu Xu, Yan Zheng, Huixuan Li, Yangyang Fan, Yi Li, and Zijian Zheng

Journal: Chemical Engineering Journal

DOI: 10.1016/j.cej.2020.126191

Statement of author contributions:

The proposal of the primary research idea. Fabric sample fabrication and carbonisation, material and sensor characterization, and application demonstrations. Preparation of tables, figures and the manuscript.

Statement of co-author contributions:

Kaili Chen supports the application demonstration. Anura Fernando, Yuan Gao, and Gang Li contribute to organizing the manuscript. Heng Zhai, Yangpeiqi Yi, Lulu Xu, Yan Zheng, Huixuan Li, and Yangyang Fan assist in the characterization of SEM, TEM, optical morphology, and electromechanical performance. Yi Li and Zijian Zheng supervise the work throughout the experimental stage and provide great support in polishing the draft manuscript.

Note: Supplementary material is available in Supporting Information.

3.1 Introduction

Wearable sensors are important cornerstones in a wide range of applications spanning from human health and activity monitoring,[76, 164-166] disease diagnosis,[167-170] to energy harvesting,[171, 172] human-computer interaction,[3, 173] and communications.[174-176] Among various sensor systems, piezoresistance-based pressure sensors are particularly attractive because of their high sensitivity and easy fabrication. Typically, these sensors are constructed in a network configuration with conductive materials including carbon nanotubes,[177, 178] metal nanowires,[179, 180] nanofibres,[39, 88] graphene,[62, 181, 182] and more recently, graphited silk and cellulosic textiles.[88, 183] The contact resistance of the conductive network changes as a function of the applied force, so as to provide sensitive pressure sensing. In order to retain the good cycling stability and the device integrity during different wearing motions, pressure sensors are often encapsulated with elastomers such as polydimethylsiloxane (PDMS). However, such an encapsulation inhibits the permeability of the device to air, moisture, and human sweat, as well as deteriorates the detection limit.

Permeability has a great impact on the microenvironment of the human/machine interface of wearable systems. Under normal condition, the human body constantly produces sweat, which evaporates from the skin surface to the environment in the form of water vapour, even when the individual is not active; this is known as involuntary physical breathing.[184, 185] Water vapour and moisture permeability of wearable devices is of importance to wearing comfort. Higher permeability enables human metabolic heat and moisture to diffuse into the environment efficiently, thus creating a more comfortable microenvironment between wearable devices and the skin. Besides, air permeability also largely determines the hygienic capability of how gas flow divulges

to the environment and how fresh air absorbed into the body. Therefore, the lack of permeability will result in discomfort and even damage to human skin.[186-189] Previous studies of pressure sensors mainly focus on enhancing the device performance, while wearing comfort, which is of paramount significance to wearable devices, has been largely overlooked.

Herein, for the first time, we report a high-performance, encapsulation-free and wearing comfortable pressure sensor made of graphited knitted hemp fabric (GKHF). Hemp is a natural fibre showing excellent strength and resilience, which are originated from its high-crystallization and outstanding oriented molecular structure, profiled cross section and straight axial fibre structures, respectively.[190, 191] By taking advantage of the remarkable resilience of hemp fibres, the GKHF shows excellent mechanical and electrical recovery from pressing at different pressures. In addition, due to the high porosity of the knitted structure, GKHF possesses comprehensive advantages including wide sensing range (up to 500 kPa), low detection limit (0.3 Pa), good sensitivity (1.012 kPa^{-1}), fast response (80.1 ms), excellent durability (10000 cycles), as well as outstanding air, water vapour and moisture permeability. We show that the GKHF does not lead to skin discomfort over a long period of wearing, and demonstrate a variety of applications of GKHF for next-generation wearable sensors to detect sound waves, perspiration, walking style, pulse, and pressure mapping of objects.

3.2 Experimental

3.2.1 Materials and Fabrication of GKHF Pressure Sensors

Hemp yarns (24 Nm, 42 twists/m) from Shanxi Lüzhou Hemp Textile co. LTD were knitted into plain, rib, and plain derivative fabrics via weft knitting. The wale density was 8 loops per 10 mm, and the course density was 8 loops per 9 mm. The fabrics were placed in a combustion boat in a tube furnace filled with a nitrogen atmosphere, which was heated to 800°C at a speed of 3°C /min and then natural cooled down to room temperature. Finally, the graphited fabrics were cut into smaller rectangular (1.2×1 cm^2) pieces and connect to external wires with silver paste (Supplied by RS Components) at two opposite edges. In terms of the sensor array, each sensor owns a size of 1.2×1 cm^2, and the gaps among sensors are around 0.3cm.

3.2.2 Characterizations of Fabric Structures and Sensors

Light microscope (VHX-100/VW-6000/5000) and scanning electron microscope (S-4800, Hitachi) were used to observe the surface morphologies of fabrics and fibres. Transmission electron microscope (Tecnai T20) was used to detect the microstructure of GKHF. Raman spectrum of pristine fabric and GKHF was measured with a Raman spectroscopy (WITec, Apyron) equipped with a 532 nm laser wavelength. All accurate loading and removal pressure were applied by a universal materials tester (Instron 5944) meanwhile with Keithley 2400 and corresponding software (Beijing Hanlei Technology co. LTD) to collect consistent electrical data. Noted that the sensor size is increased to $10 \times 10cm^2$ to research a low pressure of 0.3 Pa. A proper glass attached

on the probe of the mechanical equipment to applied desired pressure. The humidity stability test was carried out by putting the sensor, a beaker of water, as well as a hygrometer in a plastic wrap sealed box, synchronously run a universal materials tester (Instron 5566) to start and Keithley 2400 to record electrical data. The tests of air permeability, moisture permeability and water vapour permeability of fabrics were performed by an air permeability tester (MO21A, SDL), a moisture management tester (M290, SDL) and a water vapour permeability tester (M261, SDL) respectively.

3.3 Results and Discussion

3.3.1 Design, Structure and Fabrication of Pressure Sensors

As illustrated in Figure 3-1a, hemp fibres obtained from the bast of hemp plants were knitted into loops by a weft knitting machine, then the loops were fabricated into desirable knitted fabrics by altering connection pattern of the loops. The knitted hemp fabrics, made up of profiled cellulose fibres with deformed sections (e.g., elliptical and triquetrous sections), were readily carbonized into pseudo-graphitic fabrics via a thermal treatment process to yield GKHFs (details can be seen in Experimental Section). After the thermal treatment, both the yarns and fibres became distinctly thinner, and the fabric showed a weight loss and surface shrinkage by 83.8% and 45.6%, respectively (Figure 3-1b-e). The composition of surface elements of the sample was significantly changed (Figure 3-1f, and Figure 3-S1), where the atomic percentage of C, O, and N are 66.1%, 30.1%, and 3.8% respectively for pristine hemp fabric. After the thermal treatment, the content of C increased to 97.1%, while those of O and N decreased to 1.9% and 1.0%

respectively. The results can be attributed to the release of H_2O, CO_2, and CO, as well as the formations of graphite structure, during the thermal treatment.

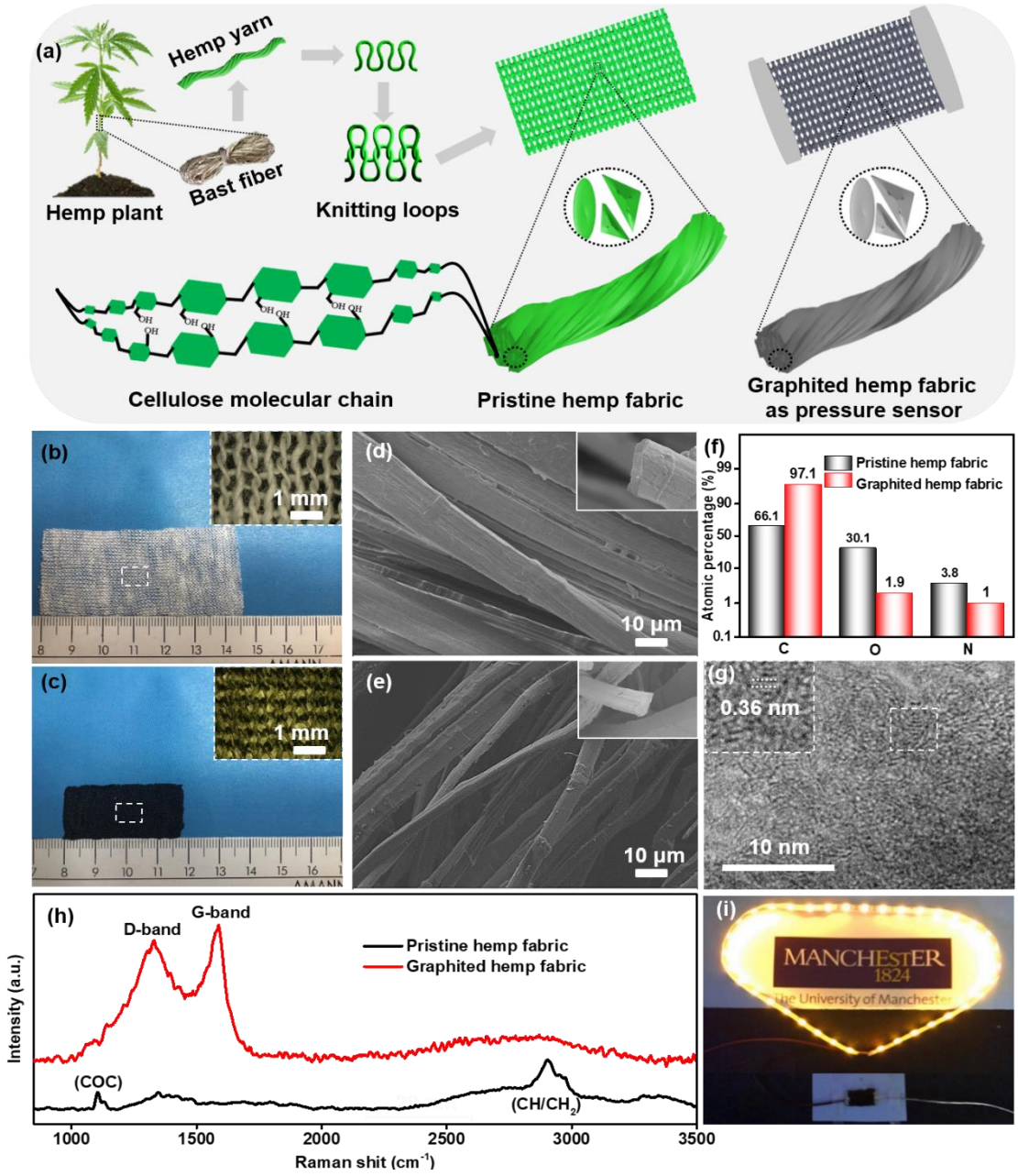

Figure 3-1. Fabrication and characterizations of graphited hemp fabric. (a) Schematic illustration of the fabrication of graphite knitted hemp fabrics (GKHFs). (b) Surface morphology of pristine knitted fabric. (c) Surface morphology of GKHF. (d) SEM image of pristine hemp fibres. (e) SEM image of GKHF fibres. (f) The surface element content of pristine and graphited fabrics. (g) TEM image of GKHF. (h) Raman spectra

of pristine and graphited hemp fabrics. (i) Showing conductivity of GKHF as interconnect to light up LEDs.

The formation of the graphitic structure was validated by transmission electron microscopy (TEM) and Raman spectroscopy. TEM showed diminutive distorted lattice streaks with an interlayer width of 0.36 nm (Figure 3-1g), which reflects the sp^2-hybridized carbon hexagonal structure of pseudo-graphitic crystalline layers.[85, 192] Raman spectra (Figure 3-1h) of the pristine hemp fabric showed two distinct characteristic peaks ~1100 cm^{-1} and ~2900 cm^{-1} associated with the signals of (COC) mode of glycosidic leakages and (CH/CH_2) mode of methine groups, respectively.[193] By contrast, GKHF showed typical G-band at ~1327 cm^{-1}, D-band at ~1586 cm^{-1} and 2D-band at ~2750cm^{-1} of graphitic structure. The highly conductive GKHF can be used as an interconnect to light up LEDs (Figure 3-1i).

3.3.2 Calibration and Mechanism of Pressure Sensing

By taking advantage of the flexibility of pattern design of knitting, we fabricated pressure sensors with three different kinds of knitted structures. Their orthogonal views of a single stitch including rib-graphited knitted (r-GKHF), plain-graphited knitted (p-GKHF) and plain derivative-graphited knitted (pd-GKHF) fabrics are presented in Figure 3-S2. The morphological details and surface diagrams of these samples are displayed in Figure 3-2a-c and Figure 3-S3 respectively. All the samples show piezo-resistive behaviour, which arises from the change of contact resistance upon applying pressure (Figure 3-2d, e). The space between knitting

loops and among the thousands of fibres of a single yarn shrinks under pressure, leading to better contact between the graphited hemp and the decrease in electrical resistance. p-GKHF acquired the highest piezo-resistive sensitivity among all the samples (Figure 3-2f and Table 3-S1); its sensitivity reached as high as 1.012 kPa^{-1} with an outstanding linear fitting of 0.993 (Table 3-S1). The resistance model of the p-GKHF and corresponding discussion are presented in Figure 3-S4. The difference in sensitivity can be attributed to their diverse knit structures. The sensitivity of r-GKHF and p-GKHF is similar, and it is better than that of pd-GKHF. The fabrics with rib and plain structures are connected by loops without floating threads, each loop has four touchpoints with surrounding loops. The equal touchpoints of r-GKHF and p-GKHF can similarly affect the resistance decrease under applied pressure. Considering the higher thickness of the rib fabric, the r-GKHF suffering larger pressure than p-GKHF to achieve the same degree of resistance changes explains the lower sensitivity of r-GKHF. The lowest sensitivity of pd-GKHF is ascribed to the floating threads in the backside of the fabric. The floating thread is closely attached to surrounding loops, thus presenting a worse sensitivity. The sensitivity of the knitted fabric-based sensors is determined by the gap between fibres, high-twist yarns with remarkable resilience is desirable to produce high-performance such sensors. We have also fabricated p-GKHF pressure sensors with the carbonisation temperature of 700°C and 900°C respectively. Their structure transformation was confirmed by the Raman spectrum (Figure 3-S5a). It shows that there are G-band and D-band in the Raman spectrum for both graphite hemp fibres, indicating the formation of a sp^2-hybridized structure. Higher temperature treatment leads to an increase in the

structural order, which is consistent with the previous study.[85] Calibration results in Figure 3-S5b show that both the sensors with 700 and 900℃ treatments exhibit lower sensitivity than the sensor experiencing 800℃ treatment. As control experiments, we encapsulated the devices with PDMS (PDMS-GKHF Figure 3-S6) and tested their piezo-resistive characteristics. The electrical response of PDMS-GKHFs showed obvious decrease over the entire testing range, because PDMS may restrict the contact of some fibres under pressure. In addition, the added weight from PDMS generates preloading, which also reduces the sensitivity of pressure sensors.[179]

3.3.3 Electromechanical Performance

Importantly, without encapsulation, p-GKHF possesses remarkable static and dynamic stability under different applied pressures. The resistance of the sensor decreased and the current passing through increased linearly against the voltage applied under different static pressure from 0.5 kPa to 480 kPa (Figure 3-3a), indicating remarkable static stability. The stable response is fully reversible without any heterosis when the sensors were loaded dynamically in different applied pressure ranges (Figure 3-3b and Figure 3-S7). It should be noted that the sensor can detect pressure as low as 0.3 Pa (equivalent to a 0.3 mg plumage tip loaded on 1×1 cm^2). Such an ultralow pressure detectivity is superior to piezoresistance-based, encapsulated pressure sensors reported by others (see Table 3-S2) by taking advantage of its encapsulation-free structure. The sensor was further loaded and unloaded repeatedly under 50 kPa for 10000 cycles. Figure 3-3c indicates that the electrical response is stable and reproducible throughout the entire fatigue test, which

attests the outstanding durability of the pressure sensor. The response time of loading from zero to 200 kPa reaches a high speed of 80.1 ms (Figure 3-3d), which meets the general requirements of wearable electronics for sensing human healthy and activities. As summarized in Table 4-S2, compared with reported pressure sensors in recent years, the encapsulation-free GKHF sensor presents conjunct assets in terms of the extremely wide working range, ultralow detection limit, and remarkable durability.

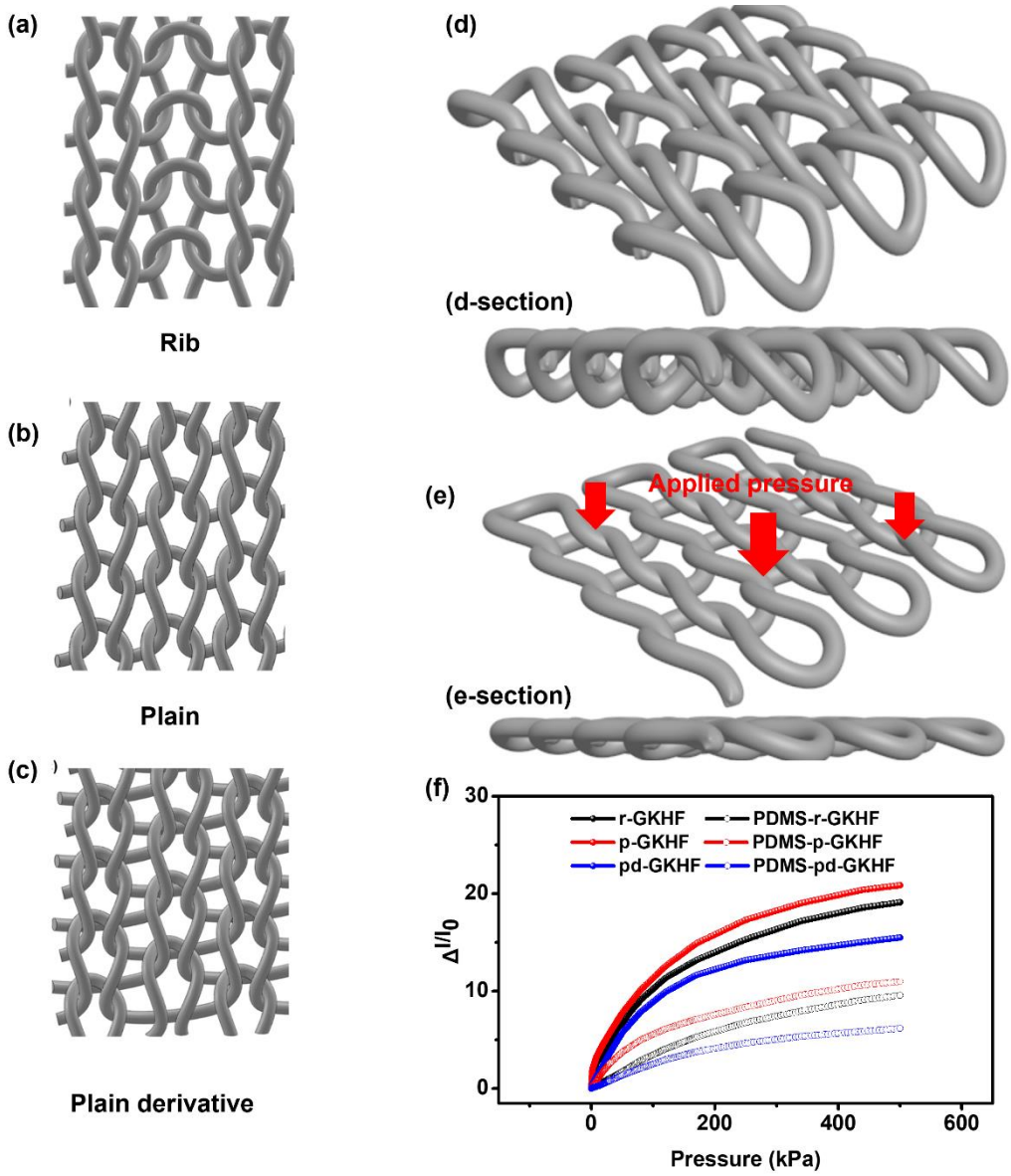

Figure 3-2. Calibration of different-structure pressure sensors. (a) Diagram of knitted rib structure. (b) Diagram of knitted plain structure. (c) Diagram of knitted plain

derivative structure. (d) Diagram of knitting structure without loading. (e) Diagram of knitting structure under applied pressure. (f) Calibration results of GKHF and PDMS-GKHF.

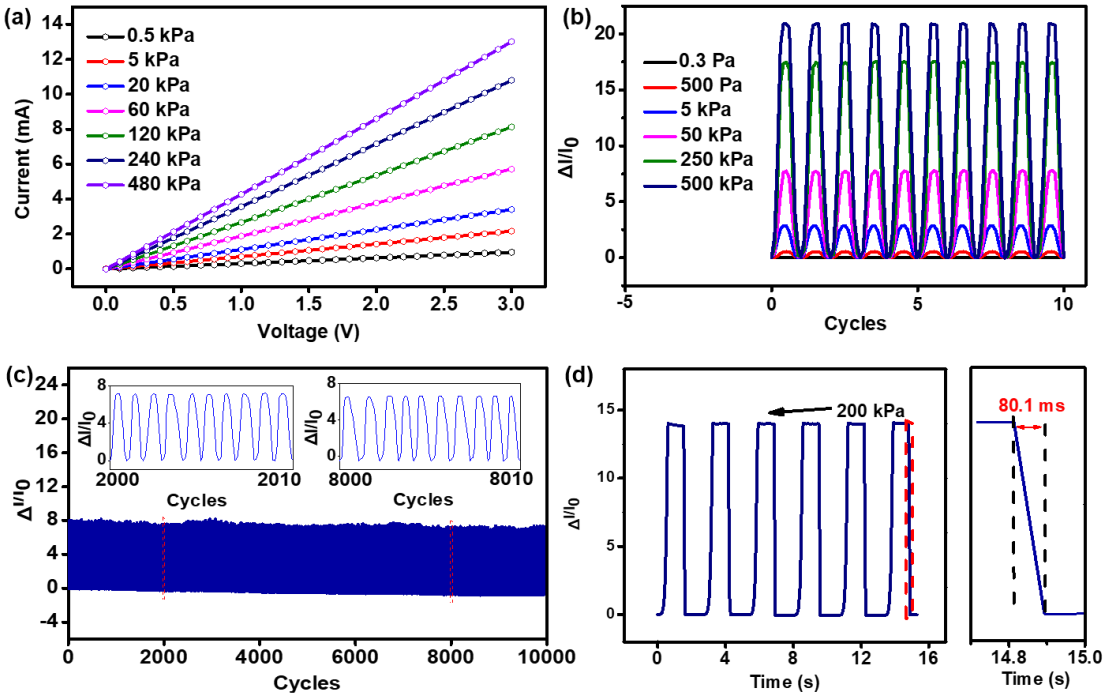

Figure 3-3. Electromechanical performance of p-GKHF. (a) Voltage-current curves of the sensor under different pressures. (b) 10-cycle pressure response under pressure ranging from 0.3 Pa to 500 kPa with the frequency of 0.25 Hz. (c) Durability test at an applied pressure of 50 kPa for 10000 cycles with the frequency of 0.5 Hz. (d) Response speed of the sensor under 200 kPa pressure.

The superior piezoresistive performance is attributed to the unique structure and high strength of hemp fibre. Hemp fibres possess solid cross-section the straight longitudinal structure. The stiffness modulus and specific Young's modulus of hemp fibre can reach 70 GPa and 47 GPa/g cm^{-3} respectively, while these are only 13 GPa and 8.4 GPa/g cm-3 for commonly used cotton fibre.[194] After heat treatment, the graphite hemp fibres maintained the solid section and straight axial structure, while there are obvious hollow

sections and twist convolution structure for graphite cotton (Figure 3-S8a-d). The diverse fibre structures result in distinctly different mechanical properties of the pressure sensor. Figure 3-S8e displays the good recovery of the stress-strain curve of graphited hemp fabrics under 50 kPa for 10 cycles and the sample can restore to the initial condition. In contrast, the graphite cotton fabric had significant mechanical degradation over each cycle (Figure 3-S8f), and the electrical output also exhibited serious drift (Figure 3-S8g) when used as a pressure sensor without encapsulation.

3.3.4 Breathability of the Pressure Sensors

The encapsulation-free GKHFs present unique advantages in high permeability to moisture, vapour, and air, which is critically important for wearable applications. There is a microenvironment between the skin and wearable devices (Figure 3-S9), poor permeability of the human-wearable devices-environment system can directly reduce comfort as it restricts human metabolite excretion. We tested the water permeability of the pressure sensors by applying a droplet of water on the top surface of the sensor and measure the water footprint on the front and back side of the device. The liquid drops completely penetrated all the GKHF samples (Figure 3-4a-d) and wet the back side of the devices. These fabric sensors are defined as water penetration devices with small spreading areas and excellent one-way transport of moisture, which process a better moisture penetration than reported polypropylene and cotton knitted fabrics.[195, 196] This superior moisture permeability is crucial to maintain a pleasant microenvironment between the skin and wearable devices.

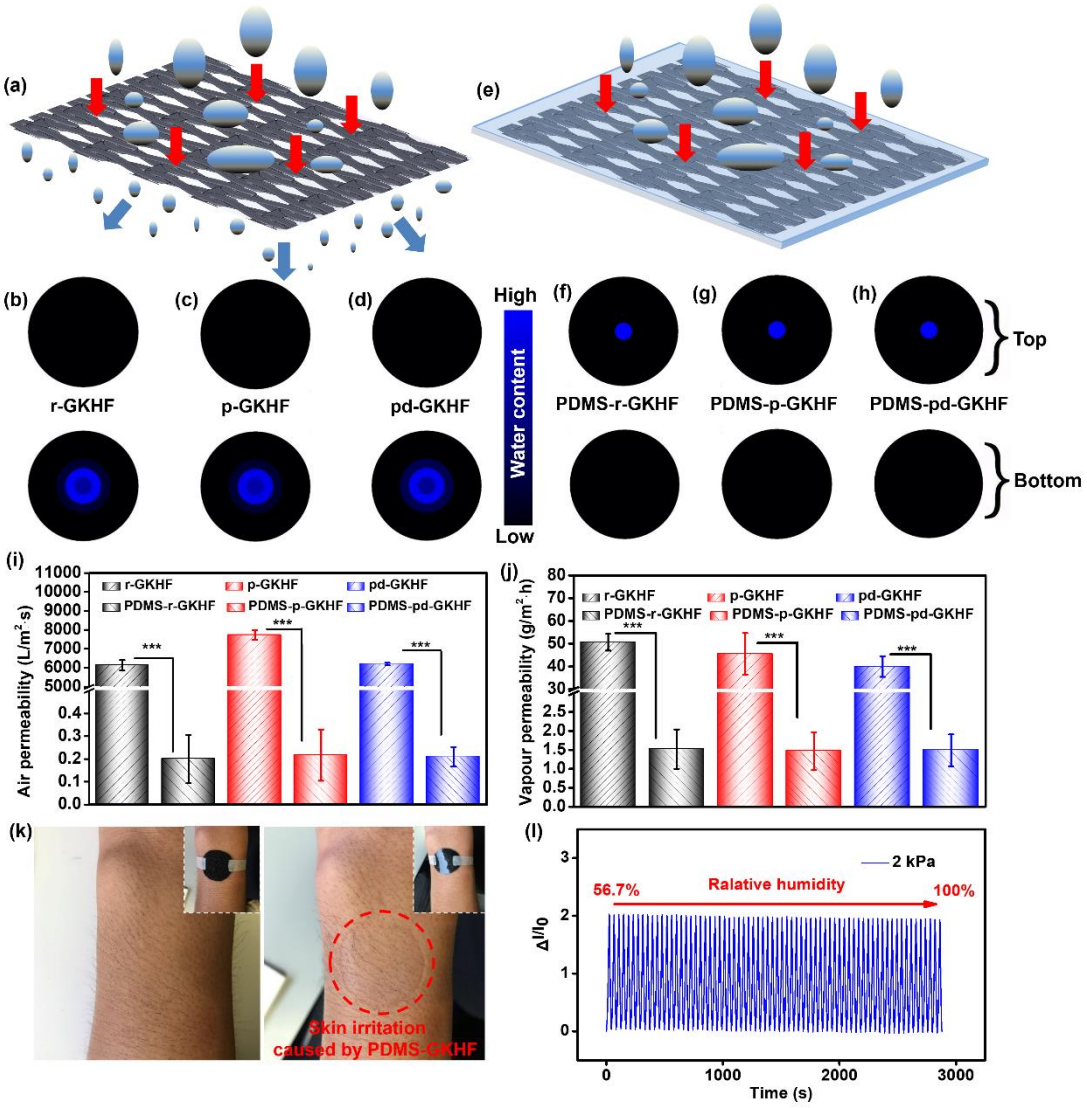

Figure 3-4. Permeability of the GKHF. (a) Illustration of high permeability of GKHF. (b-d) Liquid diffusion details of GKHF. Liquid droplets penetrated easily through the GKHF sensors. (e) Illustration of non-permeability of PDMS-GKHF. (f-h) Liquid diffusion details of PDMS-GKHF. Liquid droplets could not penetrate the PDMS-GKHF sensors. (i) Air permeability of both GKHF and PDMS-GKHF. GKHFs show much better permeability to air than PDMS-GKHFs. (j) Water vapour permeability of both GKHF and PDMS-GKHF. GKHFs show significantly higher permeability to water vapour than PDMS-GKHFs. (k) Photographic images before and after attaching GKHF and PDMS-GKHF on the skin surface for 2 h. GKHF shows high wearing comfort while PDMS-GKHF shows skin irritation. (l) High stability of p-GKHF at different humidity ranging from 56.7% to 100%.

In contrast, when the devices were encapsulated with PDMS, the water droplet remained on the front side of the device and no water penetration was observed (Figure 3-4e-h). The air permeability and water vapour permeability (Figure 3-4i, j) of GKHFs exceeded 6000 L/m^2·s and 40 g/m^2·h, which are similar to knitted fabrics, and much better than polyester nonwoven fabrics and cotton woven fabrics.[197, 198] The low-density knitted structures with many orifices enable the transmission of air and water vapour from one side to another side, guaranteeing outstanding air and water vapour permeability of the fabric sensors. PDMS-GKHFs, however, showed poor permeability to air (~0.2 L/m^2·s) or water vapour (~1.5 g/m^2·h). It should be noted that high permeability is desirable to guarantee the perspiration escaping from the skin.[185] Considering the fact that transepidermal water loss from human skin ranges from 5.6 g/m^2·h to 18.7 g/m^2·h in room condition,[199] the high permeability of GKHFs allow complete perspiration and significantly improve the wearing comfort.

As a proof-of-concept demonstration of the superiority of our encapsulation-free sensors, GKHF and PDMS-GKHF were attached on the wrist by medical adhesive tape for 2 h. No visible changes are noticed on the GKHF-attached skin, while skin irritation is obviously observed after wearing the PDMS-GKHF (Figure 3-4k). Considering the increasing humidity of human skin in hot environments and sports motions, wearing the encapsulated sensors limits the diffusion of sweat to the environment. The increased sweat humidity would lead to higher friction coefficient, resulting in higher abrasion resistance, and barrier capacity, creating a more suitable environment for bacteria proliferation, and this

will determine physical discomfort, higher degrees of skin irritation even skin rash.[200, 201] The biocompatibility is of importance to not only biomedical materials but also wearable devices.[202, 203] Previous work has shown that carbon-based materials (e.g., graphene and carbon) demonstrate good biocompatibility, which is potential for versatile applications of bioengineering and biomaterials.[204-206] Our carbon-based sensors are fabricated to monitor the human activities *in vitro*, we believe the sensor cannot result in any adverse harms to the human body due to the abovementioned good biocompatibility, especially with the protection of the skin. Notably, p-GKHF presents excellent humidity stability in that the piezoresistive response showed no characteristic change when the humidity was increased from ~56.7% (normal room conditions) to ~100% (Figure 3-4l). This ensures the wide applicability of the pressure sensor in different wearing environments.

3.3.5 Monitoring Human Activities by the Pressure Sensor

With the outstanding piezoresistive performance and high wearing comfort, the pressure sensor can be applied to a wide variety of applications that sense subtle to high pressures (Figure 3-5a). First of all, the outstanding low-detection limit of p-GKHF offers great advantage in sensing subtle pressure (below 1 kPa). As a proof of concept, 3.4 mg plumage tip (corresponding to ~0.34 Pa) and 21.6 mg rice grain (corresponding to ~14.4 Pa) were placed on top of the p-GKHF and then removed twice. The current of the device rose immediately after loading, remained stable when the loads were static, and eventually declined sharply to zero after unloading (Figure 3-5b). The sensor also responses fast to detect dynamic vibration such as sound waves of music. For example, four loops of a

music clip were recorded by p-GKHF (Figure 3-5c). The signals generated by the sensor present a good agreement with the strength and frequency of the sound wave and a remarkable reproducibility among each loop.

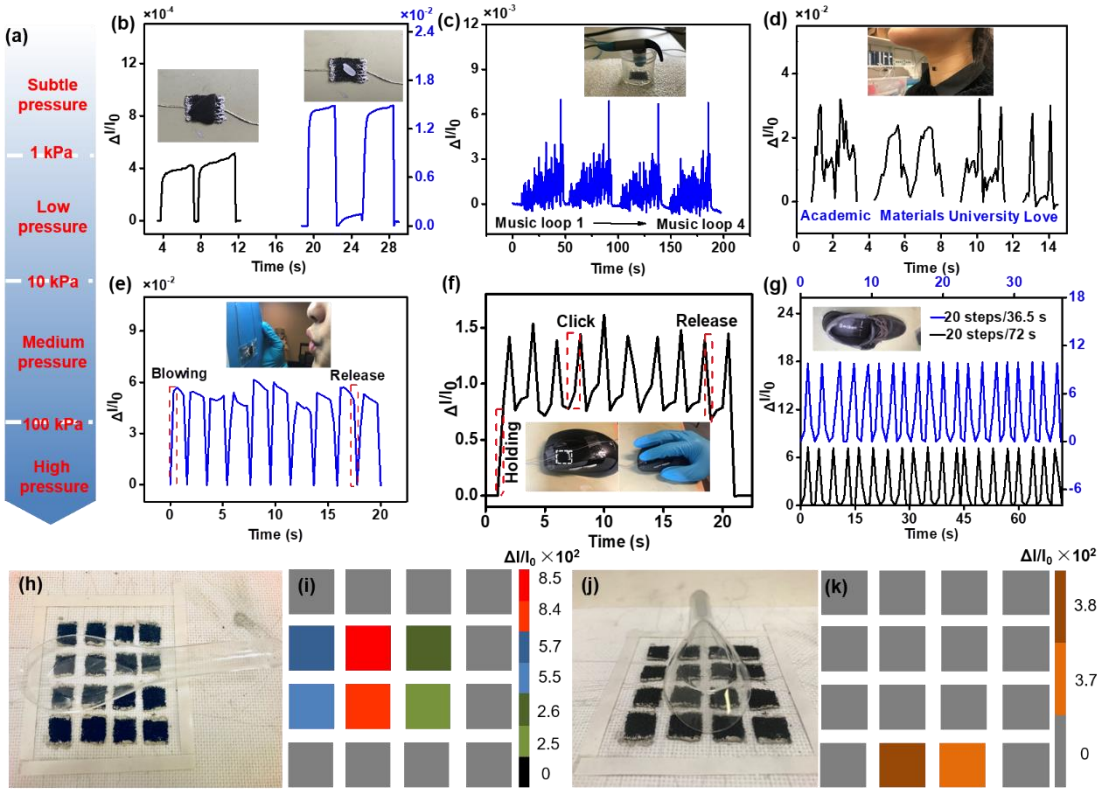

Figure 3-5. Applications of p-GKHFs. (a) Pressure distribution of pressure sensors. (b) Measurement of loading and unloading of plumage tip (3.4 mg, corresponding to ~0.34 Pa) and a grain of rice (21.6 mg, corresponding to ~14.4 Pa). (c) Detection of sound wave. A 40-second music loop was played 4 times. (d) Voice recognition. The sensor was attached to the epidermis of the throat. (e) Detection of aspiration. Blowing was applied for 10 cycles. (f) Detection of finger movements of clicking a mouse button. (g) Monitoring of running by attaching the sensor to the insole. (h-k) 4×4 p-GKHF sensor array to detect the position and orientation of a plastic spoon.

Secondly, the sensor is suitable to monitor human's physiological characteristics such as speaking, aspiration, and pulse, whose response falls in the low-pressure range (1-10 kPa). Attaching the pressure sensor onto the epidermis of the throat

allows the recognition of the voice. Figure 3-5d shows that the sensor enables to distinguish and reproduce the signals generated from the epidermis vibration in speaking words, which promises potentials in phonation rehabilitation training as well as man-machine interaction. Similarly, it records the subtle change of pulse signal (Figure 3-S10). Blowing onto the p-GKHF generates current signals in which the current intensity rises and drops as a function of the strength of the breath, which provides a low-cost respiration sensor to measure human respiratory volume and rate by suitably embedding it in a mask.

Thirdly, the sensor detects human movements in the medium-pressure range (10-100 kPa). Figure 3-5f shows a demonstration of recording the finger movement of clicking a mouse button. Figure 3-5g shows another demonstration of monitoring human's running by attaching the sensor on an insole. It reveals a slower (20 steps/72 s) and a faster (20 steps/36.5 s) running speed with a stable electrical signal output. Moreover, an array of p-GKHFs can provide mapping capability of the distribution of pressure. As a proof of concept, a 4×4 sensor array was fabricated to detect the pressure generated by a plastic spoon (Figure 3-5h-k). The signals not only reflect the position and weight of the spoon, but also its orientation.

3.4 Summary

In summary, we have developed a highly permeable pressure sensor with graphited knitted hemp fabrics. By taking advantage of the outstanding resilience of hemp fibres, GKHF sensors avoid the use of encapsulation materials, which enables remarkable

permeability (air, moisture, and water vapour) and extends the detection limit to very low pressures. High permeability of the device provides significant wearing comfort, in contrast to the conventional non-breathable pressure sensor which leads to skin irritation when wearing for a long period of time. GHKF sensors with plain structure show good sensitivity, high environmental stability, quick response, long cycling life, and large detection range spanning from 0.3 Pa to 500 kPa. GHKFs can detect and map a wide variety of static pressures and physiological signals, which are essential in health monitoring, rehabilitation, athlete training, and sports competition.

Supporting Information

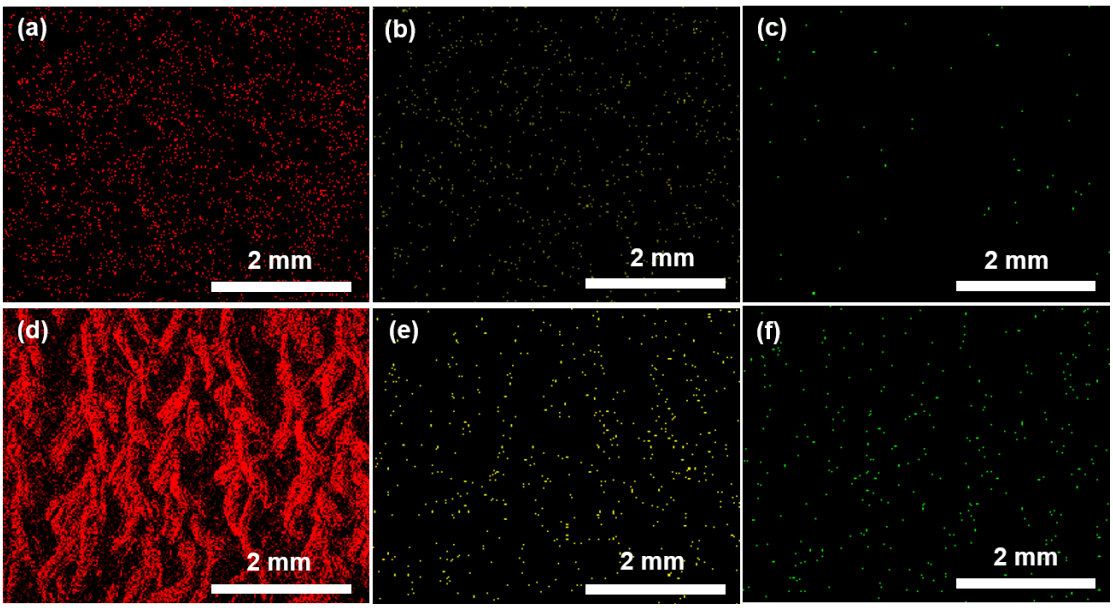

Figure 3-S1. The surface element distribution of pristine and graphited hemp fabrics. (a) C of pristine hemp fabric. (b) O of pristine hemp fabric. (c) N of pristine hemp fabric. (d) C of GKHF. (e) O of GKHF. (f) N of GKHF.

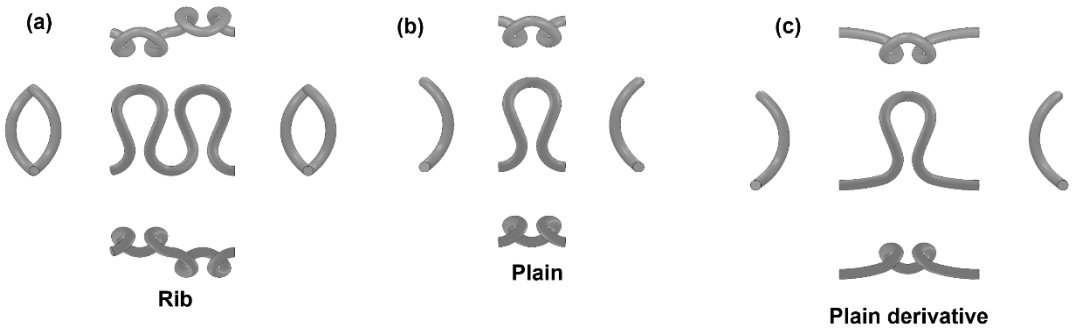

Figure 3-S2. Diagram of different knitted structures. (a) Orthogonal views of the stitch of rib structure. (b) Orthogonal views of the stitch of plain structure. (c) Orthogonal views of the stitch of plain derivative structure.

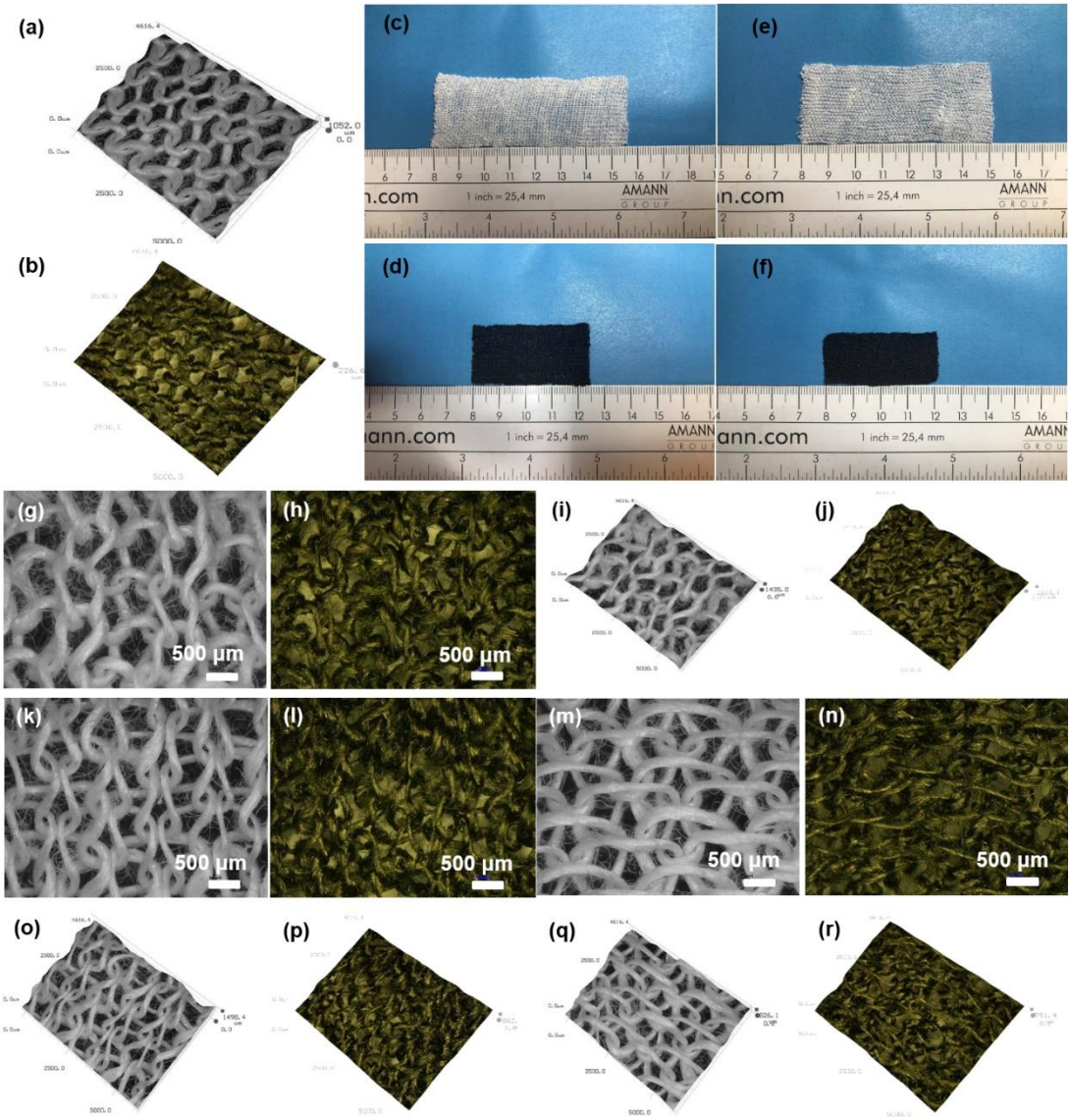

Figure 3-S3. Morphology transitions of knitted hemp fabrics before and after graphitization. (a, b) 3D images of the backside of plain fabric. (c, d) Photographs of rib fabric. (e, f) Photographs of plain derivative fabric. (g-j) Surface images and 3D images of rib fabric. (k-n) Surface images of the front and back sides of the plain derivative fabric. (o-r) 3D images of the front and back sides of the plain derivative fabric. After thermal treatment, the rib fabric experiences a weight loss and surface shrinkage by 83.8% and 48.9% respectively, while they are 83.6% and 55.1% for plain derivative fabric. The slight difference in weight loss can be attributed to experimental error, and the discrepancy of surface shrinkage is due to the different thermal shrinkage capacity resulted from knitted structures.

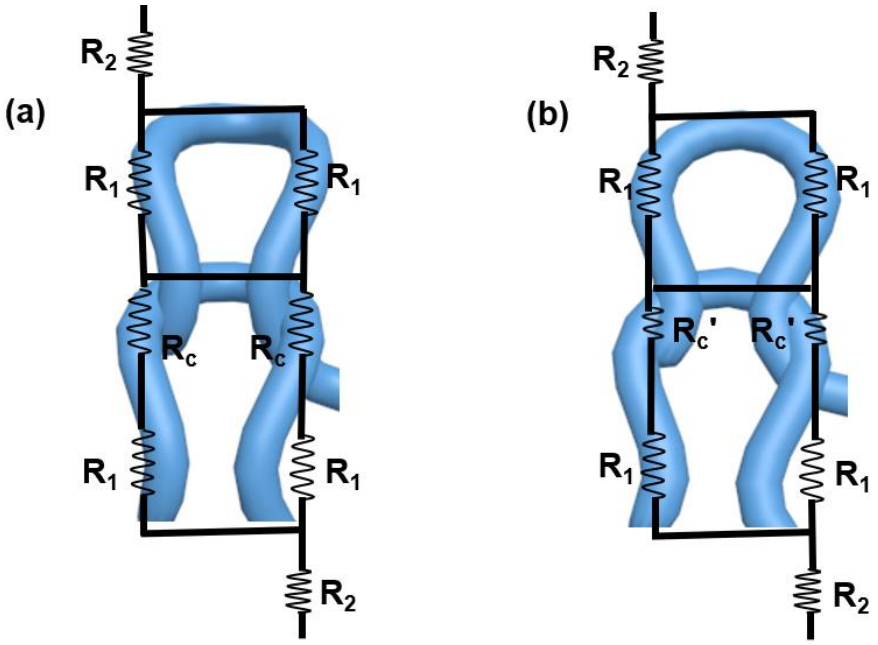

Figure 3-S4. Illustration of the resistance model of p-GKHF. R_1 and R_2 refer to the resistance of meandering half loop and surrounding resistance respectively, Rc represents the contact resistance between meandering loops in the initial state, and Rc' is the contact resistance between two meandering loops under applied pressure. (a) Resistance model of the sensor in the initial state. (b) Resistance model of the sensor under applied pressure.

Figure S4 illustrates the resistance model of p-GKHF, which is composed of the meandering half loop and surrounding loops as well as the contacts between meandering loops. According to this model, the original resistance (R) and the resistance with applied pressure (R') are described as $R=(2R_1+Rc+4R_2)/2$ and $R'=(2R_1+Rc'+4R_2)/2$ respectively. With applied pressure, the contact resistance between loops decreases due to a tighter joint of the fibres. In the equations, it can be seen that there is a positive correlation between the R and Rc, which means the R declining with the decrease of Rc. It explains how the resistance sensor converts increasing pressure into the signals of ascending electrical current.

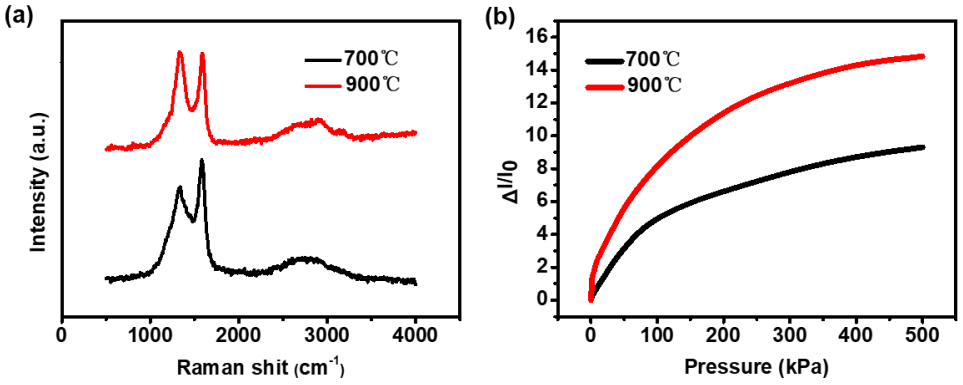

Figure 3-S5. (a) Raman spectra of hemp fabrics with the heat treatment of 700 and 900°C. (b) Calibration results of the p-GKHF with 700 and 900°C treatments.

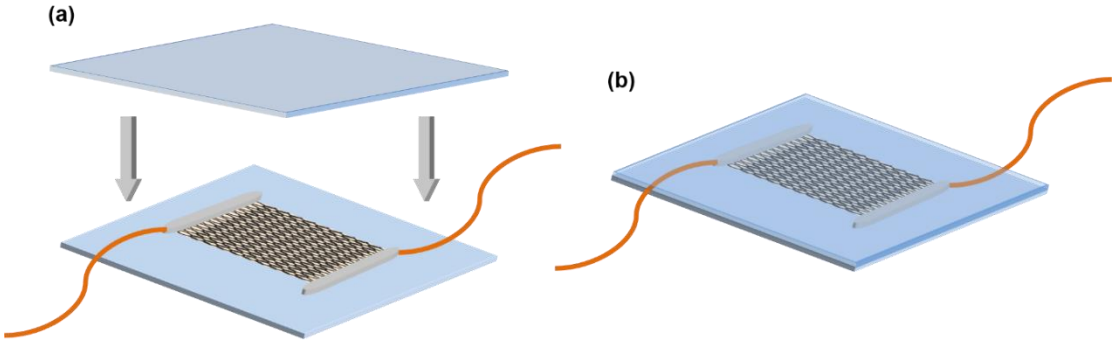

Figure 3-S6. Diagrams of PDMS encapsulation of graphited hemp fabric as a pressure sensor. (a) Encapsulation of the pressure sensor by two individual PDMS face to face with silver paste at both ends to connect wires. (b) The encapsulated pressure sensor.

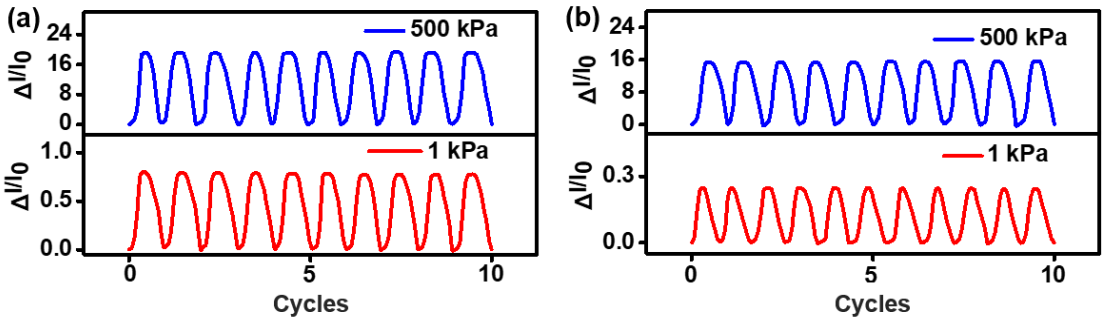

Figure 3-S7. Dynamic stability of r-GKHF and pd-GKHF. (a) 10-cycle electricity response of r-GKHF under different applied pressure. (b) 10-cycle electricity response of pd-GKHF under different applied pressure.

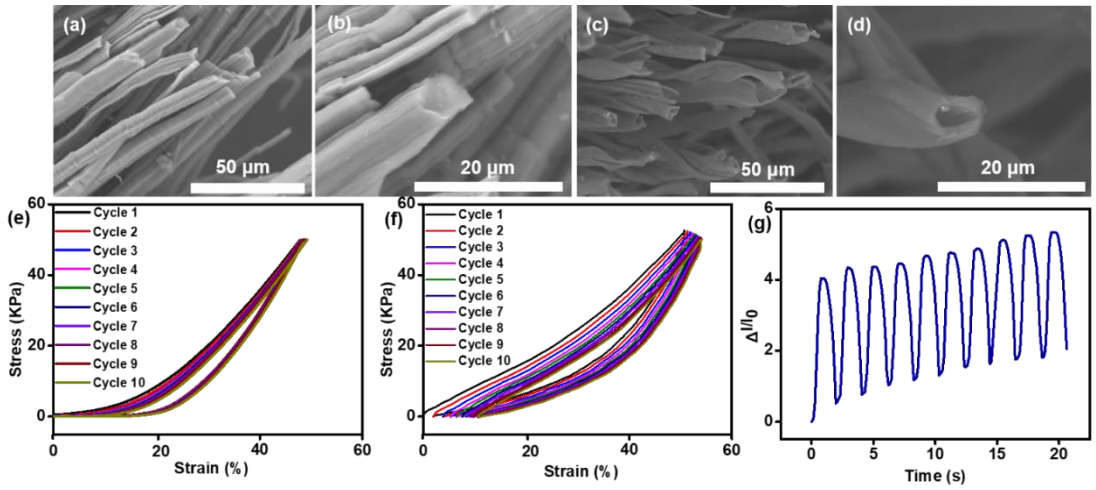

Figure 3-S8. Comparisons between graphited hemp and cotton fabrics as pressure sensors. (a, b) SEM images of graphited hemp fibres. (c, d) SEM images of graphited cotton fibres. (e) Stress-strain curves of graphited hemp fabric under the pressure of 50 kPa. (f) Stress-strain curves of graphited cotton fabric under the pressure of 50 kPa. (g) 10-cycle electrical response to applied 50 kPa pressure of graphited cotton-based pressure sensor.

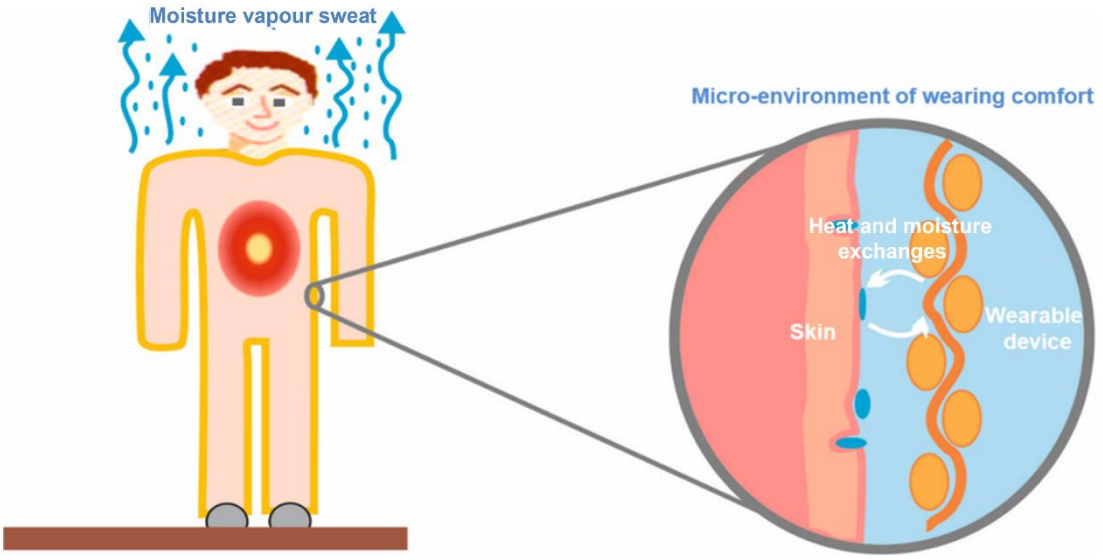

Figure 3-S9. Schematic diagram of wearing comfort in human-wearable devices-environment system.

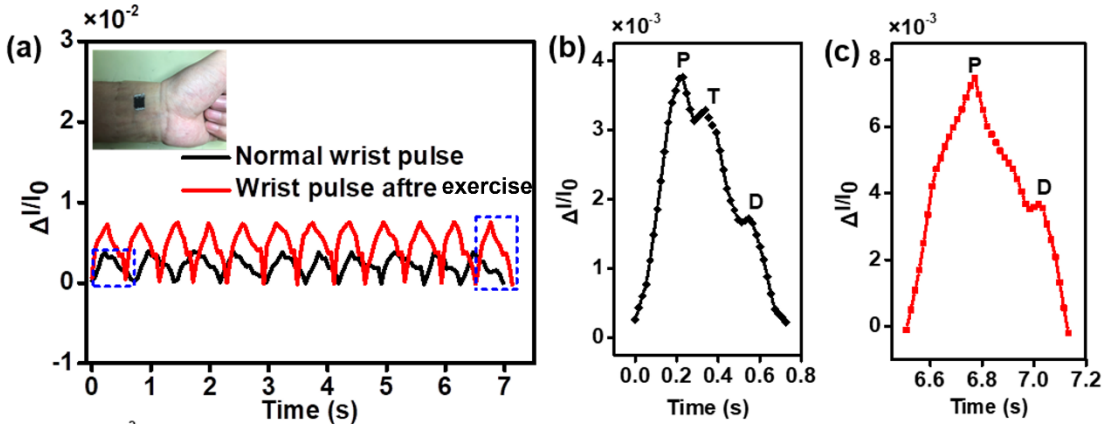

Figure 3-S10. (a) Application of the p-GKHF to detect wrist pulse, wrist pulse before (b) and after (c) excise. The p-GKHF can detect human wrist pulse by conformally attaching it onto the wrist showing a real-time radial pulse manifestation. The normal pulse is 10 beats/6.98 s (~86 beats per min) while it is 12 beats/7.13 s (~101 beats per min) after taking exercise. The discrepant wrist pulse signals not only lie in the frequency, but also the amplifying waveforms showed in Figure S8b, c. There are three weaves for a normal pulse, while two weaves left after exercise. The percussion wave (P), tidal wave (T) and diastolic wave (D) are the typical human normal pulse, and the T vanishes after exercise, which can be attributed to the transformation of human somatic function after exercise.[207, 208]

Table 3-S1 The linear fitting results between our and other's work.

Sample	Detection Range (kPa)	Sensitivity (kPa^{-1})	R-Squared (%)
r-GKHF	0-1.3	0.852	98.7
	1.3-250	0.063	94.8
	250-500	0.015	98.0
p-GKHF	0-2	1.012	99.3
	2-200	0.075	96.7
	200-500	0.017	97.1
pd-GKHF	0-80	0.103	99.2
	80-170	0.042	99.1
	170-500	0.011	97.2
PDMS-r-GKHF	0-250	0.030	98.9
	250-500	0.011	99.4
PDMS-p-GKHF	0-100	0.062	97.0
	100-500	0.014	98.0
PDMS-pd-GKHF	0-160	0.024	99.5
	160-500	0.007	97.2

Table 3-S2 The performance comparison from our work to others.

Materials	Maximum detection pressure	Detection limit	Durability	Refs
Molecule–graphene	1 kPa	7 Pa	2000 cycles	[164]
Microstructure Polypyrrole	100 kPa	0.8 Pa	-	[209]
Modified Poly(glycerol sebacate)	270 kPa	3 Pa	8000 cycles under 80 kPa	[210]
Graphene aerogel	2.5 kPa	30 Pa	-	[211]
Aligned CNT/graphene	6 kPa	0.6 Pa	35000 cycles under 150 Pa	[177]
Graphene-paper	20 kPa	-	300 cycles under 10 kPa	[83]
Carbonized silk	5 kPa	0.8 Pa	10000 cycles under 2.5 kPa	[88]
PVDF and rGO	60 kPa	1.2 Pa	100000 cycles under 500 Pa	[62]
Graphene	40 kPa	-	3000 cycles under 1.5 kPa	[212]
Silver nanowire	5 kPa	15 Pa	1500 under 1.5 kPa	[213]
Graphene	12 kPa	1 Pa	1000 cycles under 5 kPa	[214]
Graphite hemp fabrics	500 kPa	0.3 Pa	10000 cycles under 50 kPa	This work

Chapter 4
A Highly Sensitive Stretchable Strain Sensor Based on Multi-functionalized Fabric for Respiration Monitoring and Identification

This chapter focuses on the second research objective. The work has been completed and published in Chemical Engineering Journal in 2021. The details are reported below.

Authors: Zekun Liu, Zhenhong Li, Heng Zhai, Lu Jin, Kaili Chen, Yangpeiqi Yi, Yuan Gao, Lulu Xu, Yan Zheng, Sirui Yao, Zhangchi Liu, Gang Li, Qingwen Song, Pengfei Yue, Shengquan Xie, Yi Li, and Zijian Zheng

Journal: Chemical Engineering Journal

DOI: 10.1016/j.cej.2021.130869

Statement of author contributions:

The proposal of the primary research idea. Carbonisation, copper deposition, and sensor fabrication, material and sensor characterization, as well as application demonstrations. Preparation of tables, figures and the manuscript.

Statement of co-author contributions:

Zhenhong Li supports deep learning networks for the analysis of respiration signals. Heng Zhai and Yangpeiqi Yi provide support in the SEM characterization. Lu Jin, Kaili Chen, Yuan Gao, and Lulu Xu contribute result validation. Yan Zheng, Sirui Yao, Zhangchi Liu, Gang Li, Qingwen Song, Pengfei Yue, and Shengquan Xie help in polishing the language of the draft manuscript before submitting it to journals. Yi Li and Zijian Zheng supervise the work throughout.

Note: Supplementary material is available in Supporting Information.

4.1 Introduction

Human activity and health monitoring with skin-mountable and stretchable strain sensors fulfilled in a continuous and timely manner are attracting considerable research interest on account of their great possible benefits.[215-218] Much research in recent years has focused on resistance-based strain sensors due to the easy and low-cost fabrication process as well as the high sensitivity.[76, 162] Numerous experiments attempted to fabricate the strain sensors via constructing conductive network configuration with the encapsulation of elastomers. Such conductive network configuration can be implemented through electrostatic spinning, wet spinning, and surface chemical etching, which is often time-consuming and technically difficult.[35, 40, 144, 219]

Recently, it was found that β-sheet-rich silk protein and polymers would be transformed into pseudographitic structures through simple heat treatment, which aroused much attention for developing wearable sensors.[52, 86, 87, 89, 220-223] Nevertheless, the carbonized polymer-based strain sensors detecting applied strain as a function of contact resistance changes face the challenge of either limited stretchability or inferior quality in sensitivity. For example, a strain sensor made with carbonized cotton fabric showed a stable strain sensing ability up to the strain of 80%.[87] Another carbonized silk fabric sensor indicated a low gauge factor (GF) of 9.6 in the sensing range within 250%.[52] More importantly, human motion monitoring with strain sensors lacks the function of signal recognition, which is far from optimal in the practical application scenario. It is of vital importance to develop a strain sensor with the performance of high sensitivity and stretchability to reliably convert surface movements into electrical signals, and the ability for signal identification aiming for precisely alarming emergency.

Herein, we report a highly sensitive wearable strain sensor with good stretchability through polymer-assisted metal deposition (PAMD) on linen fabric with high-temperature processing. The high-performance strain sensor is readily fabricated by depositing highly conductive copper particles on a carbonized fabric (CF), then encapsulated with Ecoflex. The intermingled copper distributed on the fibre surface endows the sensor with outstanding performance. For instance, the GF of the sensor is 3557.6 and 47.8 in the strain range from 0 to 48% and from 48% to 150%, respectively. It also enables the sensor to achieve a large stretchability up to the strain of 300%. By taking advantage of the high sensitivity and stretchability, the copper-deposited carbonized fabric (CDCF) sensor with multi-sensing elements (i.e., copper particles and conductive fibre) enables to detect many human motions in real time. We also demonstrate a respiratory monitoring and warning system constructed with the sensor and a deep learning network to monitor and identify normal breath, tachypnea as well as tachypnea with cough, revealing enormous potential in the healthcare of people with respiratory diseases such as COVID-19 infected patients.

4.2 Experimental

4.2.1 Fabric Functionalization and Sensor Fabrication

The pristine linen woven fabrics (supplied by the textile lab of the University of Manchester, plain structure) were carbonized in a tube furnace at a heat-up speed of 3°C/min with the protection of nitrogen throughout. When reaching the target temperature (i.e., 700, 900 and 1100℃), the fabric naturally cooled down to room temperature before taking out. The CFs were then immersed in concentrated sulfuric acid (>96.0%) at 80°C for 1 h to increase functional groups for the consequent polymer growth. After that, the CFs were treated in a 4.0 % (v/v) [3-(methacryloyloxy) propyl] trimethoxysilane solution (solvent: 95.0 % ethyl alcohol,

1.0% acetic acid, and 4.0 % deionized water) in room temperature for 2 h. Consequently, the silanized CFs were then dipped into 50 mL mixed solution at 80°C for 1 h, solution being made up with [2-(methacryloyloxy) ethyl] trimethyl ammonium chloride (METAC) (10 mL, 75wt. % in H_2O), deionized water (40 mL), and potassium persulfate (100 mg, >99.0%). Then, the CFs were immersed in the aqueous solution of $(NH_4)_2PdCl_4$ (5×10^{-3} M L^{-1}) in a dark environment for the growth of the activator for following copper deposition. Finally, the $[PdCl_4]^{2-}$ loaded CFs were immersed into a mixture of isometric A and B for 40 min to achieve copper deposition. A is NaOH (>97.0%) (12 g L^{-1}), $CuSO_4\cdot5H_2O$ (>98.0%) (13 g L^{-1}), and $KNaC_4H_4O_6\cdot4H_2O$ (>99.0%) (29 g L^{-1}) in deionized water, and B is formaldehyde aqueous solution (9.5 mL L^{-1}). To explore the concentrations of the A and B solutions in determining the conductivity of the CDCF, the concentrations of both solutions A and B were halved and were double from the abovementioned parameters respectively. The chemicals were purchased from SIGMA.The detailed mechanism of the PAMD can be found in our previous study.[57, 217, 224] To fabricate the CF and CDCF sensors, both CF and CDCF were cut into the size of 2.2×1.0 cm^2 with silver paste and conductive tape at both ends. After the encapsulation with Ecoflex, the sensors were cured at room temperature for 24 h.

4.2.2 Characterization

The surface morphology of pristine fabric, CF, and CDCF was observed using an optical microscope (Keyence VHX-5000) and a scanning electron microscope (ZEISS Ultra-55). The atomic percentage of the surface elements of all the samples was detected by the scanning electron microscope (ZEISS Ultra-55) equipped with energy-dispersive X-ray spectroscopy (EDS), and the voltage applied for the measurement is 10 V. A Raman spectroscopy (WITec, Apyron) with a 532 nm laser wavelength and a transmission electron microscope (Tecnai T20)

were used to measure the structure of the CF. The sheet resistance of the CFs and CDCFs was measured through Keithley 2450 equipped with four-point probes and programmable software purchased from Beijing Hanlei Technology co. LTD. Targeted strain applied on the sensors was achieved by a universal mechanical instrument (Instron 3344), and all electrical signals generated from sensors were collected by a multimeter (Keithley 2000).

4.3 Results and Discussion

4.3.1 Fabric Functionalization and Sensor Fabrication

Figure 4-1a shows the procedure of functionalizing a highly conductive composite from a piece of commercial linen fabric. The fabric is firstly treated in an inert gas environment (700°C) to induce the structure transformation (from cellulose to pseudo graphite). Then the CF is modified by functional polymers, that is, silane-type initiator and METAC, following with ion pairing with palladium moieties as the activator. After that, we can get a carbonized fabric with copper deposition (Details in Experimental Section). Even though experiencing carbonisation and copper deposition, the fabric still maintains good flexibility, both of which can be folded into a collar shape (Figure 4-1b). To fabricate the CDCF sensor, the CDCF in the size of 2.2×1.0 cm^2 with silver paste and conductive tape at both ends is encapsulated with Ecoflex (Figure 4-1c). Figure 4-S1 exhibits that the overall thickness of the sensor is about 850 μm, and all the multi-functionalized fibres are well encapsulated.

With the carbonisation and PAMD, the surface morphology and microstructure of the fabric are significantly changed. Figure 4-S2a, b illustrate that the pristine fabric (11.0×2.2 cm^2) experiences a surface shrinkage after carbonisation (7.0×1.5 cm^2), which can be attributed to the release of CO_2, CO as well as H_2O during heat treatment. After PAMD, there is a layer of

visible dense particles on the surface of the fabric (Figure 4-S2c). Higher-magnification morphology in Figure 4-2a, b suggests that the surface of both pristine and carbonized linen fibres is smooth, and there is a volume shrinkage after experiencing thermal treatment, while many dense particles are attached to the surface of fibres after PAMD (Figure 4-2c).

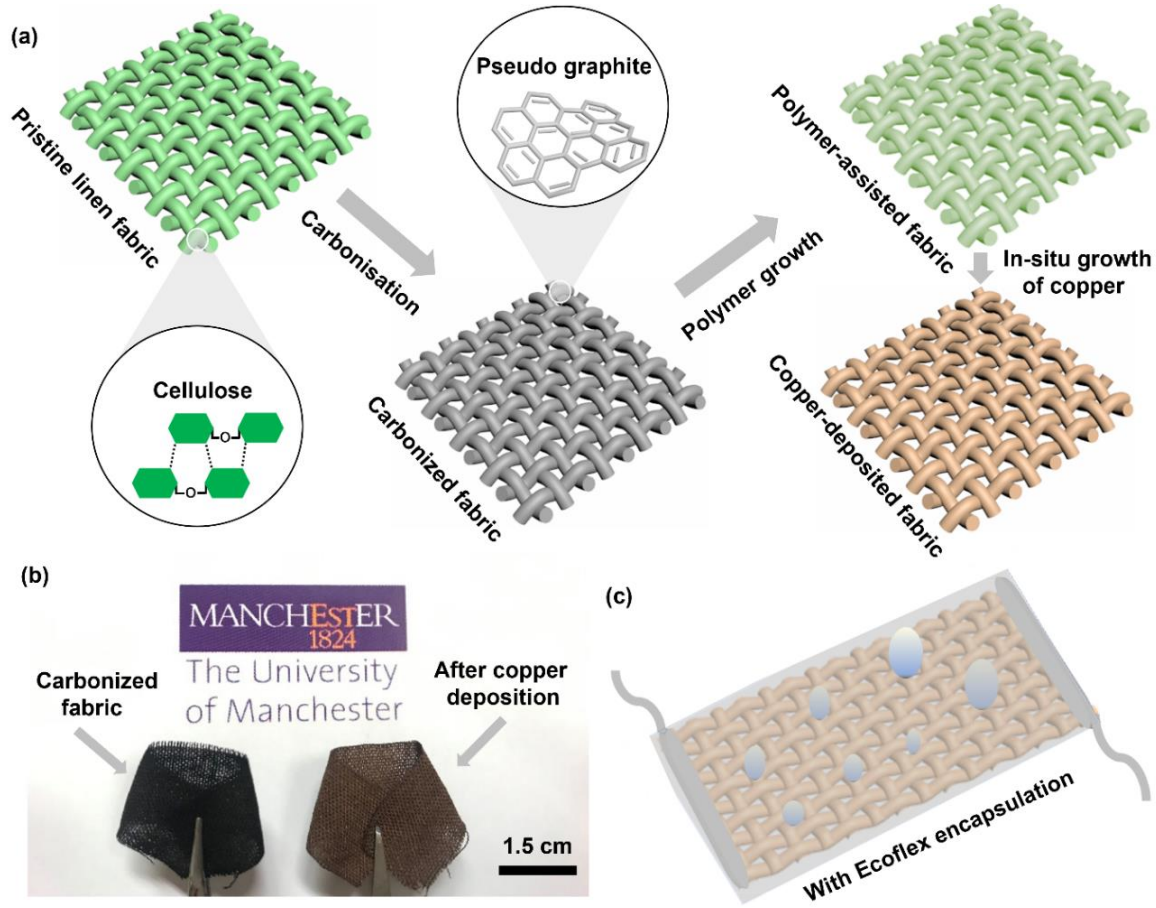

Figure 4-1. The schematic diagrams of fabrication of the CDCF sensor. (a) The procedures of producing multi-conductive fabric through carbonisation and PAMD. (b) The photographs of the CF and CDCF, showing their robustness and flexibility by bending them into collar shape. (c) The fabrication of the CDCF sensor by encapsulating the CDCF with liquid Ecoflex.

The process of the fabric functionalization significantly changes the surface elements. Measurements showed that atomic percentage of C, O, and N is 42.7%, 51.9%, and 0.9% respectively for the pristine fabric, and that of the three elements becomes 93.5%, 6.2%, and 0.2% for the fabric after thermal treatment (Figure 4-2d). After copper deposition, the chemical

elements become C, O, and Cu with the atomic percentage of 10.8%, 2.6%, and 86.5% respectively. The surface elements mainly include Cu, C, and O, and the content of N is too low to be detected. The elements conversion is also characterized by observing their distribution, it shows that the corresponding elements are even-distributed throughout without agglomeration (Figure 4-S3, Figure 4-2e).

The heating process in the inert gas atmosphere not only changes the surface morphology and chemical elements but also results in the structural transformation from cellulose to carbonaceous forms, which is validated by Raman spectroscopy as well as transmission electron microscopy (TEM). A typical TEM image of the CF shown in Figure 4-2f exhibits many tiny distorted lattice stripes with an interlayer distance of 0.35 nm, revealing the formation of pseudo-graphitic structure induced by heat treatment.[52, 223] We carbonize the pristine fabrics in the temperature of 700°C, 900°C, and 1100°C respectively, and then the CFs are modified with PAMD for the fabrication of CDCF sensors. The sheet resistance of the carbonized fabrics with the treatment of 700°C, 900°C, and 1100°C is 5.6×10^{3} Ω/cm^2, 21.36 Ω/cm^2, and 12.69 Ω/cm^2 respectively, indicating that high-temperature treatment not only promotes a high degree of structural order in the integrity of the graphite but also increase their conductivity. The sheet resistance of the CDCF (700°C) for the fabrication of the sensor is 1.3×10^{-2} Ω/cm^2 after PAMD. The conductivity is very flexible to control by changing the concentration of the reaction solution (Details in Experimental Section). With decreasing the concentration, the sheet resistance of the CDCF and surface atomic percentage of copper is 8.9×10^{-2} Ω sq^{-1} and 69.54% respectively (Figure 4-S4a). By contrast, they become 1.2×10^{-2} Ω/cm^2 and 89.63% respectively by increasing the concentration of the reaction solution (Figure 4-S4b). The Raman spectra in Figure 4-2g and Figure 4-S5a reveal that there are two distinct characteristic peaks of graphite for all the heat-treated fabrics, which represent typical G-band

and D-band located at ~1584 cm^{-1} and ~1330 cm^{-1} respectively, additionally manifesting the formation of carbonaceous structure. The change of the G-band and D-band with the increase of temperature shows that higher temperature promotes a higher degree of structural order in the integrity of the graphite. By fitting the curves of the Raman spectra (Figure 4-S5b-d), the intensity ratios of D-band and G-band (I_D/I_G) increase as a function of temperature increase (Figure 4-S5e), of which findings are consistent with reported work.[86]

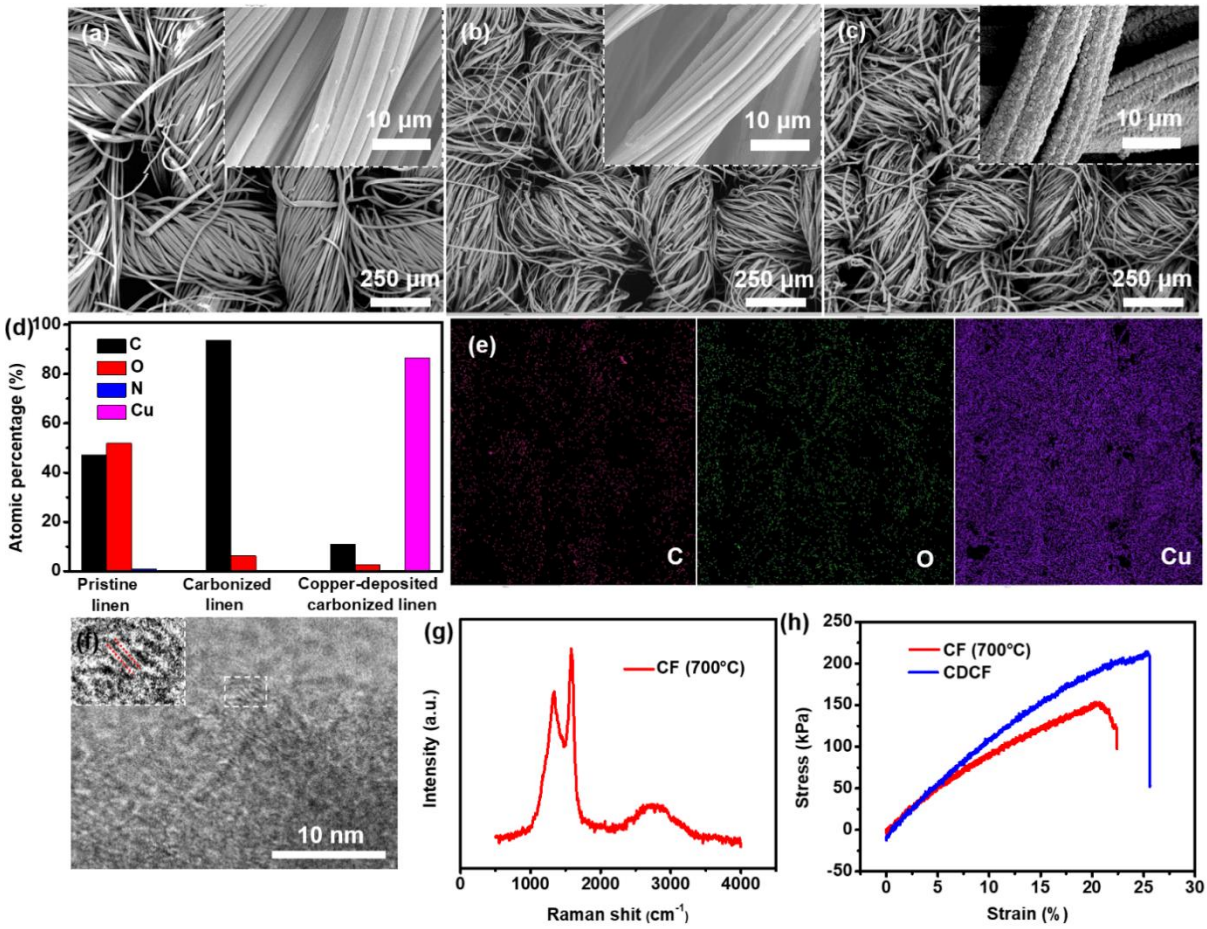

Figure 4-2. Characterization of pristine and functionalized linen fabrics. (a) Surface morphology of pristine linen fabric. (b) Surface morphology of the CF. (c) Surface morphology of the CDCF. (d) The surface elements of pristine linen fabric, and the CF as well as the CDCF. (e) The surface element distribution of the CDCF. (f) TEM image of the CF, showing its carbonaceous structure. (g) Raman spectra of the CF after the treatment of 700°C in an inert gas atmosphere. (h) The strain-stress curves of the CF and CDCF.

The high-temperature treatment not only promotes a high degree of structural order in the integrity of the graphite but also increase their conductivity. The mechanical property of the fabric significantly decreases after the carbonisation. Figure 4-S6a exhibits that the pristine fabric possesses a breaking strength of more than 10 MPa, while it becomes ~153 kPa and ~212 kPa for the CF (700°C) and the CDCF respectively (Figure 4-2h). The slight increase in breaking strength after the PAMD can be ascribed to the uniform polymer interfacial layer (i.e., METAC) that bonds the metal to the CF surface. In addition, Figure 4-S6b shows that the breaking strain and breaking stress of the CF (900℃) are ~140 kPa and ~13% respectively, while those of the CF (1100℃) are ~100 kPa and ~10% respectively. By comparing the mechanical performance of the CF treated with 700℃, it indicates that higher temperature treatment would decrease both breaking strain and breaking stress of the CF.

4.3.2 Calibration and Sensing Mechanism of the CDCF Sensor

Before the calibration of all sensors, a tensile strain with a speed of 5 mm/min served as rupturetrainning was applied until the resistance of them is infinite (CF sensor) or stable (CDCF sensor). Figure 4-S7 presents the photographs of the CDCF sensor at the tensile strain of 0%, ~40%, and ~150%, showing the formation of strain-dependent deformation. Calibration results in Figure 4-3a exhibit that the CF sensor acquires a low sensitivity with tolerable strain up to 96%, of which GF is only ~23.0 throughout the sensing range (See sensitivity details of all sensors in Table 4-S1). The sensitivity of strain sensors is indicated by the GF, which is defined as $GF=(_{\Delta}R/R_0)/\varepsilon$, where the ε is the strain of the strain sensor. The resistance of the electrical network in the sensor would be infinite with further stretching. By contrast, the sensor made with CDCF (700°C) shows remarkable sensitivity (GF~3557.6 in the strain range from 0 to 48%, GF~47.8 in the strain range from 48% to 150%), and outstanding stretchability up to 300%

(Figure 4-S8). The electrical response of the sensor in the tensile strain ranging from ~150 % to ~300 % shows very little change, it cannot detect strain changes in this range. However, this property is still very important for wearable sensors, as it would avoid the sensor to be damaged in real application when deformation over the strain of ~150%. Figure 4-3b displays that there is the formation of small cracks on the CDCF network after the rupturetrainning, and they gradually extend with increasing stretching, thus leading to an increase in resistance. The multi-layer sensing elements (i.e., copper and carbonized fibre) with the significant difference in conductivity are of vital importance to the high sensitivity and stretchability. Both of the CDCF sensors with the carbonisation temperature of 900°C and 1100°C present a lower sensitivity than the sensor treated with 700°C (Figure 4-S9), as higher temperature promotes higher conductivity of CF, thus resulting in the smaller relative change in resistance at the same-extent elongation.

The schematic diagram of the CDCF sensor in Figure 4-3c illustrates that elongation-induced fractured fibre and copper particles experience separation, and some suspended fibres perpendicular to the tensile direction maintain the conductive pathway. Notably, unlike the CF sensor with limited stretchability, the CDCF sensor is capable of suffering a larger degree of tensile strain up to 300%, which profits from the retention of copper particles (attached to the suspended fibres) in the crack gap. The sensor shows consistent electrical signals at a high degree of strain (>150%) because the further elongation fails to accelerate the separation of fractured fibre, which is consistent with the observation of the reported strain sensor.[162] To understand the sensitivity enhancement by introducing copper, the electrical models of the CDCF sensor and CF sensor are illustrated in Figure 4-3d and Figure 4-S10 respectively. According to the circuits, the equivalent resistance of the CDCF and CF sensors can be calculated with Equation (4-1) and Equation (4-2) respectively.[2, 52, 225]

$$R= (2R_1R_2+ R_1R_3+R_2R_3)/(R_1+R_2+2R_3) \quad (4\text{-}1)$$

$$R= (R_xR_c+ 2R_xR_y+2R_cR_y)/(R_x+R_c) \quad (4\text{-}2)$$

Where R_1, R_2, and R_3 represent the resistance of copper in the island, carbonized fibre, and copper in gap regions respectively. R_x, R_y, and R_c refer to the CF resistance of suspended bridge fibre, island fibre, and fractured fibre respectively. Elongation deformation would both increase the R_2 and R_3 for the CDCF sensor, while it only enhances the R_c for the CF sensor. More importantly, the same degree of stretching induces a larger relative change in resistance for the CDCF sensor due to the high conductivity of copper, thus the CDCF sensor acquires superior sensitivity.

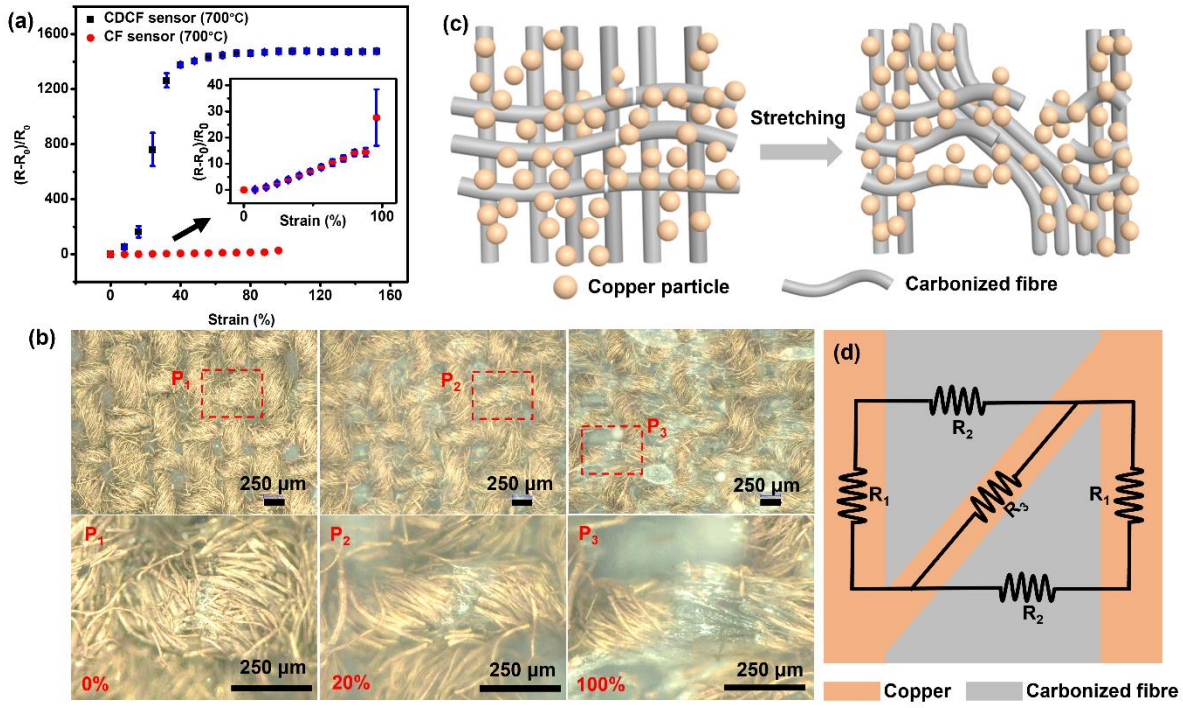

Figure 4-3. Electrical responses of the CF sensor, CDCF sensor, and corresponding mechanism. (a) Calibration results of the CF and CDCF sensors, showing the sensitivity enhancement after copper deposition. (b) The microsphere image of the CDCF sensor under the tensile strain of 0%, 20%, and 100%. (c) Schematic illustration of the CDCF sensor in original and stretched states, and (d) electrical model of the sensor, showing its sensing mechanism.

4.3.3 Electromechanical Performance

Because of the higher sensitivity and stretchability of the CDCF (700°C) sensor, further performance investigation and demonstration would mainly focus on it without explanation. To evaluate the sensing reliability in a dynamic process, we tested the electrical response of the sensor under cyclic loading-unloading in various frequencies and strains. Figure 4-4a shows that the signal generated from the sensor is reproducible at a certain strain, and consistent with calibration results. We also applied a periodic stretching–releasing strain of 10% with the frequency of 0.1 Hz, 0.5 Hz, and 1 Hz respectively. The response shown in Figure 4-4b is also stable with marginal fluctuation, indicating the sensor enables to reliably detect applied strain throughout the sensing range. By applying the tensile strain of 12.5% and 60% in 2.5 s, and maintaining the elongation, the signals are capable of reflecting the corresponding deformation, showing the real-time perception ability of the sensor (Figure 4-4c).

To precisely evaluate the response speed, a quasi-transient step strain of 0.5% with the speed of 16 mm/s was applied to the sensor. The fractional change in resistance shows that the response time reaches ~225 ms (Figure 4-4d), which can meet the general sensing requirements of many daily motions. Remarkably, Figure 4-S11 shows that when applying a strain of 0.1% onto the CDCF sensor, the pattern of the signals remains quite stable, indicating that the high-performance sensor enables to detect ultralow strains or deformations. Long-time stability and durability also play a vital role in the evolution of sensor performance. To further assess the stability of the sensor, a loading-unloading strain of 60% with a frequency of 0.5 Hz was applied to it for 6000 cycles. The electrical signals in Figure 4-4e are stable throughout the whole process with minor fluctuation, illustrating the remarkable stability. The outstanding stability of the sensor is originated from the prominent robustness of Ecoflex, corresponding mechanical output also remains steady during the process (Figure 4-S12). The strain-stress

curve of the CDCF sensor in Figure 4-S13 shows that it has an appropriate flexibility, which is important to wearability. To evaluate the durability of the sensor over a long period time, we firstly applied a strain of 2% onto the sensor with the frequency of 0.5 Hz, then tested its electrical output after one week with the same parameters. The reproducible signals in Figure 4-S14 indicate that the sensor has a good durability.

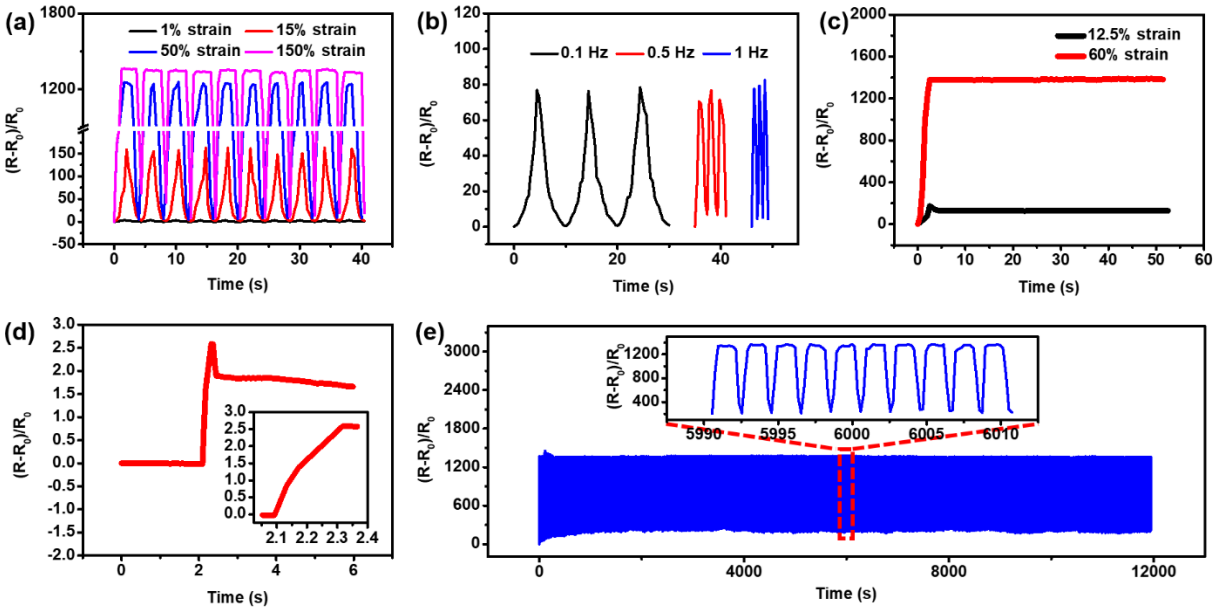

Figure 4-4. Electromechanical property of the CDCF sensor. (a) Electrical signals responding to various 10-cycle loading-unloading strain with the frequency of 0.25 Hz, and (b) electrical response to stretching-releasing strain (10%) with different frequency, showing the dynamic stability in strain and frequency. (c) The fractional change in resistance by applying step strains to the sensor to show its static reliability and low creep. (d) The response speed (~225 ms) of the sensor reflected through applying a strain of 0.5% with the speed of 16 mm/s. (e) The fractional change in resistance under the repeatable stretching-releasing strain of 60% for 6000 cycles with the frequency of 0.5 Hz, presenting the outstanding stability of the sensor.

4.3.4 Motion Monitoring and Identification by the Strain Sensor

Owing to the high sensitivity, large stretchability, fast response, prominent stability, and durability (see the performance comparison between the CDCF sensor and reported sensors in Table 4-S2), the CDCF sensor can be employed to monitor many human body motions in real

time. We firstly mount the high-performance sensor on the skin surface of the throat with viscous tape (Figure 4-S15a) to verify the availability in perceiving coughing, speaking, as well as water drinking. Figure 4-5a displays the fractional change in resistance of the CDCF sensor during coughing. The signals climb and drop with the exertion and release of cough respectively, which is consistent with corresponding epidermis vibration. On the other hand, the response is repeatable throughout with marginal deviation, indicating the high reliability and stability in such motion detection. The sensor is also capable of sensing the epidermis and muscle vibration generated from speaking. Electrical output in Figure 4-5b exhibits differentiable and reproducible patterns when speaking different words, showing great potential in the applications of phonation rehabilitation training as well as human-computer interaction. The electrical patterns from water drinking in Figure 4-5c are reproducible, revealing the application foreground in the swallowing practice and training. Besides, by assembling the sensor on the skin surface of the wrist (Figure 4-S15b), various degrees of wrist bending can be recorded. Resistance signals generated from wrist bending with tiny and larger deformation in which the intensity rises and drops as a function of the degree of bending (Figure 4-5d), showing the potential of wrist bending related movements such as the training of basketball shooting through suitably embedding the sensor in wristbands.

As a proof-concept demonstration of the sensor in the applications of monitoring and distinguishing motions, we develop an end-to-end healthcare system with the functions of respiration monitoring and recognition by combing the CDCF sensor with a convolutional neural network (CNN) model. The respiration signals are collected by attaching the CDCF sensor to the chest (Figure 4-S15c), then the respiration patterns (i.e., normal breath, tachypnea, and tachypnea with cough) are classified into three target classes by using the CNN (Figure 4-5e). Figure 4-S16 and Figure 4-5f show cyclic and typical patterns of respiration signals

respectively, it can be observed that three signals have similar amplitude but distinguishable spectrums. Hence, we use the signal spectrum as the input of CNN for the classification.

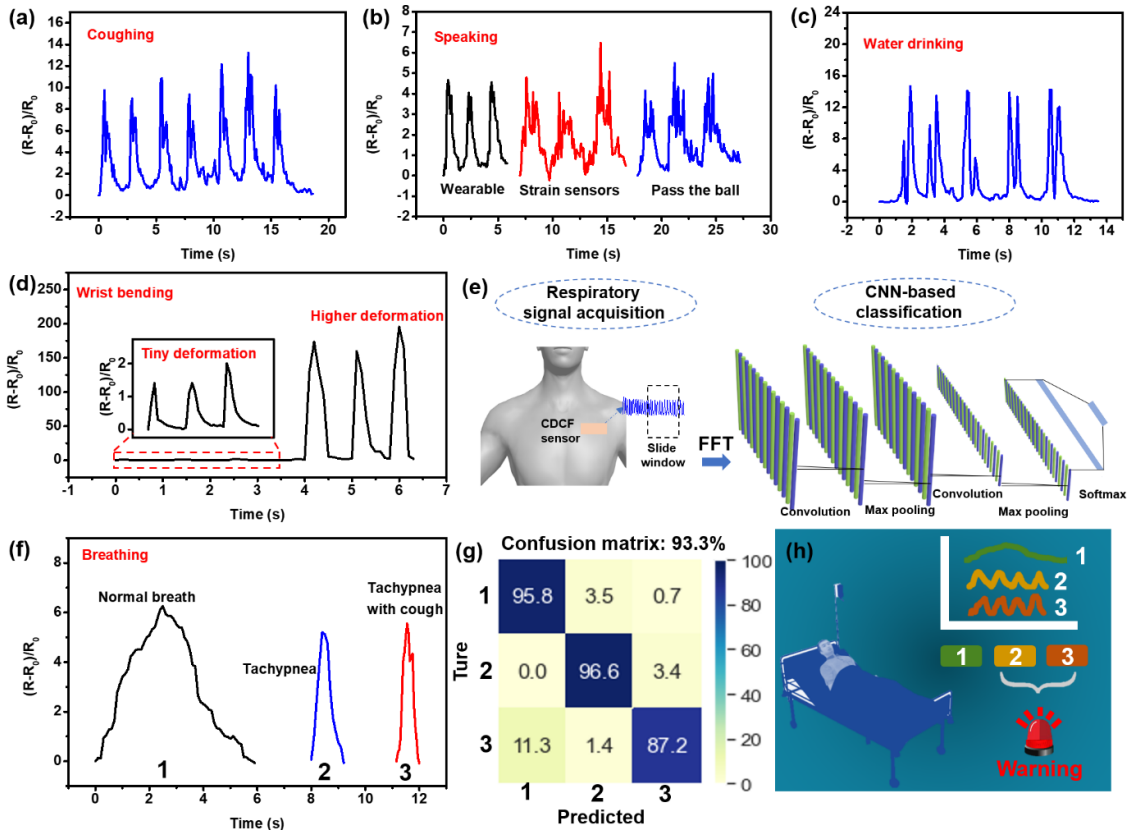

Figure 4-5. The applications of the CDCF sensor in motion detection and identification. (a) Ream-time detection of coughing, (b) speaking, and (c) water drinking by attaching the sensor to the throat. (d) Detection of the wrist bending with tiny and larger deformation through mounting the sensor on the wrist. (e) The schematic diagram of respiration monitoring and identification through integrating the CDCF sensor with a CNN model. (f) Typical electrical outputs of normal breath, tachypnea, and tachypnea with cough respectively. (g) Confusion matrix for the test set of the respiration monitoring and identification system, showing its high accuracy. (h) Illustration showing the personal respiration monitoring and emergency warning system.

For the data preparation, the output of the CDCF sensor is filtered digitally using a sixth-order low-ass Butterworth filter with a 10Hz cut-off frequency, and is segmented using a 3s sliding window with 0.2s increment. The segmented data is then transformed by applying the fast Fourier transform (FFT), and splited into 80% and 20% for training and test set of CNN,

respectively. The CNN architecture adopted in this work is shown in Figure 4-S17, which is composed of two convolutional layers i.e., a fully connected layer and a softmax classifier. The network is trained in a 32-sized mini-batch for 20 epochs using adaptive moment estimation (ADAM). The dynamic learning rate is 0.0001 with a decay rate of 0.001 for each iteration and the dropout rate is set to be 0.2. The confusion matrix for the test set in Figure 4-5g shows that the classification accuracy can reach 93.3%. By taking advantage of the high-precision respiratory monitoring and recognition system, the sensor can be applied as an emergency alarm system for the healthcare of covid-19 infected patients, which is of significance to relieve the stress on medical care personnel.

4.4 Summary

In summary, we have developed a high-performance and stretchable strain sensor through carbonisation and polymer-assisted copper deposition, based on cost-effective linen fabric. The assembling of copper on the fabric can significantly enhance both sensitivity (GF~3557.6 in the strain range from 0 to 48%, GF~47.8 in the strain range from 48% to 150%) and stretchability up to the strain of 300%, which is superior to the sensor made with CF (Stretchability up to the strain of 96% with the GF~23.0). The CDCF sensor with remarkable reliability and durability (>6000 cycles) can be dependably employed to perceive many motions in real time such as coughing, speaking, and wrist bending, etc. The healthcare system based on the sensor and a deep learning network shows the ability to monitor and distinguish normal breath, tachypnea, tachypnea along with cough with high accuracy, which is of great potential in the healthcare of patients with respiratory diseases. Particularly, the concept of assembling highly conductive elements on a conductive substrate to increase sensitivity and stretchability should be extended to many other strain sensors to improve their performance.

Supporting Information

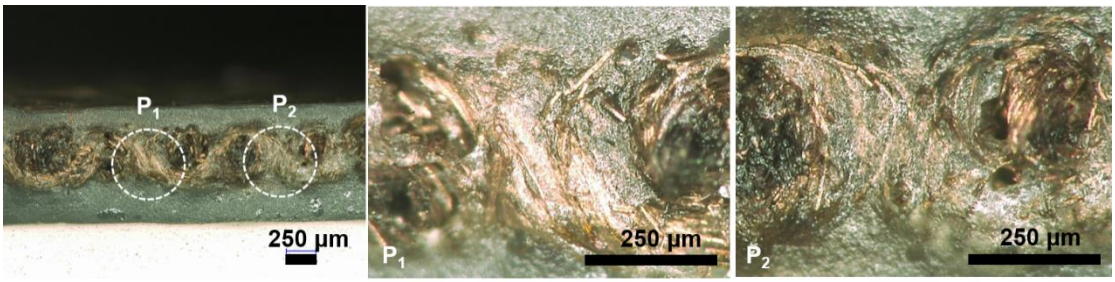

Figure 4-S1. The images of the cross-section of the CDCF sensor observed with a light microscope, showing the thickness of the sensor is around 850 μm, and the Ecoflex enables to reach almost each fibre.

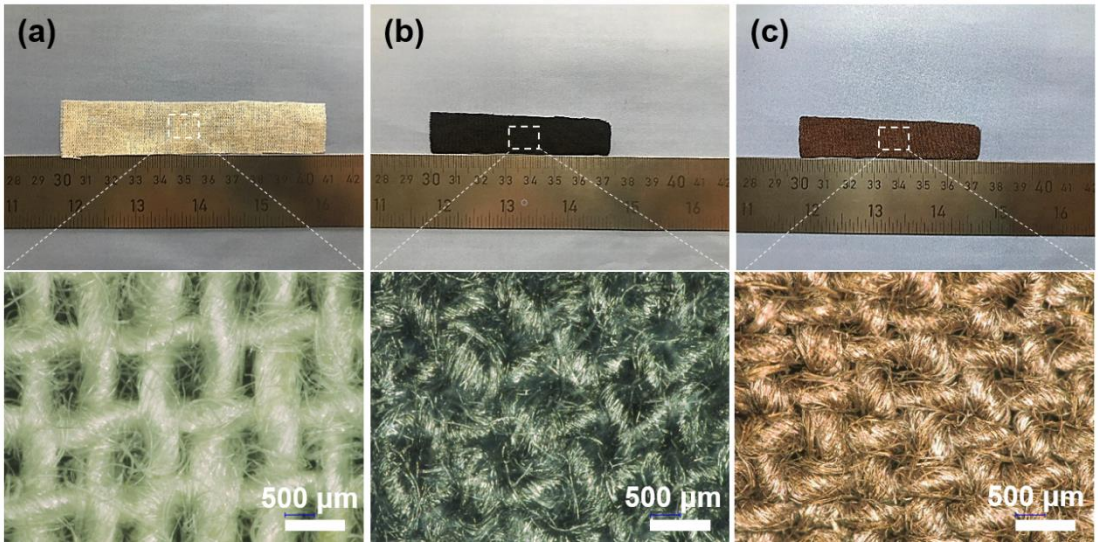

Figure 4-S2. The photographs of pristine linen fabric and the CF as well as the CDCF, and corresponding and micro-topography observed with a light microscope. (a) Surface morphology of pristine linen fabric. (b) Surface morphology of the CF. (c) Surface morphology of the CDCF.

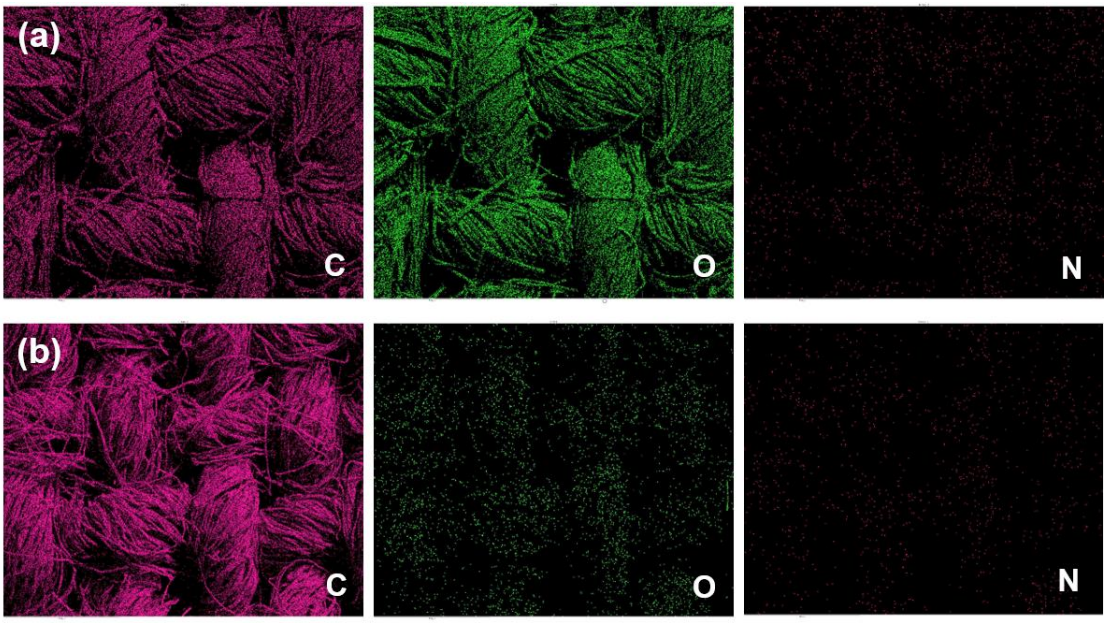

Figure 4-S3. The surface element distribution of (a) pristine linen fabric, and (b) the CF.

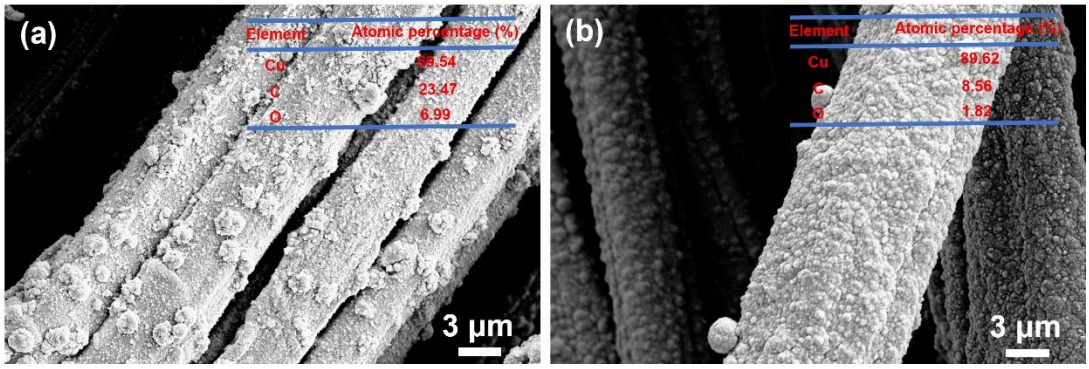

Figure 4-S4. The surface morphology and elements of the CDCF (700°C) after deposition in different concentrations of the reaction solution. (a) The surface morphology and elements of the CDCF prepared in a lower concentration of solution A (NaOH (6 g L^{-1}), $CuSO_4 \cdot 5H_2O$ (6.5 g L^{-1}), and $KNaC_4H_4O_6 \cdot 4H_2O$ (14.5 g L^{-1}) in deionized water) and B (formaldehyde aqueous solution (4.75 mL L^{-1})). (b) The surface morphology and elements of the CDCF prepared in a higher concentration of solution A (NaOH (24 g L^{-1}), $CuSO_4 \cdot 5H_2O$ (26 g L^{-1}), and $KNaC_4H_4O_6 \cdot 4H_2O$ (58 g L^{-1}) in deionized water) and B (formaldehyde aqueous solution (19 mL L^{-1})).

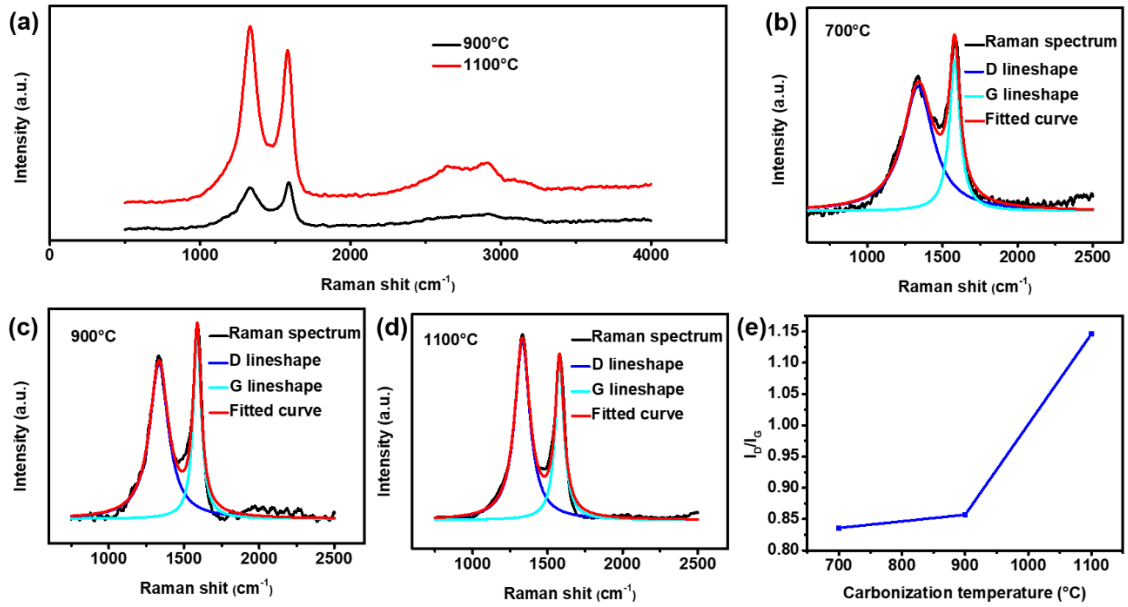

Figure 4-S5. Raman spectra of the CFs with different-temperature pyrolysis. (a) Raman spectra of the CFs with the treating temperature of 700°C and 900°C respectively. (b-d) Curve fitting graphs of the Raman spectra of the CF treated in 700°C, 900°C and 1100°C respectively. (e) The intensity ratios of D-band and G-band (I_D/I_G) in the Raman spectra for the CFs with the treatment of 700°C, 900°C, and 1100°C.

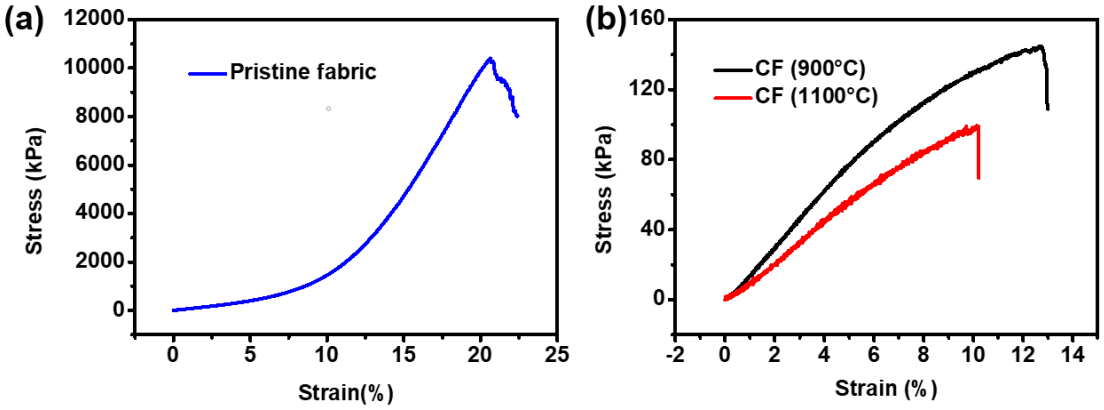

Figure 4-S6. The strain-stress curves of the pristine and carbonized linen fabrics. (a) The mechanical performance of the pristine linen fabric. (b) The mechanical performance of the fabrics with the carbonisation temperature of 900℃ and 1100℃.

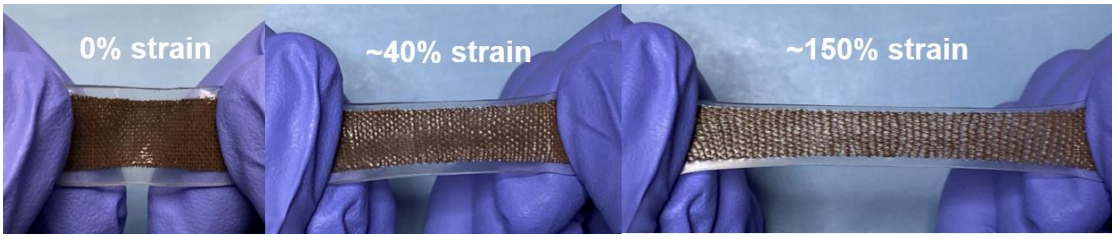

Figure 4-S7. Photograph of the CDCF sensor, showing the stretchability and strain-dependent deformation.

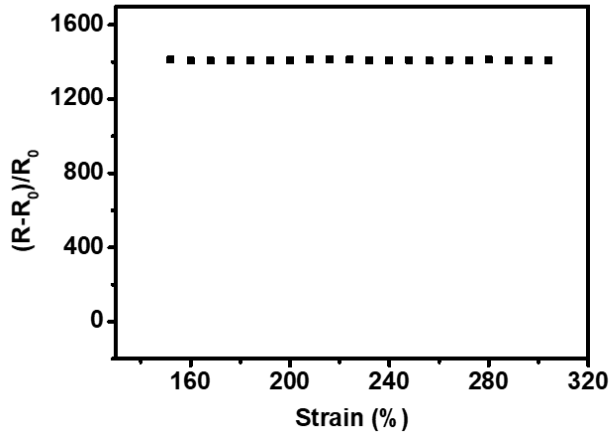

Figure 4-S8. The electrical response of the CDCF (700°C) sensor in the tensile strain ranging from ~150% to ~300%.

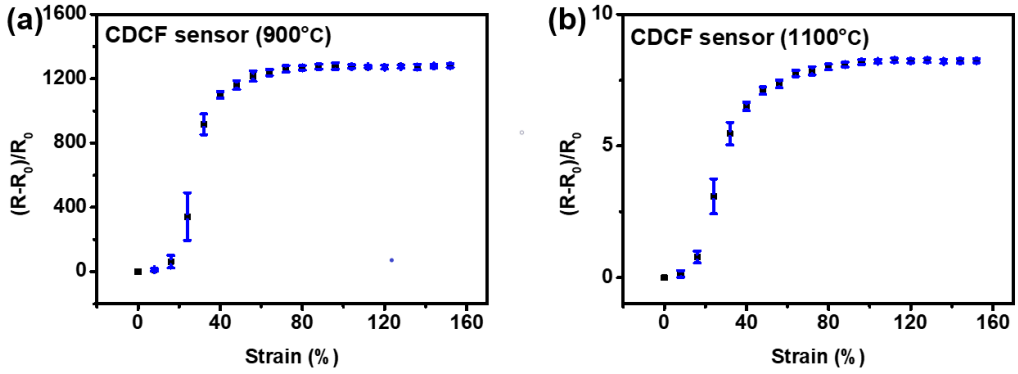

Figure 4-S9. The calibration results of the CDCF sensors treated with (a) 900°C, and (b) 1100°C.

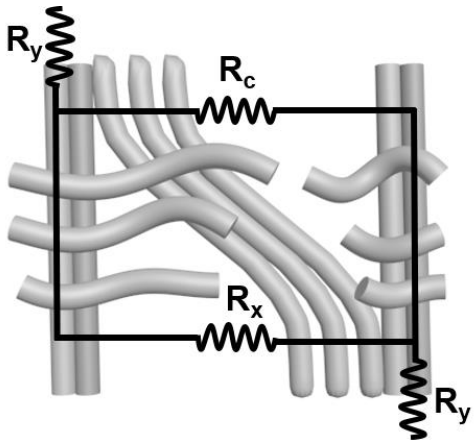

Figure 4-S10. Schematic illustration and electrical model of the CF sensor to show its sensing mechanism.

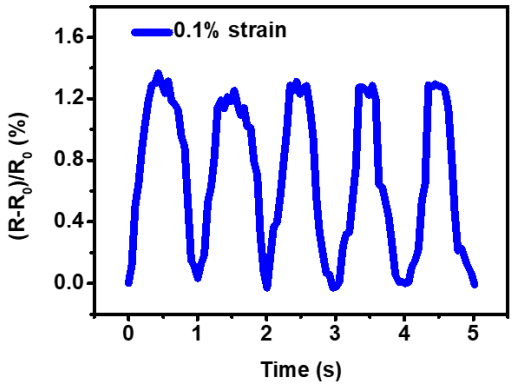

Figure 4-S11. The electrical response of the CDCF sensor by applying a strain of 0.1% with the frequency of 1Hz, showing the remarkable detection limit of the sensor that can reach the strain of 0.1%.

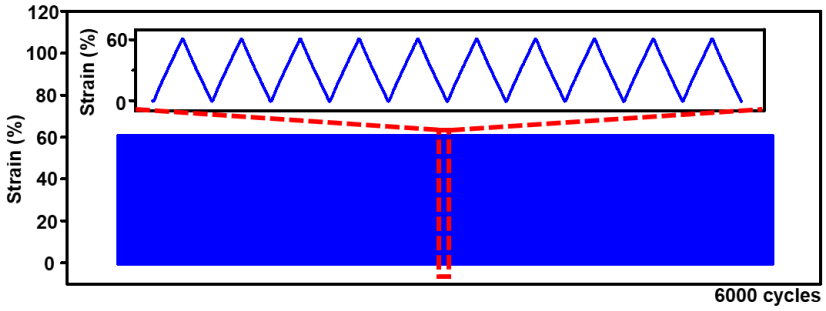

Figure 4-S12. The mechanical output of the CDCF sensor under a repeatable stretching-releasing strain of 60% for 6000 cycles with the frequency of 0.5 Hz, showing the outstanding stability of the sensor.

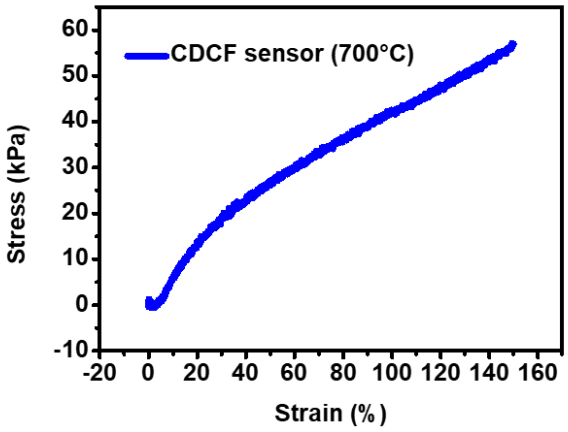

Figure 4-S13. The strain-stress curve of the CDCF sensor (700°C) to show its flexibility.

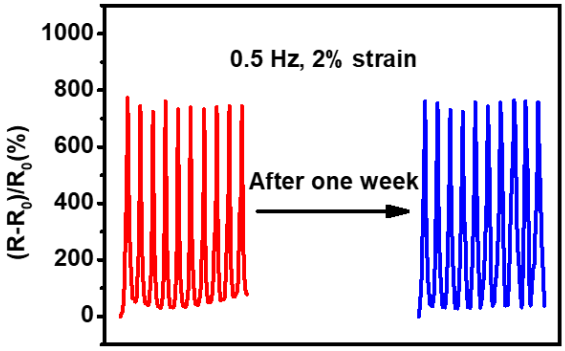

Figure 4-S14. The electrical response of the CDCF sensor over one week, showing its durability.

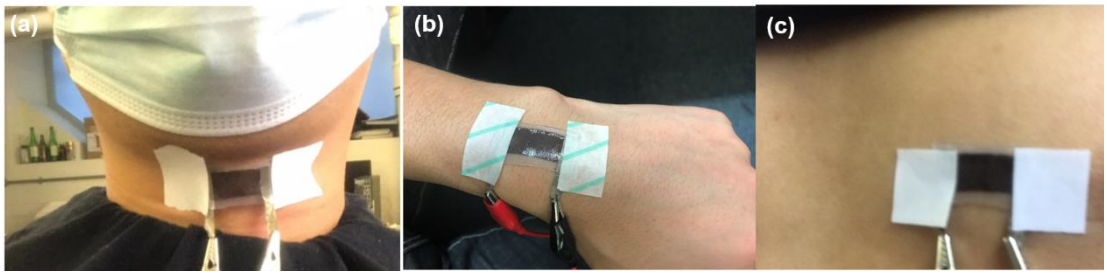

Figure 4-S15. The photograph of attaching the CDCF sensor to the skin surface by viscous tape. (a) Sensor mounted on the throat to detect speaking, coughing, and water drinking. (b) Sensor attached to the wrist to detect wrist bending. (c) Sensor mounted on the chest to detect respiration.

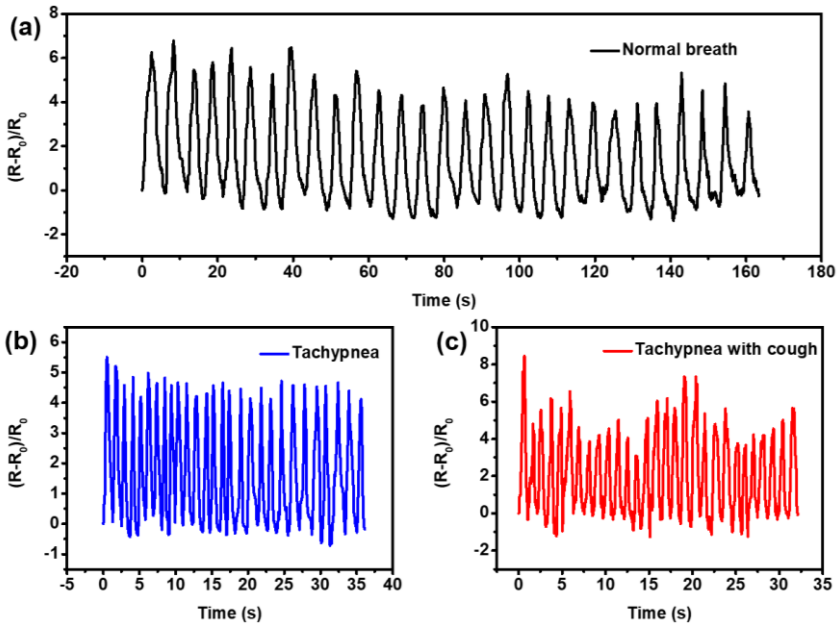

Figure 4-S16. Cyclic electrical signals under different respiration patterns by attaching the CDCF sensor to the chest. a) Normal breath. b) Tachypnea. c) Tachypnea with cough.

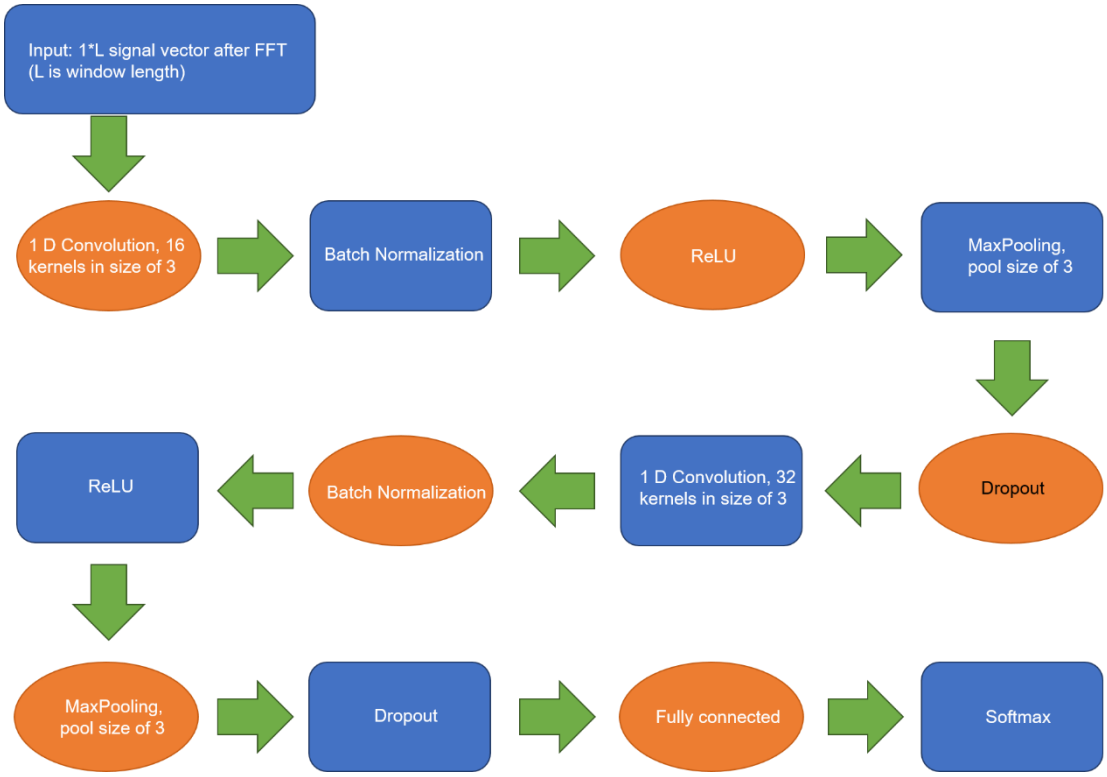

Figure 4-S17. The CNN architecture adopted to distinguish the respiration signals generated by the CDCF sensor.

Table 4-S1. The linear fitting results of strain sensors showing their sensitivity.

Sample	Strain Range (%)	Gauge Factor (GF)	R^2 (%)
CDCF sensor	0-48	3557.6	90.0
(700°C)	48-150	47.8	56.9
CF sensor (700°C)	0-96	23.0	84.8
CDCF sensor	0-48	2905.6	88.6
(900°C)	48-150	73.9	49.7
CDCF sensor	0-48	17.3	93.3
(1100°C)	48-150	0.9	66.4

Table 4-S2. The performance comparison from our work to others.

Sensing materials	Maximum stretchable strain (%)	Gauge factor in first sensing range	Durability	Refs
Carbon nanocoils	50	25	-	[226]
Hollow polyaniline spheres	493	2.9	1000 cycles under the strain of 30%	[216]
Conductive hydrogel	400	6.9	-	[227]
XG-Fe^{3+}/PAAm-Gl organohydrogel	500	2.41	300 cycles under the strain of 100%	[228]
CNTs	300	6.29	-	[229]
rGO	40	3	500 cycles under the strain of 40%	[76]
rGO and CNTs	120	7.23	-	[215]
Copper	200	49.5	3000 cycles under the strain of 50%	[217]
CNTs	100	12274	-	[225]
Carbonized silk fibre	500	9.6	6000 cycles under the strain of 100%	[52]
Carbonized cotton fibre	140	25	2000 cycles under the strain of 50%	[87]
Carbonized linen fibre and copper	300	3557.6	6000 cycles under the strain of 50%	This work

Chapter 5
Molecular Engineering Humidity Sensing for Environmental and Wearable Detection

This chapter focuses on the third objective. The research work has been completed and submitted to Nature Communications in 2022. The details are reported below.

Authors: Yangpeiqi Yi, Chuang Yu, Heng Zhai, Lu Jin, Dongxu Cheng, Yifeng Lu, Zhongda Chen, Lulu Xu, Jiashen Li, Qinwen Song, Pengfei Yue, Zekun Liu, Yi Li

Journal: Nature Communications (Submitted)

Statement of author contributions:

The proposal of the primary research idea, and supervision of this work. Fabric carbonisation, and material characterization in mechanical and some electromechanical performance. Demonstration for applications. Preparation of tables, figures and the manuscript.

Statement of co-author contributions:

The work was conceived by Zekun Liu and performed by Yangpeiqi Yi. Yi Li and Zekun Liu supervised this work throughout the whole process. Zekun Liu organized the manuscript, Yangpeiqi Yi and Yi Li supported the writing. Chuang Yu helped with the deep learning networks, Heng Zhai, Lu Jin, Dongxu Chen, Yifeng Lu, Zhongda Chen, and Lulu Xu gave support in material characterization and sample preparation. Qinwen Song, Pengfei Yue and Jiashen Li revised the manuscript, and all authors discussed the results.

Note: Supplementary material is available in Supporting Information.

5.1 Introduction

Humidity detection and management play a vital role in creating a pleasant, safe, green, and energy-efficient environment. Measuring humidity within the environment has been a dramatic proliferation of research in the applications spanning from the governance of the atmosphere and soil to the management of industrial manufacture, agricultural production and physiological health.[230-232] Besides, moisture constantly evaporates from the mouth and the skin surface because of the sensible and insensible perspirations. The ubiquitous body humidity serving as a biomarker allows the construction of noncontact body area sensing networks for emerging wearable digital healthcare and wellbeing.[233, 234] It becomes particularly important when direct-touching detection and manipulation through tactile sensors are unimplementable considering the risk of infection since the outbreak of the global Covid-19 epidemic.[97] One intriguing research prevailing in this context is to develop a flexible and high-performance humidity sensor for the abovementioned environmental and wearable detection.

Cutting-edge flexible humidity sensors are always fabricated by combining humidity-response materials with soft substrates through physically coating or blending.[95, 97, 98, 235, 236] However, the active materials in the nonintegrated configuration are neither wettable nor machine washable due to the damages of sensor structures, loss and/or redispersion of the active materials when interacting with water. This greatly limits practical applications as humidity sensing frequently subjects to high humidity condensation and interaction with liquid water. The humidity sensor with composite laminated structure also fails to avoid interference from mechanical deformations, which deteriorates the sensing reliability and accuracy in practical humidity monitoring. It has been a critical challenge to explore a straightforward approach to develop a robust humidity sensor that has a stable open porous structure to allow free

movement of water vapour molecules and liquid water with outstanding wettability, washability, and sensing reliability when exposing to challenging environments.

Herein, this work first proposes a molecular engineering humidity sensing strategy by creating a stable open porous graphite structure and controlling the content of functional groups, which can be realized through direct carbonisation and in-situ oxidation of waste textiles. The humidity sensor shows tunable initial resistance and sensitivity by controlling carbonisation temperature and oxidation degree respectively. Due to the free-standing configuration (the humidity-response material is the substrate itself), the sensor exhibits prominent reliability to water liquid wetting and machine washing, and negligible dependence to mechanical inputs and geometry deformation. The realization of environmental monitoring, and wearable noncontact body area sensing networks is successfully demonstrated for the detection of atmospheric humidity and soil wetness, hand gesture and motion, as well as various respiration models. Noteworthy to mention that it first finds directly carbonized fabric (CF) with humidity sensing ability, and the oxidated carbonized fabric (OCF) shows an improvement in sensitivity. We also prove that this strategy is applicative to many textiles (e.g., cotton, linen, and silk fabrics) as a new strategy for flexible, eco-friendly, and high-performance humidity sensors.

5.2 Experimental

5.2.1 Fabrication of the CF and OCF Sensors

Waste cotton woven fabrics (supplied by the textile lab, University of Manchester, plain structure) were carbonized in a tube furnace with nitrogen atmosphere with heating rate of 2°C/min. After reaching carbonisation temperature (i.e., 600, 800 and 1000°C), samples

naturally cooled down to room temperature. The oxidation was performed by immersing the CFs in a sulfuric acid/nitric acid mixture (v/v 3:1) at 70°C for 1, 2, and 3 h respectively to induce the growth of functional groups. The OCF sensors with the oxidation treatment of 1, 2, and 3 h are defined as the OCF-1 h, OCF-2 h and OCF-3 h respectively. The sulfuric acid (≥95%, Analytical reagent grade) was purchased from Fisher Chemical. The nitric acid (70%, Analytical reagent grade) was purchased from Sigma Aldrich. After oxidation, samples were washed in distilled water three times and dried overnight in fume cupboard. The CF and OCF samples were finally cut into the size of 3 × 2 cm^2 with conductive tapes at both ends for the fabrication of humidity sensors.

5.2.2 Material and Sensor Characterizations

The surface morphology and structure of the CFs and OCFs were characterized by a SEM (ZEISS Ultra-55) and TEM (Tecnai T20). The atomic percentage and element distribution were detected by the SEM (Quanta 200) equipped with energy-dispersive X-ray spectroscopy (EDS). We evaluated mechanical performance of samples by a universal mechanical testing machine (Instron 3344L). Raman spectra were performance with a Raman spectroscopy (WITec, Apyron) with a laser excitation wavelength of 532 nm. X-ray Photoelectron Spectroscopy (XPS) analysis was performed using an Axis Ultra Hybrid spectrometer (Kratos Analytical, Manchester, United Kingdom). Water drops (2 μl) in wettability test were applied by Kruss Drop Shape Analyzer (DSA100). The sheet resistance of the CFs and OCFs (N=3) was measured following four-point mode of Keithley 2450 at 25 °C and 50% RH. Humidity sensing performance of sensors was implemented in a conditioning cabinet (Datacolor CONDITIONE), the RH is programmable from 30% to 90%. To achieve the higher humidity level (i.e., > 90% RH), 100 mL boiled water was placed inside the cabinet. A commercial humidity sensor

(Sensirion SHT4x Smart Gadget) monitored the humidity during experiments. We collected the electrical signals of sensors through Keithley 2000/2450. The evaporation rate of the sensors was characterized via dropping water (~40 mL) on samples, where a multimeter and a thermal camera (FLIR-C3) and were used to measure resistance and temperature change of sensor surface respectively. We measured electrical signals, weight absorption, and humidity level of sensors (N=3) to investigate their relationship by synchronously using a multimeter, a precise balance (Mettler, AE100) from 40% to 90% RH in the humidity cabinet (21℃). Washability was evaluated by washing the OCF-3 h sensor at room temperature through a commercial washing fastness tester according to BS EN ISO 105 C06A1S. Air permeability was measured by the instruments of SDL ATLAS AirPerm.

5.2.3 Application Demonstrations

Atmospheric humidity monitor was implemented by attaching the OCF-3 h sample onto a drone (DJI FPV) with a wireless data transmission setup (i.e., NFC antenna and smartphone). We flew the drone to 30 m and 200 m height with a 5 min hover, respectively. The initial humidity level was measured by a commercial sensor, then the humidity 30 m and 200 m above was calculated based on the humidity on the ground and the sensor sensitivity. Environmental/soil humidity monitoring system was achieved by embedding the sensor inside the soil (1 cm depth) and attaching another one above the soil (1 cm height). Before the experiment, soil was dried at 80 °C overnight. The water drainage in soil was demonstrated through embedding three sensors at 1 cm, 2cm, and 3 cm under the soil. Multi-channel wireless data transmission system including Bluetooth-based signal processing unit (TruEbox), and visualization software (TruEbox-01RC) matched with smartphone was supplied from LinkZill Technology Co., Ltd (Hangzhou, China).

5.3 Results and Discussion

5.3.1 Molecular Engineering Humidity Sensor Demonstration

Figure 5-1a illustrates the fabrication of the oxidized CF (OCF) humidity sensor via step-by-step functionalization through two steps: carbonize pristine cotton fabric under 600°C to induce the transformation from cellulose to pseudo-graphite structure; immerse the CF in an acid mixture to promote the in-situ growth of oxygen-related groups on fibre surfaces (see details in Methods). The OCF enables to capture and absorb the moisture from surroundings due to the functional groups. Proton hopping within the bonded consecutive water molecules decreases the OCF resistance, implementing humidity sensing by converting humidness into electrical outputs. (Figure 5-1b).[98, 237] The free-standing OCF sensor is capable of monitoring environment by detecting atmospheric humidity, plant moisturizing, and the soil water content in extreme conditions (Figure 5-1c). It also shows potential in emerging wearables for digital wellbeing, respiration monitoring, and noncontact interfaces by constructing body area humidity sensing networks (Figure 5-1d).

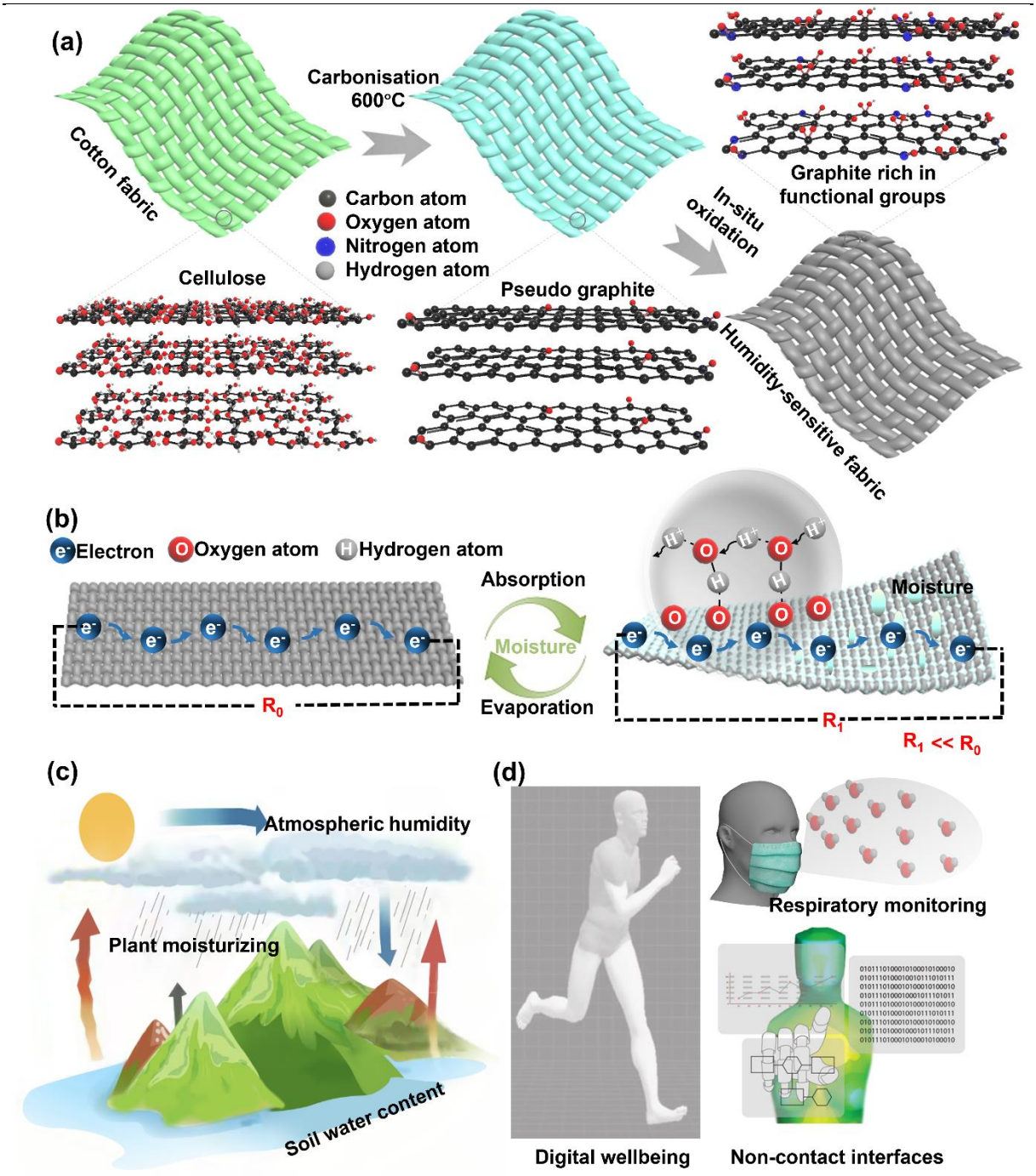

Figure 5-1. Illustration of fabrication and applications of the OCF humidity sensor. (a) Step-by-step structural transformation of the cotton fabric after carbonisation and oxidation. (b) Working mechanism of the OCF sensor, where proton hopping increasing the amount of moving electrons and decreasing the resistance. (c, d) Proof-of-concept demonstration of the OCF sensor in (c) environmental and (d) wearable detection.

5.3.2 Materials Characterization

The functionalization significantly changes the molecule structure. With thermal degradation, the fabric undergoes both surface shrinkage and weight loss, while it remains fabric structure (Figure 5-S1a-c). Neither the carbonisation nor oxidation destroys the fibre integrality, they evenly motivate the element transformation of fibre surfaces (Figure 5-2a, b and Figure 5-S1d, e). The carbonisation-induced structure transformation from cellulose to pseudo graphite is confirmed by observing many tiny distorted lattice stripes with an interlayer distance of ~0.35 nm in a typical transmission electron microscope (TEM) image (Figure 5-S2a), of which observation is consistent with previous work.[52, 238] The strain-stress curves of the CF, OCFs (Figure 5-2c), and pristine cotton fabric (Figure 5-S2b) show that both carbonisation and oxidation deteriorate their breaking strain and stress, while the OCF-3 h remains high breaking stress of ~0.24 MPa. Figure 5-2d and Figure 5-S3a displays that the conductivity of the CF is significantly affected by carbonisation temperature, where sheet resistance drops from 1.56×10^6 to 5 Ω/sq when temperature from 600°C to 1000°C. The improvement in conductivity is attributed to the temperature-induced increase in structural order, which is proved by the full width at half maximum (FWHM) in the Raman D-band (Figure 5-S3b-f).[86] On the other hand, enhanced oxidation time gradually weakens the conductivity, which is due to the increase of defects in the pseudo-graphite structure (Figure 5-2e). We evaluate the defects by comparing the I_D/I_G ratio, of which ratio is 0.89 and 1.11 for the CF and OCF-3 h respectively (Figure 5-S4). Such trend is in agreement with reported work.[239, 240]

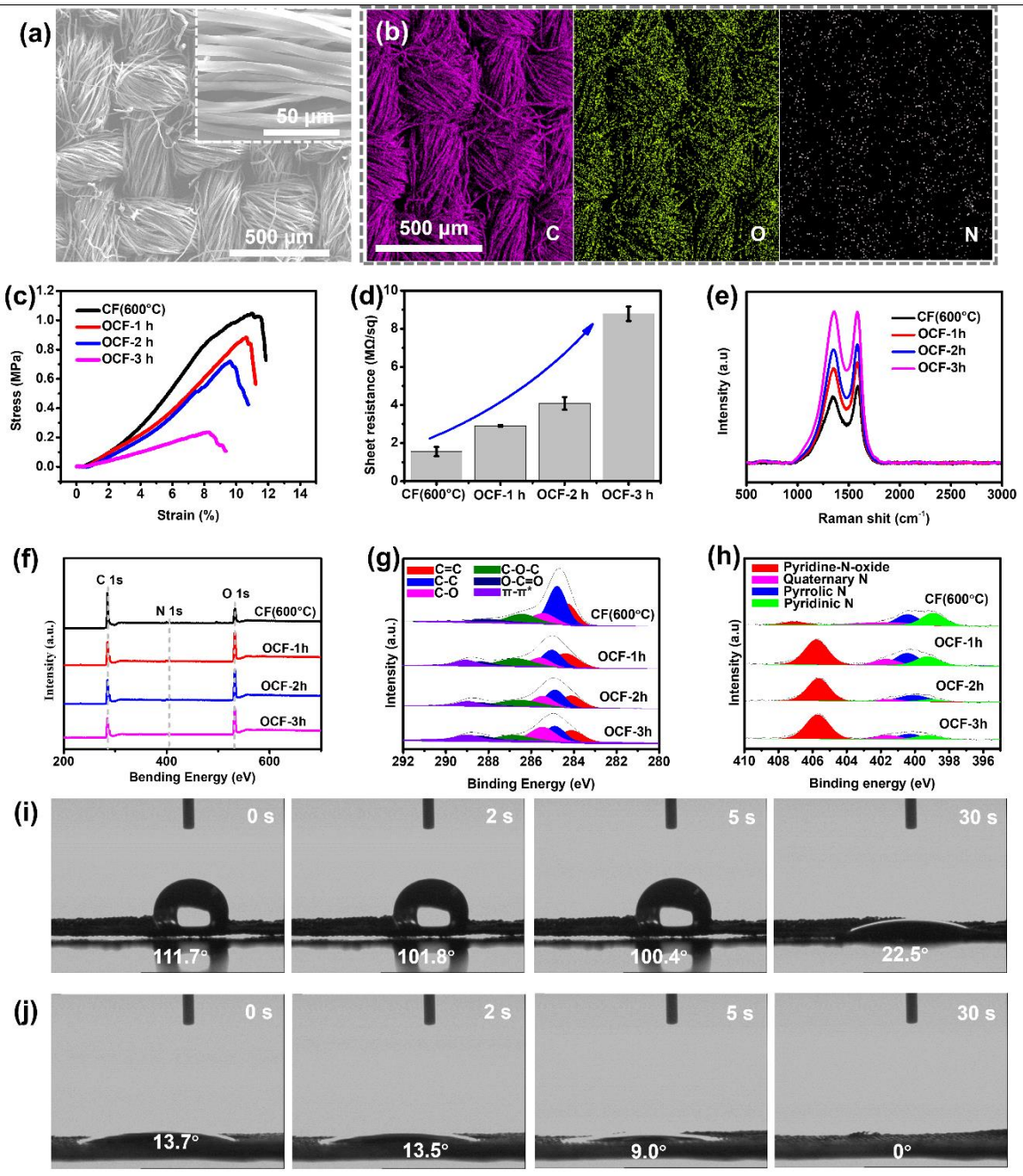

Figure 5-2. Characterization of the CF and OCFs. (a) Surface morphology (the insert is high magnification SEM of fibres), and (b) surface element distribution of the OCF-3 h. (c) Strain–stress curves, (d) sheet resistance, and (e) Raman spectra of the CF, OCF-1h, OCF-2h, and OCF-3 h. (f) Wide-scan XPS spectrum, (g) high-resolution XPS spectrum of the C1s XPS peak, and (h) high-resolution XPS spectrum of the N 1s XPS peak for the CF, OCF-1h, OCF-2h, and OCF-3 h. (i, j) Photographs of water droplets on the (i) CF, and (j) the OCF-3 h, showing their surface hydrophilicity.

Surface elements and hydrophilicity also change as a function of carbonisation and oxidation. The wide-scan X-ray spectroscopy mapping (XPS) spectrum (Figure 5-2f), high-resolution spectrum of the C 1s peak (Figure 5-2g), and high-resolution spectrum of the N 1s peak of the fabrics show that their chemical state of the heteroatoms with increased oxidation time. By fitting the C 1s peak at the binding energy of 284.1 eV (belonging to C=C), 284.8 eV (belonging to C-C), 285.5 eV (belonging to C-O), 286.8 eV (belonging to C-O-C), 288.4 (belonging to O-C=O), and 290 (belonging to π-π*).[86, 239, 241, 242] Figure 5-S5a indicates that the O content rises from 17.7% to 30.9%, while the C drops from 80.2% to 66.3% after oxidizing for 3 h. Figure 5-S5b displays that the C=O and O-C=O percentages sharply raise after oxidating treatment, and then slightly increase with the enhancement of oxidation time. A new nitrogen oxide species peak at ~405.7 eV (Figure 5-2h, and Figure 5-S5c) confirms the existence of -NO_x.[52, 85, 243] The functional groups on the OCFs have significant improvement in surface hydrophilicity. Figure 5-2i shows the CF acquires a contact angle of 111.7° (at 0 s), and the contact angle gradually drops with time. The instantaneous contact angles throughout 0 to 30 s decrease with the increase of oxidating time (Figure 5-S6). The contact angle of the OCF-3 h at 0 s is just 13.7° (Figure 5-2j), and it can absorb most of the water droplet within a short period (~5 s). On the contrary, incremental carbonisation temperature deteriorates surface hydrophilicity. Figure 5- S7 presents that both the CFs (800°C, and 1000°C) have a higher contact angle at corresponding time, and the water droplets are not completely absorbed after 30 s.

5.3.3 Humidity Response and Sensing Mechanism

We explore the carbonisation temperature and oxidation time to determine the electrical response to humidity. Figure 5-S8a shows the electrical change of the CF (600°C) is less than

that of the OCF sensors when directly moving them into a chamber with relative humidity (RH) of 90% from room ambient (~50% RH). The response rises as a functions of increasing oxidation time, which is highly stable and reproducible from patch to patch (Figure 5-S8b). It also shows enhanced oxidation endows the sensor with a slower recover speed. It is because oxidation increased groups bond with large content of water molecules in the molecular chain, it takes more time to get released. This phenomenon is additionally confirmed by wetting the sensor with the same amount of water liquids and observing the electrical recover. Figure3a indicate moisture evaporation by absorbing heat (insert images) takes more time when the sample with raised oxidation time. The electrical change of the CF sensors carbonized in 800°C and 1000°C is very limited (Figure 5-S9a). It can be explained by the lower amount of oxygen element on the CF surface after higher temperature carbonisation (Figure 5-S9b). Noted that the CF carbonized in 400°C owns too high electrical resistance to measure, which is not suitable to detect humidity. Besides, we oxidized the CF carbonized in 800°C. The electrical response towards humidity enlarges with increased oxidation time (Figure 5-S10). It exhibits the validity of oxidation treatment in enhancing the electrical change no matter what the carbonisation temperature is. Through controlling carbonisation temperature and oxidation time, the sensors reveal tunable initial resistance and sensitivity (Table 5-S1), which is of prime importance to adapt practical applications. we treated other textiles to further verify the effectiveness and expansibility of the functionalization strategy. It proves this approach is extendable to linen (Figure 5-S11a-c) and silk fabrics (Figure 5-S11d-f). Their humidity response trend is consistent with that of the humidity sensors based on cotton.

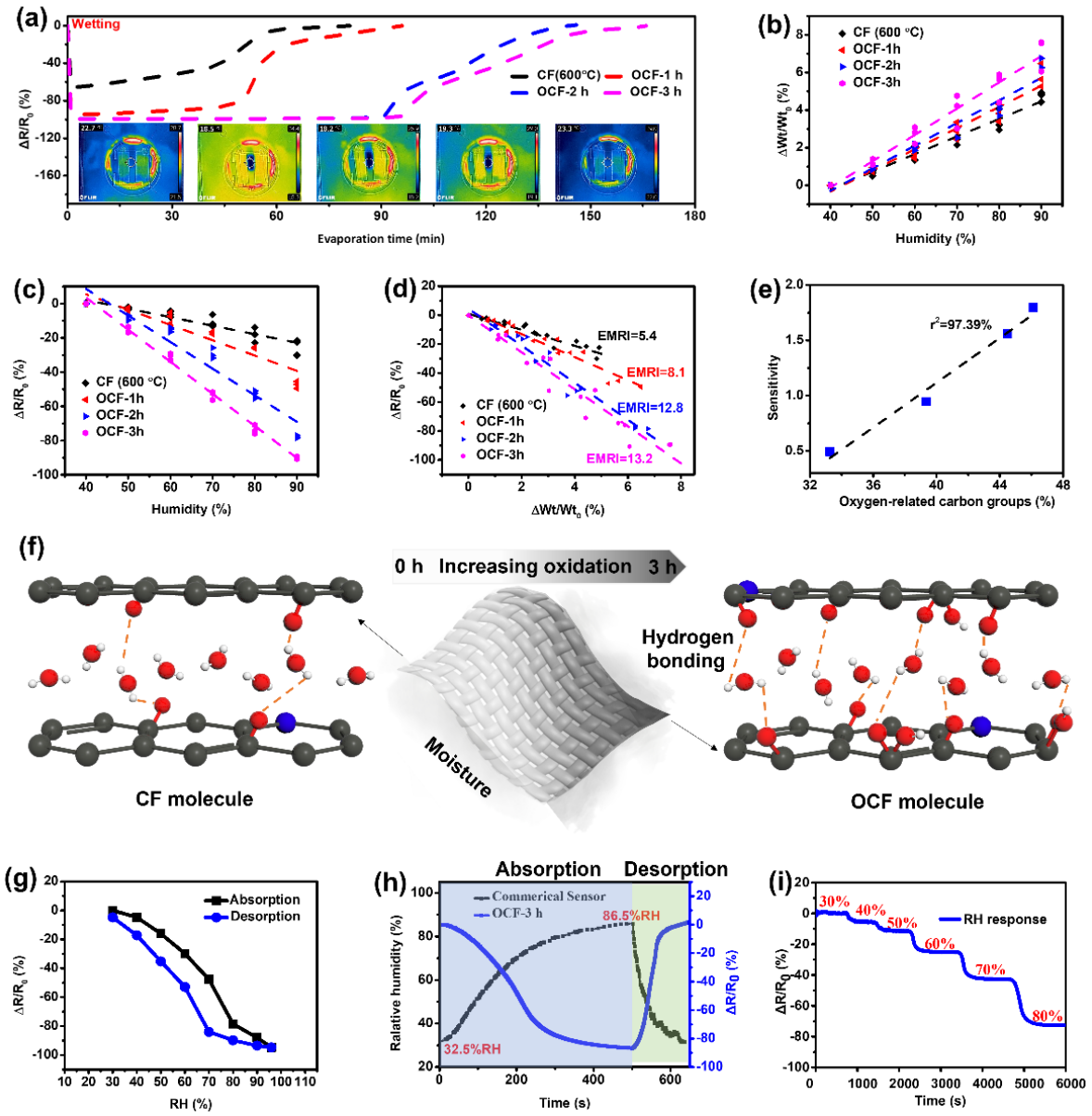

Figure 5-3. Electrical response of the CF and OCF sensors, and the sensing mechanism. (a) Wet-dry electrical response of sensors. Inserts are the heat distribution images during the evaporation. (b) Moisture sorption isotherm. (c) Electricity -humidity response isotherm. (d) Electricity-moisture sorption isotherm. The EMRI refers to electricity-moisture response index, showing sensors' electrical response to per unit moisture. (e) The relationship between sensors' sensitivity and their OCGs. (f) Humidity sensing mechanism illustration. (g) Electrical signals of the OCF-3 h sensor in absorption-desorption humidity. (h) Comparison between the OCF-3 h sensor and a commercial humidity sensor in absorption-desorption RH from 32.5% to 86.5%. (i) Dynamic electrical response of the OCF-3 h sensor to step-by-step increasing RH from 30% to 80%.

We investigate the sensing mechanism by correlating functional group content of the CF and OCF sensors (600°C) with their electrical response at different humidity level in absorbing humidity process (detailed setup in Methods). Moisture sorption isotherm (Figure3b) and electricity-humidity response isotherm (Figure3c) show that the sensors experience resistance decrease with absorbing moisture. Oxidation treatment improves both moisture sorption capacity and electrical response ability. By designing a three factor (i.e., absorbed water, RH, and oxygen-related carbon group) and four level (i.e., oxidation for 0, 1, 2, and 3 h) orthogonal experiment, and inputting the data into "MATLAB". The relationship of absorbed water, RH, and oxygen-related carbon group (OCG) is given by Equation (5-1), the relationship among absorbed water, electrical change, and OCG is given by Equation (5-2).

$$WWC = 0.001166\ RH + 0.000827\ OCG - 0.08278 \quad (5\text{-}1)$$

$$RC = -10.513\ WWC - 0.01537\ OCG + 0.6544 \quad (5\text{-}2)$$

By substituting Equation (5-1) into Equation (5-2), we can get Equation (5-3).

$$RC = -0.01226\ RH - 0.02406\ OCG + 1.5274 \quad (5\text{-}3)$$

Based on the Equation (5-3), RH is expressed as

$$RH = -81.5\ RC - 1.962\ OCG + 205.87 \quad (5\text{-}4)$$

where the WWC, RH, RC, and OCG refer to relative water weight change (%), environmental relative humidity RH (%), relative resistance change (%), and OCG content (%) respectively. Based on Equation (5-4), RH can be correlated to the RC and OCG of sensors. We expect it can calculate humidity level by directly measuring the OCG content and RC. According to the relationship between the WWC and RC (Figure 5-3d), we define an index: electricity-moisture response index (EMRI) (i.e., absolute value of slope) to reflect electrical response capacity to

unit moisture content. The humidity sensor acquiring a larger EMRI shows a higher sensitivity. Our theoretical hypothesis is that the OCG on the graphite sheets can attract moisture molecules and polarize them. The absorbed moisture molecules can bridge the graphite sheets by linking with the OCG on different sheets. The more OCG forms more bridges, thus leading to a higher sensitivity. By comparing the sensors' sensitivity with their OCG content, it reveals the sensitivity is positively related to the amount of the OCG (Figure 5-3e), which supports our hypothesis. The proposed humidity sensing mechanism in molecular level in Figure 5-3f shows oxidation-induced enhancement in the OCG can improve the bridges, hence increasing electrical response to the same content of RH increase.

The OCF-3 h sensor possesses a high sensitivity, following sensing evaluation and demonstration would focus on it. Figure 5-3g illustrates the electrical signals of the sensor in absorption-desorption humidity (30%-96% RH) process, where the loading and unloading electrical outputs maintain good consistency, and the response to humidity absorption (Figure 5-S12) shows remarkable linearity (r^2=96.87%). We compare the sensor to a commercial humidity detector by placing them in the same humidity environment. There is an outstanding consistency in humidity response (Figure 5-3h), and the electrical signals during humidity absorption (Figure 5-S13) revel a prominent synchronism (r^2=96.6%). Figure 5-3i depicts the sensor is reliable in a series of dynamic and static humidity, where the electrical outputs are highly consistent with the step-by-step increase of RH from 30% to 80%.

5.3.4 Sensing Reliability

Apart from high electrical response, the sensor presents remarkable sensing reliability in

complex environments, and negligible dependence to many mechanical inputs. The sensor has high flexibility in shapes (flat, bend, twist, and knot), and more importantly, no matter what shape is, the response to humidity remains a similar level (Figure 5-4a). The deformation-resilient property enables the sensor to reliably detect humidity when being wrapped around tubes with various diameters (Figure 5-4b). It responds to the humidity in low dependence of bending radius. It ensures humidity sensing reliability considering frequently involved bending in practical wearable and environmental applications. By applying cyclic bending (Figure 5-4c) and pressuring (Figure 5-4d), the sensor shows insensitivity to the inputs, which is of significance to ensure sensing accuracy by suppressing frequently involved mechanical interference. Unlike conventional humidity sensors with weak interaction between sensing materials and substrate,[96-98] the free-standing sensor displays remarkable wettability and machine-washing ability. Water drops were applied to the sensor and gradually evaporated (Figure 5-4e), the cyclically recoverable peaks prove that the sensor is water liquid wettable. Both the resistance (Figure 5-4f) and humidity sensing ability (Figure 5-4g) are stable with minor fluctuation after machine washing for 3 h. As the OCG has high bonding energy with the graphite sheets, which are much higher than the hydrogen bonds, hence the oxidized graphite sheet structure is stable in wetting and washing. Therefore, the moisture sorption and desorption are reversible. It is a significant breakthrough considering humidity-response devices are neither wettable nor washable due to the structure damage of sensors, and/or hydrophilicity and redispersion of active materials to water.

Figure 5-4h shows the temperature in affecting the sensing performance of the sensor. At low temperature (25°C), the adsorption of water molecules takes a longer time (~400s) to reach saturated. While at high temperature (>35°C), it presents a quicker response to the humidity

change. Though the response speed difference, the sensor still has a similar electrical change finally. The open porous structure sensor also exhibits high permeability to air (Figure 5-S14a) and moisture (Figure 5-S14b) like a piece of cotton cloth, which avoids skin irritation in wearable applications[129]. Based on the above evaluation, the sensor possesses combined merits comparing to state-of-the-art humidity sensors reported (details in Table 5-S2), including tunable initial resistance and sensitivity, high linearity, breathability and flexibility, prominent reliability in withstanding machine washing, various deformations and mechanical inputs.

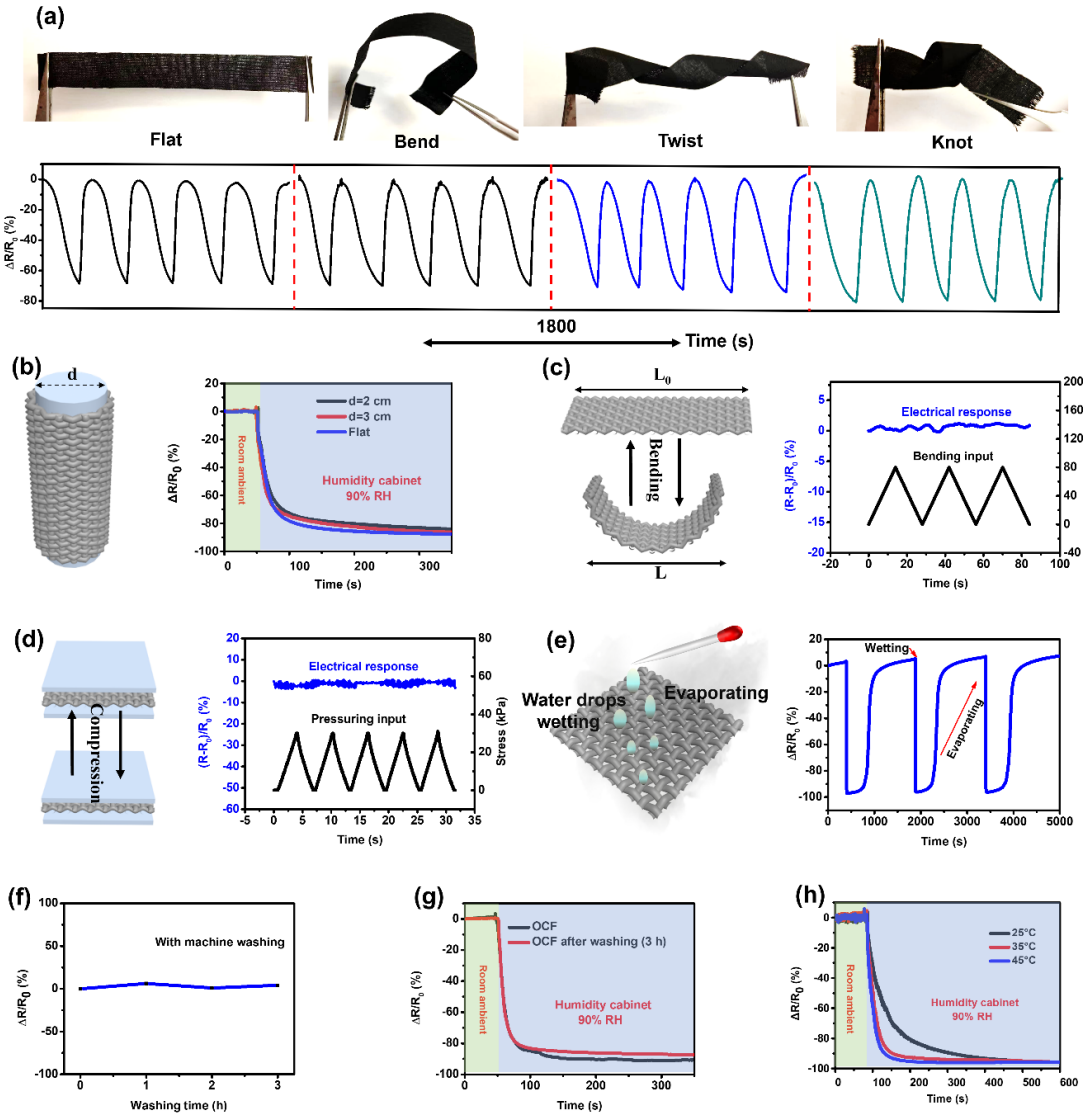

Figure 5-4. Humidity sensing reliability of the OCF-3 h sensor. (a) The sensor under different shapes (flat, bend, twist, and knot), and corresponding electrical response in a cyclic RH

ranging from 30 to 80%. (b) Schematic diagram of wrapping the sensor around tubes with different diameters, and the electrical outputs while moving in a 90% RH chamber. (c) Schematic diagram of bending deformation, and corresponding electrical response under cyclic bending (0-80%). The bending is calculated through distance change ($L-L_0$) dividing initial length (L_0). (d) Schematic diagram of pressuring, and corresponding electrical response under cyclic pressuring (0-30 kPa). (e) Illustration of water drops applied on the sensor and gradually evaporated, and corresponding electrical change. (f) Resistance changes of the OCF after machine washing. (g) Humidity sensing comparisons before and after washing. (h) Temperature impact on the sensing performance of the sensor.

5.3.5 Application Demonstration in Environmental and Wearable Detection

With the abovementioned sensing superiority, the sensor can be used in broad-range applications from environmental and wearable detection. We demonstrate an atmospheric humidity detection system (Figure 5-5a) based on the sensor, a drone, and a NFC antenna[244]. Figure 5-5b shows the relative resistance change of the sensor when flying from the ground to 50 m height and back, then to 200 m height and back again. The signals are roughly the same in each round with minor fluctuation, which may be attributed to wind-induced humidity undulation. The sensor in 200 m height reported an intense response, indicating its higher humidity. By measuring the ground RH using a commercial sensor, humidity across the air can be calculated according to the sensor response curves to humidity. Taking advantage of the remarkable wettability, the sensor indicates all-weather detection ability to monitor atmospheric humidity in high humidity and even raining conditions.

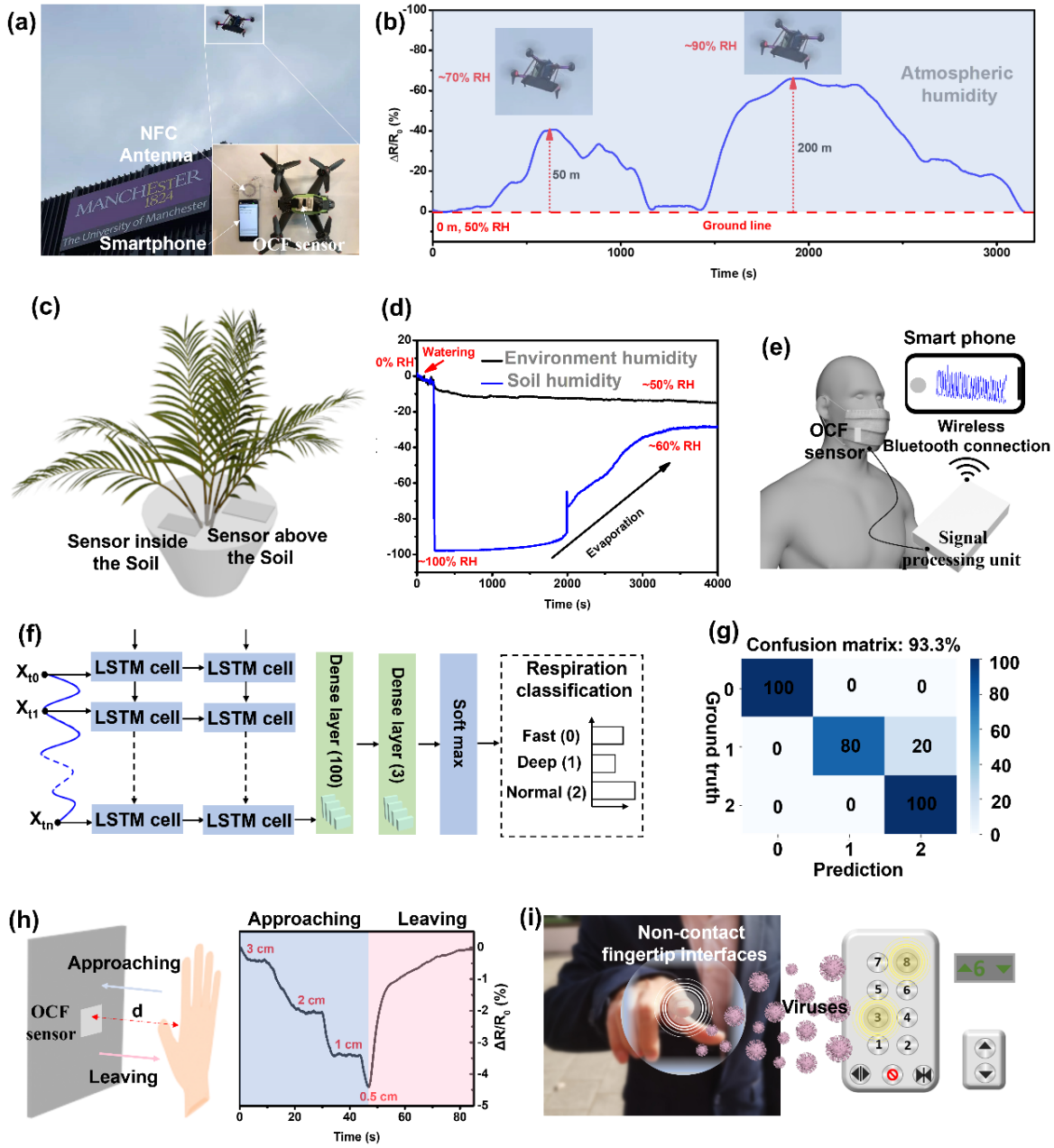

Figure 5-5. Application demonstration in environmental and wearable detection. (a, b) Atmospheric humidity detection system through (a) a platform comprising the sensor, a drone, and an NFC antenna, and (b) corresponding signals. (c) Illustration of the moisture monitoring of a plant by two sensors, and (d) corresponding signals. (e) A smart mask-based on the sensor with wireless data collect unit. (f) An artificial recurrent neural network for respiration identification, and (g) confusion matrix showing the high accuracy in recognizing breathing models. (h) Illustration of hand approaching and leaving and corresponding electrical response of the sensor. (i) Proof-of-concept illustration of non-contact fingertip interfaces.

Soil water content determination is another critical issue in environmental governance considering the water content with a dominant impact on soil desertification and plant root growth. Two sensors near a plant were assembled inside and above the soil respectively (Figure 5-5c). They are used to detect humidity around the plant branches and root soil moisture during watering process. Figure 5-5d displays that the soil humidity sharply drops after watering, and gradually recovers with evaporation. By contrast, environment humidity around plant branches slightly decreases after watering, and maintains stable in evaporation process. The RH can also be calculated based on initial humidity level. This demonstration shows the sensor's application prospects in intelligent and customized plant cultivating. By putting the sensors in the soil with gradient depth (Figure 5-S15), electrical outputs during watering can reflect soil drainage, which shows how quickly excess water leaves from the soil. It is an important index in determining soil erosion and land desertification.

Through capturing the water molecules generated from the human body, we demonstrate the sensor in the implementation of wearable noncontact detection. The human mouth contains a large amount of exhaled/inhaled moisture results in a significant electrical resistance response of the OCF sensor. Considering the high breathability, the sensor is very competitive to be embed into a mask with the functions of monitoring cough and speak, as well as recognizing respiration models by integrating with a deep learning network. Figure 5-S16a displays the electrical change of the sensor generated by coughing, where continuous up-and-down signals are highly consistent with corresponding motion. Also, the slight moisture difference during pronouncing makes it is possible to detect the speaking of various words (Figure 5-S16b-c). The smart mask equipped with wireless data collect unit (Figure 5-5e), and long short-term memory (LSTM) builds up a respiratory recognition system. The LSTM contains two LSTM

layers, two dense layers, and a final softmax layer (Figure 5-5f). The artificial recurrent neural network as an end-to-end architecture can directly take the raw respiratory data as input and classify the data into three classes (i.e., deep, normal, and fast breathing). The respiratory monitoring and discrimination system obtain a high recognition ability with an overall accuracy of 93.3% shown in the confusion matrix in Figure 5-5g. The high-precision mask can monitor patients with respiratory diseases, showing feasibility in personal and public digital healthcare.

The interface between a hand and the sensor can be monitored by collecting the electrical signals from the sensor (Figure 5-5h). It shows that such response is highly in keeping with corresponding hand approaching and leaving. This also works on the detection of fingertip moving towards the sensor (Figure 5-S17a), where lower distance leads to a more obvious resistance change (Figure 5-S17b). Figure 5-S17c illustrates the reproducible sensing ability during cyclic forwards and backwards, which confirms the sensor can perceive fingertip motions continuously. Taking advantage of the reliable hand/finger non-contact detection, we demonstrate a 3×3 sensor array equipped with a multi-channel wireless resistance collection unit for motion reconstruction (Figure 5-S18). In one scenario, we utilize the array to discriminate the fingertip sliding. Figure 5-S19a shows the fingertip trajectory by writing a slash. The electrical signals in Figure 5-S19b reveal the distribution is compatible to the position of sliding fingertip across the sensor array from (1, 1) to (3, 3). A more complicated '*T*' sliding is also precisely reflected by the sensor array (Figure 5-S19c, d). We also apply the noncontact sensing array in blowing detection. Figure 5-S20a displays blowing above the centre of the sensor array (2, 2). The centre shows a higher electrical response, while four corners present a relatively lower electrical change (Figure 5-S20b). On the other hand, if blowing from one corner (1, 1) (Figure 5-S20c), the closest point (1, 1) shows the highest response peak, and the rest of the points exhibits a gradient decrease with respect to the distance

from the blowing point (Figure 5-S20d).

By altering the array construction, Figure 5-S21a shows a gesture monitoring panel, where sensor 1-5 refer to the fingertip from thumb to little finger successively, and sensor 6 represents the palm. The resistance change at each point through the stimulation of different hand gestures can accurately monitor corresponding motions in real time (Figure 5-S21b). These demonstrations successfully show the enormous potential of the sensor in noncontact detection based on fingertips. Figure 5-5i presents the potential of the sensor in contactless fingertip interaction interfaces. By integrating the OCF sensor into control panels such as elevator buttons and coded locks, users can remotely perform desired actions through the fingertip, lowering the risk of virus infection. It is a profound revolution to prevent the virus spreading during the covid-19 pandemic.

5.4 Summary

In summary, we have proposed a humidity sensing strategy by controlling the content of humidity-response functional groups on carbonized waste textiles. The sensor demonstrates outstanding wettability, and machine washability, as well as high reliability upon mechanical stress and geometrical deformations by taking advantage of its free-standing structure, in contrast to the conventional humidity sensor with poor sensing reliability. It is a significant progress considering humidity sensors are always not washable due to the hydrophilicity and/or redispersion of the active materials to water. The developed sensor exhibits tremendous potential in environment monitoring and governance, wearable digital healthcare with the function of preventing the spread of bacteria and viruses. To the best of our knowledge, this work first reports that carbonized fabric can detect humidity, and the sensitivity is improvable

by oxidation. The concept is applicative to cellulose (e.g., linen, hemp, viscose, etc) and silk (e.g., cocoon and spider silk) fabrics, as well as many carbonatable polymers. We envision this humidity sensing strategy would arouse attention in flexible humidity sensors using waste textiles, papers, and carbon-based materials (e.g., graphene, carbon nanotube, carbon black) for developing smart green sustainable ecosystem.

Supporting Information

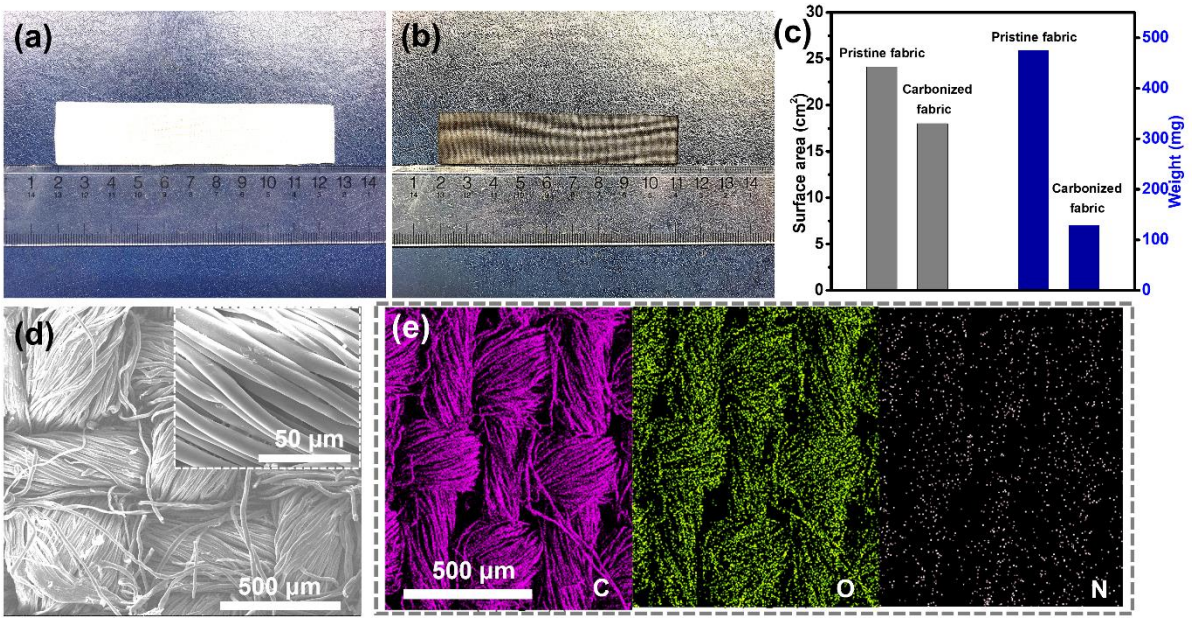

Figure 5-S1. The surface morphology and element distribution of pristine cotton fabric and the CF (600°C). (a, b) Photographs of (a) pristine cotton fabric, and (b) the CF. (c) Comparison of surface area and weight of the pristine fabric and the CF, presenting the surface shrinkage and weight loss after carbonisation. (d) SEM image of the CF. The insert is a high magnification image, which illustrates the carbonized fabric remains fibre shape. (e) Surface element (i.e., C, N, and O) distribution on the CF surface.

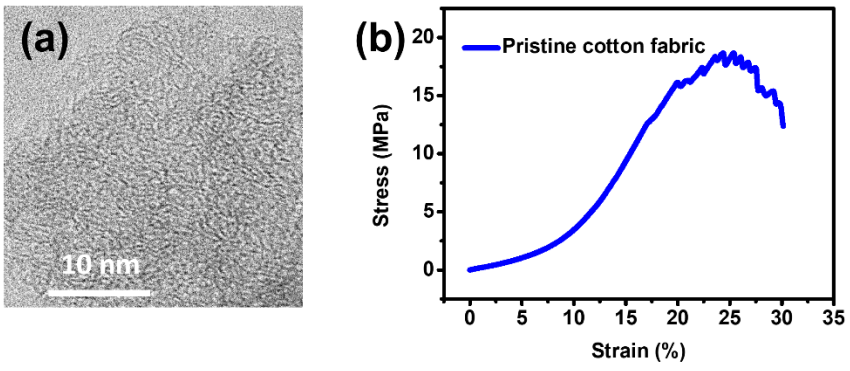

Figure 5-S2. (a) Typical TEM image of the CF (600°C), showing its pseudo graphite structures. (b) Strain-stress curve of pristine cotton fabric.

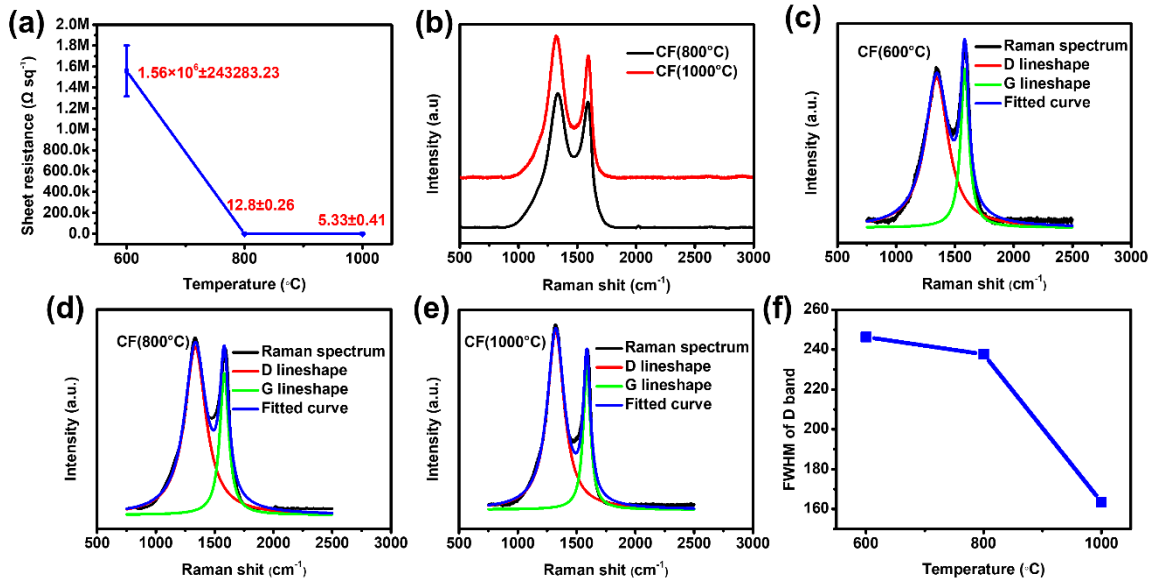

Figure 5-S3. Resistance and structural change after carbonisation under 600°C, 800°C, and 1000°C. (a) Sheet resistances of the CFs, showing higher carbonisation temperature results in the lower electrical resistance. (b) Raman spectrum of the CFs (800°C, 1000°C). (c) Fitted D-band and G-band of the CF (600°C). (d) Fitted D-band and G-band of the CF (800°C). (e) Fitted D-band and G-band of the CF (1000°C). (f) Full width at half maximum (FWHM) of D-band according to the (c-e) fitting. The decrease of FWHM of the D-band represents the increase of structural order.

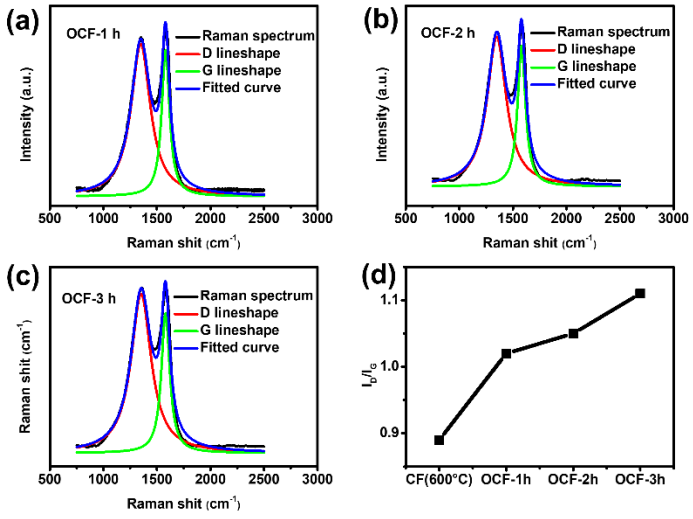

Figure 5-S4. Fitted Raman spectra of the OCFs after oxidating treatment for 1, 2, and 3 h. (a-c) Fitted D-band and G-band of (a) the OCF-1h, (b) the OCF-2h, and (c) the OCF-3h. (d) I_d/I_g ratio of the CF and OCF according to the (a-c) fitting. The increase of I_d/I_g ratio performs the

increase of structural defect.

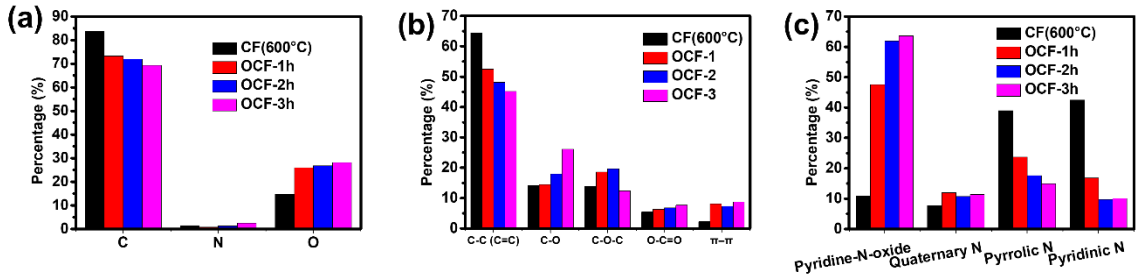

Figure 5-S5. XPS analysis of the CF and OCFs. (a) Atomic percentage of C, N, and O, illustrating the decrease of C and the increase of O after oxidation. (b) Distribution of functional groups in C 1s including C-C, C-O, C-O-C, C=O, O-C=O, and π-π* in C 1s peak. (c) Distribution of functional groups in N 1s including Pyridine-N-oxide, Quaternary N, pyrrolic N, and pyridinic N in N 1s peak, where pyridinic N-peak at 399.0 eV, pyrrolic N-peak at 400.1 eV, quaternary N-peak 401.2 eV, and pyridine-N-oxide N-peak at 405.6 eV.

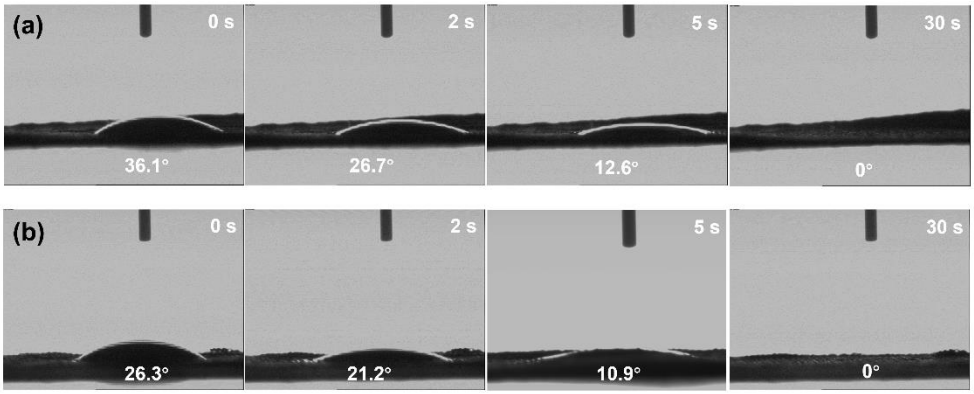

Figure 5-S6. Contact angles of (a) the OCF-1 h, and (b) the OCF-2 h at 0s, 2 s, 5 s, and 30 s.

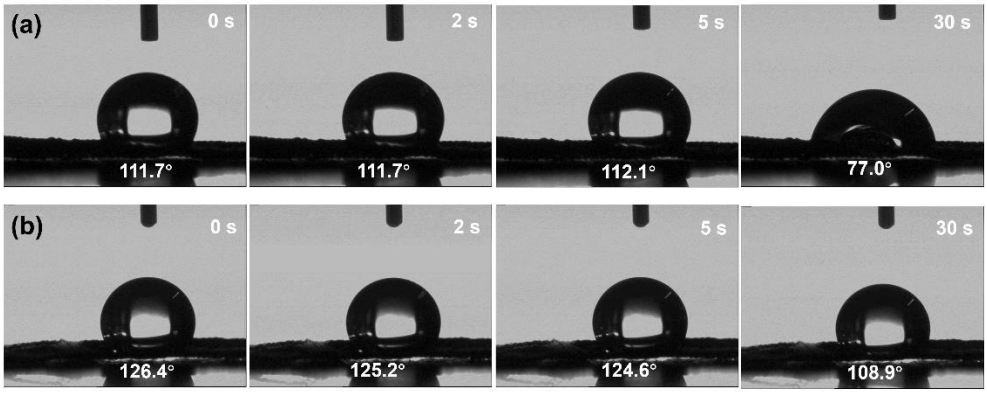

Figure 5-S7. Contact angles of (a) the CF (800°C), and (b) the CF (1000°C) at 0 s, 2 s, 5 s, and 30 s.

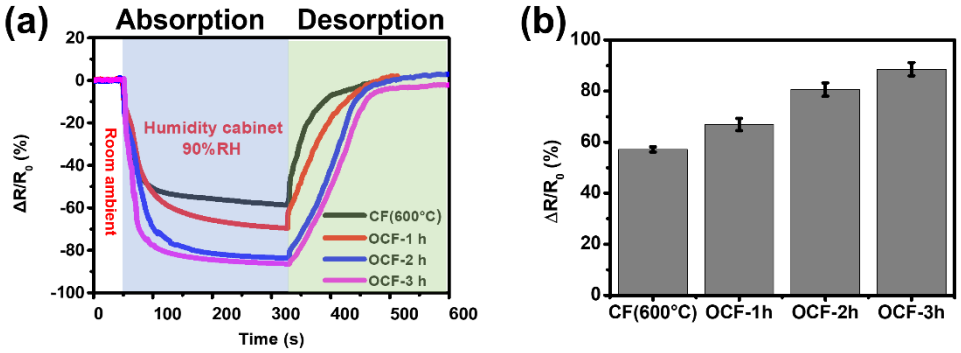

Figure 5-S8. The electrical response of the CF and OCF sensors. (a) The relative resistance changes of the sensors by moving them inside a chamber with 90% RH from room condition (~50% RH). (b) The maximum electrical change of the sensors from patch to patch, showing the functionalization is stable and reproducible.

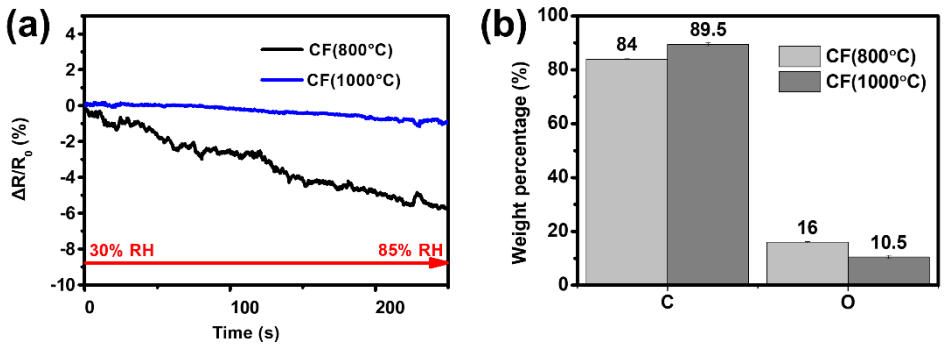

Figure 5-S9. Humidity response of the CF (800°C, and 1000°C) sensors and their surface element content. (a) Humidity response of the CF sensors to the RH from 30% to 85%. (b) Element percentage of C, O for the CFs through the measurement of EDS, where C element increases, and O decreases with carbonisation temperature increase.

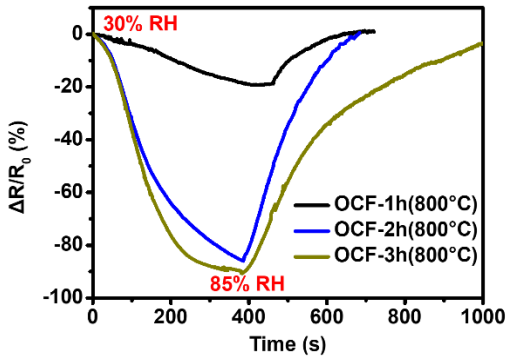

Figure 5-S10. Humidity response of the OCF (800°C) sensor with 1, 2, 3 h oxidation, showing

the functionalization strategy is effective and extendable.

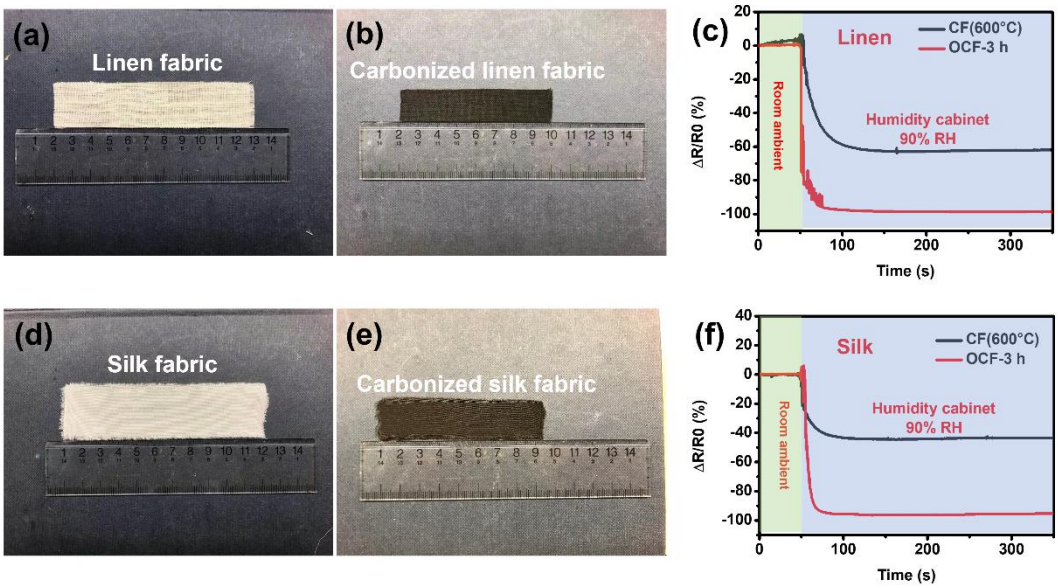

Figure 5-S11. Functionalized linen and silk fabrics and their response to humidity. (a, b) Photograph of (a) pristine linen fabric, and (b) carbonized linen fabric (600°C), showing the surface shrinkage after carbonisation. (c) Humidity response of the carbonized linen fabric sensors with (3 h) and without oxidation by moving them from room ambient to a chamber with 90% RH. (d, e) Photograph of (d) pristine silk fabric, and (e) carbonized silk fabric (600°C), showing the size shrinkage after carbonisation. (f) Humidity response of the carbonized silk fabric sensors with (3 h) and without oxidation by moving them from room ambient to a chamber with 90% RH.

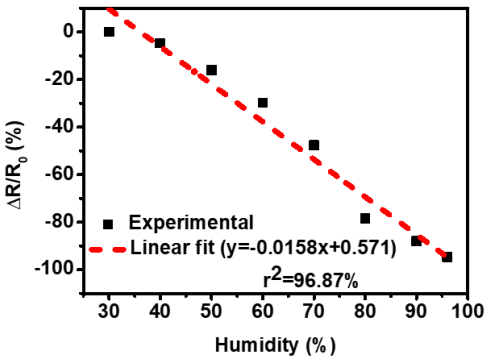

Figure 5-S12. The electrical response of the OCF-3 h sensor in absorption humidity, showing its high linearity.

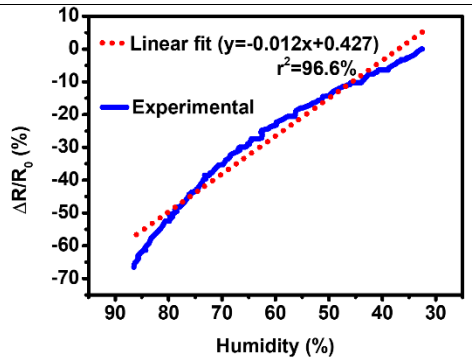

Figure 5-S13. The high synchronism of the OCF-3 h sensor to a commercial humidity detector in humidity absorption.

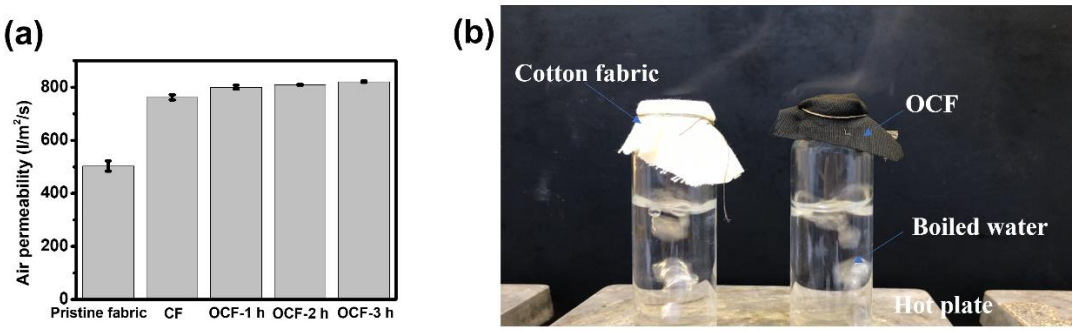

Figure 5-S14. Breathability evaluation of the CF and OCF sensors. (a) Air permeability of pristine cotton fabric, CF and OCFs. (b) Covering a cotton cloth and the OCF-3 h above boiled water in bottles, showing the moisture permeability of the sensor like a fabric.

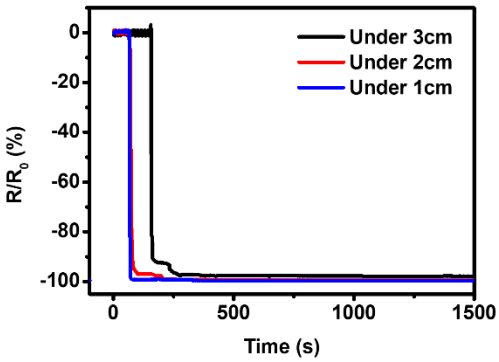

Figure 5-S15. Relative resistance changes of the sensor inside the soil with gradient depth.

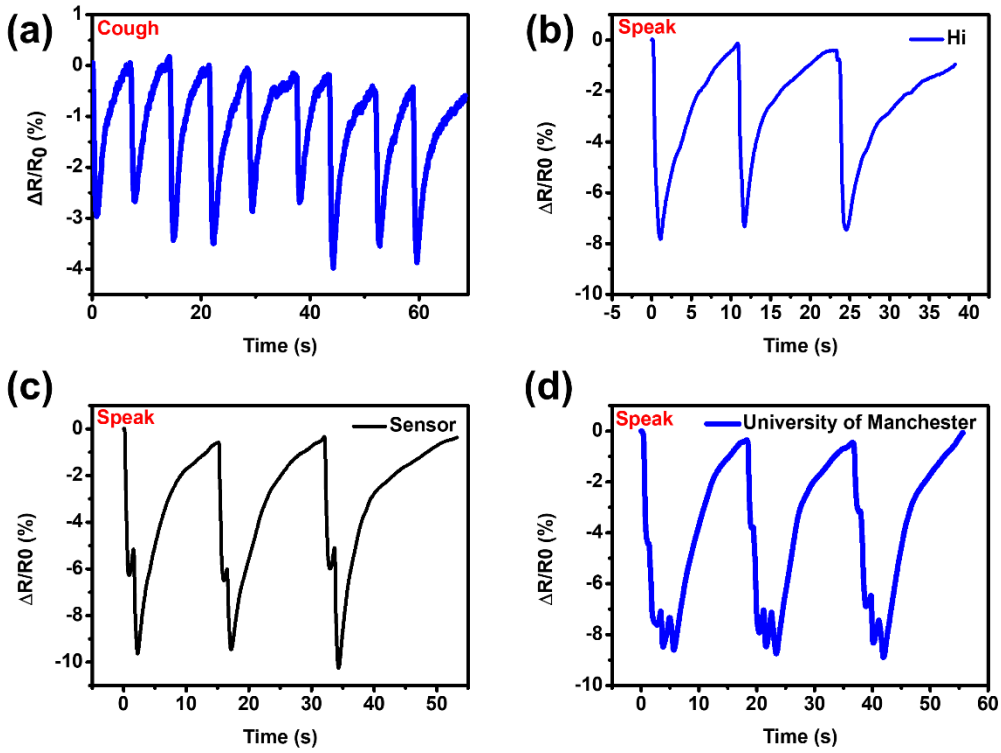

Figure 5-S16. Cough and speak detection. (a) Relative resistance changes during cough. (b-d) Relative resistance changes while speaking (b) “Hi”, (c) “Sensor”, and (d) “University of Manchester”.

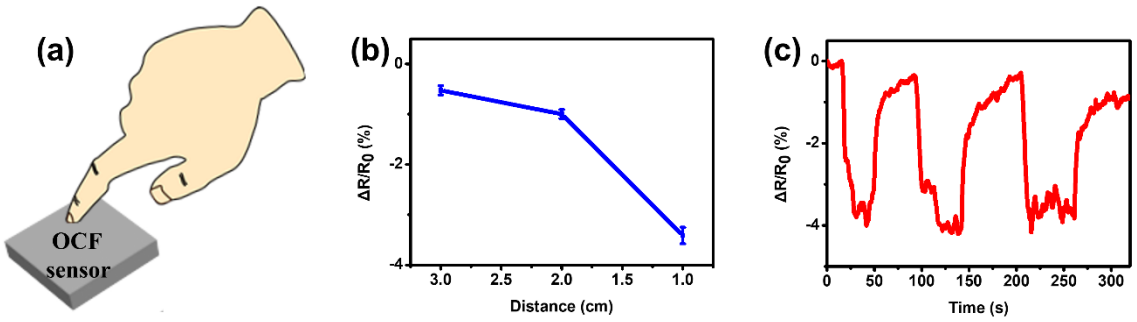

Figure 5-S17. Non-contact fingertip detection. (a) Schematic of the finger moving towards the OCF sensor. (b) Relative resistance change depending on the distance between the fingertip and the OCF sensor. (c) Repeatable moving towards and backwards.

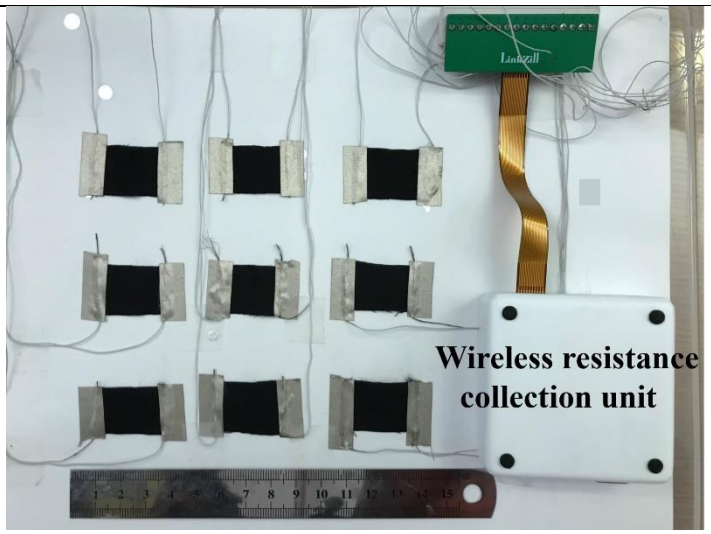

Figure 5-S18. The photograph of a 3×3 sensor array equipped with a multi-channel wireless resistance collection unit for motion detection.

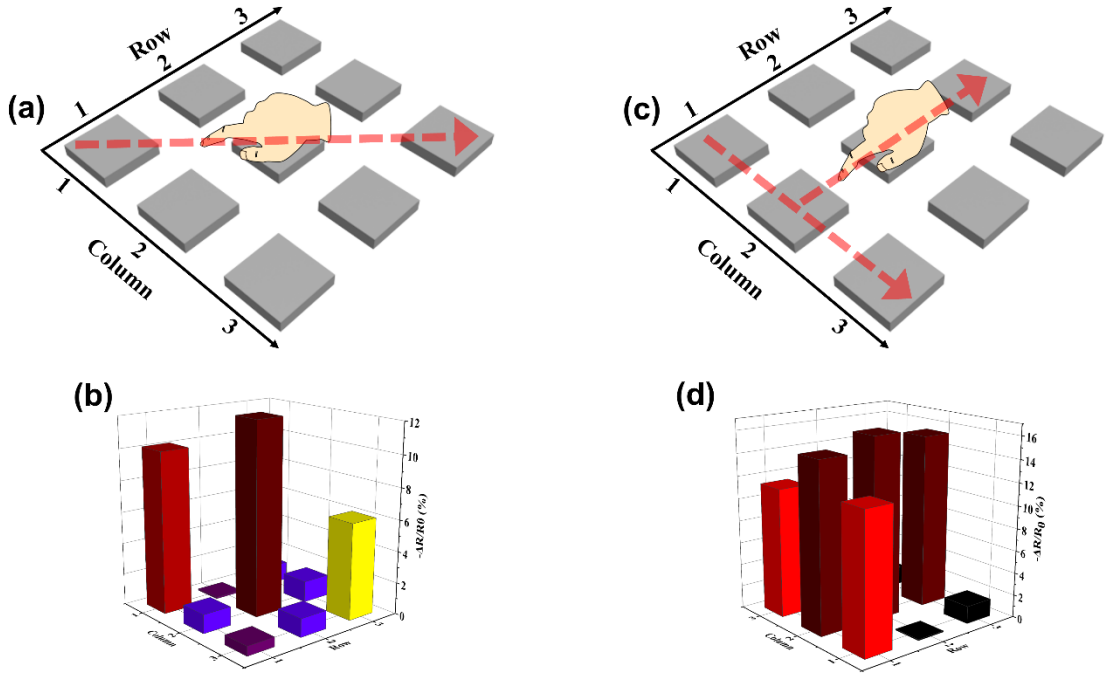

Figure 5-S19. (a) Diagram of 3×3 sensor array with writing a slash by fingertip, and (b) corresponding electrical response of the sensor array. (c) Diagram of 3×3 sensor array with writing ‘T’ by fingertip, and (d) corresponding electrical response.

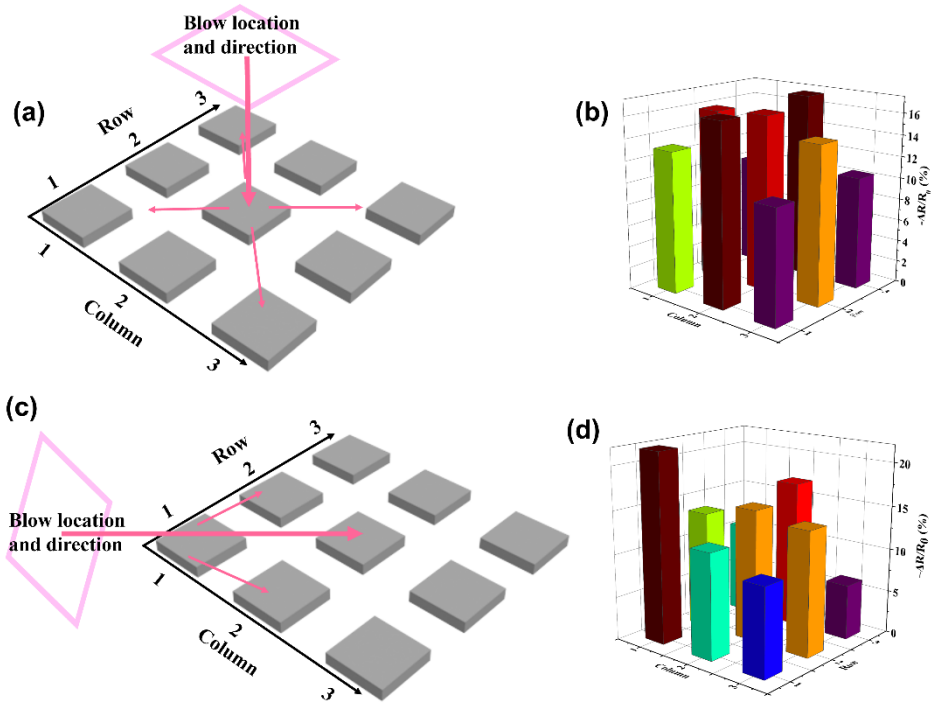

Figure 5-S20. Blowing detection. (a) Schematic diagram of blowing above the centre of 3×3 sensor array (2, 2), and (b) corresponding maximum electrical changes at each point. (c) Schematic diagram of blowing from one corner (1, 1), and (d) corresponding maximum electrical changes at each point.

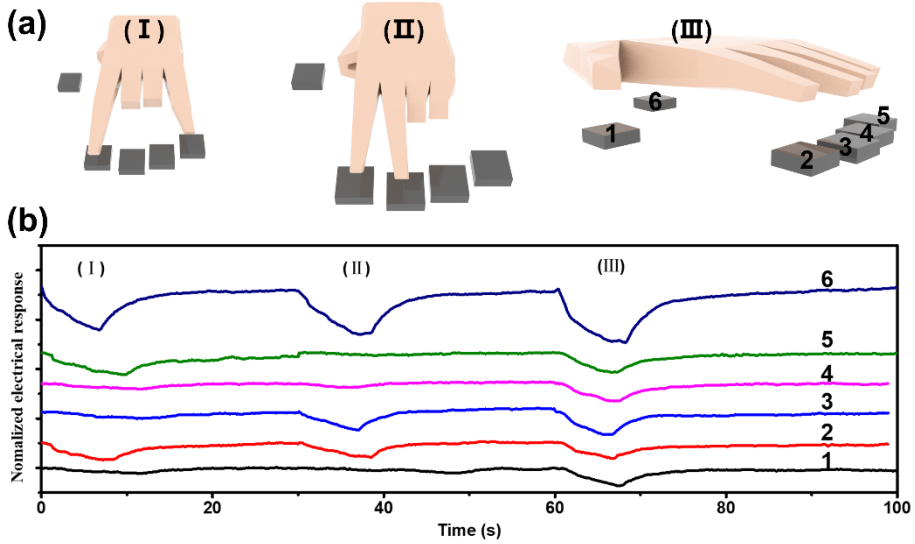

Figure 5-S21. Non-contact fingertip gesture monitoring panel. Sensors 1-5 refer to the fingertip from the thumb-little finger successively, and sensor 6 represents the palm. (a) Schematic diagram of finger gestures, (I) forefinger and little finger (2, 5), (II) forefinger and middle finger (2, 3), and (III) all finger open (1-6). (b) Corresponding normalized electrical changes.

Table 5-S1. Resistance and electrical response to humidity (30-85% RH) of the CF and OCF sensor, showing the tunable initial resistance and sensitivity.

Sample No	**Sheet resistance (Ohms/sq)**	**Sensitivity ((ΔR/R)/ΔRH)**
CF(600°C)	1.56E+06	0.56
OCF-1h(600°C)	2.90E+06	1.03
OCF-2h(600°C)	4.08E+06	1.42
OCF-3h(600°C)	8.79E+06	1.56
CF(800°C)	12.72	0.11
OCF-1h(800°C)	7.19E+02	0.35
OCF-2h(800°C)	1.92E+05	1.56
OCF-3h(800°C)	7.12E+05	1.65
CF(1000°C)	5.38	0.02

Table 5-S2. Performance comparisons between the OCF-3h sensor and state-of-the-art humidity sensors.

Sensor types	Active materials	Tunable resistance	Tunable sensing range	Linearity (R^2%)	Air/moisture permeability	Machine washability	Sensing at bend/twist/knot	Refs
Resistive	OCF	✓	✓	96.9	✓	✓	✓	Our work
	GO	-	✗	76.6	✓	✗	-	98
	Carbon nanocoils	-	✗	99.1	-	✗	-	95
	Ti3C2Tx	-	✗	83.9	✓	✗	-	96
	Acidified carbon nanotube	-	✗	97.2	✓	✗	-	94
	Graphene	✓	✗	91.2	✓	✗	✓	97
	SWCNT/PVA	-	✓	56.8	✓	✗	-	93
	Grinded Pyrolyzed bamboo	-	✗	95.2	✗	✗	-	245
	Pyrolyzed softwood pellets/oil seed rape	✓	✓	-	✗	✗	-	
Capacitive	PVA/KOH	✓	✓	98.9	✗	✗	-	236
	GO/Ag	-	✓	93.8	✗	✗	✗	246
	Cleancool yarn	-	✗	62.0	✓	✗	-	235
Piezoelectric	SnS_2/RGO	-	✗	93.2	✗	✗	-	247
	PDA/ hydroxy group	-	✗	99.7	✗	✗	-	248

Chapter 6
Highly Breathable and Stretchable Strain Sensors with Insensitive Response to Pressure and Bending

This chapter focuses on the fourth research objective. The work has been completed and published in Advanced Functional Materials in 2021. The details are reported below.

Authors: Zekun Liu, Yan Zheng, Lu Jin, Kaili Chen, Heng Zhai, Qiyao Huang, Zhongda Chen, Yangpeiqi Yi, Muhammad Umar, Lulu Xu, Gang Li, Yi Li and Zijian Zheng

Journal: Advanced Functional Materials

DOI: 10.1002/adfm.202007622

Statement of author contributions:

The proposal of the primary research idea. Copper deposition onto yarns, strain sensor fabrication, material and sensor characterization, as well as application demonstrations. Preparation of tables, figures and the manuscript.

Statement of co-author contributions:

Yan Zheng greatly supports the embroidery technique from sample design, and fabrication, trouble shouting during sensor fabrication. Lu Jin, Kaili Chen, Heng Zhai, Zhongda Chen, Yangpeiqi Yi, Muhammad Umar, and Lulu Xu contribute the experiments from copper deposition, SEM, EDS, and mechanical characterization to result discussion. Qiyao Huang and Gang Li assist in checking the language of the rough manuscript before submitting it to journals. Yi Li and Zijian Zheng supervise this work in both experiments and the paper organization.

Note: Supplementary material is available in Supporting Information.

6.1 Introduction

Real-time tactile measurement with wearable strain sensors is an important and indispensable function in the understanding of human-machine interaction and the application for health monitoring.[3, 249, 250] Typical electrical strain sensors measure the change of electric changes of the device as a function of tensile strain through conformal contact with the surfaces of human bodies or machines. The vast majority of surface movements at the time of tensile strain also contain a combination of bending and compression, it has been very challenging to develop an anti-jamming strain sensor to detect tensile strain alone in complex conditions.[251]

Many studies in recent years attempted to improve the sensitivity (revealed by gauge factor (GF)), sensing range, and reliability of strain sensors by encapsulating conductive network configuration with elastomers (e.g., PDMS, Ecoflex).[146, 252, 253] The elastomers always lack permeability to air and sweat vapour, which brings about discomfort and even skin irritation during body sensing.[129-131, 189, 254] The irritation will be further enhanced with the increase of sweat vapour produced from the body in the condition of hypermetabolism. Although reported encapsulation-free fabric strain sensors exhibit a certain degree of permeability,[72, 77] as a matter of fact, they also inevitably display significant response to pressure and bending. These sensors are also far from optimum in body sensing network (BSN) to monitor health and activities, especially during diversified movements. It is highly desirable to develop a breathable, pressure and bending insensitive strain (PBIS) sensor that can freely excrete skin metabolites, and precisely measure only tensile strain on moving surfaces.

Herein, for the first time, this paper reports a highly breathable PBIS sensor, which is artistically constructed by embroidering elastic and conductive yarns on a water-dissolvable

substrate. The continuously conductive yarns make up a strain sensing network after removing the substrate. It reveals outstanding sensitivity to tensile strain, which is several orders of magnitude better than bending (GF~ -0.09, at 75% bending) and pressure (~0.006 kPa^{-1} at the pressure of 100 kPa). Remarkably, the sensor shows excellent linearity and high sensitivity throughout a wide sensing range (GF~49.5, 0-100% strain, R^2=0.995). Owing to the high porosity of fabric structure, the PBIS sensor exhibits good breathability to air, moisture and water vapour, which guarantees a wearing comfort of the micro-environment between the skin surface and the wearable sensor.

6.2 Experimental Section

6.2.1 Preparation of Copper Deposited Viscose Yarn

Pristine viscose yarn (supplied by the textile fabrication lab of the University of Manchester, diameter is around 300 μm, two-thread yarn) was selected because of the large number of hydrophilic groups on the cellulose molecular surfaces, which provide binding sites for polymer growth and following copper deposition. It was firstly immersed into a mixed solution with 47.5 mL ethyl alcohol, 0.5 mL acetic acid, 2 mL deionized water, and 2 mL trimethoxysilane in room temperature for 2 h. After that, the silanized viscose was dipped into another aqueous mixture with 40 mL deionized water, 10 mL trimethyl ammonium chloride (METAC), and 100 mg potassium persulfate in 80 °C for 1h. Then the METAC-coated viscose was immersed into 5×10^{-3} M/L $(NH_4)_2PdCl_4$ aqueous solution in room temperature and dark environment for 30 min. Finally, the $[PdCl4]^{2-}$ loaded viscose was immersed into a bath with 1:1 (v/v) mixture of solution A and B to accomplish copper deposition. Solution A is an aqueous mixture including NaOH (12g/L), $CuSO_4 \cdot 5H_2O$ (13g/L), and $KNaC_4H_4O_6 \cdot 4H_2O$ (29g/L) in

deionized water. Solution B is formaldehyde (9.5mL/L) aqueous solution. The chemicals are the same with the chemicals used in Chapter 4, which were purchased from SIGMA. There is a several-time rinsing process between each procedure. The mechanism of the polymer assisted copper deposition has been reported by our previous works. [57, 255]

6.2.2 Fabrication of PBIS Sensors

The nylon covered Lycra yarn (supplied by textile fabrication lab of University of Manchester, Lycra yarn is in the core and two-thread nylon yarn is on the out layer) was firstly fixed by PVA yarn on a PVA substrate (from Madeira Company, Germany) via a commercial embroidery machine (JCZA 0109-550, Germany), the tension of Lycra is 0.06 N. After that, copper-deposited viscose yarn was embroidered in rectangular Lycra track (6×2.4 cm^2) by the embroidery machine. The distance between adjacent two viscose yarns is set as 400, 600 and 800 μm to acquire different-density sensors. Finally, the sample was immersed in water to remove PVA, and the final area of the sensor is 4.5×2 cm^2. Then, the distance between viscose yarns of PBIS sensors became 300, 450, and 600 μm respectively. The sensor is insensitive to bending and pressuring inputs in that the conductive copper-deposited yarns are obstructed by the non-conductive yarns (Lycra).

6.2.3 Characterizations of Structure and Sensor Performance

Optical Microscope (Keyence VHX-5000) and electron microscope (electron microscope) were used to observe the morphology of pristine and copper deposited viscose yarns. The surface elements and their distribution of the yarns were obtained by the electron microscope equipped with energy-dispersive X-ray spectroscopy (EDX). Mechanical tests and electrical

properties of sensors were performed using a universal testing machine (Instron 3344) and a multimeter (Keithley 2000) respectively. There are two conductive tapes as electrodes at both ends of the sensor to connect with the multimeter for signal collection. The humidity stability of the sensor was carried out in the Instron. The sensor was in a box and increasing humidity was acquired by injecting humidity to the box using a humidifier. Commercialized instruments (M021A, SDL), (M216, SDL) were used to detect the air and water vapour permeability of the sensor respectively. The moisture permeability of the sensors was reflected by testing corresponding-parameter fabrics via another commercialized instrument (M290, SDL).

6.3 Results and Discussion

6.3.1 Fabrication Process of the PBIS Sensors

Figure 6-1a shows the schematic depiction of the in-situ growth of copper on viscose fibres by polymer-assisted metal deposition (PAMD) reported in our previous work.[57, 255] Briefly, the viscose substrate was firstly modified by functional polymers i.e., silane-type initiator and trimethyl ammonium chloride, following with ion pairing with palladium moieties as the activator, after which a PAMD of dense copper nanoparticles onto the viscose yarn was fulfilled from the polymer layers (see detailed procedures in Experimental Section). The pristine viscose yarn has a smooth surface (Figure 6-S1a), while a layer of serried copper nanoparticles can be observed on copper deposited viscose yarn (Figure 6-S1b). By capitalizing on PAMD, the copper deposition reaches each fibre of the twisted viscose yarn, which is verified by the fibre surface of unfasten-twist yarn (Figure 6-1b). The elemental composition of the viscose surface is significantly changed (Figure 6-S1c-i), where the atomic levels of C, O, and N are 58.28%, 41.01%, and 0.71% respectively for pristine viscose yarn. After PAMD, the content of C and

O decreases by 32.89% and 10.84% respectively, while the Cu significantly increases by 56.27%. The serried copper nanoparticles on the fibre surface endow viscose yarn with low linear resistance (~0.23 Ω/cm). The breaking strength of the pristine yarn is ~55 kPa, while it is more than 100 kPa after copper deposition (Figure 6-S2).

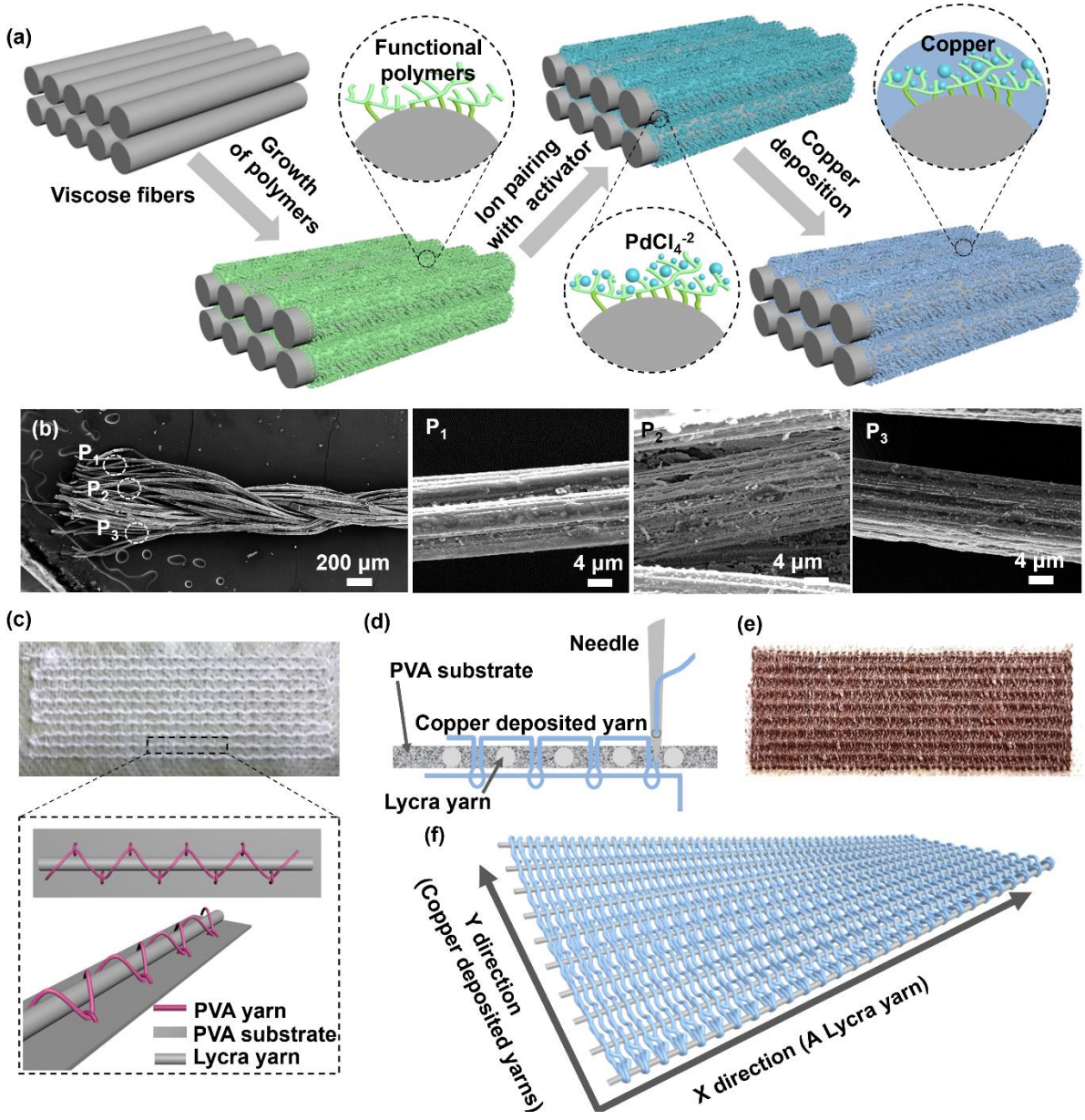

Figure 6-1. The schematic diagrams of conductive viscose yarn by PAMD and construction of PBIS sensor. (a) The procedure of room-temperature PAMD onto viscose substrate. (b) The morphology of copper deposited viscose yarn, showing the deposition can reach every single fibre. (c) The image of the rectangular Lycra track (6×2.4 cm^2) fixed onto PVA substrate by PVA yarn. (d) The diagram of embroidering copper deposited yarn in the Lycra track via lock-

stitch embroidery. (e) The surface image of the embroidery pattern with copper deposited yarn and the Lycra track. (f) The diagram of the PBIS sensor after dissolving PVA, which is constructed with elastic Lycra yarn and copper deposited yarn in warp and weft direction respectively.

By taking advantage of pattern flexibility and high precision of embroidery technique, the PBIS sensor was exquisitely fabricated by an embroidery machine equipped with tailored fibre placement and lock-stitch embroidery (Figure 6-S3a). A pattern of rectangular nylon-covered Lycra (Figure 6-1c) was firstly stitched onto a water-soluble polyvinylalcohol (PVA) substrate by PVA yarn via tailored fibre placement (Figure 6-S3b-d). After that, two copper-deposited viscose yarns served as needle thread and bobbin thread respectively were precisely locked on the elastic yarn track (Figure 6-1d) by lock-stitch embroidery (Figure 6-S3e). The inter-locked pattern (Figure 6-1e) was then immersed in deionized water to dissolve PVA. The PBIS sensor was eventually fabricated with copper-deposited viscose yarns in the y direction, and an elastic yarn in x direction (Figure 6-1f). Noted that the inter-locked pattern experienced a surface shrinkage (Figure 6-S3f, g) after dissolving PVA due to the pre-tension of elastic yarn during tailored fibre placement (detail in Experimental Section). The high elasticity of Lycra, and the remarkable conductivity of copper deposited viscose endow the stretchable fabric with strain sensing ability. We investigated the performance of PBIS sensors with varied density in x direction. The sensors were denoted as PBIS-300, PBIS-450, and PBIS-600 corresponding to the devices with the distance between adjacent conductive yarns of 300, 450 and 600 μm respectively.

6.3.2 Calibration and Working Mechanism

The PBIS sensors show remarkable sensitivity with sufferable tensile strain up to 200%, while

negligible responses to wide-range bending and pressure (Figure 6-2a). It depicts PBIS-300 acquired superior sensitivity throughout 200% tensile strain compared to PBIS-450 and PBIS-600 (linear fitting results in Table 6-S1). This could be understood that higher density PBIS possesses lower initial resistance, which corresponds to a higher relative resistance increase when tensile strain is applied. GF of all samples significantly decreases when strain reaching ~150%, which is ascribed to the decrescent diameter of elastic yarn during the tensile process (Figure 6-S4). The smaller diameter yarn cannot prominently drive the separation of weft conductive yarns, thus the GF is slightly raised with further tensile.

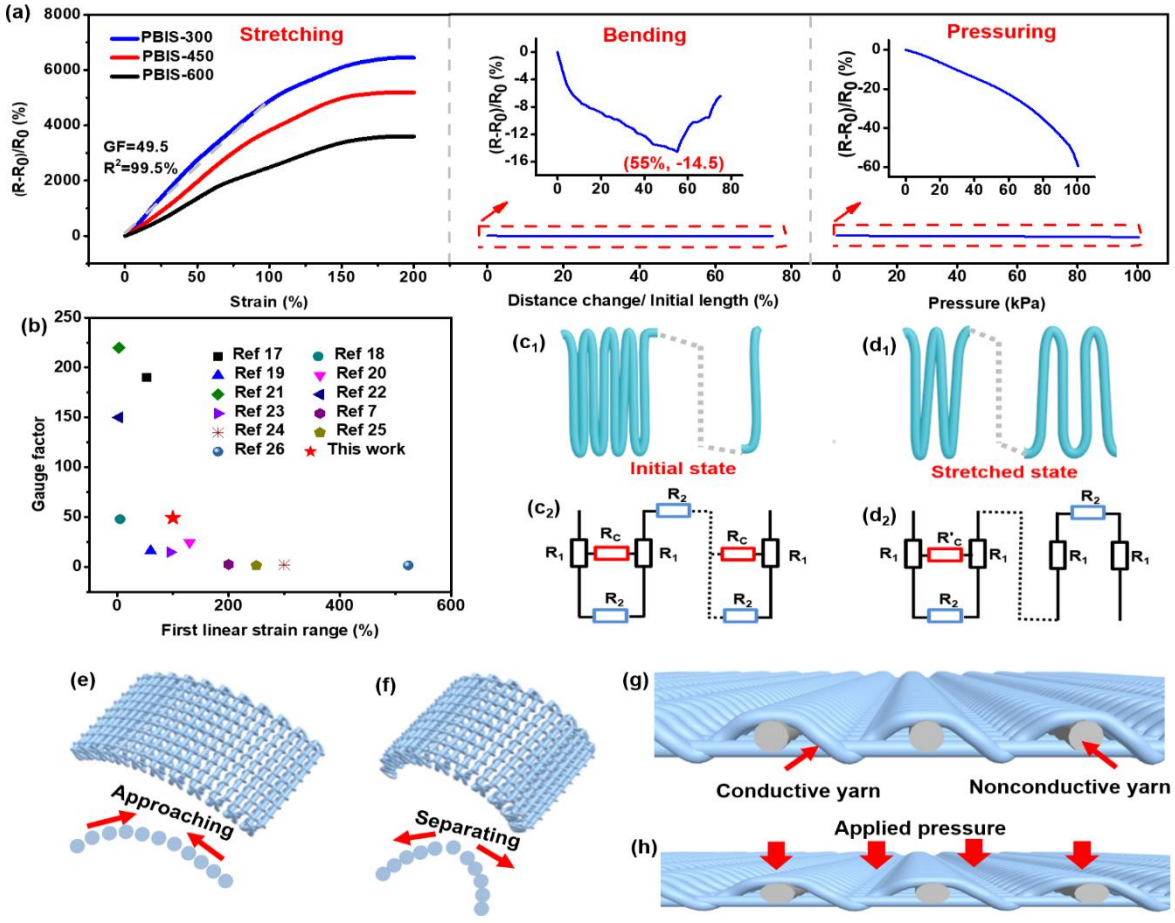

Figure 6-2. Electrical responses and corresponding mechanism of PBIS sensors under stretching, and bending as well as compression. (a) The calibration of different-density PBIS sensors with tensile strain, and the electrical properties of PBIS-300 under bending and compression. (b) Comparisons of the sensing performance in terms of first linear strain range and corresponding gauge factor, showing the superiority of PBIS-300 than previous work. (c)

The initial sensing network, and corresponding resistance model. (d) The stretched sensing network, and corresponding resistance model. (e) Schematic illustration of PBIS-300 during 0-55% bending. (f) Schematic illustration of PBIS-300 during 55-75% bending. (g) The sectional view of the PBIS sensor, and (h) the sectional view of the PBIS sensor under applied pressure, showing the insensitivity under compression because two layers of conductive yarn are separated by nonconductive yarn.

By contrast, the electrical response of the PBIS sensor to bending and compression is negligible. We tested the electrical properties of PBIS-300 with the inputs of wide-range bending and high pressure, it shows that the sensor acquires marginal response to both bending (GF of -0.09 at 75% bending) and high compression (0.006 kPa^{-1} at the pressure of 100 kPa). The bending was calculated by distance change/initial length of the sample during bending test, which is shown in Figure 6-S5. The sensor has very limited response to bending, and the resistance change to bending is almost negligible when tensile strain is over 2.5%. The resistance change of the sensor with the tensile strain of 5% is several times higher than that of wide range of pressure input. However, it should be noted that the small tensile strain detection of most body movements by stretchable sensors seldom contains neither high degree of bending nor very high pressure. Therefore, our sensor is always sensitive to tensile strain, insensitive to both bending and pressure in real applications. Figure 6-S6a shows that the sensor presents a much less GF than that in the x direction, which means the sensor enables to detect only tensile strain in x direction. More importantly, with only a 15% y-direction strain, the force would quickly reach more than 200 N (Figure 6-S6b). The high and rapid mechanical response ensures the sensor can precisely perceive x-direction strain without disturbance, as such high force is generally unattainable in body-wearable applications. Notably, PBIS-300 presents excellent linearity (R^2=99.5%) with high sensitivity (GF=49.5) from 0-100% tensile strain, which is superior to reported sensors in terms of combined GF and first linear sensing strain range

(Figure 6-2b).[33, 70, 109, 253, 256-262]

The highly sensitive PBIS sensor is originated from its novel structure, of which the sensing network is constructed by conductive yarn in the x direction. In Figure 6-2c, continuously conductive threads without elongation form a parallel circuit, and it becomes a hybrid circuit in the stretched state (Figure 6-2d). The initial resistance (R) of the sensor can be calculated with Equation (6-1).

$$R=n\frac{R_C R_2+2R_1R_C+2R_1R_2}{R_C+R_2} \quad (6\text{-}1)$$

where R_1, and R_2 are the resistances of linear part and curved part of the threads respectively, and R_C refers to the contact resistance between two adjacent threads. From initial state to a certain range of stretch, Equation (6-1) can depict the whole resistance of the sensor. The R increases with the increase of R_C with tensile elongation, thus leading to an incremental resistance of the sensor. With sufficient deformation, the conductive threads experience a separation. Some threads have limited contacts with surrounding threads, the contact resistance (R'_C) becomes larger. On the other hand, some threads are completely separated, and the threads form a series circuit. In this case, the resistance (R') of the sensor can be calculated with Equation (6-2). The above equations and models could explain the mechanism of stretch-induced increasing resistance of the sensor.

$$R'=m\frac{R'_C R_2+2R_1R'_C+2R_1R_2}{R'_C+R_2}+(n-m)\,(2R_1+R_2) \quad (6\text{-}2)$$

The insensitive electrical response to bending presents a diverse trend during 0-75% bending. Resistance gradually decreases when bending changes from 0-55%, which can be ascribed to the approaching of conductive threads (Figure 6-2e). On the contrary, an inverse increase resulted from the separation of intermediate threads (Figure 6-2f) arises under large-extent

bending (55-75%). The marginal electrical output of the PBIS sensor to pressure benefits from the nonconductive elastic yarns between needle threads and bobbin threads. As it insulates two layers of threads (Figure 6-2g), the obstruct can be well maintained under applied pressure (Figure 6-2h).

6.3.3 Electromechanical Performance

Unlike conventional stretchable fabric-based strain sensors with obvious hysteresis,[77] the Lycra yarn in the PBIS sensor shows little hysteresis (Figure 6-S7). The conductive yarns are not directly subject to tensile stress nor strain during tensile elongation, while the elastic Lycra yarns can achieve good stretching ratios with very low hysteresis. This is why our PBIS sensor has shown very small hysteresis under loading-unloading cycles (Figure 6-3a). Figure 6-3b shows the dynamic stability by applying cyclic 10% strain with the frequency ranging from 0.1-1 Hz, and Figure 6-3c exhibits the dynamic strain stability from 5-180% strain with the frequency of 0.2 Hz (dynamic strain stability of PBIS-450 and PBIS-600 in Figure 6-S8). Noted that the nylon layer covered on Lycra (Figure 6-S4) is of importance to the dynamic stability of the sensor, as it can ensure the conductive threads repeatable separation and recovery during loading-uploading strain (Figure 6-S9a-c). This is confirmed by changing the covered Lycra into pure Lycra, the electrical output of the sensor made with uncovered Lycra becomes a bit unstable (Figure 6-S9d). We also demonstrate the bending and pressure responses of the sensor are stably insensitive during dynamic bending and pressure (Figure 6-S10), which guarantees the sensor can accurately detect tensile strain along even in a complex dynamic state. By stretching the sensor by 30%, 60%, and 120% strain to illustrate its outstanding static stability, the electrical signal in Figure 6-3d shows little overshoots and swiftly remains stable.

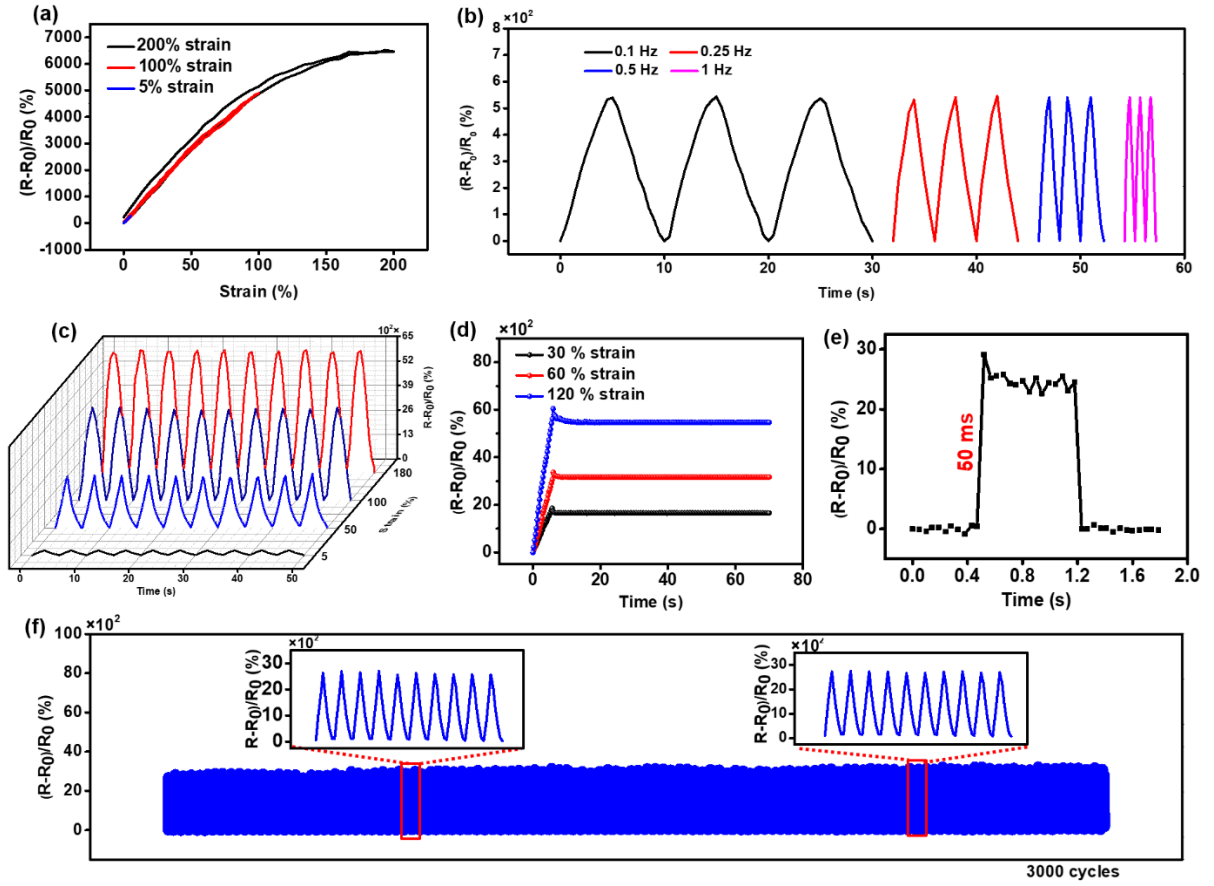

Figure 6-3. Electromechanical properties of PBIS-300. (a) Electrical responses of different stretching–releasing strain with the speed of 20% strain S^{-1}, showing the hysteresis of the sensor. (b) Dynamic stability of the sensor at various frequencies ranging from 0.1 to 1Hz. (c) Dynamic stability of the sensor at various strains ranging from 5 to 180%. (d) The relative resistance change of the sensor with a step strain to show low creep and static stability. (e) The real-time relative resistance change of the sensor subjected to a fast-speed 0.5% strain, showing the response time can reach ~50 ms. (f) Electrical responses under 50% loading and unloading strain, with the frequency of 0.5 Hz for 3000 cycles, showing the durability of the sensor.

To accurately determine its response speed, a 0.5% strain with the speed of 16 mm/s was applied on the sensor. Figure 6-3e displays that the responding time of the sensor reaches ~50 ms, which can generally meet many needs of strain sensing applications. To further judge the stability and durability of the sensor, a 50% loading-uploading strain was applied to it with the frequency of 0.5 Hz for 3000 cycles. Figure 6-3f exhibits that the electrical response is

reproducible throughout the overall fatigue with slight fluctuation, where the brilliant durability benefits from the nondestructive sensing network as well as the remarkable elasticity and robustness of Lycra (Figure 6-S11). Figure 6-S12a presents the washing of PBIS-300 with laundry liquid in room temperature for 30 mins. After the washing, the calibration result in Figure 6-S12b shows that the sensitivity of the sensor slightly decreases compared with the sensor without washing, which may be ascribed to the damage of the copper layer during the washing process. It should be noted that even with the washing process, the sensor still acquires outstanding sensitivity throughout the 200% strain, guaranteeing a good strain sensing ability. To explore the effect of wear-out issue on the electrical output of the PBIS sensor, we firstly tested the electrical signals of PBIS-300 by applying a recurrent 40% strain, then gave friction to the sensor by hands, and finally tested the electrical outputs again. The response of the sensor in Figure 6-S13 shows that the friction would not weaken the sensing ability and performance. From the above, the sensor shows conjunct merits of high sensitivity to tensile deformation while insensitivity to bending and pressure, remarkable linearity, outstanding stability, and durability, as well as fast responding time.

6.3.4 Breathability

Conventional techniques for wearable sensing always rely on components and approaches developed for strain detection outside of the real wearable environment, such sensing techniques may not prioritize the physical comfort of the sensing components. The encapsulation-free PBIS sensor with porous structure possesses outstanding permeability to air and vapour as well as moisture, which is of vital significance for wearing comfort. We evaluated the moisture permeability by applying several drops of water from the top layer of the sensors for 20 s, then measure the water content and track the water footprint. Figure 6-4a

shows that the water drops can freely and immediately transfer from top to bottom layer (footprints in Figure 6-S14), presenting the excellent moisture permeability of all sensors. Air and vapour permeability also plays a major role in determining the wearing comfort of sensors in that human metabolites always excrete out in the forms of vapour and gas. Figure 6-4b, c exhibit that lower-density sample possesses better permeability to air and water vapour, as low-density sample with more pore channel for the efficient transportation of these components. It also shows that the air and water vapour permeability of all sensors exceeds 1500 $l/m^2/s$ and 25 $g/m^2/h$ respectively, which guarantees the sensor with outstanding breathability like general garments.

In many cases, wearable electronics implement applications in diverse environments as the humidity and temperature of air and skin surface may be totally different, especially during exercising. We tested the electrical response of PBIS-300 under recurrent 8% strain in a wide range of humidity. Figure 6-4d exhibits that the sensor is steady in a relative humidity of ~39.28% (room condition), this humidity stability well maintains with an increasing relative humidity up to ~100%. Similarly, we tested the electrical response of PBIS-300 under recurrent 10% strain (0.1 Hz) from the temperature of ~23.2°C (room condition) to ~40.1°C in a self-built device (Figure 6-S15a). Figure 6-S15b exhibits that the electrical outputs of the sensor are not significantly affected by the temperature change, ensuring the sensor can detect body motions without the disturbance of a certain degree of temperature range. As a proof-of-concept illustration of the breathability of the PBIS sensor, we show a schematic diagram of the skin-wearable sensor-environment system in Figure 6-4e. It reveals the skin metabolites can freely discharge to air in the form of water vapour due to the outstanding permeability of the PBIS sensor, and the sensor can stably detect surface strain during various climate owing to the prominent humidity and temperature stability.

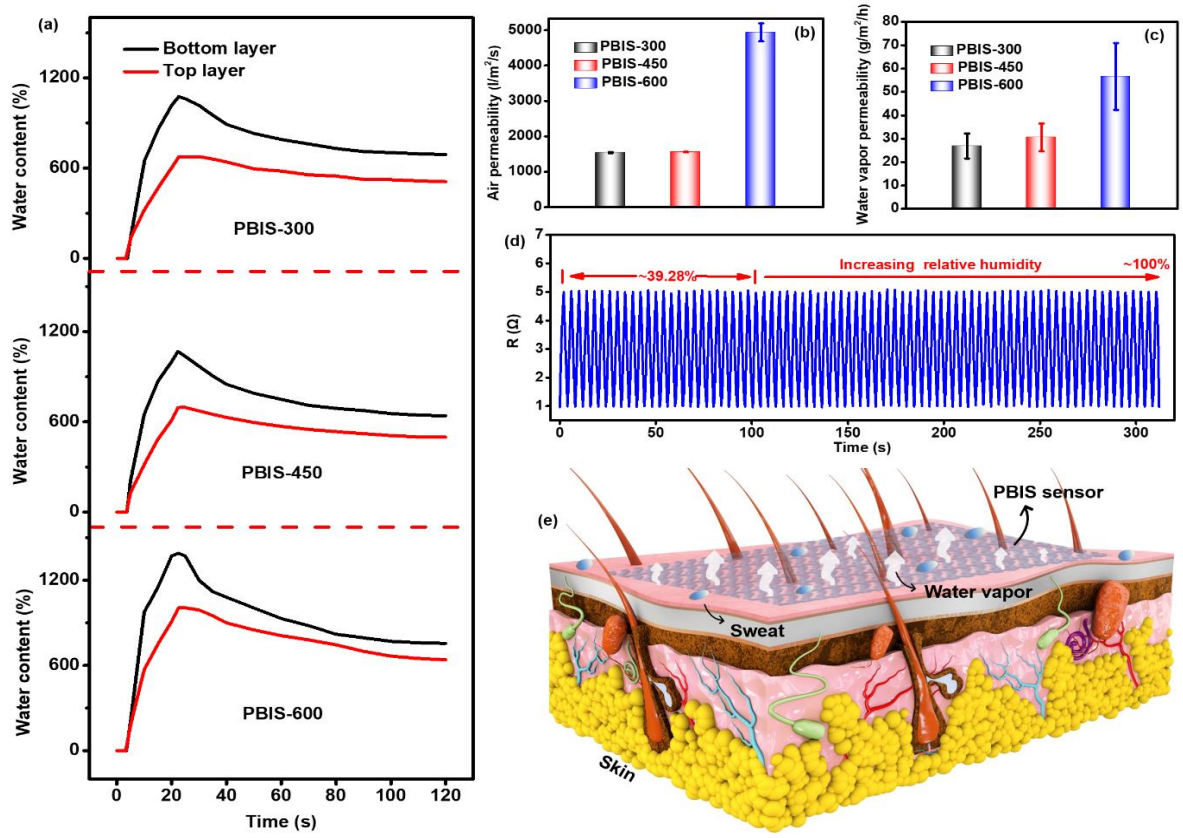

Figure 6-4. The breathability of PBIS sensors. (a) Liquid diffusion details by applying water drops from the top layer of the sensors for 20 s, showing the remarkable moisture permeability. (b) The air permeability of the sensors. (c) Water vapour permeability of the sensors. (d) The stable resistance change of PBIS-300 with 8% cyclic strain during ~39.28 (room condition) to ~100% relative humidity, showing high stability of the sensor in wide-range humidity. (e) Schematic diagram of the skin-wearable sensor-environment system, as proof-of-concept illustration of PBIS sensor breathability.

6.3.5 Applications

Different from conventional rubber-encapsulated strain sensors with poor wearability, the pure fibre-based PBIS sensor possesses good compatibility to clothes, which is essential for real wearable occasions. Figure 6-5a shows the image of a sensor-assembled cloth through suture approach, showing the sensor can be well integrated with daily wears to implement applications. Figure 6-5b shows the locations of full-range BSN made with the sensor for the application of

human activity recognitions spanning from tiny to large body deformations during running. Tiny body motions such as chewing, throat vibration as well as respiration can be promptly and precisely sensed by the sensor. In Figure 6-5c, the sensor was attached to the cheek to recognize the state of gum chewing. It displays there is an up-down resistance change for chewing once and many fluctuations for chewing several times, of which signals are highly consistent with the expansion of masticatory muscle. For further demonstrations of detecting the tiny throat movements, we measured the relative resistance changes during cough (Figure 6-5d), water drinking (Figure 6-5e) and speaking (Figure 6-5f). The measurement results show that the motions are tracked with high reproducible signaling patterns for different motion activities. Figure 6-5g exhibits the signals of human normal breath and the breath during running, indicating a discernable respiratory rate and depth during the two diverse conditions.

In addition to tiny body movements, the broad-sensing-range sensor could also detect large body deformations. We fixed the sensor on the index finger to monitor finger bending. Electrical outputs in Figure 6-S16a exhibit the motion is explicitly reflected by the sensor. Figure 6-5h shows the demonstration of monitoring motion of the knee joint during walking and running. It reveals that the movements are precisely discriminated by the response frequency and intensity of the sensor, where the walking and running speed is ~1.8 s/steps and ~0.59 s/steps respectively. Similarly, the diverse motions can also be well rebuilt by attaching the sensor to the arm joint (Figure 6-S16b). The sensor maintains a stable response during walking and running due to its advantage of insensitivity to pressure and bending, which has great potential applications in athletic training, sports competition as well as rehabilitation exercises (Rider monitoring in Figure 6-S17). Based on the high sensitivity, real-time recognition, broad sensing range as well as remarkable breathability, we believe the sensor can accomplish all motions rebuilding through BSN.

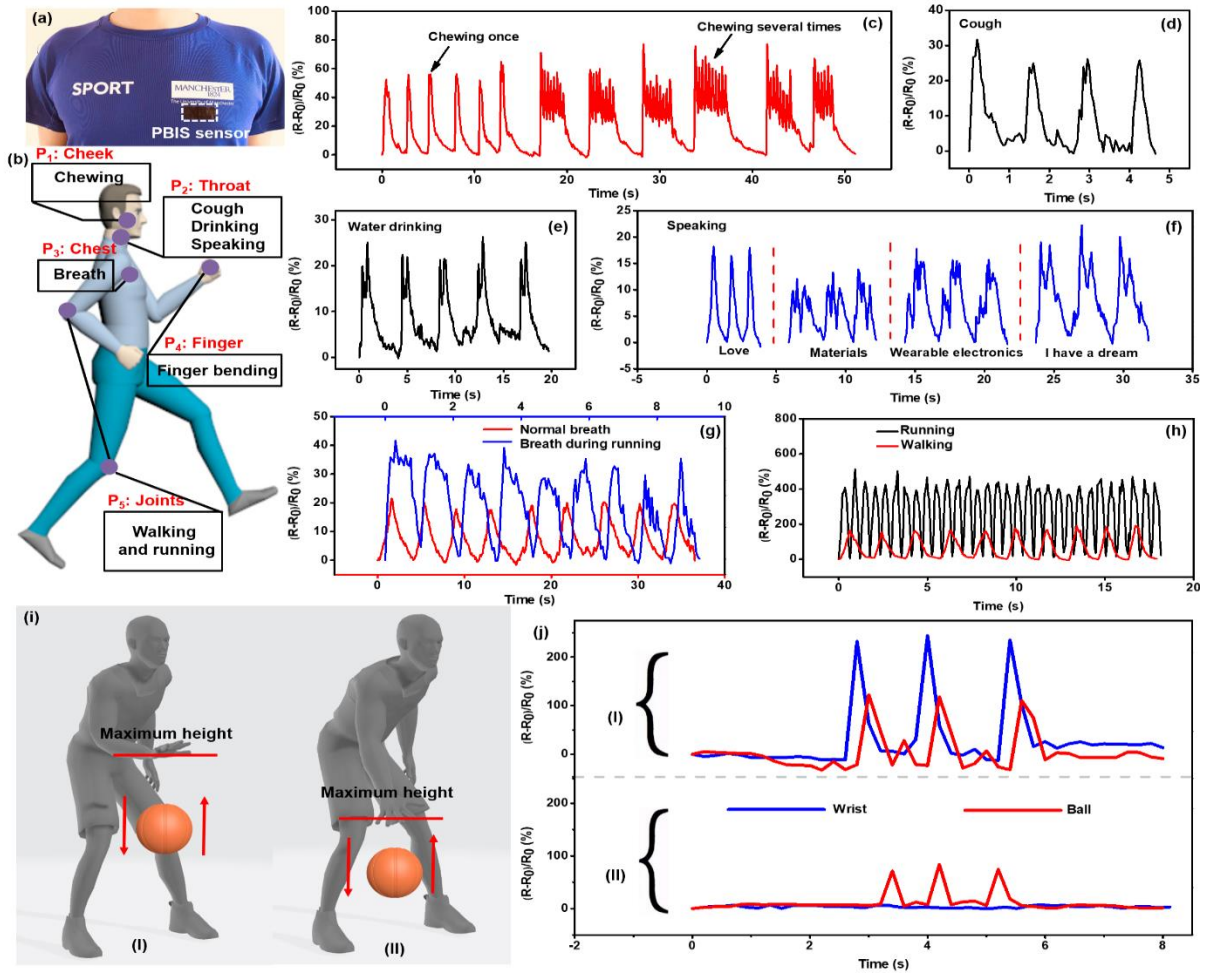

Figure 6-5. Applications of PBIS-300. (a) Integration of the sensor with clothes, showing its good compatibility. (b) An overview of the locations of BSN. (c) Corresponding signals of chewing gum in different conditions by attaching the sensors to the cheek. (d) Detection of the throat vibration during cough. (e) Detection of human motion of drinking water. (f) Signals of the throat epidermis vibration during speaking different words. (g) Relative resistance changes of normal breath and breath during running. (h) Detection of human walking and running styles by attaching the sensor to the knee. (i) Illustration of two modes of dribbling, (I) dribbling with wrist bending and the ball with a higher path, (II) dribbling without wrist bending and the ball with a lower path. (j) Corresponding signals of the dribbling modes collected from the sensor on the wrist and the ball.

As a further proof-of-concept demonstration of man-machine interaction, we additionally attached the PBIS sensors to a ball and the wrist to measure time-dependent single signal of

the sensors. Figure 6-5i shows the two modes of dribbling, mode I represents dribbling with wrist bending and the ball with a higher path, while mode II refers to such motion without wrist bending and the ball with a lower path. In Figure 6-5j, by applying wrist bending for high-path dribbling, the relative resistance changes of the sensor on the wrist and the ball record the stimulations of the wrist bending and the ball swelling respectively. By contrast, low-path dribbling leads to a weaker signal from the sensor on the ball due to lower ball swelling, and the signal from the wrist sensor is stable throughout. This demonstration exhibits high application potential in dribbling correction, athletic training as well as human-computer interaction.

6.4 Summary

In summary, we have reported a brilliantly breathable, and highly sensitive strain sensor through polymer assisted copper deposition and a novel embroidery approach, which exhibits extremely low sensitivity to both pressure and bending. The all fibre-based sensors possess remarkable breathability, ennobling outstanding permeability to moisture, air as well as water vapour. The sensor with higher density (PBIS-300) shows fast response, superior environment stability, and durability, as well as high sensitivity (GF=49.5) and prominent linearity (R^2=0.995) throughout the broad detection range (0-100% strain). Particularly, the creationary construction of the sensor could be rapidly extended to almost any conductive and elastic yarns, paving a new way for the low-cost and scalable fabrication of high-performance, encapsulation-free, bending and pressure insensitive strain sensors.

Supporting Information

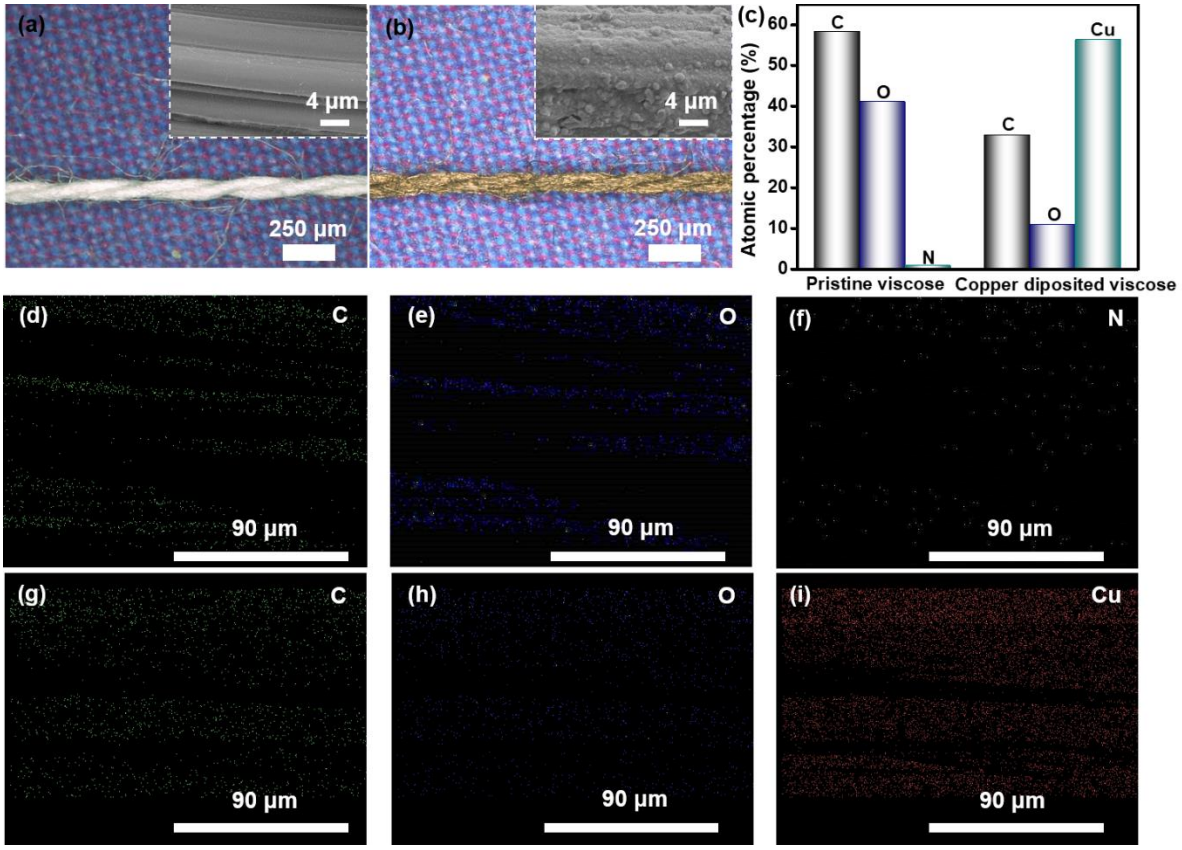

Figure 6-S1. The surface morphology and element distribution of pristine and copper deposited viscose yarns. (a) Surface morphology of pristine viscose yarn. (b) Surface morphology of copper deposited viscose yarn. (c) The surface element content of pristine and copper deposited viscose yarns. (d) C distribution of pristine viscose. (e) O distribution of pristine viscose. (f) N distribution of pristine viscose. (g) C distribution of copper deposited viscose. (h) O distribution of copper deposited viscose. (i) Cu distribution of copper deposited viscose.

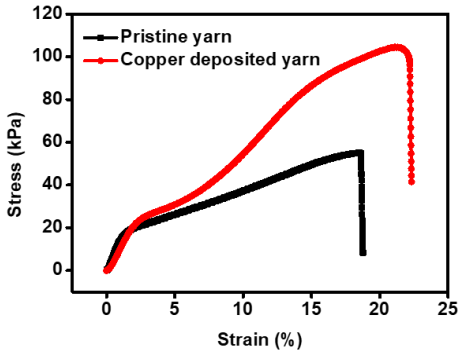

Figure 6-S2. The mechanical performance of pristine and copper-deposited yarns.

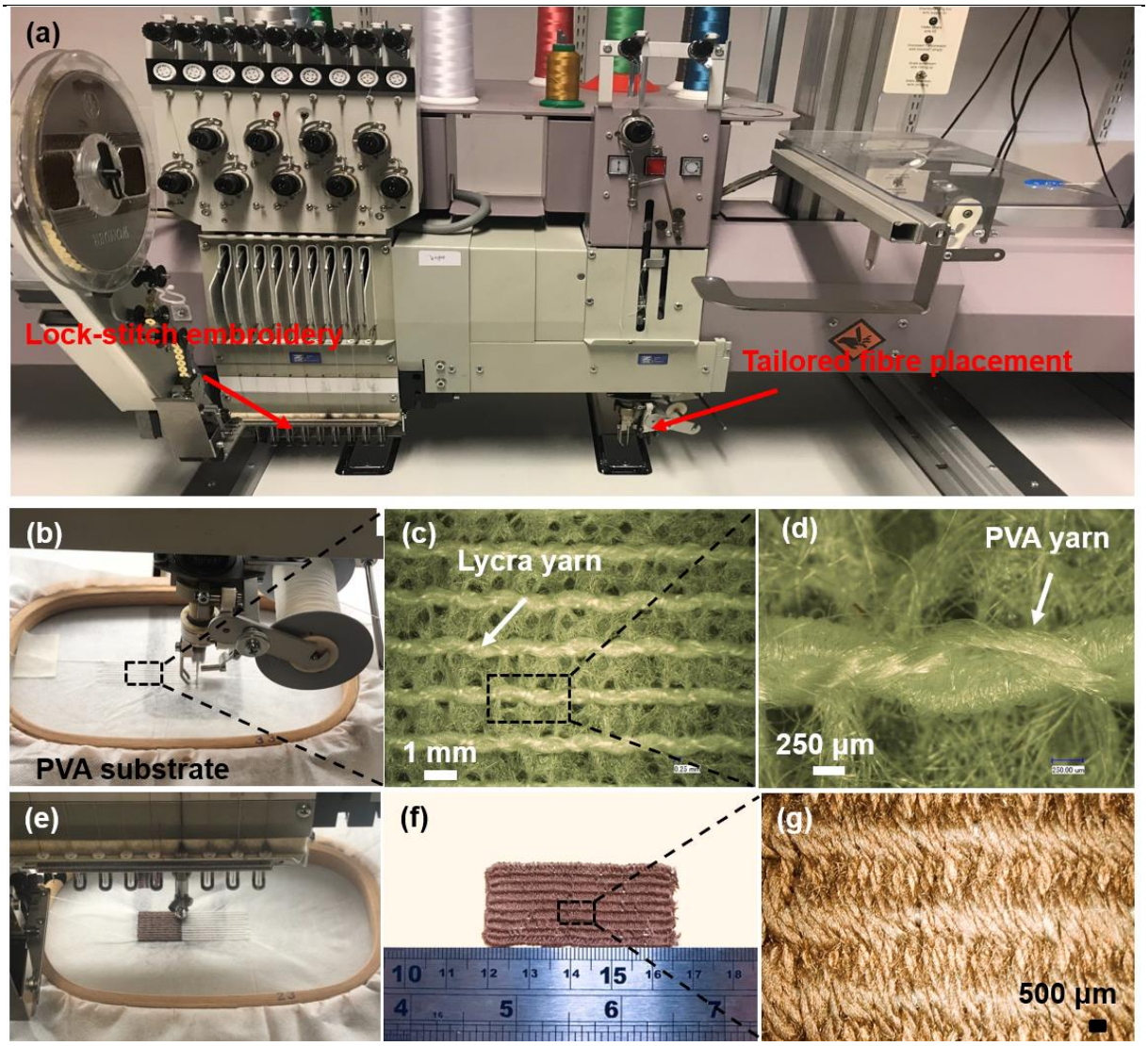

Figure 6-S3. Fabrication details of PBIS sensor by embroidery technology. (a) A commercial embroidery machine equipped with tailored fibre placement and lock-stitch embroidery. (b) A Lycra track fixed on PVA substrate by PVA yarn via tailored fibre placement. (c) Close-up of the Lycra track. (d) Close-up of PVA yarn on the track. (e) The process of embroidering copper deposited yarn in the Lycra track via lock-stitch embroidery. (f) The image of the PBIS sensor (4.5×2 cm^2) by dissolving PVA in water. (g) Close-up of the PBIS sensor.

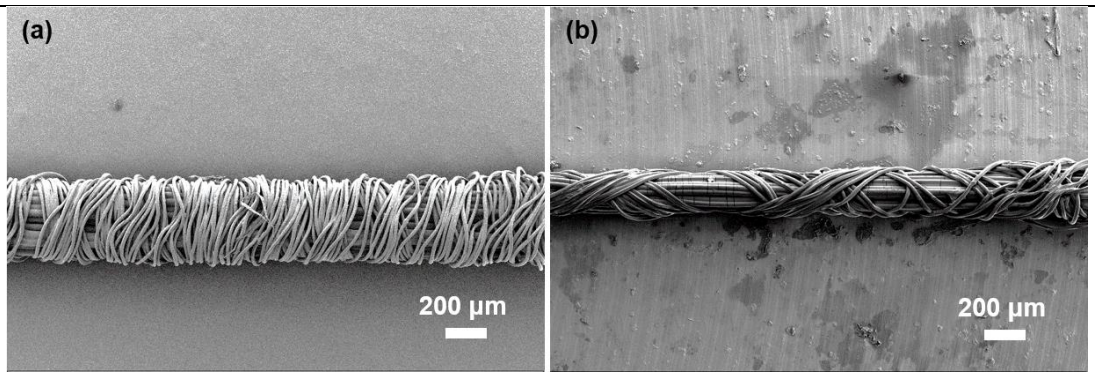

Figure 6-S4. Images of original and stretched nylon-covered Lycra yarns. (a) Original nylon-covered Lycra. (b) Nylon-covered Lycra under 150% strain.

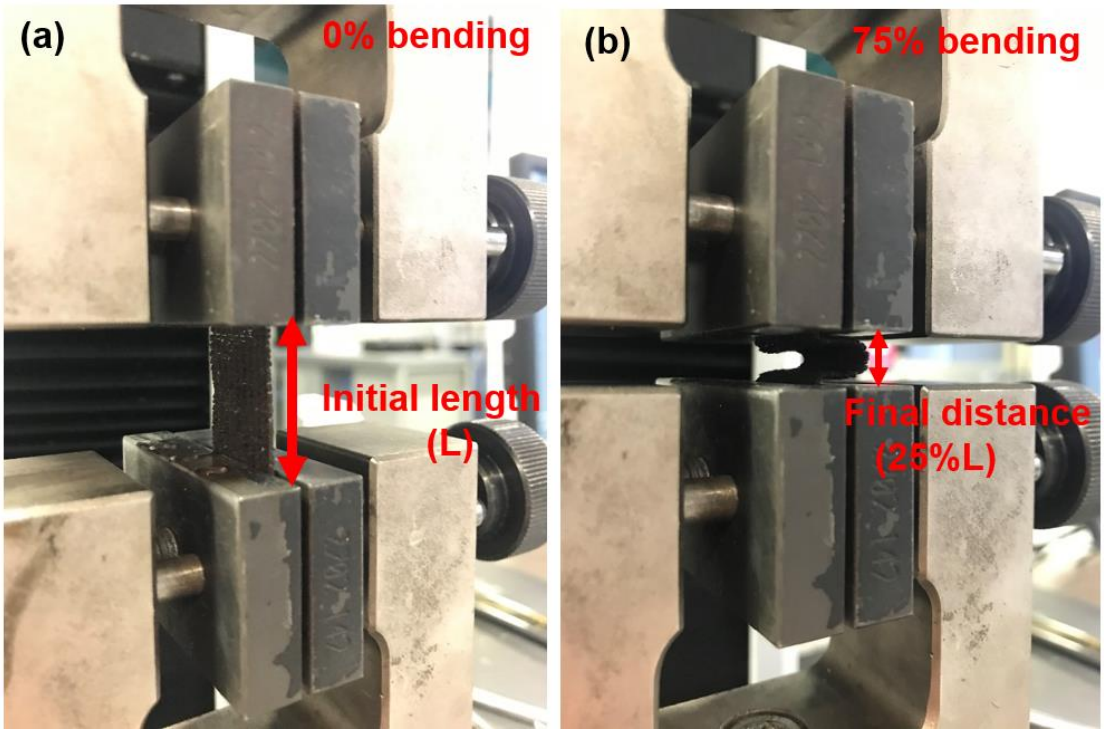

Figure 6-S5. Illustration of bending tests of PBIS-300. (a) Image of the sensor without bending. (b) Image of the sensor with 75% bending.

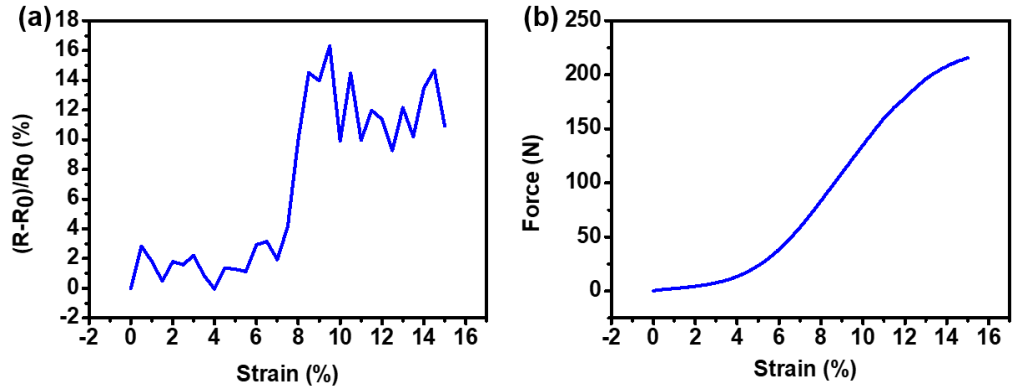

Figure 6-S6. Relative resistance and mechanical changes of PBIS-300 in y-direction strain. (a) Relative resistance changes of the sensor, and (b) corresponding mechanical performance.

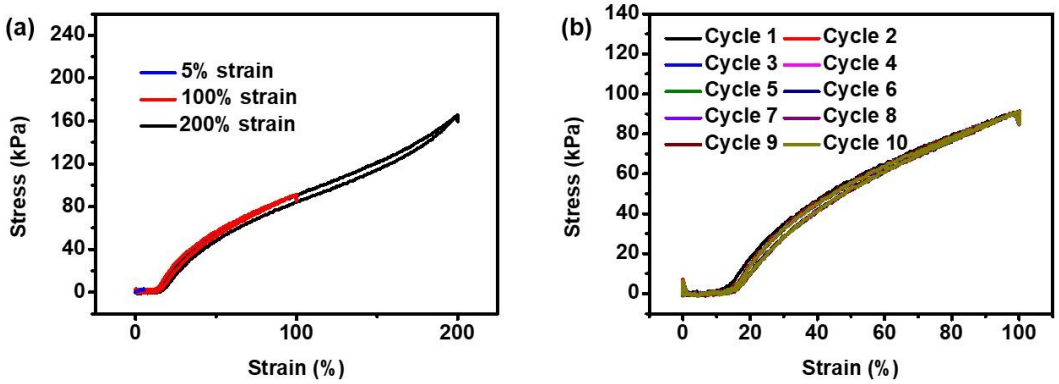

Figure 6-S7. Strain-stress curves of PBIS-300. (a) The strain-stress curve of the sensor under different loading-unloading strain, and (b) the strain-stress curve of the sensor under repeated loading-unloading strain of 100%, showing the little mechanical hysteresis of the sensor.

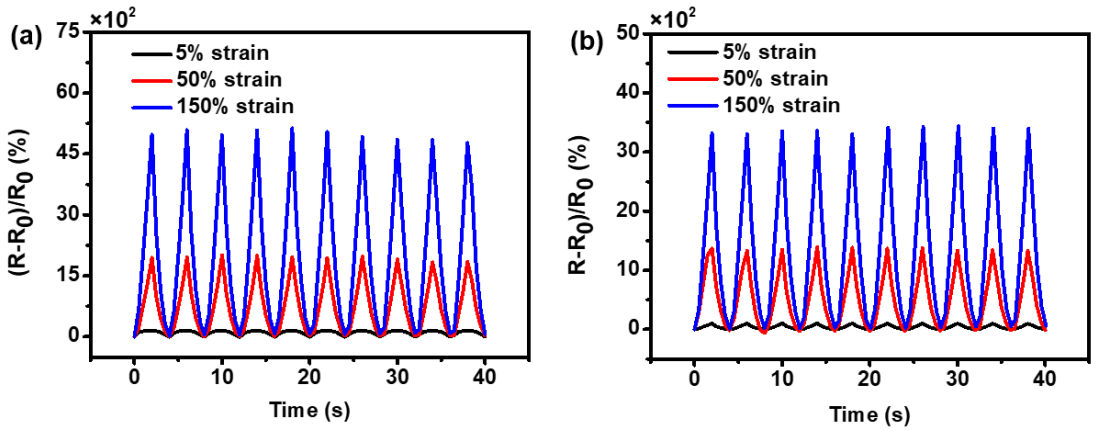

Figure 6-S8. The dynamic electrical stability of PBIS-450 and PBIS-600 under different tensile strain. (a) Electrical response of PBIS-450 with 5, 50, and 150% strain for ten cycles respectively. (b) Electrical response of PBIS-600 with 5, 50, and 150% strain for ten cycles

respectively.

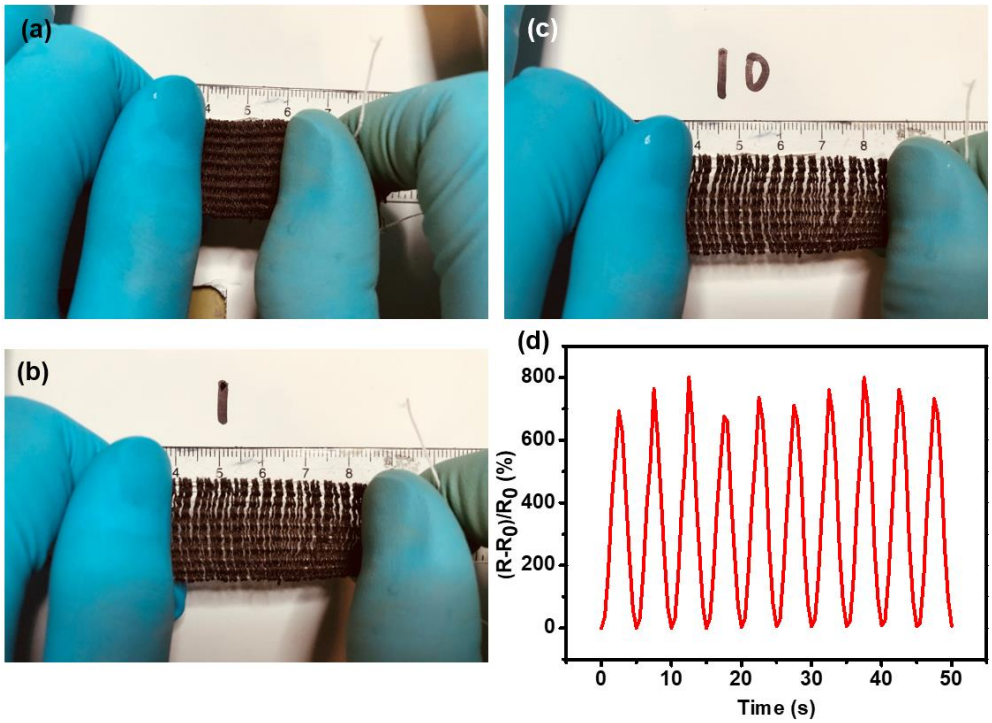

Figure 6-S9. Stability of PBIS-300. (a) The image of the unstretched sensor. (b) The image of the sensor under a first-time ~100% strain. (c) The image of the sensor under tenth time ~100% strain. (d) Unstable electrical response of the strain sensor (under 20% tensile strain) with uncovered Lycra in the warp direction, showing the superiority of covered Lycra-based sensor.

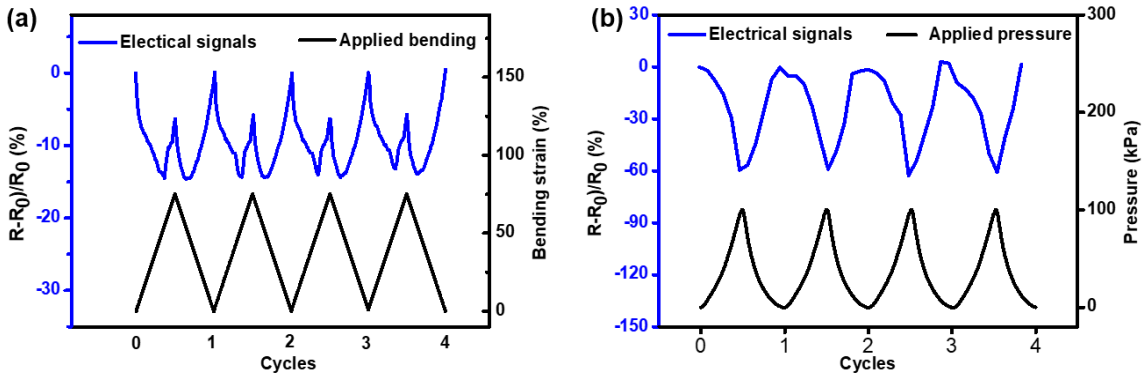

Figure 6-S10. The electrical response of PBIS-300 to applied bending and pressure. (a) Electrical signals of the sensor under repetitive 0-75% bending, showing its consistent insensitivity to bending. (b) Electrical outputs of the sensor under cyclic 0-100 kPa pressure, showing its continuous insensitivity to pressure.

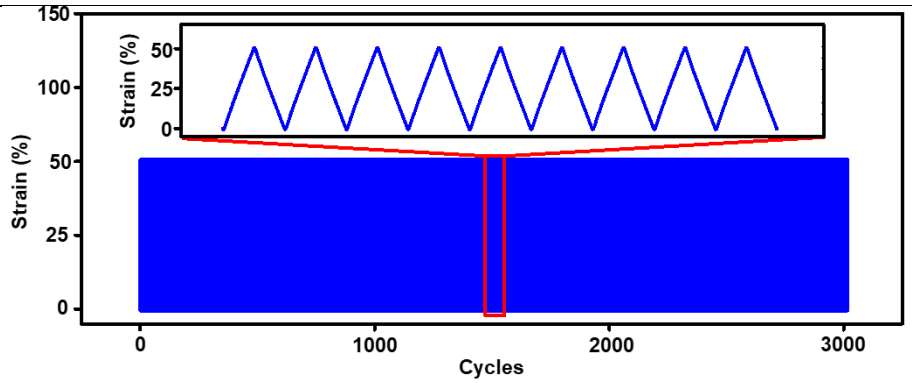

Figure 6-S11. Mechanical performance of PBIS-300 under 0-50 % loading-uploading strain for 3000 cycles, showing the remarkable mechanical durability of the sensor.

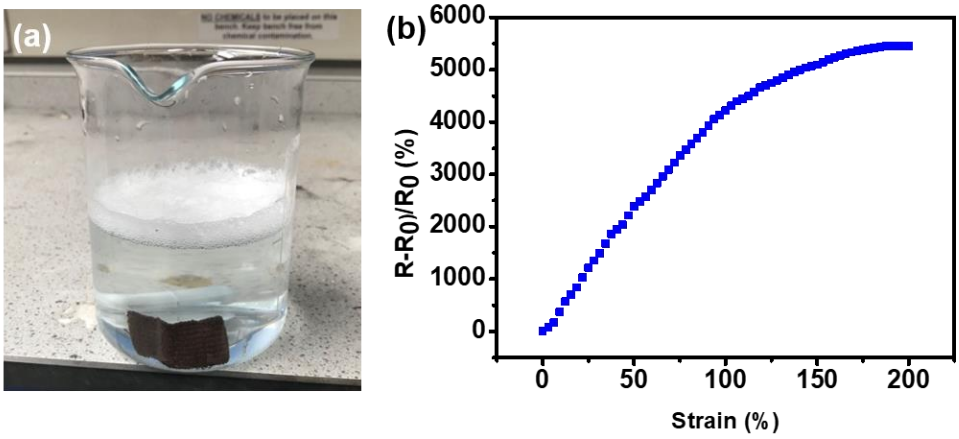

Figure 6-S12. The PBIS-300 with washing process and the relative resistance response to applied tensile strain after washing. (a) The sensor washed with laundry liquid in room temperature for 30 mins. (b) The calibration of the sensor after washing, maintaining remarkable sensitivity even with a slight decrease.

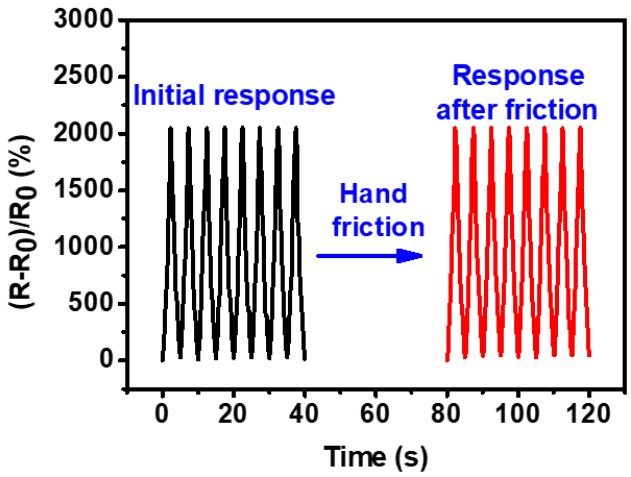

Figure 6-S13. The electrical signals of the PBIS-300 before and after hand friction.

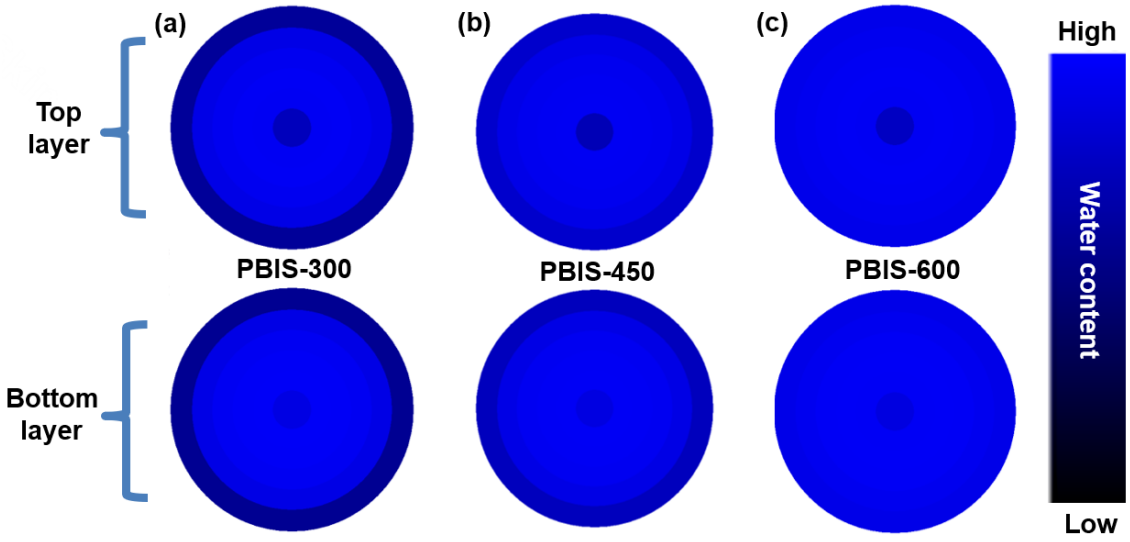

Figure 6-S14. Moisture permeability of PBIS sensors. (a) The water footprint of the top and bottom layers of PBIS-300. (b) The water footprint of the top and bottom layers of PBIS-450. (c) The water footprint of the top and bottom layers of PBIS-600.

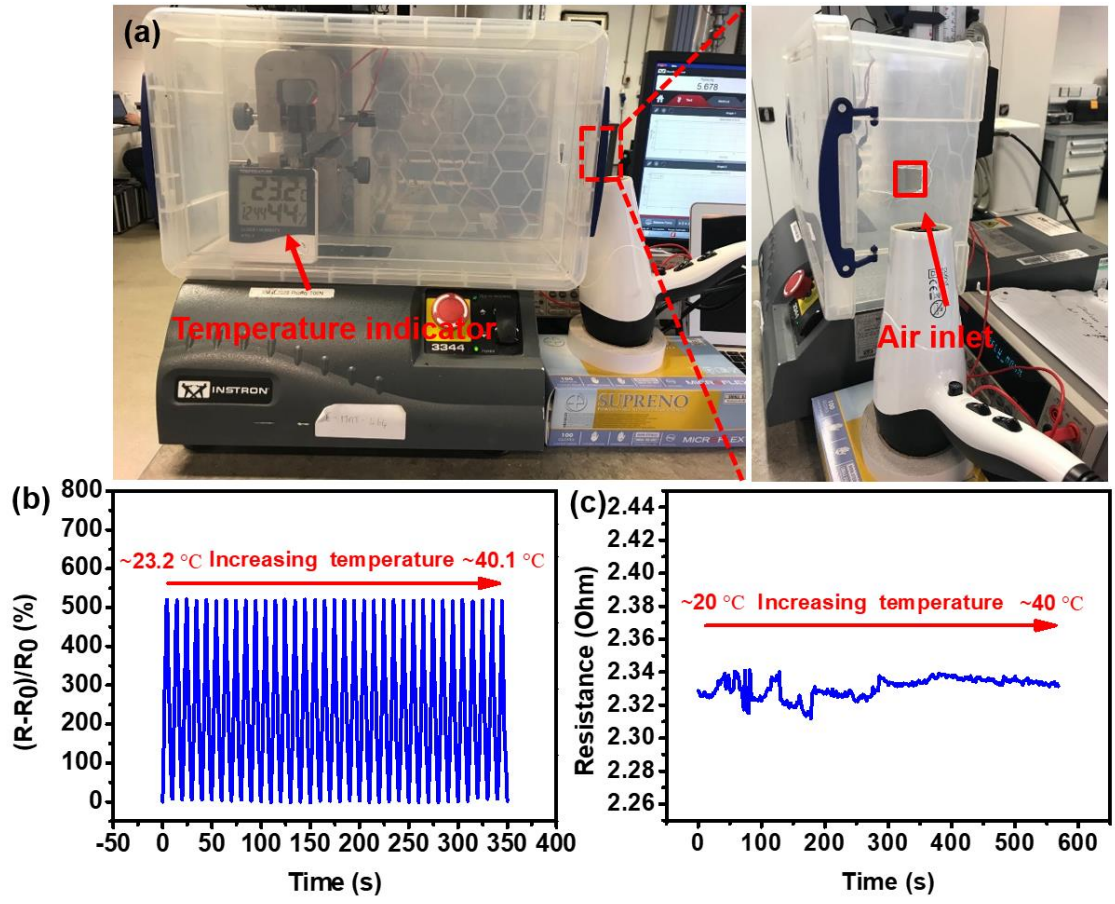

Figure 6-S15. The temperature dependence of PBIS-300 and copper-deposited yarn. (a) The

image of a self-built device for the evaluation of temperature dependence of the sensor. The device contains a box matched with a mechanical instrument, and a temperature indicator inside the box, as well as a hairdryer alongside the box to enhance temperature in the box. (b) The relative resistance changes of PBIS-300 with 10% cyclic strain from ~23.2°C (room condition) to ~40.1°C, showing good stability of the sensor in different temperatures. (c) The temperature dependence of a copper-deposited yarn accomplished in an oven, showing its good electrical stability within a limited temperature range.

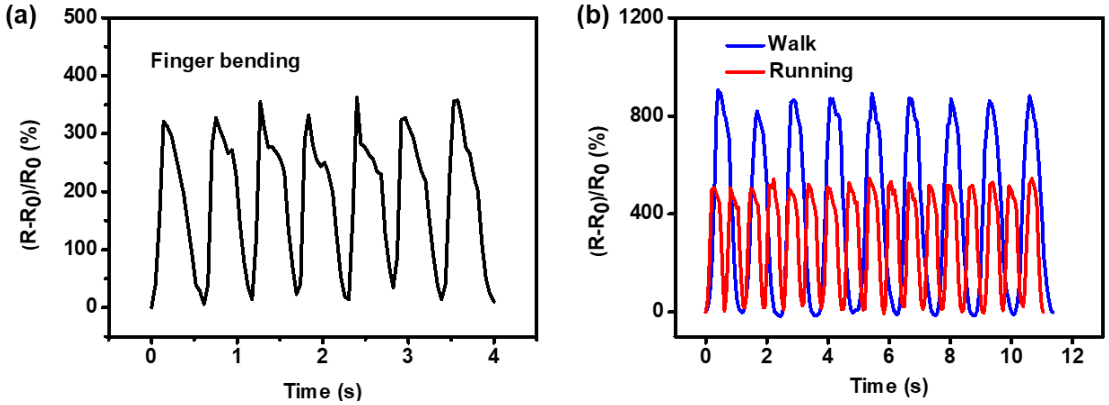

Figure 6-S16. Applications of PBIS-300. (a) Signals of index finger bending of the sensor. (b) Electrical output during running by attaching the sensor to the arm joint.

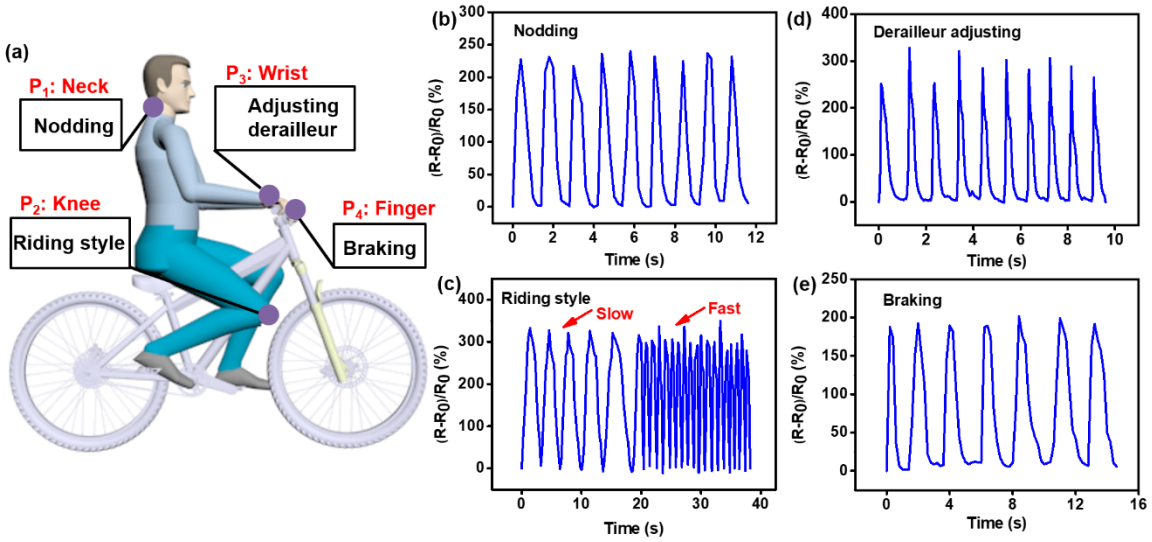

Figure 6-S17. Applications of PBIS-300 in monitoring the motions of a cyclist. (a) Overview of the body locations to address detection. (b) The relative resistance changes of the sensor during nodding. (c) Signals generated from different-speed riding. (d) Electrical response to adjusting derailleur by attaching the sensor to the middle finger. e) Signals of the sensor during braking.

The sensor is assembled onto locations of the neck, wrist, middle finger and knee joint of a bike rider respectively (Figure 6-S16a). The electrical output (Figure 6-S16b) induced by nodding during the acceleration process is highly coincident with the cycling state. Also, the riding style and accurate riding speed can be shown by collecting the electrical signals of the sensor on the knee joint (Figure 6-S16c). Besides, motions of adjusting derailleur and braking during bicycling are also monitored by the sensor. Figure 6-S16d and Figure 6-S16e show the signals generated from the actions of regulating derailleur and braking respectively, which reveals huge possibilities in movement monitoring and man-machine interaction.

Table 6-S1. The linear fitting results of PBIS sensors

Sample	Strain Range (%)	GF	R^2 (%)
PBIS-300	0-100	49.5	99.5
	100-150	23.7	99.3
	150-200	6.9	86.5
PBIS-450	0-100	40.1	99.7
	100-150	23.9	99.6
	150-200	4.0	79.7
PBIS-600	0-75	28.3	99.7
	75-150	18.4	99.9
	150-200	4.5	83.6

Chapter 7
Conclusions and Perspectives

7.1 Conclusions

In summary, this work has investigated fibre-based wearable sensors for monitoring human health and activities, concerning fibre material functionalization by carbonisation, PADM, and in situ oxidation, device fabrication through knitting, weaving, and embroidery, and application demonstrations in body area sensing networks. It aims to improve performance of fibre-based wearable sensors in aspects such as wearing comfort, washability, sensitivity and sensing range, sensing reliability in complicated and volatile wearable microclimates and interfaces. The developed sensors with remarkable wearability and sensing performance have exhibited huge potential in full-range body sensing networks for motion detection and health management.

(1) The fabrication and evaluation of a breathable pressure sensor made with carbonized hemp fabrics for the application of monitoring human health and activities.

By taking advantage of the high resilience of hemp fibres, the encapsulation-free sensor owns high permeability to air, water vapour and moisture. It also extends its sensing limit to very low pressure by avoiding the use of an encapsulation layer. The high permeability significantly improves wearing comfort, in contrast to the conventional sensors which bring about skin irritation for long-term wearing. It reports a scientific understanding of achieving both sensing performance and wearing comfort of wearable pressure sensors. The sensor also reveals outstanding sensing performance including high sensitivity, broad sensing range, quick response and splendid durability, which can detect many motion and health signals such as

speak, blowing, wrist pulse, walking and running, etc. This demonstration shows the sensor shows great prospects in future healthcare.

(2) Development of a strategy for a highly sensitive stretchable strain sensor by carbonisation and PAMD based on a piece of cost-effective linen fabric.

Unlike conventional sensors with one layer of sensing elements, the multi-functionalized fabric sensor has two layers of active materials (i.e., carbonized fibre and copper particles). The assembling of copper on the fabric can significantly enhance both sensitivity (GF~3557.6 in the strain range from 0 to 48%, GF~47.8 in the strain range from 48% to 150%) and stretchability up to the strain of 300%, which is superior to the sensor made with pure CF (Stretchability up to the strain of 96% with the GF~23.0). The sensor is capable of perceiving many motions in real time such as coughing, speaking, and wrist bending, etc. A healthcare system is also demonstrated based on the sensor and a deep learning network, which reveals the ability to monitor and distinguish normal breath, tachypnea, tachypnea along with cough with high accuracy. This work paves a new route to increase the stretchability and sensitivity of wearable strain sensors by utilising two active sensing elements.

(3) Strategy establishment for the fabrication of high-performance flexible humidity sensors based on a piece of cotton fabric through carbonisation and in situ oxidation.

By changing carbonisation temperature and oxidation time, the initial resistance and sensitivity of the fabric sensor can be controlled. It also finds that the sensitivity highly depends on the humidity-response functional groups on the fibre surface, which is induced by an oxidation process. Unlike conventional humidity sensors with a non-integrated combination, the sensor

reveals outstanding washability and splendid reliability by taking advantage of its free-standing structure. On the other hand, the free-standing structure endows the sensor with an insensitive response to many mechanical inputs such as bending and compression. It shows huge application capacity in remotely monitoring and identifying body motions by integrating with an artificial recurrent neural network. Particularly, the concept of developing humidity sensors through carbonizing fabrics is applicative to cellulose (e.g., linen, hemp, viscose, etc.) and silk (e.g., cocoon and spider silk) fabrics, as well as many carbonatable polymers. This works reports a new-concept humidity sensing approach by controlling the functional groups at molecular level, which addresses the huge challenges (wettability, washability, sensing reliability) of wearable humidity sensors.

(4) Development of a pressure and bending insensitive, stretchable strain sensor based on PAMD and a novel embroidery technique.

The sensor shows both high sensitivity and broad sensing range. Benefiting from its all fibre-based structure, the fabric sensor also depicts high permeability to water, water vapour and moisture, ensuring a pleasant wearing microenvironment between human and the sensor. The sensor with fast response, and durability, as well as high sensitivity (GF=49.5) and prominent linearity (R^2=0.995) throughout a broad detection range (0-100% strain), is successfully demonstrated in full-range body sensing networks for monitoring many body movements. Notably, the novel embroidery construction could be rapidly extended to almost any conductive and elastic yarns, paving a new way for the low-cost and scalable fabrication of high-performance, encapsulation-free, bending and pressure insensitive strain sensors. More importantly, the concept of developing unimodal sensor could rapidly arouse much attention in the research of wearables.

7.2 Major Contributions of the Research

1) A carbonized hemp-based pressure sensor was developed for the application of detecting body area pressure, which shows high sensing performance and broad sensing range, as well as good permeability to air, water vapour and moisture. This work has been published in Chemical Engineering Journal. (DOI: 10.1016/j.cej.2020.126191)

2) A highly sensitive stretchable strain sensor made with multi-functionalization (carbonisation and copper deposition) was fabricated for the detection of body movements and vital signals, demonstrating an effective approach to improve the sensitivity and stretchability of strain sensors. This work has been published in Chemical Engineering Journal. (DOI: 10.1016/j.cej.2021.130869)

3) A free-standing fabric humidity sensor was reported through carbonisation and in situ oxidation, endowing it with washability, tunable initial resistance and sensitivity, as well as insensitivity to many mechanical inputs. It shows great potential in health and activity monitoring by catching body humidity. This work was submitted to Nature Communications.

4) A high-performance stretchable strain sensor with insensitivity to bending and compression was produced by stitching copper-deposited yarns into elastic networks via an embroidery machine. It can detect almost any body movement serving as a full-range body sensing network. This work was published in Advanced Functional Materials. (DOI: 10.1002/adfm.202007622).

5) A critical review titled “Functionalized fibre-based strain sensors: pathway to next-generation wearable electronics” summarizes the latest advances in functionalization and device fabrication of fibre materials towards applications in fibre-based wearable strain sensors. It describes the approaches for preparing conductive fibres such as spinning, surface modification, and structural transformation. It also introduces the fabrication and sensing

mechanisms of state-of-the-art sensors, and analyses their merits and demerits. The applications towards motion detection, healthcare, man-machine interaction, future entertainment, and multifunctional sensing are summarized with typical examples. It finally critically analyses tough challenges and future remarks of fibre-based strain sensors, aiming to implement them in real applications. This work was published in Nano-Micro Letters. (https://doi.org/10.1007/s40820-022-00806-8)

7.3 Limitation

Due to time limitation especially the campus shutdown during the covid-19 epidemic, there are serval limitations in the thesis, which is listed as follows.

1) It lacks theoretically mechanical models of carbonized hemp fibre to verify the high resilience of the carbonized hemp-based pressure sensor.

2) The response to tensile strain, bending and compression of the carbonized pressure sensor is not investigated.

3) Visual and intelligent platform for observing and analyzing body vital signals is not explored in the work.

7.4 Perspectives

Even though some high-performance fibre-based wearable sensors are fabricated and demonstrated in the thesis, there are many challenges in this research area. Future researchers may consider the following direction:

1) Developing a highly stable sensor that detects target inputs without interference from complicated and volatile wearable microenvironments and interfaces.

2) Integrating many sensing functionalities together implements multi-objective detection such as humidity and strain sensing, pressure and temperature sensing, moisture and twist sensing, etc.

3) Endowing wearable sensing devices with additional functionalities, such as a sensor with heating, cooling, and wicking feature, etc.

References

1. C. Tan, Z. Dong, Y. Li, H. Zhao, X. Huang, Z. Zhou, J.-W. Jiang, Y.-Z. Long, P. Jiang and T.-Y. Zhang, *Nature Communications*, 2020, **11**, 1-10.
2. T. Yamada, Y. Hayamizu, Y. Yamamoto, Y. Yomogida, A. Izadi-Najafabadi, D. N. Futaba and K. Hata, *Nature Nanotechnology*, 2011, **6**, 296.
3. C. M. Boutry, Y. Kaizawa, B. C. Schroeder, A. Chortos, A. Legrand, Z. Wang, J. Chang, P. Fox and Z. Bao, *Nature Electronics*, 2018, **1**, 314.
4. C. Pang, G.-Y. Lee, T.-i. Kim, S. M. Kim, H. N. Kim, S.-H. Ahn and K.-Y. Suh, *Nature materials*, 2012, **11**, 795-801.
5. R. Yin, D. Wang, S. Zhao, Z. Lou and G. Shen, *Advanced Functional Materials*, 2021, **31**, 2008936.
6. H. Souri, H. Banerjee, A. Jusufi, N. Radacsi, A. A. Stokes, I. Park, M. Sitti and M. Amjadi, *Advanced Intelligent Systems*, 2020, **2**, 2000039.
7. S. Gong, L. W. Yap, Y. Zhu, B. Zhu, Y. Wang, Y. Ling, Y. Zhao, T. An, Y. Lu and W. Cheng, *Advanced Functional Materials*, 2020, **30**, 1910717.
8. S. Z. Homayounfar and T. L. Andrew, *SLAS TECHNOLOGY: Translating Life Sciences Innovation*, 2020, **25**, 9-24.
9. X. Liao, W. Wang, L. Wang, K. Tang and Y. Zheng, *ACS applied materials & interfaces*, 2018, **11**, 2431-2440.
10. Z. Liu, T. Zhu, J. Wang, Z. Zheng, Y. Li, J. Li and Y. Lai, *Nano-Micro Letters*, 2022, **14**, 1-39.
11. A. D. La Rosa and S. A. Grammatikos, *Fibers*, 2019, **7**, 101.
12. T. Jia, Y. Wang, Y. Dou, Y. Li, M. Jung de Andrade, R. Wang, S. Fang, J. Li, Z. Yu and R. Qiao, *Advanced Functional Materials*, 2019, **29**, 1808241.

13. A. Koeppel and C. Holland, *ACS Biomaterials Science & Engineering*, 2017, **3**, 226-237.

14. C. D. Delhom, B. Kelly and V. Martin, in *Cotton fiber: Physics, chemistry and biology*, Springer, 2018, pp. 41-73.

15. K. Millington and J. Rippon, in *Structure and properties of high-performance fibers*, Elsevier, 2017, pp. 367-408.

16. H. Zhang, Z. Zhong and L. Feng, *International Journal of Simulation Systems, Science & Technology*, 2016, **17**, 18.11-18.15.

17. Y. Lu, M. Tian, X. Sun, N. Pan, F. Chen, S. Zhu, X. Zhang and S. Chen, *Composites Part A: Applied Science and Manufacturing*, 2019, **117**, 202-210.

18. Y. Chen, B. Xu, J. Gong, J. Wen, T. Hua, C.-W. Kan and J. Deng, *ACS Applied Materials & Interfaces*, 2018, **11**, 2120-2129.

19. Y. Liu, S. Shang, S. Mo, P. Wang and H. Wang, *International Journal of Precision Engineering and Manufacturing-Green Technology*, 2020, 1-24.

20. B. Choi, J. Lee, H. Han, J. Woo, K. Park, J. Seo and T. Lee, *ACS Applied Materials & Interfaces*, 2018, **10**, 36094-36101.

21. Y. Gao, G. Yu, T. Shu, Y. Chen, W. Yang, Y. Liu, J. Long, W. Xiong and F. Xuan, *Advanced Materials Technologies*, 2019, **4**, 1900504.

22. H. Hong, J. Hu and X. Yan, *ACS Applied Materials & Interfaces*, 2019, **11**, 27318-27326.

23. Y. Yu, C. Yan and Z. Zheng, *Advanced Materials*, 2014, **26**, 5508-5516.

24. Y. Li, H. Zhu, F. Shen, J. Wan, X. Han, J. Dai, H. Dai and L. Hu, *Advanced Functional Materials*, 2014, **24**, 7366-7372.

25. B. Fang, L. Peng, Z. Xu and C. Gao, *ACS Nano*, 2015, **9**, 5214-5222.

26. N. He, W. Shan, J. Wang, Q. Pan, J. Qu, G. Wang and W. Gao, *Journal of Materials Chemistry A*, 2019, **7**, 6869-6876.

27. J.-Y. Kim, W. Lee, Y. H. Kang, S. Y. Cho and K.-S. Jang, *Carbon*, 2018, **133**, 293-299.

28. K. Jost, D. P. Durkin, L. M. Haverhals, E. K. Brown, M. Langenstein, H. C. De Long, P. C. Trulove, Y. Gogotsi and G. Dion, *Advanced Energy Materials*, 2015, **5**, 1401286.

29. Y. Lu, J. Jiang, S. Yoon, K.-S. Kim, J.-H. Kim, S. Park, S.-H. Kim and L. Piao, *ACS Applied Materials & Interfaces*, 2018, **10**, 2093-2104.

30. Y. Zhao, D. Dong, S. Gong, L. Brassart, Y. Wang, T. An and W. Cheng, *Advanced Electronic Materials*, 2019, **5**, 1800462.

31. S. Ryu, P. Lee, J. B. Chou, R. Xu, R. Zhao, A. J. Hart and S.-G. Kim, *ACS Nano*, 2015, **9**, 5929-5936.

32. S. Seyedin, J. M. Razal, P. C. Innis, A. Jeiranikhameneh, S. Beirne and G. G. Wallace, *ACS Applied Materials & Interfaces*, 2015, **7**, 21150-21158.

33. J. Zhou, X. Xu, Y. Xin and G. Lubineau, *Advanced Functional Materials*, 2018, **28**, 1705591.

34. Z. He, G. Zhou, J.-H. Byun, S.-K. Lee, M.-K. Um, B. Park, T. Kim, S. B. Lee and T.-W. Chou, *Nanoscale*, 2019, **11**, 5884-5890.

35. Z. Tang, S. Jia, F. Wang, C. Bian, Y. Chen, Y. Wang and B. Li, *ACS Applied Materials & Interfaces*, 2018, **10**, 6624-6635.

36. S. J. Choi, H. Yu, J. S. Jang, M. H. Kim, S. J. Kim, H. S. Jeong and I. D. Kim, *Small*, 2018, **14**, 1703934.

37. G.-F. Yu, J.-T. Li, W. Pan, X.-X. He, Y.-J. Zhang, M.-G. Gong, M. Yu, Z.-M. Zhang and Y.-Z. Long, *Composites Science and Technology*, 2017, **139**, 1-7.

38. Y. Shang, X. He, Y. Li, L. Zhang, Z. Li, C. Ji, E. Shi, P. Li, K. Zhu and Q. Peng, *Advanced Materials*, 2012, **24**, 2896-2900.

39. O. Y. Kweon, S. J. Lee and J. H. Oh, *NPG Asia Materials*, 2018, **10**, 540.

40. F. Liu, Y. Dong, R. Shi, E. Wang, Q. Ni and Y. Fu, *Materials Today Communications*, 2020, **24**, 100909.

41. S. Yu, X. Wang, H. Xiang, L. Zhu, M. Tebyetekerwa and M. Zhu, *Carbon*, 2018, **140**, 1-9.

42. Z. He, J.-H. Byun, G. Zhou, B.-J. Park, T.-H. Kim, S.-B. Lee, J.-W. Yi, M.-K. Um and T.-W. Chou, *Carbon*, 2019, **146**, 701-708.

43. L. Wang, Y. Chen, L. Lin, H. Wang, X. Huang, H. Xue and J. Gao, *Chemical Engineering Journal*, 2019, **362**, 89-98.

44. Y. Wang, J. Hao, Z. Huang, G. Zheng, K. Dai, C. Liu and C. Shen, *Carbon*, 2018, **126**, 360-371.

45. B. Sun, Y.-Z. Long, S.-L. Liu, Y.-Y. Huang, J. Ma, H.-D. Zhang, G. Shen and S. Xu, *Nanoscale*, 2013, **5**, 7041-7045.

46. J. Zheng, X. Yan, M.-M. Li, G.-F. Yu, H.-D. Zhang, W. Pisula, X.-X. He, J.-L. Duvail and Y.-Z. Long, *Nanoscale Research Letters*, 2015, **10**, 475.

47. Q. Liu, M. Zhang, L. Huang, Y. Li, J. Chen, C. Li and G. Shi, *ACS Nano*, 2015, **9**, 12320-12326.

48. J. R. Bautista-Quijano, P. Pötschke, H. Brünig and G. Heinrich, *Polymer*, 2016, **82**, 181-189.

49. M. Zhang, C. Wang, Q. Wang, M. Jian and Y. Zhang, *ACS Applied Materials & Interfaces*, 2016, **8**, 20894-20899.

50. Y.-Q. Li, P. Huang, W.-B. Zhu, S.-Y. Fu, N. Hu and K. Liao, *Scientific Reports*, 2017, **7**, 1-7.

51. B. Liang, Z. Lin, W. Chen, Z. He, J. Zhong, H. Zhu, Z. Tang and X. Gui, *Nanoscale*, 2018, **10**, 13599-13606.

52. C. Wang, X. Li, E. Gao, M. Jian, K. Xia, Q. Wang, Z. Xu, T. Ren and Y. Zhang, *Advanced Materials*, 2016, **28**, 6640-6648.

53. L. Zhu, X. Zhou, Y. Liu and Q. Fu, *ACS Applied Materials & Interfaces*, 2019, **11**, 12968-12977.

54. S. Chen, Z. Lou, D. Chen, K. Jiang and G. Shen, *Advanced Materials Technologies*, 2016, **1**, 1600136.

55. X. Liao, Q. Liao, Z. Zhang, X. Yan, Q. Liang, Q. Wang, M. Li and Y. Zhang, *Advanced Functional Materials*, 2016, **26**, 3074-3081.

56. Z. Liu, D. Qi, G. Hu, H. Wang, Y. Jiang, G. Chen, Y. Luo, X. J. Loh, B. Liedberg and X. Chen, *Advanced Materials*, 2018, **30**, 1704229.

57. P. Li, Y. Zhang and Z. Zheng, *Advanced Materials*, 2019, **31**, 1902987.

58. R. Guo, Y. Yu, J. Zeng, X. Liu, X. Zhou, L. Niu, T. Gao, K. Li, Y. Yang and F. Zhou, *Advanced Science*, 2015, **2**, 1400021.

59. C. Zhu, X. Guan, X. Wang, Y. Li, E. Chalmers and X. Liu, *Advanced Materials Interfaces*, 2019, **6**, 1801547.

60. J. Eom, R. Jaisutti, H. Lee, W. Lee, J.-S. Heo, J.-Y. Lee, S. K. Park and Y.-H. Kim, *ACS Applied Materials & Interfaces*, 2017, **9**, 10190-10197.

61. J. Lee, S. Shin, S. Lee, J. Song, S. Kang, H. Han, S. Kim, S. Kim, J. Seo and D. Kim, *ACS Nano*, 2018, **12**, 4259-4268.

62. Z. Lou, S. Chen, L. Wang, K. Jiang and G. Shen, *Nano Energy*, 2016, **23**, 7-14.

63. X. Wang, B. Ding, J. Yu and M. Wang, *Journal of Materials Chemistry*, 2011, **21**, 16231-16238.

64. X. Wu, Y. Han, X. Zhang and C. Lu, *ACS Applied Materials & Interfaces*, 2016, **8**, 9936-9945.

65. Y. Cheng, R. Wang, J. Sun and L. Gao, *Advanced Materials*, 2015, **27**, 7365-7371.

66. J. Zhong, Q. Zhong, Q. Hu, N. Wu, W. Li, B. Wang, B. Hu and J. Zhou, *Advanced Functional Materials*, 2015, **25**, 1798-1803.

67. X. Wang, Y. Qiu, W. Cao and P. Hu, *Chemistry of Materials*, 2015, **27**, 6969-6975.

68. X. Li, H. Hu, T. Hua, B. Xu and S. Jiang, *Nano Research*, 2018, **11**, 5799-5811.

69. X. Li, P. Sun, L. Fan, M. Zhu, K. Wang, M. Zhong, J. Wei, D. Wu, Y. Cheng and H. Zhu, *Scientific Reports*, 2012, **2**, 395.

70. X. Liu, C. Tang, X. Du, S. Xiong, S. Xi, Y. Liu, X. Shen, Q. Zheng, Z. Wang and Y. Wu, *Materials Horizons*, 2017, **4**, 477-486.

71. T. Lee, W. Lee, S. W. Kim, J. J. Kim and B. S. Kim, *Advanced Functional Materials*, 2016, **26**, 6206-6214.

72. N. Karim, S. Afroj, S. Tan, P. He, A. Fernando, C. Carr and K. S. Novoselov, *ACS Nano*, 2017, **11**, 12266-12275.

73. S. He, B. Xin, Z. Chen and Y. Liu, *Cellulose*, 2018, **25**, 3691-3701.

74. J. Ren, C. Wang, X. Zhang, T. Carey, K. Chen, Y. Yin and F. Torrisi, *Carbon*, 2017, **111**, 622-630.

75. Y.-F. Fu, Y.-Q. Li, Y.-F. Liu, P. Huang, N. Hu and S.-Y. Fu, *ACS Applied Materials & Interfaces*, 2018, **10**, 35503-35509.

76. L. Xu, Z. Liu, H. Zhai, X. Chen, R. Sun, S. Lyu, Y. Fan, Y. Yi, Z. Chen, L. Jin, J. Zhang, Y. Li and T. T. Ye, *ACS Applied Materials & Interfaces*, 2020, **12**, 13265-13274.

77. Z. Yang, Y. Pang, X.-l. Han, Y. Yang, J. Ling, M. Jian, Y. Zhang, Y. Yang and T.-L. Ren, *ACS Nano*, 2018, **12**, 9134-9141.

78. G. Cai, M. Yang, Z. Xu, J. Liu, B. Tang and X. Wang, *Chemical Engineering Journal*, 2017, **325**, 396-403.

79. M. S. Sadi, J. Pan, A. Xu, D. Cheng, G. Cai and X. Wang, *Cellulose*, 2019, **26**, 7569-7579.

80. C. Zhang, G. Zhou, W. Rao, L. Fan, W. Xu and J. Xu, *Cellulose*, 2018, **25**, 4859-4870.

81. H. Liu, Q. Li, Y. Bu, N. Zhang, C. Wang, C. Pan, L. Mi, Z. Guo, C. Liu and C. Shen, *Nano Energy*, 2019, **66**, 104143.

82. H. Jiyong, Z. Xiaofeng, L. Guohao, Y. Xudong and D. Xin, *Autex Research Journal*, 2016, **16**, 7-12.

83. L.-Q. Tao, K.-N. Zhang, H. Tian, Y. Liu, D.-Y. Wang, Y.-Q. Chen, Y. Yang and T.-L. Ren, *ACS Nano*, 2017, **11**, 8790-8795.

84. J. Zhu, N. Zhang, Y. Yin, B. Xu, W. Zhang and C. Wang, *Advanced Materials Interfaces*, 2022, **9**, 2101498.

85. S. Y. Cho, Y. S. Yun, S. Lee, D. Jang, K.-Y. Park, J. K. Kim, B. H. Kim, K. Kang, D. L. Kaplan and H.-J. Jin, *Nature Communications*, 2015, **6**, 7145.

86. C. Wang, M. Zhang, K. Xia, X. Gong, H. Wang, Z. Yin, B. Guan and Y. Zhang, *ACS Applied Materials & Interfaces*, 2017, **9**, 13331-13338.

87. M. Zhang, C. Wang, H. Wang, M. Jian, X. Hao and Y. Zhang, *Advanced Functional Materials*, 2017, **27**, 1604795.

88. Q. Wang, M. Jian, C. Wang and Y. Zhang, *Advanced Functional Materials*, 2017, **27**, 1605657.

89. C. Wang, K. Xia, M. Jian, H. Wang, M. Zhang and Y. Zhang, *Journal of Materials Chemistry C*, 2017, **5**, 7604-7611.

90. S. Chen, Y. Song, D. Ding, Z. Ling and F. Xu, *Advanced Functional Materials*, 2018, **28**, 1802547.

91. K. Kim, M. Jung, S. Jeon and J. Bae, *Smart Materials and Structures*, 2019, **28**, 065019.

92. Y. Li, Y. A. Samad and K. Liao, *Journal of Materials Chemistry A*, 2015, **3**, 2181-2187.

93. G. Zhou, J.-H. Byun, Y. Oh, B.-M. Jung, H.-J. Cha, D.-G. Seong, M.-K. Um, S. Hyun and T.-W. Chou, *ACS Applied Materials & Interfaces*, 2017, **9**, 4788-4797.

94. X. Huang, B. Li, L. Wang, X. Lai, H. Xue and J. Gao, *ACS Applied Materials & Interfaces*, 2019, **11**, 24533-24543.

95. J. Wu, Y.-M. Sun, Z. Wu, X. Li, N. Wang, K. Tao and G. P. Wang, *ACS Applied Materials & Interfaces*, 2019, **11**, 4242-4251.

96. X. Zhao, L.-Y. Wang, C.-Y. Tang, X.-J. Zha, Y. Liu, B.-H. Su, K. Ke, R.-Y. Bao, M.-B. Yang and W. Yang, *ACS Nano*, 2020, **14**, 8793-8805.

97. L. Lu, C. Jiang, G. Hu, J. Liu and B. Yang, *Advanced Materials*, 2021, **33**, 2100218.

98. L. Xu, H. Zhai, X. Chen, Y. Liu, M. Wang, Z. Liu, M. Umar, C. Ji, Z. Chen and L. Jin, *Chemical Engineering Journal*, 2021, **412**, 128639.

99. S. Jang, J. Kim, D. W. Kim, J. W. Kim, S. Chun, H. J. Lee, G.-R. Yi and C. Pang, *ACS Applied Materials & Interfaces*, 2019, **11**, 15079-15087.

100. W. S. Lee, D. Kim, B. Park, H. Joh, H. K. Woo, Y. K. Hong, T. i. Kim, D. H. Ha and S. J. Oh, *Advanced Functional Materials*, 2019, **29**, 1806714.

101. J. Wu, Z. Ma, Z. Hao, J. T. Zhang, P. Sun, M. Zhang, Y. Liu, Y. Cheng, Y. Li and B. Zhong, *ACS Applied Nano Materials*, 2019, **2**, 750-759.

102. J. Ryu, J. Kim, J. Oh, S. Lim, J. Y. Sim, J. S. Jeon, K. No, S. Park and S. Hong, *Nano Energy*, 2019, **55**, 348-353.

103. Y. Wang, L. Wang, T. Yang, X. Li, X. Zang, M. Zhu, K. Wang, D. Wu and H. Zhu, *Advanced Functional Materials*, 2014, **24**, 4666-4670.

104. X. Li, R. Zhang, W. Yu, K. Wang, J. Wei, D. Wu, A. Cao, Z. Li, Y. Cheng and Q. Zheng, *Scientific Reports*, 2012, **2**, 870.

105. B. Yin, Y. Wen, T. Hong, Z. Xie, G. Yuan, Q. Ji and H. Jia, *ACS Applied Materials & Interfaces*, 2017, **9**, 32054-32064.

106. F. Guo, X. Cui, K. Wang and J. Wei, *Nanoscale*, 2016, **8**, 19352-19358.

107. J. J. Park, W. J. Hyun, S. C. Mun, Y. T. Park and O. O. Park, *ACS Applied Materials & Interfaces*, 2015, **7**, 6317-6324.

108. M. Li, H. Li, W. Zhong, Q. Zhao and D. Wang, *ACS Applied Materials & Interfaces*, 2014, **6**, 1313-1319.

109. K. H. Kim, N. S. Jang, S. H. Ha, J. H. Cho and J. M. Kim, *Small*, 2018, **14**, 1704232.

110. H. Song, J. Zhang, D. Chen, K. Wang, S. Niu, Z. Han and L. Ren, *Nanoscale*, 2017, **9**, 1166-1173.

111. X. Liao, Z. Zhang, Z. Kang, F. Gao, Q. Liao and Y. Zhang, *Materials Horizons*, 2017, **4**, 502-510.

112. H. Zhao, Y. Zhang, P. D. Bradford, Q. Zhou, Q. Jia, F.-G. Yuan and Y. Zhu, *Nanotechnology*, 2010, **21**, 305502.

113. A. Lekawa-Raus, K. K. Koziol and A. H. Windle, *ACS Nano*, 2014, **8**, 11214-11224.

114. Q. Liao, M. Mohr, X. Zhang, Z. Zhang, Y. Zhang and H.-J. Fecht, *Nanoscale*, 2013, **5**, 12350-12355.

115. J.-H. Pu, X.-J. Zha, M. Zhao, S. Li, R.-Y. Bao, Z.-Y. Liu, B.-H. Xie, M.-B. Yang, Z. Guo and W. Yang, *Nanoscale*, 2018, **10**, 2191-2198.

116. M. Hempel, D. Nezich, J. Kong and M. Hofmann, *Nano Letters*, 2012, **12**, 5714-5718.

117. J. Ma, P. Wang, H. Chen, S. Bao, W. Chen and H. Lu, *ACS Applied Materials & Interfaces*, 2019, **11**, 8527-8536.

118. C. Yan, J. Wang, W. Kang, M. Cui, X. Wang, C. Y. Foo, K. J. Chee and P. S. Lee, *Advanced materials*, 2014, **26**, 2022-2027.

119. X. Xiao, L. Yuan, J. Zhong, T. Ding, Y. Liu, Z. Cai, Y. Rong, H. Han, J. Zhou and Z. L. Wang, *Advanced Materials*, 2011, **23**, 5440-5444.

120. M. Amjadi, A. Pichitpajongkit, S. Lee, S. Ryu and I. Park, *ACS Nano*, 2014, **8**, 5154-5163.

121. S. Seyedin, P. Zhang, M. Naebe, S. Qin, J. Chen, X. Wang and J. M. Razal, *Materials Horizons*, 2019, **6**, 219-249.

122. M. Amjadi, K. U. Kyung, I. Park and M. Sitti, *Advanced Functional Materials*, 2016, **26**, 1678-1698.

123. Z. Jing, Z. Guang-Yu and S. Dong-Xia, *Chinese Physics B*, 2013, **22**, 057701.

124. S. Zhu, J. H. So, R. Mays, S. Desai, W. R. Barnes, B. Pourdeyhimi and M. D. Dickey, *Advanced Functional Materials*, 2013, **23**, 2308-2314.

125. Y.-h. Wu, R.-m. Zhen, H.-z. Liu, S.-q. Liu, Z.-f. Deng, P.-p. Wang, S. Chen and L. Liu, *Journal of Materials Chemistry C*, 2017, **5**, 12483-12491.

126. F. Xu and Y. Zhu, *Advanced Materials*, 2012, **24**, 5117-5122.

127. A. Frutiger, J. T. Muth, D. M. Vogt, Y. Mengüç, A. Campo, A. D. Valentine, C. J. Walsh and J. A. Lewis, *Advanced Materials*, 2015, **27**, 2440-2446.

128. L. Chen, M. Lu, H. Yang, J. R. S. Avila, B. Shi, L. Ren, G. Wei, X. Liu and W. Yin, *ACS Nano*, 2020.

129. Z. Liu, K. Chen, A. Fernando, Y. Gao, G. Li, L. Jin, H. Zhai, Y. Yi, L. Xu and Y. Zheng, *Chemical Engineering Journal*, 2020, 126191.

130. Z. Li, M. Zhu, J. Shen, Q. Qiu, J. Yu and B. Ding, *Advanced Functional Materials*, 2019, 1908411.

131. Z. Zhao, Q. Huang, C. Yan, Y. Liu, X. Zeng, X. Wei, Y. Hu and Z. Zheng, *Nano Energy*, 2020, 104528.

132. X. Liu, D. Liu, J.-h. Lee, Q. Zheng, X. Du, X. Zhang, H. Xu, Z. Wang, Y. Wu and X. Shen, *ACS Applied Materials & Interfaces*, 2018, **11**, 2282-2294.

133. J. Ge, L. Sun, F. R. Zhang, Y. Zhang, L. A. Shi, H. Y. Zhao, H. W. Zhu, H. L. Jiang and S. H. Yu, *Advanced Materials*, 2016, **28**, 722-728.

134. J. Pan, M. Yang, L. Luo, A. Xu, B. Tang, D. Cheng, G. Cai and X. Wang, *ACS Applied Materials & Interfaces*, 2019, **11**, 7338-7348.

135. W. Root, T. Wright, B. Caven, T. Bechtold and T. Pham, *Polymers*, 2019, **11**, 784.

136. K. Kim, G. Song, C. Park and K.-S. Yun, *Sensors*, 2017, **17**, 2582.

137. S. Wang, H. Ning, N. Hu, Y. Liu, F. Liu, R. Zou, K. Huang, X. Wu and S. Weng, *Advanced Materials Interfaces*, 2020, **7**, 1901507.

138. S. Park, S. Ahn, J. Sun, D. Bhatia, D. Choi, K. S. Yang, J. Bae and J. J. Park, *Advanced Functional Materials*, 2019, **29**, 1808369.

139. J. Foroughi, G. M. Spinks, S. Aziz, A. Mirabedini, A. Jeiranikhameneh, G. G. Wallace, M. E. Kozlov and R. H. Baughman, *ACS Nano*, 2016, **10**, 9129-9135.

140. Y. Huang, S. V. Kershaw, Z. Wang, Z. Pei, J. Liu, Y. Huang, H. Li, M. Zhu, A. L. Rogach and C. Zhi, *Small*, 2016, **12**, 3393-3399.

141. S. Yang, C. Li, X. Chen, Y. Zhao, H. Zhang, N. Wen, Z. Fan and L. Pan, *ACS Applied Materials & Interfaces*, 2020, **12**, 19874-19881.

142. J. Xie, H. Long and M. Miao, *Smart Materials and Structures*, 2016, **25**, 105008.

143. O. Atalay, W. R. Kennon and M. D. Husain, *Sensors*, 2013, **13**, 11114-11127.

144. Y. Yang, L. Shi, Z. Cao, R. Wang and J. Sun, *Advanced Functional Materials*, 2019, **29**, 1807882.

145. S. Duan, Z. Wang, L. Zhang, J. Liu and C. Li, *Advanced Materials Technologies*, 2018, **3**, 1800020.

146. J. H. Lee, J. Kim, D. Liu, F. Guo, X. Shen, Q. Zheng, S. Jeon and J. K. Kim, *Advanced Functional Materials*, 2019, **29**, 1901623.

147. B. Wang, K. Yang, H. Cheng, T. Ye and C. Wang, *Chemical Engineering Journal*, 2020, 126393.

148. N. Gogurla, B. Roy, J.-Y. Park and S. Kim, *Nano Energy*, 2019, **62**, 674-681.

149. S. L. Zhang, Y. C. Lai, X. He, R. Liu, Y. Zi and Z. L. Wang, *Advanced Functional Materials*, 2017, **27**, 1606695.

150. S. Huang, B. Zhang, Z. Shao, L. He, Q. Zhang, J. Jie and X. Zhang, *Nano Letters*, 2020, **20**, 2478-2485.

151. O. Atalay, A. Atalay, J. Gafford, H. Wang, R. Wood and C. Walsh, *Advanced Materials Technologies*, 2017, **2**, 1700081.

152. Y. Wang, Y. Wang and Y. Yang, *Advanced Energy Materials*, 2018, **8**, 1800961.

153. L. Pan, G. Liu, W. Shi, J. Shang, W. R. Leow, Y. Liu, Y. Jiang, S. Li, X. Chen and R.-W. Li, *Nature Communications*, 2018, **9**, 1-10.

154. J. Lee, S. J. Ihle, G. S. Pellegrino, H. Kim, J. Yea, C.-Y. Jeon, H.-C. Son, C. Jin, D. Eberli and F. Schmid, *Nature Electronics*, 2021, **4**, 291-301.

155. H. Wu, Q. Liu, W. Du, C. Li and G. Shi, *ACS Applied Materials & Interfaces*, 2018, **10**, 3895-3901.

156. S. Niu, N. Matsuhisa, L. Beker, J. Li, S. Wang, J. Wang, Y. Jiang, X. Yan, Y. Yun and W. Burnett, *Nature Electronics*, 2019, **2**, 361-368.

157. R. Lin, H.-J. Kim, S. Achavananthadith, S. A. Kurt, S. C. Tan, H. Yao, B. C. Tee, J. K. Lee and J. S. Ho, *Nature Communications*, 2020, **11**, 1-10.

158. Y. J. Yun, J. Ju, J. H. Lee, S. H. Moon, S. J. Park, Y. H. Kim, W. G. Hong, D. H. Ha, H. Jang and G. H. Lee, *Advanced Functional Materials*, 2017, **27**, 1701513.

159. Y. Zhang, Y. Huang, X. Sun, Y. Zhao, X. Guo, P. Liu, C. Liu and Y. Zhang, *IEEE Sensors Journal*, 2020, **20**, 6450-6459.

160. S. Choi, K. Yoon, S. Lee, H. J. Lee, J. Lee, D. W. Kim, M. S. Kim, T. Lee and C. Pang, *Advanced Functional Materials*, 2019, **29**, 1905808.

161. M. Zhu, Z. Sun, Z. Zhang, Q. Shi, T. He, H. Liu, T. Chen and C. Lee, *Science Advances*, 2020, **6**, eaaz8693.

162. O. A. Araromi, M. A. Graule, K. L. Dorsey, S. Castellanos, J. R. Foster, W.-H. Hsu, A. E. Passy, J. J. Vlassak, J. C. Weaver and C. J. Walsh, *Nature*, 2020, **587**, 219-224.

163. S. Takamatsu, T. Lonjaret, E. Ismailova, A. Masuda, T. Itoh and G. G. Malliaras, *Advanced Materials*, 2016, **28**, 4485-4488.

164. C. B. Huang, S. Witomska, A. Aliprandi, M. A. Stoeckel, M. Bonini, A. Ciesielski and P. Samorì, *Advanced Materials*, 2019, **31**, 1804600.

165. T. Zhu, Y. Cheng, C. Cao, J. Mao, L. Li, J. Huang, S. Gao, X. Dong, Z. Chen and Y. Lai, *Chemical Engineering Journal*, 2020, **385**, 123912.

166. L. Jin, Y. Zheng, Z. Liu, J. Li, H. Zhai, Z. Chen and Y. Li, *ACS Applied Materials & Interfaces*, 2019.

167. K. Meng, J. Chen, X. Li, Y. Wu, W. Fan, Z. Zhou, Q. He, X. Wang, X. Fan and Y. Zhang, *Advanced Functional Materials*, 2019, **29**, 1806388.

168. R. Vishinkin and H. Haick, *Small*, 2015, **11**, 6142-6164.

169. H. Jin, T.-P. Huynh and H. Haick, *Nano Letters*, 2016, **16**, 4194-4202.

170. P. Shyamkumar, P. Rai, S. Oh, M. Ramasamy, R. Harbaugh and V. Varadan, *Electronics*, 2014, **3**, 504-520.

171. Y. Hu, J. Yang, Q. Jing, S. Niu, W. Wu and Z. L. Wang, *ACS Nano*, 2013, **7**, 10424-10432.

172. Y. Yang, H. Zhang, Z.-H. Lin, Y. S. Zhou, Q. Jing, Y. Su, J. Yang, J. Chen, C. Hu and Z. L. Wang, *ACS Nano*, 2013, **7**, 9213-9222.

173. T. Bu, T. Xiao, Z. Yang, G. Liu, X. Fu, J. Nie, T. Guo, Y. Pang, J. Zhao and F. Xi, *Advanced Materials*, 2018, **30**, 1800066.

174. A. Kos, V. Milutinović and A. Umek, *Future Generation Computer Systems*, 2019, **92**, 582-592.

175. J. A. Rogers, T. Someya and Y. Huang, *Science*, 2010, **327**, 1603-1607.

176. S. Chen, T. Huang, H. Zuo, S. Qian, Y. Guo, L. Sun, D. Lei, Q. Wu, B. Zhu and C. He, *Advanced Functional Materials*, 2018, **28**, 1870331.

177. M. Jian, K. Xia, Q. Wang, Z. Yin, H. Wang, C. Wang, H. Xie, M. Zhang and Y. Zhang, *Advanced Functional Materials*, 2017, **27**, 1606066.

178. S. J. Park, J. Kim, M. Chu and M. Khine, *Advanced Materials Technologies*, 2018, **3**, 1700158.

179. S. Gong, W. Schwalb, Y. Wang, Y. Chen, Y. Tang, J. Si, B. Shirinzadeh and W. Cheng, *Nature Communications*, 2014, **5**, 3132.

180. Y. Wei, S. Chen, X. Dong, Y. Lin and L. Liu, *Carbon*, 2017, **113**, 395-403.

181. Q. Sun, D. H. Kim, S. S. Park, N. Y. Lee, Y. Zhang, J. H. Lee, K. Cho and J. H. Cho, *Advanced Materials*, 2014, **26**, 4735-4740.

182. H. B. Yao, J. Ge, C. F. Wang, X. Wang, W. Hu, Z. J. Zheng, Y. Ni and S. H. Yu, *Advanced Materials*, 2013, **25**, 6692-6698.

183. S. Chen, Y. Song and F. Xu, *ACS Applied Materials & Interfaces*, 2018, **10**, 34646-34654.

184. E. A. Tansey and C. D. Johnson, *Advances in Physiology Education*, 2015, **39**, 139-148.

185. V. Kothari, Journal of Accounting and Economics, 2006, 41, 1-2.

186. T.-H. Chen, W.-P. Chen and M.-J. J. Wang, *Journal of Occupational and Environmental Hygiene*, 2014, **11**, 366-376.

187. K. Atkins and M. Thompson, *Journal of Exercise Science & Fitness*, 2011, **9**, 100-108.

188. J. Fan and L. Hunter, *Engineering Apparel Fabrics and Garments*, 2009, **1**, 201-250.

189. W. Zeng, L. Shu, Q. Li, S. Chen, F. Wang and X. M. Tao, *Advanced Materials*, 2014, **26**, 5310-5336.

190. K. L. Pickering, G. Beckermann, S. Alam and N. J. Foreman, *Composites Part A: Applied Science and Manufacturing*, 2007, **38**, 461-468.

191. A. Shahzad, *Journal of Composite Materials*, 2012, **46**, 973-986.

192. S. B. Yoon, G. S. Chai, S. K. Kang, J.-S. Yu, K. P. Gierszal and M. Jaroniec, *Journal of the American Chemical Society*, 2005, **127**, 4188-4189.

193. S. K. Kovur, K. Schenzel, E. Grimm and W. Diepenbrock, *BioResources*, 2008, **3**, 1081-1091.

194. K. L. Pickering, M. A. Efendy and T. M. Le, *Composites Part A: Applied Science and Manufacturing*, 2016, **83**, 98-112.

195. E. Öner, H. Atasağun, A. Okur, A. Beden and G. Durur, *Journal of the Textile Institute*, 2013, **104**, 699-707.

196. G. Supuren, N. Oglakcioglu, N. Ozdil and A. Marmarali, *Textile Research Journal*, 2011, **81**, 1320-1330.

197. S. Debnath and M. Madhusoothanan, Journal of Industrial Textile, 2010, **3**, 215-231.

198. S. Mondal and J. Hu, *Carbohydrate Polymers*, 2007, **67**, 282-287.

199. R. Aly, C. Shirley, B. Cunico and H. I. Maibach, *Journal of Investigative Dermatology*, 1978, **71**, 378-381.

200. R. Zimmerer, K. Lawson and C. Calvert, *Pediatric Dermatology*, 1986, **3**, 95-101.

201. C. Ogawa-Fuse, N. Morisaki, K. Shima, M. Hotta, K. Sugata, T. Ichihashi, M. Oguri, O. Yoshida and T. Fujimura, *Contact Dermatitis*, 2019, **80**, 228-233.

202. Z. Liu, G. Li, Z. Zheng, Y. Li, Y. Han, D. L. Kaplan and X. Wang, *Journal of Materials Science: Materials in Medicine*, 2018, **29**, 46.

203. Z. Liu, Z. Zheng, K. Chen, Y. Li, X. Wang and G. Li, *Colloids and Surfaces B: Biointerfaces*, 2019.

204. N. Dubey, R. Bentini, I. Islam, T. Cao, A. H. Castro Neto and V. Rosa, *Stem Cells International*, 2015, **2015**.

205. R. Ormsby, T. McNally, P. O'Hare, G. Burke, C. Mitchell and N. Dunne, *Acta Biomaterialia*, 2012, **8**, 1201-1212.

206. I. Rajzer, E. Menaszek, L. Bacakova, M. Rom and M. Blazewicz, *Journal of Materials Science: Materials in Medicine*, 2010, **21**, 2611-2622.

207. W. W. Nichols, *American Journal of Hypertension*, 2005, **18**, 3S-10S.

208. S. Munir, B. Jiang, A. Guilcher, S. Brett, S. Redwood, M. Marber and P. Chowienczyk, *American Journal of Physiology-Heart and Circulatory Physiology*, 2008, **294**, H1645-H1650.

209. L. Pan, A. Chortos, G. Yu, Y. Wang, S. Isaacson, R. Allen, Y. Shi, R. Dauskardt and Z. Bao, *Nature Communications*, 2014, **5**, 3002.

210. C. M. Boutry, A. Nguyen, Q. O. Lawal, A. Chortos, S. Rondeau-Gagné and Z. Bao, *Advanced Materials*, 2015, **27**, 6954-6961.

211. J. Xiao, Y. Tan, Y. Song and Q. Zheng, *Journal of Materials Chemistry A*, 2018, **6**, 9074-9080.

212. Y. Pang, K. Zhang, Z. Yang, S. Jiang, Z. Ju, Y. Li, X. Wang, D. Wang, M. Jian and Y. Zhang, *ACS Nano*, 2018, **12**, 2346-2354.

213. Y. Joo, J. Byun, N. Seong, J. Ha, H. Kim, S. Kim, T. Kim, H. Im, D. Kim and Y. Hong, *Nanoscale*, 2015, **7**, 6208-6215.

214. G. Y. Bae, S. W. Pak, D. Kim, G. Lee, D. H. Kim, Y. Chung and K. Cho, *Advanced Materials*, 2016, **28**, 5300-5306.

215. S. Wang, Y. Fang, H. He, L. Zhang, C. a. Li and J. Ouyang, *Advanced Functional Materials*, 2021, **31**, 2007495.

216. H. Zhou, Z. Wang, W. Zhao, X. Tong, X. Jin, X. Zhang, Y. Yu, H. Liu, Y. Ma and S. Li, *Chemical Engineering Journal*, 2021, **403**, 126307.

217. Z. Liu, Y. Zheng, L. Jin, K. Chen, H. Zhai, Q. Huang, Z. Chen, Y. Yi, M. Umar and L. Xu, *Advanced Functional Materials*, 2021, 2007622.

218. M. Wang, Z. Yan, T. Wang, P. Cai, S. Gao, Y. Zeng, C. Wan, H. Wang, L. Pan and J. Yu, *Nature Electronics*, 2020, **3**, 563-570.

219. S. Seyedin, S. Uzun, A. Levitt, B. Anasori, G. Dion, Y. Gogotsi and J. M. Razal, *Advanced Functional Materials*, 2020, **30**, 1910504.

220. W. Qi, M. Jian, C. Wang and Y. Zhang, *Advanced Functional Materials*, 2017, **27**, 1605657.

221. Z. Liu, K. Chen, A. Fernando, Y. Gao, G. Li, L. Jin, H. Zhai, Y. Yi, L. Xu and Y. Zheng, *Chemical Engineering Journal*, 2021, **403**, 126191.

222. K. Xia, X. Chen, X. Shen, S. Li, Z. Yin, M. Zhang, X. Liang and Y. Zhang, *ACS Applied Electronic Materials*, 2019, **1**, 2415-2421.

223. S. Y. Cho, Y. S. Yun, S. Lee, D. Jang, K.-Y. Park, J. K. Kim, B. H. Kim, K. Kang, D. L. Kaplan and H.-J. Jin, *Nature communications*, 2015, **6**, 1-7.

224. J. Chang, J. Shang, Y. Sun, L. K. Ono, D. Wang, Z. Ma, Q. Huang, D. Chen, G. Liu and Y. Cui, *Nature communications*, 2018, **9**, 4480.

225. K.-H. Kim, S. K. Hong, S.-H. Ha, L. Li, H. W. Lee and J.-M. Kim, *Materials Horizons*, 2020, **7**, 2662-2672.

226. S. Xu, Z. Fan, S. Yang, Y. Zhao and L. Pan, *Chemical Engineering Journal*, 2021, **404**, 126064.

227. Y. Yang, Y. Yang, Y. Cao, X. Wang, Y. Chen, H. Liu, Y. Gao, J. Wang, C. Liu and W. Wang, *Chemical Engineering Journal*, 2021, **403**, 126431.

228. Q. Yu, Z. Qin, F. Ji, S. Chen, S. Luo, M. Yao, X. Wu, W. Liu, X. Sun and H. Zhang, *Chemical Engineering Journal*, 2021, **404**, 126559.

229. J. Wei, J. Xie, P. Zhang, Z. Zou, H. Ping, W. Wang, H. Xie, J. Z. Shen, L. Lei and Z. Fu, *ACS Applied Materials & Interfaces*, 2021, **13**, 2952-2960.

230. F. Wang, B. Wang, X. Zhang, M. Lu, Y. Zhang, C. Sun and W. Peng, *Nanomaterials*, 2021, **11**, 1134.

231. J. A. Gilbert and B. Stephens, *Nature Reviews Microbiology*, 2018, **16**, 661-670.

232. S. Van Delden, M. SharathKumar, M. Butturini, L. Graamans, E. Heuvelink, M. Kacira, E. Kaiser, R. Klamer, L. Klerkx and G. Kootstra, *Nature Food*, 2021, **2**, 944-956.

233. M. Bariya, H. Y. Y. Nyein and A. Javey, *Nature Electronics*, 2018, **1**, 160-171.

234. M. Bariya, L. Li, R. Ghattamaneni, C. H. Ahn, H. Y. Y. Nyein, L.-C. Tai and A. Javey, *Science advances*, 2020, **6**, eabb8308.

235. L. Ma, R. Wu, A. Patil, S. Zhu, Z. Meng, H. Meng, C. Hou, Y. Zhang, Q. Liu and R. Yu, *Advanced Functional Materials*, 2019, **29**, 1904549.

236. T. Li, L. Li, H. Sun, Y. Xu, X. Wang, H. Luo, Z. Liu and T. Zhang, *Advanced Science*, 2017, **4**, 1600404.

237. T. Delipinar, A. Shafique, M. S. Gohar and M. K. Yapici, *ACS omega*, 2021, **6**, 8744-8753.

238. Z. Liu, Z. Li, H. Zhai, L. Jin, K. Chen, Y. Yi, Y. Gao, L. Xu, Y. Zheng and S. Yao, *Chemical Engineering Journal*, 2021, 130869.

239. G. Zhang, S. Sun, D. Yang, J.-P. Dodelet and E. Sacher, *Carbon*, 2008, **46**, 196-205.

240. Y.-R. Shin, S.-M. Jung, I.-Y. Jeon and J.-B. Baek, *Carbon*, 2013, **52**, 493-498.

241. X. Yan, T. Xu, G. Chen, S. Yang, H. Liu and Q. Xue, *Journal of Physics D: Applied Physics*, 2004, **37**, 907.

242. H.-W. Tien, Y.-L. Huang, S.-Y. Yang, J.-Y. Wang and C.-C. M. Ma, *Carbon*, 2011, **49**, 1550-1560.

243. H. Jung, H. K. Choi, S. Kim, H.-S. Lee, Y. Kim and J. Yu, *Composites Part A: Applied Science and Manufacturing*, 2017, **103**, 17-24.

244. L. Xu, Z. Liu, X. Chen, R. Sun, Z. Hu, Z. Zheng, T. T. Ye and Y. Li, *Advanced Intelligent Systems*, 2019, **1**, 1900056.

245. A. S. Afify, S. Ahmad, R. A. Khushnood, P. Jagdale and J.-M. Tulliani, *Sensors and Actuators B: Chemical*, 2017, **239**, 1251-1256.

246. N. Li, X. Chen, X. Chen, X. Ding and X. Zhao, *Rsc Advances*, 2017, **7**, 45988-45996.

247. D. Zhang, Z. Xu, Z. Yang and X. Song, *Nano Energy*, 2020, **67**, 104251.

248. L. Li, Z. Chen, M. Hao, S. Wang, F. Sun, Z. Zhao and T. Zhang, *Nano letters*, 2019, **19**, 5544-5552.

249. S. Pan, Z. Liu, M. Wang, Y. Jiang, Y. Luo, C. Wan, D. Qi, C. Wang, X. Ge and X. Chen, *Advanced Materials*, 2019, **31**, 1903130.

250. T. Huang, P. He, R. Wang, S. Yang, J. Sun, X. Xie and G. Ding, *Advanced Functional Materials*, 2019, **29**, 1903732.

251. J. Oh, J. C. Yang, J.-O. Kim, H. Park, S. Y. Kwon, S. Lee, J. Y. Sim, H. W. Oh, J. Kim and S. Park, *ACS nano*, 2018, **12**, 7546-7553.

252. Y. Gao, Q. Li, R. Wu, J. Sha, Y. Lu and F. Xuan, *Advanced Functional Materials*, 2019, **29**, 1806786.

253. D. Zhang, K. Zhang, Y. Wang, Y. Wang and Y. Yang, *Nano energy*, 2019, **56**, 25-32.

254. A. Miyamoto, S. Lee, N. F. Cooray, S. Lee, M. Mori, N. Matsuhisa, H. Jin, L. Yoda, T. Yokota and A. Itoh, *Nature nanotechnology*, 2017, **12**, 907.

255. J. Chang, J. Shang, Y. Sun, L. K. Ono, D. Wang, Z. Ma, Q. Huang, D. Chen, G. Liu and Y. Cui, *Nature communications*, 2018, **9**, 1-11.

256. Y. Yang, Z. Cao, P. He, L. Shi, G. Ding, R. Wang and J. Sun, *Nano Energy*, 2019, **66**, 104134.

257. Q. Liu, J. Chen, Y. Li and G. Shi, *ACS nano*, 2016, **10**, 7901-7906.

258. X. Shi, S. Liu, Y. Sun, J. Liang and Y. Chen, *Advanced Functional Materials*, 2018, **28**, 1800850.

259. J. Zhou and Y.-L. Hsieh, *ACS applied materials & interfaces*, 2018, **10**, 27902-27910.

260. Z. Qin, X. Sun, Q. Yu, H. Zhang, X. Wu, M. Yao, W. Liu, F. Yao and J. Li, *ACS Applied Materials & Interfaces*, 2020.

261. X. Sun, Z. Qin, L. Ye, H. Zhang, Q. Yu, X. Wu, J. Li and F. Yao, *Chemical Engineering Journal*, 2020, **382**, 122832.

262. G. Chen, H. Wang, R. Guo, M. Duan, Y. Zhang and J. Liu, *ACS Applied Materials & Interfaces*, 2020, **12**, 6112-6118.